# Chapter 4: Future global climate: scenario-based projections and near-term information

**Coordinating Lead Authors:**
June-Yi Lee (Republic of Korea), Jochem Marotzke (Germany)

**Lead Authors:**
Govindasamy Bala (India/USA), Long Cao (China), Susanna Corti (Italy), John Dunne (USA), Francois Engelbrecht (South Africa), Erich Fischer (Switzerland), John Fyfe (Canada), Christopher Jones (UK), Amanda Maycock (UK), Joseph Mutemi (Kenya), Ousmane Ndiaye (Senegal), Swapna Panickal (India), Tianjun Zhou (China)

**Contributing Authors:**
Kyle Armour (USA), Michael Byrne (UK/Ireland), Christophe Cassou (France), Hannah Christensen (UK), Sybren Drijfhout (Netherlands), Christopher Fletcher (Canada/UK), David Keller (Germany), Ben Kravitz (USA), Andrew MacDougall (Canada), Matthew Menary (France/UK), William Merryfield (Canada/USA), Sebastian Milinski (Germany), Dirk Notz (Germany), Emilia Sanchez-Gomez (France/Spain), Javier García-Serrano (Spain), Aimée Slangen (Netherlands), Malte F. Stuecker (USA/Germany), Ranjini Swaminathan (UK), Danila Volpi (Italy), Kyung-Sook Yun (Republic of Korea), Giuseppe Zappa (UK/Italy)

**Review Editors:**
Krishna Kumar Kanikicharla (Qatar/India), Vladimir Kattsov (Russia), Masahide Kimoto (Japan)

**Chapter Scientists:**
Sebastian Milinski (Germany), Kyung-Sook Yun (Republic of Korea)

**Date of Draft:**
02/03/2020

**Notes:**
TSU compiled version

**Table of Contents**

## Executive Summary

This chapter assesses simulations of future global climate change, spanning time horizons from the near-term (2021–2040) out to year 2300. Change is assessed relative to both the recent past (1995–2014) and the approximation to the pre-industrial period (1850–1900). The chapter provides the global reference for the later chapters that cover processes and regional change.

The projection results assessed here are mainly based on a new range of scenarios, Shared Socio-economic Pathways (SSPs) used in the Coupled Model Intercomparison Project Phase 6 (CMIP6). Among the SSPs, we focus on the five scenarios SSP1-1.9, SSP1-2.6, SSP2-4.5, SSP3-7.0, and SSP5-8.5. In the SSP labels, the first number refers to the assumed shared socio-economic pathway, and the second number refers to the approximate global effective radiative forcing by year 2100. Where appropriate, this chapter also assesses results from CMIP5, which used scenarios based on Representative Concentration Pathways (RCPs); the differences between the two scenario sets matter less than the differences between two generations of models. {1.6, 4.2.2, Cross-Chapter Box 7.1}

### *Temperature*

**Compared to the recent past (1995–2014), average global surface air temperature over the period 2081–2100 is *very likely* to be higher by 0.3°C–0.9°C in the low-emission scenario SSP1-1.9 and by 2.6°C–4.7°C in the high-emission scenario SSP5-8.5.** For the scenarios SSP1-2.6, SSP2-4.5, and SSP3-7.0, the corresponding *very likely* ranges are 0.6°C–1.4°C, 1.3°C–2.5°C, and 2.0°C–3.8°C, respectively. This assessment is based on multiple lines of evidence, combining new projections for the SSP scenarios with observational constraints based on past simulated warming, as well as the AR6-updated assessment of equilibrium climate sensitivity and transient climate response. Including lines of evidence in addition to the projection simulations has been possible through substantial research progress since previous IPCC assessments and has both reduced the assessed uncertainty ranges and increased the confidence in them. The uncertainty ranges for the period 2081–2100 continue to be dominated by the uncertainty in equilibrium climate sensitivity and transient climate response (*very high confidence*). {4.3.1, 4.3.4, 4.4.1, 7.5}

**A warming level of 1.5°C in globally averaged surface air temperature, relative to the period 1850–1900, is, in the near-term period 2021–2041, *very likely* to be reached in scenarios SSP3-7.0 and SSP5-8.5, *likely* to be reached in scenarios SSP1-2.6 and SSP2-4.5, and *more likely than not* to be reached in Scenario SSP1-1.9 (*high confidence)*.** The best estimate for reaching a global warming level of 1.5°C – neglecting the influence of natural internal variability – is around 2030, across all scenarios assessed here (*medium confidence*). There is *medium confidence* that a combination of equilibrium climate sensitivity and transient climate response near the lower end of the assessed *very likely* range delays reaching 1.5°C to later than during the near-term for scenario SSP1-2.6 and avoids it altogether for scenario SSP1-1.9. This broader assessment of when 1.5°C is reached encompasses the SR1.5 assessment of 1.5°C *likely* being reached in the period 2030–2052, with year 2040 as the best estimate, assuming that the current warming rate continues. However, the best estimate for when a global warming level of 1.5°C relative to 1850–1900 will be reached is assessed here in Chapter 4 to be about ten years earlier than the best estimate of the SR1.5 (*medium confidence*). The dominant cause of this re-assessment is the provision of enhanced estimates of the historical observational record. {2.3.1, 4.3.1, 4.4.1, BOX 4.1:}

**The CMIP6 multi-model ensemble range of projected warming by the end of the 21st century, relative to the period 1995–2014, is approximately 20% larger than the CMIP5 range.** The range increases mainly because the upper end of the projected warming range increases, due to models with higher equilibrium climate sensitivity in CMIP6, compared to CMIP5 (*high confidence*). {4.3.1, 4.3.4, 7.6}

**CMIP6 models with *very unlikely* high warming rates, assessed as low-probability high-warming storylines, project patterns of large wide-spread temperature and precipitation changes that strongly exceed the multi-model mean in all scenarios.** CMIP6 models consistent with such high-warming storylines cannot be excluded (*medium confidence*) and simulate particularly large changes in temperatures over extratropical land. {4.8}

**Uncertainty in near-term (2021–2040) projections of globally and annually averaged surface air temperature arises in roughly equal measure from natural internal variability and model uncertainty (*high confidence*).** By contrast, near-term projections exhibit only minor dependence on the scenario chosen, consistent with the AR5 assessment. Predictions initialized from recent observations simulate globally and annually averaged surface air temperature changes for the period 2019–2028 relative to the recent past that are consistent with the assessed *very likely* range (*high confidence*). These assessments assume that there will be no large volcanic eruption in the near term. Volcanic eruptions increase the frequency of globally extremely cold individual years and the likelihood of decades with cooling trends in globally averaged surface temperature (*high confidence*) {4.4.1, 4.4.4, BOX 4.1:}

**It is *virtually certain* that the average warming over land will be higher than over the ocean in the period 2081–2100 (*high confidence*). It is *very likely* that the warming in the Arctic will be more pronounced than on global average over the 21st century (*high confidence*)** The warming pattern *likely* varies across seasons with northern high latitudes warming more during boreal winter than summer (*medium confidence*). Models project regions with increasing and decreasing year-to-year variability of seasonal mean temperatures. Despite a projected widespread reduction in relative humidity over extratropical land regions, heat stress, expressed as a combination of temperature and humidity, will *very likely* increase over land regions with increasing GSAT (*high confidence*). {4.5.1}

**It is *very likely* that projected long-term tropospheric warming will be larger than the global mean in the Arctic lower troposphere and near surface (*high confidence).*** It is *very likely* that global mean stratospheric cooling will be larger for scenarios with higher atmospheric $CO_2$ concentrations (*high confidence*). It is *likely* that tropical upper tropospheric warming will be larger than at the tropical surface, but with an uncertain magnitude owing to discrepancies between modelled and observed temperature trends. {4.5.1}

***Precipitation***

**Global-mean land and global-mean ocean precipitation are *very likely* to increase as global surface air temperature increases over the 21st century under all five SSPs (*high confidence*). The multi-model mean change in annual global-mean land precipitation during 2081–2100 relative to 1995–2014 is 2.7% (5–95% range: 0.6–4.8%) in the low-emission scenario SSP1-1.9 and 8.2% (5–95% range: 2.5–13.8 %) in the high-emission scenario SSP5-8.5, respectively (*high confidence*).** The corresponding mean and, in parentheses, 5–95% range are 3.2% (0.7–5.6%) in SSP1-2.6, 4.7% (1.7–6.4%) in SSP2-4.5, and 5.5% (0.5–10.4%) in SSP3-7.0, respectively (*high confidence*). Based on multiple lines of evidence, global-mean land precipitation is *very likely* to increase approximately 1–3% per 1°C warming in globally averaged surface air temperature. For scenarios where the individual CMIP6 simulations unanimously agree on a global warming above 1.5°C, 2°C, and 3°C relative to 1850–1900, the ensemble-mean increase in annual global-mean land precipitation is about 1.7%, 2.9%, and 4.6%, respectively, relative to 1850–1900 (*high confidence*). {4.3.1, 4.5.1, 4.6.1}

**It is *virtually certain* that the pattern of projected precipitation changes will exhibit substantial regional and seasonal contrast in response to global warming (*high confidence*). With increased warming, a larger land area will experience statistically significant increase or decrease in precipitation (*medium confidence*).** With additional warming, the increase of area fraction with significant precipitation increase will be larger over land than over the ocean, but the increase of area with significant decrease will be larger over the ocean than over land (*medium confidence*). The change in global-mean (land plus ocean) precipitation will be constrained by global energy balance, whereas regional precipitation changes will be dominated by thermodynamic moisture convergence and dynamical processes (*high confidence*). Precipitation will increase in large parts of monsoon region, tropics and high latitude but decrease over the Mediterranean and large parts of the subtropics in response to greenhouse-gas-induced warming (*high confidence*). Interannual variability of precipitation over many land regions will be strengthened in a warmer world (*medium confidence*).{4.5.1, 4.6.1, 8.4.1}

**Near-term projected changes in precipitation are uncertain mainly because of natural internal variability and uncertainty in natural and anthropogenic aerosol forcing (*medium confidence*).** In the near term, no discernible differences in precipitation changes are projected between different SSPs (*high confidence*). The anthropogenic aerosol forcing decreases in most scenarios, contributing to increasing global-mean surface air temperature (*medium confidence*) and global-mean land precipitation (*low confidence*). Observational and modelling studies show that volcanic eruptions generally result in decreased global-mean land precipitation for up to a few years following the eruption, with climatologically wet regions drying and dry regions wetting (*medium confidence*). {4.3.1, 4.4.1, 4.4.4}

**In response to greenhouse-gas-induced warming, it is *very likely* that global land monsoon precipitation will increase, particularly in the Northern Hemisphere, although Northern Hemisphere monsoon circulation will weaken (*high confidence*).** In the long-term, monsoon rainfall change will feature a robust north-south asymmetry characterized by more increase in the Northern Hemisphere than in the Southern Hemisphere and an east-west asymmetry characterized by enhanced Asian-African monsoons and weakened North American monsoon (*high confidence*). The near-term changes in global monsoon precipitation and circulation will be affected by natural internal variability such as Atlantic Multidecadal Variability and Interdecadal Pacific Oscillation (*medium confidence*). {4.4.1, 4.5.1, 8.4.1}

***Large-scale circulation and modes of variability***

**In the near term (2021–2040), the Southern Annular Mode trend in austral summer is *likely* to be weaker than observed during the late 20$^{th}$ century under all five SSPs assessed (*high confidence*).** This is because of the opposing influence in the near- to mid-term from stratospheric ozone recovery and increases in other greenhouse gases on the Southern Hemisphere summertime mid-latitude circulation (*high confidence*). Natural internal variability will therefore *likely* obscure forced trends in the Southern Annular Mode in the near term. {4.3.3, 4.4.3}

**In the long term (2081–2100), models project a poleward shift and strengthening of the Southern Hemisphere mid-latitude jet under SSP5-8.5 relative to the recent past (1995–2014, *medium confidence*).** This is *very likely* to be accompanied by an increase in the Southern Annular Mode index in all seasons relative to 1995–2014 (*medium confidence*). It is *likely* that wind speeds associated with extratropical cyclones will intensify in the Southern Hemisphere storm track for high-emission scenarios (*high confidence*). {4.5.1, 4.5.3}

**The future boreal wintertime Northern Annular Mode is *very likely* to become slightly more positive in the future under SSP5-8.5 *(high confidence)*.** Substantial uncertainty and thus *low confidence* remain in projecting regional changes in Northern Hemisphere storm tracks and blocking, especially for the North Atlantic basin in winter; this is due to large natural internal variability and structural differences amongst models. Nevertheless, some models project responses in the North Atlantic storm track that are large compared to natural internal variability; these can be used to construct storylines for regional European and Mediterranean climate impacts. {4.5.1}

**It is *virtually certain* that the El Niño–Southern Oscillation will remain the dominant mode of interannual variability in a warmer world (*high confidence*).** There is no consensus from models for a systematic change in amplitude of El Niño–Southern Oscillation sea surface temperature variability over the 21st century in any of the SSP scenarios assessed (*medium confidence*). However, it is *very likely* that El Niño–Southern Oscillation rainfall variability, which is used for defining extreme El Niños and La Niñas, will be enhanced significantly regardless of amplitude changes in El Niño–Southern Oscillation sea surface temperature variability by the latter half of the 21st century in the scenarios SSP2-4.5, SSP3-7.0, and SSP5-8.5 (*high confidence*). {4.3.3, 4.5.3, 8.4.2}

***Cryosphere and ocean***

**Following the SSP2-4.5, SSP3-7.0, and SSP5-8.5 scenarios, it is *likely* that the Arctic Ocean will become effectively ice-free (coverage below 1 million km$^2$) in September averaged over 2081–2100 (*high***

***confidence*).** For the CMIP6 models, including those models whose ensemble spread across their individual realizations due to internal variability include the observational range of uncertainty, the vast majority of simulations show an ice-free Arctic for the first time in September before 2050, and before future cumulative anthropogenic $CO_2$ emissions reach 1000 $GtCO_2$ (*high confidence*). {4.3.2}

**Under the five scenarios assessed here, it is *very likely* that there will be a continued rise in Global Mean Sea Level (GMSL) through the 21st century, with more than a third of that rise due to thermal expansion (*high confidence*).** Under the highest emissions scenario, SSP5-8.5, the 5–95% ranges of GMSL increase by 2081–2100, relative to 1995–2014, are 0.50 m–1.07 m, with a corresponding contribution from thermal expansion of 0.21 m–0.34 m (*medium confidence*). {4.3.2}

**It is *likely* that the Atlantic Meridional Overturning Circulation (AMOC) will decrease in strength through the 21st century (*medium confidence*).** It is *likely* that under stabilization of global warming at 1.5°C, 2.0°C, or 3.0°C relative to 1850–1900, the AMOC will continue to weaken for several decades and then strengthen to historical values over several centuries (*medium confidence*). {4.3.2}

**It is *very likely* that the net uptake of carbon by the ocean and by land will increase through to the end of the 21st century (*high confidence*).** The net uptake of carbon by the ocean rises from 1850 to the end of the 21st century by about 240 PgC under SSP1-1.9 and by about 530 PgC under SSP5-8.5 based on the CMIP6 models (*high confidence*). Carbon uptake by land shows greater increases but with greater uncertainties than for ocean carbon uptake. Ocean surface pH will decrease steadily through the 21st century, except for SSP1-2.6, the lowest-emissions scenario for which results are available (*high confidence*). {4.3.2}

***Climate response to mitigation, carbon dioxide removal, and solar radiation modification***

**Emissions reductions as represented in the low-emissions scenarios SSP1-1.9 and SSP1-2.6 are *virtually certain* to limit globally averaged surface warming in the latter half of the 21st century, but the effect of emissions reductions on the globally averaged warming rate in the near term (2021–2040) will be hard to detect due to masking by natural internal variability (*high confidence*).** In contrast to previous IPCC reports, the degree of this masking can now be quantified using large initial-condition ensembles. Because of internal variability, global-mean warming rates over the near term can be larger than over the previous twenty years even under emission reductions (*medium confidence*). Conversely, a lack of warming or even a cooling trend can occur at all individual points on the globe, even under the high-emissions scenarios (*medium confidence*). The detection time of mitigation benefits for surface air temperature is in about 25–30 years for the global mean and near the end of the century at regional scales (*medium confidence)*. {4.6.3}

**Emission pathways that limit globally averaged warming to 1.5°C or 2°C typically assume the use of carbon dioxide removal (CDR) approaches in combination with emissions reductions. However, under high-emission scenarios, model-based assessments suggest that CDR approaches currently considered viable have limited potential in mitigating warming (*medium confidence*).** The climate system response is expected to lag behind the deployment of CDR (*high confidence*). Termination effects of CDR are expected to be small for the deployment of CDR that is applied at scales as large as currently deemed possible (*medium confidence*). {4.6.3}

**Solar radiation modification (SRM) can diminish greenhouse-gas-induced warming but is *likely* to impact climate at regional spatial scales and seasonal timescales *(high confidence).* There are large uncertainties in important climate processes associated with SRM options and the interactions among these processes *(high confidence)*.** Since the AR5, more modelling work has been conducted on SRM with more sophisticated treatment of aerosol-based SRM approaches, but the uncertainties such as cloud-aerosol-radiation interactions are still large (*high confidence*).There is *high confidence*, as assessed in AR5, that a sudden and sustained termination of SRM would cause a rapid increase in temperature, but a gradual phase-out of SRM combined with mitigation and CDR is *likely* to avoid large rates of warming**.** {4.6.3}

***Climate change commitment and change beyond 2100***

**Initial results from idealized numerical experiments are inconclusive whether the Zero Emissions Commitment (the rise in globally averaged surface air temperature after all $CO_2$ emissions cease) on decadal timescales is either positive or negative, with values spanning from approximately –0.4°C to 0.2°C.** There is therefore *low confidence* in the sign and magnitude of the Zero Emissions Commitments and its potential impact on the assessed remaining carbon budgets for 1.5°C or 2°C. {4.7.2, 5.5.2}

**Climate impacts of overshooting temperature goals such as 2°C persist beyond 2100 (*medium confidence*).** Some scenarios include a peak and decline in atmospheric $CO_2$ concentration, representing an attempt at recovery from a temporary overshoot of global warming above a given temperature level. Under such a scenario, SSP5-3.4-OS, some climate metrics such as globally averaged surface air temperature begin to decline, but do not fully reverse by 2100 to levels prior to the $CO_2$ peak (*medium confidence*). Global sea level continues to rise in all models up to 2100 despite a reduction in $CO_2$ to 2040 levels (*high confidence*). {4.6.3, 4.7.1, 4.7.2}

**AR5 assessments on post-2100 zero-emission commitment trajectories and reversibility based on Earth system models of intermediate complexity have now largely been confirmed with comprehensive Earth system models (*high confidence*)**. Particularly important among these advances has been the reduction in uncertainty in the requirement for net-zero $CO_2$ emissions for temperature stability. Multi-decadal reversibility has been substantiated for many atmospheric, land surface, and sea ice climate metrics following sea surface temperature recovery. Some metrics such as Atlantic Meridional Overturning Circulation have been found to undergo recovery even under temperature stabilization. Centennial-scale irreversibility of ocean warming and sea level rise is further substantiated. {4.7.2}

## 4.1 Scope and Overview of this Chapter

This chapter is the first in the WGI contribution to the IPCC Sixth Assessment Report (AR6) to assess simulations of future climate change, covering both near-term and long-term global changes. The chapter will assess simulations of physical indicators of global climate change, such as global surface air temperature (GSAT), global land precipitation, Arctic sea ice area (SIA), and global mean sea level (GMSL). Furthermore, the chapter will cover indices and patterns of properties and circulation that have global significance. The choice of quantities to be assessed is summarized in Box 2.1 and comprises a subset of the quantities covered in Chapters 2 and 3. This chapter provides consistent coverage from near-term to long-term global changes and provides the global reference for the later chapters covering important processes and regional change.

Essential input to the simulations assessed here is provided by future scenarios of concentrations or anthropogenic emissions of radiatively active substances; the scenarios represent plausible sets of decisions by humanity, without any implication that one set of decisions is more probable to occur than any other set. As in previous assessment reports, these scenarios are used for projections of future climate using global atmosphere-ocean general circulation models (AOGCMs) and Earth system models (ESMs); the latter include representation of various biogeochemical cycles such as the carbon cycle, the sulphur cycle, or ozone (e.g., Flato, 2011; Flato et al., 2013). This chapter thus provides a comprehensive assessment of the future global climate response to plausible future anthropogenic perturbations to the climate system.

A crucial element of this chapter is a comprehensive assessment of the sources of uncertainty of future projections. Uncertainty can be broken down into scenario uncertainty, model uncertainty involving both model biases and model spread, and the uncertainty arising from internal variability (Cox and Stephenson, 2007; Hawkins and Sutton, 2009). Assessment of uncertainty relies on multi-model ensembles such as the Coupled Model Intercomparison Project Phase 6 (CMIP6, Eyring et al., 2016b), large initial-condition ensembles (e.g., Kay et al., 2015), and ensembles initialized from the observed climate state (decadal predictions, e.g., Meehl et al., 2014a; Boer et al., 2016; Marotzke et al., 2016). Ensemble evaluation methods include assessment of model performance and independence (e.g., Knutti et al., 2017; Boe, 2018; Abramowitz et al., 2019); emergent and other observational constraints (e.g., Allen and Ingram, 2002; Hall and Qu, 2006; Cox et al., 2018); and the uncertainty assessment of equilibrium climate sensitivity and transient climate response in Chapter 7. Ensemble evaluation is assessed in BOX 4.1: through the inclusion of lines of evidence in addition to the projection ensembles, including implications for potential model weighting.

The uncertainty assessment in this chapter builds on one particularly noteworthy advance since the IPCC fifth Assessment Report (AR5). Internal variability, which constitutes irreducible uncertainty over much of the time horizon considered here (Hawkins et al., 2016; Marotzke, 2019), can be diagnosed precisely in models even under a changing climate through the use of large initial-condition ensembles (Kay et al., 2015). Compared to the forced climate change signal, internal variability is dominant in any individual realization – including the one that will unfold in reality – in the near term (Kirtman et al., 2013; Marotzke and Forster, 2015), is substantial in the mid-term, and is still recognizable in the long term in many quantities (Deser et al., 2012a; Marotzke and Forster, 2015). This chapter will use the enhanced information on internal variability throughout.

The expanded treatment of uncertainty allows this chapter a more comprehensive assessment than in the AR5 of the benefits from mitigation, as well as the climate response to Carbon Dioxide Removal (CRD) and Solar Radiation Modification (SRM), and how to detect them against the backdrop of internal variability. Important advances since the AR5 have been made in the detection and attribution of mitigation, CDR, and SRM (Bürger and Cubasch, 2015; Lo et al., 2016); exploring the “time of emergence” (ToE) of responses to assumed mitigation (Tebaldi and Friedlingstein, 2013; Hawkins et al., 2014; Lehner et al., 2017); and the attribution of decadal events to forcing changes that reflect mitigation (Marotzke, 2019; Spring et al., submitted).

Intimately related to the benefits of mitigation is the question of the potential crossing of thresholds relative

to global temperature goals (Geden and Loeschel, 2017); a prerequisite is an assessment of how robustly magnitudes of warming can be defined (Millar et al., 2017). This chapter provides an update to the IPCC Special Report on 1.5°C warming (SR1.5, Masson-Delmotte et al., 2018) and constitutes a reference point for later chapters on the effects of mitigation, including a robust uncertainty assessment.

The chapter is organized as follows. After Section 4.2 on the methodologies used in the assessment, Section 4.3 assesses projected changes in key global climate indicators throughout the 21st century, relative to the period 1995–2014, which comprises the last twenty years of the historical simulations of CMIP6 (Eyring et al., 2016b) and hence the most recent past simulated with the observed atmospheric composition. The global climate indicators assessed include GSAT, global land precipitation, Arctic sea ice area (SIA), global mean sea level (GMSL), the Atlantic Meridional Overturning Circulation (AMOC), global mean ocean surface pH, carbon uptake by land and ocean, the global monsoon, the Northern and Southern Annular Modes (NAM and SAM), and the El Niño–Southern Oscillation (ENSO). Section 4.3 also synthesizes assessment of GSAT using multiple lines of evidence in addition to the CMIP6 projection simulations.

Section 4.4 covers near-term climate change, defined here as the period 2021–2040 and taken relative to the period 1995–2014. Section 4.4 focuses on global and large-scale climate indicators, including rainfall and circulation indices and important modes of variability, as well as on the spatial distribution of warming. The potential roles of short-lived climate forcers (SLCFs) and volcanic eruptions on near-term climate change are also discussed. Section 4.4 synthesizes information from initialized predictions and non-initialized projections for the near-term change.

Section 4.5 then covers mid-term and long-term climate change, defined here as the periods 2041–2060 and 2081–2100, respectively, again relative to the period 1995–2014. The mid-term period is thus chosen as the twenty-year period following the short-term period and straddling the mid-century point, year 2050; it is during the mid-term that differences between different scenarios are expected to emerge against internal variability. The long-term period is defined, as in the AR5, as the twenty-year period at the end of the century. Section 4.5 assesses the same set of indicators as Section 4.4, as well as changes in internal variability and in large-scale patterns, both of which are expected to emerge in the mid- to long-term. The chapter sub-division according to time slices (near term, mid-term, and long-term) is thus to a large extent motivated by the different roles that internal variability plays in each period, compared to the expected forced climate-change signal.

Section 4.6 assesses the implications of climate policies, as simulated with climate models. First, Section 4.6 assesses patterns of climate change expected for various levels of GSAT rise including 1.5°C, 2°C, 3°C, and 4°C, compared to the proxy for the pre-industrial period 1850–1900 to facilitate immediate connection to the SR1.5 and the temperature targets specified in the Paris agreement (COP21, 2015). Section 4.6 continues with climate targets, path-dependence, and overshoot, as well as the climate response to mitigation, CDR, and SRM.

Section 4.7 assesses changes in selected global climate indicators including GSAT, GMSL, and AMOC beyond 2100, emphasizing the period out to 2300. Section 4.7 continues with climate-change commitment and the potential for irreversibility and abrupt climate change.

This chapter concludes with Section 4.8 on the potential for low-probability–high-impact changes, followed by a discussion of limitations to the assessment performed here. Answers to three frequently asked questions (FAQs) are assembled at the end of the chapter.

## 4.2 Methodology

### *4.2.1 Models, Model Intercomparison Projects, and Ensemble Methodologies*

Similar to the approach used in AR5 (Flato et al., 2013), this chapter primarily relies on comprehensive climate models (Atmosphere-Ocean General Circulation Models, AOGCMs) and Earth System Models

(ESMs); ESMs differ from AOGCMs by including representations of various biogeochemical cycles. We will here also exploit inputs from Earth System Models of Intermediate Complexity (EMICs, Claussen et al., 2002; Eby et al., 2013) and other types of model where appropriate. This chapter focuses on a particular set of coordinated multi-model experiments known as model intercomparison projects (MIPs). These recommend and document standards for experimental design for running AOGCMs and ESMs to minimise the chance of differences in results being misinterpreted. The CMIP is an activity of the World Climate Research Programme (WCRP), and the latest generation is CMIP6 (Eyring et al., 2016b). To establish robustness of results, it is vital to assess the performance of these models in mean state, variability, and response to external forcings. That evaluation has been dome using the CMIP6 'Diagnostic, Evaluation and Characterization of Klima' (DECK) and historical simulations in AR6 Chapter 3, which conclude that there is *high confidence* that the available multi-model ensembles (CMIP5 and CMIP6) span the true behaviour of the climate system for long-term changes in continental-scale averages of temperature and precipitation, Arctic sea ice extent, and global ocean heat content (Chapter 3 Section 3.8.3.2).

This chapter draws mainly on future projections referenced both against the period 1850–1900 and the recent past, 1995–2014, performed primarily under ScenarioMIP (O'Neill et al., 2016). Other MIPs also target future scenarios with a focus on specific processes or feedbacks and are summarised in Table 4.1:. The coupling between climate and the carbon cycle is represented in C4MIP, the implications of land use and cover change for climate and carbon is explored in LUMIP, the detection and attribution of climate response to chemistry and aerosol processes is explored in AerChemMIP, SRM and CDR solutions to climate warming are explored in GeoMIP and CDRMIP, respectively.

**[START TABLE 4.1 HERE]**

**Table 4.1:** MIPs utilized in Chapter 4.

| MIP / experiment | Usage | Chapter/section | Reference |
|---|---|---|---|
| DECK, 1%, 4×$CO_2$ | Diagnosing climate sensitivity | Assessed in Ch7 | (Eyring et al., 2016b) |
| CMIP6 Historical | Evaluation, baseline | Assessed in Ch3 | (Eyring et al., 2016b) |
| ScenarioMIP | Future projections | throughout Ch.4 | (O'Neill et al., 2016) |
| AerChemMIP | Aerosols and trace gases | 4.4.4 | (Collins et al., 2017a) |
| CDRMIP | Carbon Dioxide Removal | 4.6.3 | (Keller et al., 2018) |
| GeoMIP | Solar Radiation Modification | 4.6.3 | (Kravitz et al., 2011) |
| LongRunMIP | Very long term behaviour | 4.7.2 | (Rugenstein et al., 2019a) |
| PDRMIP | Forcing dependence of precipitation | 4.6.2, | (Myhre et al., 2017) |
| SIMIP | Sea ice assessment | 4.3 | (Notz et al., 2016) |
| ZECMIP | Zero emissions commitment | 4.7.2 | (Jones et al., 2019a) |
| CMIP5 | RCP scenario assessment | 4.7.1 | (Taylor et al., 2012) |

**[END TABLE 4.1 HERE]**

Multi-model ensembles provide the central focus of projection assessment. While single-model experiments have great value for exploring new results and theories, multi-model ensembles additionally allow

assessment of the robustness, reproducibility, and uncertainty attributable to model internal structure and processes variability (Hawkins and Sutton, 2009) (see Section 4.2.5). However, these multi-model 'ensembles of opportunity' often include an uneven mixture of related and dissimilar models and a suboptimal number of simulations per model for quantifying individual sources of uncertainty in projection of future climate change. Progress has been made since the AR5 in understanding the interdependence of the growing number of models contributing to CMIP (Boe, 2018). While techniques to weight model output based on performance and dependence have been proposed (Knutti et al., 2017; Olson et al., 2018; Abramowitz et al., 2019), consensus has not been reached on how to determine optimality (Weigel et al., 2010; Herger et al., 2018). Techniques underlying the combination of evaluation and weighting that are applied in this chapter are synthesized in BOX 4.1:, drawing on assessments across WGI AR6.

Perturbed-physics ensembles (Murphy et al., 2004) can account for parameter uncertainty in a given model. In the perturbed-parameter approach, uncertain model parameters are identified based on the sensitivities of results to specific parameters and the joint probability density functions to sub-select combinations of model parameters that conform to emergent observational constraints (e.g., Collins et al., 2011). These parameters are then changed between ensemble members to systematically sample the impact of parameter uncertainty on climate (Johnson et al., 2018; Regayre et al., 2018). Different ensemble members in a perturbed-parameter ensemble may have different climate biases and sensitivities. It is possible to weight ensemble members according to some performance metric or emergent constraint (Murphy et al., 2004; Fasullo et al., 2015) to improve the ensemble distribution.

Internal variability challenges identification of forced climate signals, especially when considering regional climate signals over short timescales (up to a few decades), such as local trends over the satellite era (Hawkins and Sutton, 2009; Deser et al., 2012a; Xie et al., 2015; Lovenduski et al., 2016; Suárez-Gutiérrez et al., 2017). Large initial-condition ensembles, where the same model is run repeatedly under identical forcing but with initial conditions varied through small perturbations or by sampling different times of a pre-industrial control run, have substantially grown in their use since the AR5 (Selten et al., 2004; Deser et al., 2012a; Kay et al., 2015; Rodgers et al., 2015; Hedemann et al., 2017; Stolpe et al., 2018; Maher et al., 2019). Such large ensembles have shown potential, therefore, to be used to quantify uncertainty due to internal variability (Hawkins et al., 2016; McCusker et al., 2016; Sigmond and Fyfe, 2016; Lehner et al., 2017; McKinnon et al., 2017; Marotzke, 2019) and thereby extract the forced signal from the internal noise; moreover, they allow the investigation of forced changes in internal variability (e.g., Maher et al., 2018). An alternative approach is to evaluate the combination of internal variability and structural uncertainty in a given model is stochastic physics. In this technique, a stochastic term is included into the model formulation to account for unresolved small-scale processes (Berner et al., 2017). The approach has proven useful in representing uncertainty in initialised ensembles on seasonal climate timescales (Weisheimer et al., 2014); (MacLachlan et al., 2015). Stochastic parameterisations benefit initialised forecasts by increasing the variability among individual ensemble members (Christensen and Berner, 2019), and have proven beneficial in uninitialized climate models. Stochastic physics has the potential to also improve the representation of internal variability, including the Madden-Julian Oscillation (Wang et al., 2016), ENSO variability (Christensen et al., 2017; Yang et al., 2019), variability in the Indian summer monsoon (Strømmen et al., 2018), precipitation variability (Davini et al., 2017; Watson et al., 2017), and variability in the mid-latitudes (Dawson and Palmer, 2015) with impacts for near-term projections. Stochastic physics can correct long-standing mean-state biases in climate models (Sanchez et al., 2016) and can influence the climate sensitivity of a model (Seiffert and von Storch, 2008; Meccia et al., 2019; Strommen et al., 2019).

### *4.2.2 Scenarios*

The AR5 drew heavily on four main scenarios, known as Representative Concentration Pathways (RCPs: Meinshausen et al., 2011; van Vuuren et al., 2011), and simulation results from CMIP5 (Taylor et al., 2012, see Subsection 4.2.1). The RCPs were labelled by the approximate radiative forcing reached at the year 2100, going from 2.6, 4.5, 6.0 to 8.5 W $m^{-2}$.

This chapter will draw on model simulations from CMIP6 (Eyring et al., 2016b) using a new range of

scenarios based on Shared Socio-economic Pathways (SSPs: O'Neill et al., 2016). The set of SSPs is described in detail in Chapter 1 (see Section 1.6) and recognizes that global radiative forcing levels can be achieved by different pathways of $CO_2$, non-$CO_2$ greenhouse gases (GHGs), aerosols (Amann et al., 2013; Rao et al., 2017), and land use; the set of SSPs therefore establishes a matrix of global forcing levels and socio-economic storylines. ScenarioMIP (O'Neill et al., 2016) identifies four priority (tier-1) scenarios that participating modelling groups are required to perform, SSP1-2.6 for sustainable pathways, SSP2-4.5 for middle-of-the-road, SSP3-7.0 for regional rivalry, and SSP5-8.5 for fossil-fuel-rich development. This chapter will focus its assessment on these, plus the SSP1-1.9 scenario, which is directly relevant to assessment of the 1.5°C climate target. Further, this chapter discusses these scenarios and their extensions past 2100 in the context of the very long-term climate change in Section 4.7.1.

ScenarioMIP simulations include advances in techniques to better harmonize with historical forcings relative to CMIP5. For example, projected changes in the solar cycle include long-term modulation rather than a repeating solar cycle (Matthes et al., 2017). Background aerosols are ramped down to an average historical level used in the control simulation by 2025 and background volcanic forcing is ramped up from the value at the end of the historical simulation period (2015) over 10 years to the same constant value prescribed for the piControl simulations in the DECK, and then kept fixed – both changes are intended to avoid uncertainty in unknowable natural forcing to impact the near-term projected warming.

Complete backward comparability between CMIP5 and CMIP6 scenarios cannot be established for detailed regional assessments, because the SSP scenarios include regional forcings - especially from land use and aerosols - that are different from the CMIP5 RCPs. At a global level, however, a quantitative comparison is possible between corresponding SSP and RCP radiative forcing levels. The RCP scenarios assessed in the AR5 all showed similar, rapid reductions in Short-Lived Climate Forcers (SLCFs) and emissions of SLCF precursor species over the 21st century; the CMIP5 projections hence did not sample a wide range of possible trajectories for future SLCFs. The SSP scenarios assessed in the AR6 offer more scope to explore SLCF pathways as they sample a broader range of air quality policy options (Gidden et al., 2018) and relationships of $CO_2$ to non-$CO_2$ greenhouse gases (Meinshausen et al., 2019a). Other MIPs (see Section 4.2.1) have been designed to explicitly explore some of the implications of the different socio-economic storylines for a given radiative forcing level. While this chapter focuses mainly on scenarios out to 2040 as near-term and 2100 as long-term, it also includes extensions out to 2300 as described in ScenarioMIP (O'Neill et al., 2016; Meinshausen et al., 2019b).

### *4.2.3 Sources of Near-Term Information*

This subsection describes the three main sources of near-term information used in Chapter 4. These are 1) the projections from the CMIP6 multi-model ensemble introduced in Section 4.2.1 (Eyring et al., 2016b; O'Neill et al., 2016), 2) observationally constrained projections (Gillett et al., 2013; Stott et al., 2013), and 3) the initialized predictions contributed to CMIP6 from the Decadal Climate Prediction Project (DCPP, Boer et al., 2016). The projections under 1) and the observational constraints under 2) are used for all time horizons considered in this chapter, whereas the initialized predictions under 3) are relevant only in the near-term.

Observationally constrained projections (Gillett et al., 2013; Stott et al., 2013) use detection and attribution (D&A) methods to correct for systematic model biases and thus provide improved projections of near-term change. Notable advances have been made since the AR5, illustrated through the example of observationally constrained estimates of Arctic sea-ice loss when global average surface temperature is stabilized at 1.5°C, 2.0°C, and 3.0°C warming above pre-industrial (Shiogama et al., 2016; Screen and Williamson, 2017; Jahn, 2018; Screen, 2018; Sigmond et al., 2018). There is *high confidence* that these approaches can reduce the uncertainties involved in such estimates.

The AR5 was the first IPCC report to assess decadal climate predictions initialized from the observed climate state (Kirtman et al., 2013), and assessed with *high confidence* that these predictions exhibit positive skill for near-term average surface temperature information, globally and over large regions, for up to ten years. Substantially more experience in producing initialized decadal predictions has been gained since the

AR5; the remainder of this subsection assesses the advances made.

Because the "memory" that potentially enables prediction of multi-year to decadal internal variability resides mainly in the oceans, some systems initialize the ocean state only (e.g., Yeager et al., 2018a), whereas others incorporate observed information in the initial atmospheric states (e.g., Pohlmann et al., 2013; Knight et al., 2014) or other non-oceanic drivers that provide further sources of predictability (Bellucci et al., 2015a). Ocean initialization techniques generally use one of two strategies. Under full-field initialization, estimates of observed climate states are represented directly on the model grid. A potential drawback is that predictions initialized using the full-field approach tend to drift toward the biased climate preferred by the model (Smith et al., 2013a; Bellucci et al., 2015b; Kröger et al., 2018). Such drifts can be as large as, or larger than, the climate anomaly being predicted and may therefore obscure predicted climate anomalies unless corrected for through post-processing. By contrast, anomaly initialization reduces drifts by adding observed anomalies (i.e. deviations from mean climate) to the mean model climate (Pohlmann et al., 2013; Smith et al., 2013a; Thoma et al., 2015b; Cassou et al., 2018). For both approaches, unrealistic features in the observation data used for initialization may induce unrealistic transient behavior (Pohlmann et al., 2017; Teng et al., 2017). As yet, neither of the initialization strategies has been clearly shown to be superior (Hazeleger et al., 2013; Magnusson et al., 2013; Smith et al., 2013a; Marotzke et al., 2016), although such comparisons may be sensitive to the model, region, and details of the initialization and forecast assessment procedures considered (Polkova et al., 2014; Bellucci et al., 2015b).

There is also a wide range of techniques employed to assimilate observed information into models in order to generate suitable initial conditions (Polkova et al., 2019). These range in complexity from simple relaxation towards observed time series of sea surface temperature (SST) (Mignot et al., 2016) or wind stress anomalies (Thoma et al., 2015a, 2015b), to relaxation toward three-dimensional ocean and sometimes atmospheric state estimates from various sources (e.g., Pohlmann et al., 2013; Knight et al., 2014), to sophisticated data assimilation methods such as the ensemble Kalman filter (Msadek et al., 2014; Karspeck et al., 2015; Polkova et al., 2019) and the initialization of sea ice (Guemas et al., 2016; Kimmritz et al., 2018). In addition, decadal predictions necessarily consist of ensembles of forecasts to quantify uncertainty as discussed in Section 4.2.1. A common way to generate an ensemble is through sets of initial conditions containing small variations that lead to different subsequent climate trajectories. A variety of methods and assumptions has been employed to generate and filter initial-condition ensembles for decadal prediction (e.g., Marini et al., 2016; Kadow et al., 2017; Cassou et al., 2018). As yet, there is no clear consensus as to which initialization and ensemble generation techniques are most effective, and evaluations of their comparative performance within a single modelling framework are needed (Cassou et al., 2018).

A consequence of model imperfections and resulting model systematic errors or biases is that estimates of these errors must be removed from the prediction to isolate the predicted climate anomaly. Because of the tendency for systematic drifts to occur following initialization, bias corrections generally depend on time since the start of the forecast, often referred to as lead time. In practice, the lead-time-dependent biases are calculated using ensemble retrospective predictions, also known as hindcasts, and recommended basic procedures for such corrections are provided in previous studies (Goddard et al., 2013; Boer et al., 2016). Besides mean climate as a function of lead time, further aspects of decadal predictions may be biased, and additional correction procedures have thus been proposed to remove biases in representing long-term trends (Kharin et al., 2012; Kruschke et al., 2016; Balaji et al., 2018), as well as more general dependences of drift on initial conditions (Fučkar et al., 2014; Nadiga et al., 2019).

Many skill measures exist that describe different aspects of the correspondence between predicted and observed conditions, and no single metric should be considered exclusively. Important aspects of forecast performance captured by different skill measures include: 1) the ability to predict the sign and phase of future climate variability; 2) the typical magnitude of differences between predicted and observed values, forecast reliability and resolution (Corti et al., 2012); and 3) whether the forecast ensemble appropriately represents uncertainty in the predictions. A framework for skill assessment (also called verification) that encompasses each of these aspects of forecast quality has been proposed (Goddard et al., 2013).

One additional aspect of forecast quality assessment is that estimated skill can be degraded by errors in

observational datasets used for verification, in addition to errors in the predictions (Massonnet et al., 2016; Ferro, 2017; Karspeck et al., 2017; Juricke et al., 2018). This suggests that skill may tend to be underestimated, particularly for climate variables whose observational uncertainties are relatively large, and that the predictions themselves may prove useful for assessing the quality of observational datasets (Massonnet, 2019).

Skill assessments have shown that initialized predictions can out-perform their uninitialized counterparts (Doblas-Reyes et al., 2013; Meehl et al., 2014a; Bellucci et al., 2015a; Smith et al., 2018, 2019b; Yeager et al., 2018b), although such comparisons are sensitive to the region and variable considered and multi-model predictions are generally more skilful than individual models (Doblas-Reyes et al., 2013; Smith et al., 2013b, 2019c). Considerable skill, especially for temperature, can be attributed to external forcings such as changes in GHG and aerosol concentrations. This contribution to skill has been found to exceed that from the prediction of internal variability except in the early stages (about one year for global SST) of the forecast (Corti et al., 2015; Sospedra-Alfonso and Boer, 2019), though idealized potential skill measures suggest that improving the prediction of internal variability could extend this crossover to longer lead times (Boer et al., 2013). In some cases, part of the skill arises from the ability of initialised predictions to capture observed transitions of major modes of climate variability (Meehl et al., 2016) such as the Pacific Decadal Variability (PDV) and the Atlantic Multidecadal Variability (AMV) (see Sections 4.4.3.3, 4.4.3.5 and Technical Annex AVI.7 and AVI.8). Although the skill added by initialization tends to be modest, particularly over land and at longer lead times, an alternative approach of assessing the relative skill of initialized and uninitialized predictions in forecasting observed variability suggests the value added by initialization may be greater than previously thought (Scaife and Smith, 2018; Kushnir et al., 2019; Smith et al., 2019c).

Initialized predictions of near-surface temperature are particularly skilful over the North Atlantic, a region of high potential and realised predictability (Pohlmann et al., 2009; Boer et al., 2013; Yeager and Robson, 2017) (*high confidence*). Much of this predictability is associated with the North Atlantic subpolar gyre (Wouters et al., 2013), where skill in predicting ocean conditions is typically high (Hazeleger et al., 2013) and shifts in ocean temperature and salinity potentially affecting surface climate can be predicted up to several years in advance (Robson et al., 2012; Hermanson et al., 2014), although such assessments remain challenging due to incomplete knowledge of the state of the ocean during the hindcast evaluation periods (Menary and Hermanson, 2018). A significant improvement in temperature skill is also found over some land regions including Europe and the Middle East (Smith et al., 2019c).

In contrast to the relatively high skill in the North Atlantic, near-surface temperature forecast skill is low or even negative throughout much of the central and north-eastern Pacific (Doblas-Reyes et al., 2013), although some evidence for multi-year skill in forecasting shifts in the Interdecadal Pacific Oscillation and its impacts on global temperature has been found (Guemas et al., 2013b; Meehl et al., 2014b, 2016; Thoma et al., 2015a). Skill for multi-year to decadal precipitation forecasts is generally much lower than for temperature, although one exception is Sahel rainfall (Sheen et al., 2017), due to its dependence on predictable variations in North Atlantic SST (Martin and Thorncroft, 2014a). In addition, decadal predictions having large ensemble sizes appear to be able to predict multi-annual temperature (Sienz et al., 2016; Sospedra-Alfonso and Boer, 2019), precipitation (Yeager et al., 2018a; Smith et al., 2019c), and atmospheric circulation (Smith et al., 2019d) anomalies over certain land regions although with ensemble-mean magnitudes that are much weaker than observed. This discrepancy may be symptomatic of an apparent deficiency in climate models that causes predictable signals to be much weaker than in nature (Eade et al., 2014; Scaife and Smith, 2018; Smith et al., 2019d).

Evidence is accumulating that additional properties of the Earth system relating to ocean variability may be skilfully predicted on multi-annual time scales. These include levels of Atlantic hurricane activity (Caron et al., 2017), drought and wildfire (Chikamoto et al., 2017), and variations in the ocean carbon cycle including $CO_2$ uptake (Li et al., 2016b, 2019; Lovenduski et al., 2019) and chlorophyll (Park et al., 2019).

In summary, there is *high confidence* that information from initialized predictions reduces the uncertainty of projections of future temperature on a global scale and for large regions over multiannual to decadal scales. For example, Smith et al. (2018) apply a multi-model prediction ensemble to assess the likelihood that global

warming of 1.5°C above pre-industrial level will be temporarily exceeded in the near future. By contrast, there is *medium* or *low confidence* for similar uncertainty reductions for other climate quantities.

### *4.2.4 Pattern Scaling*

The CMIP6 projections of future climate change under different SSPs are representative of a range of transient and stabilization scenarios (O'Neill et al., 2016). Projected climate change futures are typically represented for specific periods in the future, for example in this chapter, projections are presented for near-term (2021–2040), mid-term (2041–2060), and long-term (2081–2100) periods. One important source of uncertainty in projections presented for fixed future time-slabs is the underlying scenario used to force the AOGCMs. Another is the structural uncertainty associated with AOGCM climate sensitivity. Presenting projections and associated measures of uncertainty for specific future time-slabs (see Sections 4.4 and 4.5) remains the most widely applied methodology towards informing climate change impact studies. It is becoming increasingly important, however, from the perspective of climate change and mitigation policy, to present projections of future climate change not only as a function of different periods in the future, but also as a function of the increase in GSAT (see Section 1.6.2). In particular, the IPCC SR1.5 report (Masson-Delmotte et al., 2018b) assessed the regional patterns of warming and precipitation change for increase in GSAT of 1.5°C and 2°C above 1850–1900 levels. The report compared impacts at 1.5°C and 2°C of global warming. For such an analysis, it is important to develop an understanding of the spatial variations of temperature and other climate variables for a particular increase in GSAT. Techniques used to represent the spatial variations in climate at a given increase in GSAT are referred to as 'pattern scaling'.

In the original (or traditional) methodology as applied in IPCC AR5 (Collins et al., 2013), patterns of climate change in space are calculated as the product of the change in GSAT at a given point in time and a spatial pattern of change that is constant over time and the scenario under consideration, and which may or may not depend on a particular climate model (Allen and Ingram, 2002; Mitchell, 2003; Lambert and Allen, 2009; Andrews and Forster, 2010; Bony et al., 2013; Lopez et al., 2014). This approach assumes that external forcing does not affect the internal variability of the climate system, which may be regarded a stringent assumption when taking into account decadal and multi-decadal variability (Lopez et al., 2014) and the potential nonlinearity of the climate change signal. Moreover, pattern scaling is expected to have lower skill for variables with large spatial variability (Tebaldi and Arblaster, 2014). Pattern scaling also fails to capture changes in boundaries that moves poleward such as sea ice extent and snow cover (Collins et al., 2013), and temporal frequency quantities such as frost days that decrease under warming but are bounded at zero. Spatial patterns are also expected to be different between transient and equilibrium simulations because of the long adjustment time scale of the deep ocean.

Modifications of the AR5 approach have since explored the role of aerosols in modifying regional climate responses at a specific degree of global warming and also the effect of different GCMs and scenarios on the scaled spatial patterns (Frieler et al., 2012; Levy et al., 2013). Furthermore, the modified forcing-response framework (Kamae and Watanabe, 2012, 2013; Sherwood et al., 2015), which decomposes the total climate change into fast adjustments and slow response, identifies the fast adjustment as forcing-dependent and the slow response as forcing-independent, scaling with the change in GSAT.

For precipitation change, there is suppression during the fast-adjustment phase for $CO_2$ and black-carbon radiative forcing (Andrews et al., 2009; Bala et al., 2010; Cao et al., 2015a), but there is near-zero fast adjustment for solar forcing. By contrast, the slow response in precipitation change is independent of the forcing. This indicates that pattern scaling is not expected to work well for climate variables that have a large fast-adjustment component. Even in such cases, pattern scaling still works for the slow response component, but a correction for the forcing-dependent fast adjustment would be necessary to apply pattern scaling to the total climate change signal. In a multi-model setting, it has been shown that temperature change patterns conform better to pattern scaling approximation than precipitation patterns (Tebaldi and Arblaster, 2014).

Most recently, (Herger et al., 2015) have explored the use of multiple predictors for the spatial pattern of change at a given degree of global warming, following the approach of Joshi et al. (2013) that explored the

role of the land-sea warming ratio as a second predictor. They found that the land-sea warming contrast changes in a non-linear way with GSAT, and that it approximates the role of the rate of global warming in determining regional patterns of climate change. The inclusion of the land-sea warming contrast as the second predictor provides the largest improvement over the traditional technique. However, as pointed out by Herger et al. (2015), multiple-predictor approaches still cannot detect nonlinearities (or internal variability), such as the apparent dependence of spatial temperature variability in the mid to high latitudes on GSAT (e.g. Screen, 2014; Fischer and Knutti, 2014).

An alternative to the traditional pattern scaling approach is the time-shift method described by Herger et al. (2015) which is applied in this chapter (also called the epoch approach, see Section 4.6.1). When applied to a transient scenario such as SSP5-8.5, a future time-slab is referenced to a particular increase in the GSAT (e.g., 1.5°C or 2°C of global warming above pre-industrial levels). The spatial patterns that result represent a direct scaling of the spatial variations of climate change at the particular level of global warming. An important advantage of this approach is that it ensures physical consistency between the different variables for which changes are presented (Herger et al., 2015). The internal variability does not have to be scaled and is consistent with the GSAT change. The time-shift method furthermore allows for a partial comparison of how the rate of increase in GSAT influences the regional spatial patterns of climate change. For example, spatial patterns of change for global warming of 2°C can be compared across the SSP2-4.5 and SSP5-8.5 scenarios. Direct comparisons can also be obtained between variations in the regional impacts of climate change for the case where global warming stabilizes at, for instance, 1.5°C or 2°C of global warming, as opposed to the case where the GSAT reaches and then exceeds the 1.5°C or 2°C thresholds (Tebaldi and Knutti, 2018a). An important potential caveat is that forcing mechanisms such as aerosol radiative forcing are represented differently in different models, even for the same SSP. This may imply different regional aerosol direct and indirect effects, implying different regional climate change patterns. Hence, it is important to consider the variations in the forcing mechanisms responsible for a specific increase in GSAT towards understanding the uncertainty range associated with the variations in regional climate change. A minor practical limitation of this approach is that stabilization scenarios at 1.5°C or 2°C of global warming, such as SSP1-2.6, do not allow for spatial patterns of change to be calculated from these scenarios at higher levels of global warming, while it is possible in scenarios such as SSP5-8.5 (Herger et al., 2015).

In this chapter, the spatial patterns of change as a function of increase in the GSAT are thus constructed using the time-shift approach to consider various nonlinearities and internal variability that influence the projected climate change signal. This implies a reliance on large ensemble sizes to quantify the role of uncertainties in regional responses to different degrees of global warming. The assessment in Section 4.6.1 also explores how the rate of global warming (as represented by different SSPs), aerosol effects, and transient as opposed to stabilization scenarios influence the spatial variations in climate change at specific levels of global warming.

### *4.2.5 Quantifying Various Sources of Uncertainty*

The spread across individual runs within a multi-model ensemble represents a combination of different sources of uncertainties (see Chapter 1 Section 1.4.2), specifically scenario or future radiative forcing uncertainties, climate response uncertainties (also referred to as model uncertainties) due to parametric and structural uncertainties in the model representation of the climate system and internal variability (e.g., Hawkins and Sutton, 2009; Kirtman et al., 2013). While the nature of these uncertainties has already been introduced in Section 1.4.2, this subsection assesses methods to disentangle different sources of uncertainties and quantify their contributions to the overall ensemble spread.

As discussed extensively already in the AR5 (Collins et al., 2013), ensemble spread in projections performed with different climate models accounts for only part of the entire model uncertainty, even when considering the uncertainty in the radiative forcing in projections (Vial et al., 2013) or in the forced response. Obtaining a full assessment of the uncertainty in an ensemble of projections thus continues to pose a fundamental epistemological challenge (Parker, 2009; Frisch, 2015; Baumberger et al., 2017). Assessing these shared errors in projections remains fundamentally very difficult. Emergent constraints are also used as one way to

reduce uncertainties in projections (e.g., Hall and Qu, 2006; Cox et al., 2018).

The AR5 uncertainty characterisation (Kirtman et al., 2013) followed Hawkins and Sutton (2009) and diagnosed internal variability through a high-pass temporal filter. This approach has deficiencies particularly if internal variability manifests itself also on the multi-decadal timescales (Deser et al., 2012a; Marotzke and Forster, 2015) and is classified as (model) response uncertainty instead of internal variability. Single-model initial-condition large ensembles revealed that the AR5 approach underestimates the role of internal variability and overestimates the role of model uncertainty (Maher et al., 2018; Stolpe et al., 2018) particularly at the local scale. On the other hand it has been shown that the separation yields a reasonable approximation for uncertainty separation for GSAT (Lehner et al., 9999).

The availability of single-model initial-condition large ensembles thus represents a crucial step towards a cleaner separation of model uncertainty and internal variability (Deser et al., 2014, 2016; Saffioti et al., 2017; Milinski et al., 2019; Sippel et al., 2019). For time horizons beyond the limit of decadal predictability (Branstator and Teng, 2010; Meehl et al., 2014a; Marotzke et al., 2016), internal variability constitutes an uncertainty that is irreducible, but can be accurately quantified (Fischer et al., 2013; Deser et al., 2016; Hawkins et al., 2016; Maher et al., 2019).

Future radiative forcing or scenario uncertainty cannot be quantified due to the impossibility of attaching reliable probabilities to societal decisions (Schneider, 2001). A more comprehensive representation of SSPs induces additional uncertainties, for example the response to land use changes (van Vuuren et al., 2011b; Ciais et al., 2013; O'Neill et al., 2016; Christensen et al., 2018). Additional uncertainty comes from climate carbon-cycle feedbacks and the residence time of atmospheric constituents, and are at least partly accounted for in emission-driven simulations as opposed to concentration-driven simulations (Friedlingstein et al., 2014; Hewitt et al., 2016). The climate carbon-cycle feedbacks affect the transient climate response to emissions (TCRE). Constraining this uncertainty is crucial for the assessment of remaining carbon budgets consistent with global mean temperature levels (Millar et al., 2017; Masson-Delmotte et al., 2018b) and is covered in Chapter 5 of this report.

The relative magnitudes of model uncertainty and internal variability depend on the time horizon of the projection, location, spatial and temporal aggregation, variable, and signal strength (Rowell, 2012; Fischer et al., 2013; Deser et al., 2014; Saffioti et al., 2017; Kirchmeier-Young et al., 2019). New literature published after the AR5 systematically discusses the role of different sources of uncertainty and shows that the relative contribution of internal variability is larger for short than for long projection horizons (Marotzke and Forster, 2015), larger for high latitudes than for low latitudes, larger for land than for ocean variables, larger at station level than continental than global means, larger for annual maxima/minima than for multi-decadal means, larger for dynamic quantities (and, by implication, precipitation) than for temperature (Fischer et al., 2014).

The method introduced by Hawkins and Sutton (2009) to GSAT projections reveals that by the end of the 21st century, the climate response or model uncertainty in CMIP6 is larger than in CMIP5 at the expense radiative forcing or scenario uncertainty (Lehner et al., 9999). This is the case even when sub-selecting pathways and scenarios that are most similar in CMIP5 and CMIP6, i.e. the range from RCP2.6 to RCP8.5 vs. SSP1-2.6 to SSP5-8-5, respectively (Lehner et al., 9999). The larger range of response uncertainty is further consistent with the larger range of TCR and GSAT warming for a comparable pathway in CMIP6 than CMIP5 (Forster et al., 2019; Tokarska et al., 9999).

Some uncertainties are not or only partially accounted for in the CMIP6 experiments, such as long-term Earth system feedbacks including missing land-ice feedbacks or some long-term carbon-cycle feedbacks (Fischer et al., 2018). Where appropriate, this chapter will use results from non-CMIP ESMs or EMICs to assess the role of these feedbacks.

### *4.2.6 Display of Model Agreement and Spread*

Maps of multi-model mean changes provide an average estimate for the forced model climate response to a certain forcing. However, they do not include any information on the robustness of the response across models nor on the significance of the change with respect to unforced internal variability (Tebaldi et al., 2011). Models can consistently show absence of significant change, in which case they should not be expected to agree on the sign of a change (e.g., Tebaldi et al., 2011; Fischer et al., 2014). In a multi-model mean map of precipitation where the median shows no change, it is unclear whether the models consistently project both small and insignificant increases and decreases or whether projections span both substantial increases and substantial decreases (Tebaldi et al., 2011; McSweeney and Jones, 2013). Therefore, a set of different methods have been introduced in literature to display model robustness and to put a climate change signal into the context of internal variability. The AR5 Box 12.1 provides a detailed assessment of different methods of mapping model robustness.

The combination of several large initial-condition (e.g., Kay et al., 2015) and multi-model ensembles (Taylor et al., 2012; Eyring et al., 2016b) provides new opportunities to separate internal variability from model uncertainty and to better understand whether individual model realizations disagree due to internal variability or model differences. Most methods of quantifying robustness assume, however, that only one realization from each model is applied. There are new challenges that arise from having inhomogeneous multi-model ensembles with many members for some models and single members for others (Olonscheck and Notz, 2017). Furthermore, the methods that map model robustness usually ignore that sharing parametrizations or entire components across coupled models can lead to substantial model interdependence (Fischer et al., 2011; Kharin et al., 2012; Knutti et al., 2013a, 2017; Leduc et al., 2015; Sanderson et al., 2015, 2017a; Annan and Hargreaves, 2017; Boe, 2018; Abramowitz et al., 2019). This may lead to an overestimation of model agreement if a substantial fraction of models is interdependent. However, quantifying and accounting for model dependence in a robust way remain challenging (Abramowitz et al., 2019).

Furthermore, absence of significant mean change in a certain climate variable does not imply absence of substantial impact, because there may be substantial change in variability, which is typically not mapped (McSweeney and Jones, 2013).

The following sections use the same methodology as the AR5 to map model robustness and significance of the signal (Eyring et al., 2016c). The approach uses stippling to mark regions where the multi-model mean change exceeds two standard deviations of internal variability and where at least 90% of the models agree on the sign of change. Thus, the stippling can be interpreted as ‘large change with high model agreement’. Regions where the model mean is less than one standard deviation of internal variability are hatched and interpreted as small signal or low agreement of models. This approach represents a compromise between transparency and comprehensiveness of the diverse mapping methodologies and has the advantage that a broad community is used to interpret this mapping methodology. The approach used here has the limitation that it does not explicitly differentiate areas of no or little change and areas of low model agreement where for instance half of the models show a significant increase and the other half a significant decrease that cancel each other in the multi-model mean (see AR5 Chapter 12 Section 12.1). More comprehensive approaches differentiate these areas with a third type of overlay (Knutti et al., 2013b). Such cases are in this chapter discussed as text and, where necessary, illustrated with storylines accounting for different and potentially opposing signals (see Chapter 1.4.3). It should further be noted that changes smaller than two or even one standard deviation can have potential impacts particularly if they persist over sustained periods, that is of several decades. Maps of mean changes further ignore potential changes in variability addressed by a more comprehensive assessment of changes in temperature variability and modes of internal variability in this chapter.

The degree to which climate change drivers and processes are known and formulated in the various models is very important in the display of projections. This display makes it straightforward to extract long-term policy-relevant information (magnitudes, robustness, significance, and certainty levels). Recent developments in climate change modelling including more physically consistent schemes used in CMIP6 runs and new analysis methods applied to both CMIP5 and CMIP6 have brought out information with

smaller spread and increased convergence of change evidence at specific warming levels (Notz and Stroeve, 2016; Knutti et al., 2017). These are substantial advancements of the AR6 above AR5 in the display and assessment of model agreement.

**[START BOX 4.1 HERE]**

**BOX 4.1: Ensemble Evaluation and Weighting**

The IPCC AR5 used a pragmatic approach to quantify the uncertainty in CMIP5 climate projections (Collins et al., 2013). One realization per model per scenario was picked and defined the ensemble. For most quantities, the 5–95% ensemble range was used to characterize the uncertainty, but the 5–95% ensemble range was interpreted as the 17–83% (*likely*) uncertainty range. The uncertainty was thus explicitly assumed to contain sources not represented by the model range. While straightforward and clearly communicated, this approach had several drawbacks.

i) The uncertainty breakdown into scenario uncertainty, model uncertainty, and internal variability (Cox and Stephenson, 2007; Hawkins and Sutton, 2009) in the AR5 followed Hawkins and Sutton (2009) and diagnosed internal variability through a high-pass temporal filter (Kirtman et al., 2013), but it has since become clear that even multi-decadal trends contain substantial internal variability relative to the forced response (e.g., Deser et al., 2012a, 2020; Marotzke and Forster, 2015; Lehner et al., 2020); hence a more comprehensive approach is needed.

ii) The uncertainty characterization ignores observation-based information about internal climate variability during the most recent past, such as is used in initialized predictions. While this may matter little for the long-term projections (Collins et al., 2013), it is very important for the near-term future (Kirtman et al., 2013). It was necessary to include additional uncertainty quantification for the near-term projections in the AR5 (Kirtman et al., 2013), and while this addition was necessary and justified, it created an inconsistency in the transition from near-term to long-term GSAT assessment in the AR5.

iii) The ensemble-range-based uncertainty characterization for equilibrium climate sensitivity (ECS) was distinct from the *likely* range assessed for ECS in the AR5 (Collins et al., 2013), and while the CMIP5 range in ECS and the AR5 ECS *likely* range did not differ much, the difference did create an inconsistency. Furthermore, WGIII in the AR5 used the assessed *likely* range for ECS in their calculations of carbon budgets (IPCC, 2014), and as recent discussion has shown (e.g., Millar et al., 2017, 2018a, 2018b; Schurer et al., 2018), these uncertainties matter a great deal when assessing remaining carbon budgets consistent with a given ambitious global mean temperature goal such as limiting global warming to 1.5°C above pre-industrial levels.

Another important consideration concerns the potential weighting of model contributions to an ensemble, based on model independence, model performance during the historical period, or both. Such model weighting (in fact, model selection) was performed in the AR5 for the projections of Arctic sea ice (Collins et al., 2013), but that particular application has subsequently been shown by Notz (2015) to be contaminated by internal variability, making the resulting weighting questionable (see also Stroeve and Notz (2015)). For a general cautionary note, see Weigel et al. (2010). Approaches that take into account internal variability and model independence have been proposed since the AR5 (Knutti et al., 2017; Boe, 2018; Abramowitz et al., 2019).

There are hence good reasons for basing an assessment of future global climate on lines of evidence in addition to the projection simulations. However, despite some progress, there does not yet exist a universal, robust method for weighting a projection ensemble. Therefore the default in this chapter follows the AR5 approach (Collins et al., 2013) and interprets the CMIP6 5–95% ensemble range as the *likely* uncertainty range. Deviation from this default is flagged explicitly.

Additional lines of evidence enter the assessment particularly for the most important indicator of global climate change, GSAT. The CMIP6 ensemble range of projected warming by the end of the 21st century, relative to the average over the period 1995–2014, is approximately 20% larger than the CMIP5 range (Section 4.3.1, Section 4.3.4). The range has increased mainly because the upper end of the projected warming range has increased, due to models with higher ECS in CMIP6, compared to CMIP5 (e.g., Meehl et

al., 2020; Meinshausen et al., 2020; Tokarska et al., 2020; Zelinka et al., 2020, *high confidence*). Because change in several other important climate quantities scales with change in GSAT (Section 4.2.4), bringing in additional lines of evidence is particularly important for the GSAT assessment.

The Chapter 4 assessment uses information from the following sources, combining them where the existing literature allows:

(i) The CMIP6 multi-model ensemble (Eyring et al., 2016b), see Section 4.2.1 for a detailed listing), augmented if appropriate by the CMIP5 ensemble (Taylor et al., 2012).

(ii) Single-model large initial-condition ensembles (e.g., Kay et al., 2015; Sigmond and Fyfe, 2016; Maher et al., 2019) and combinations of control runs with CMIP transient simulations (e.g., Thompson et al., 2015; Olonscheck and Notz, 2017) to characterize internal variability. Several analyses using multiple large ensembles have recently become available and add robustness to the results (Maher et al., 2018, 9999a, 9999b; Deser et al., 9999; Lehner et al., 9999).

(iii) Assessed best estimates, *likely*, and *very likely* ranges of ECS and transient climate response (TCR) based on multiple lines of evidence (Section 7.5, Collins et al., 2013). The ECS and TCR ranges are converted into GSAT ranges using as an emulator a two-layer energy balance model (e.g., Held et al., 2010) that is driven by the effective radiative forcing (ERF) assessed in Chapter 7 (see Cross-Chapter Box 7.1). Assuming the best estimate for ERF resulting from a doubling of the $CO_2$ concentration, $f_{2\times}$=4.0 $Wm^{-2}$ (Section 7.3), and using the so-called zero-layer approximation to the EBM (e.g., Marotzke and Forster, 2015; Jiménez-de-la-Cuesta and Mauritsen, 2019) permits a one-to-one translation of any pair of ECS and TCR into a pair of climate feedback parameter $\lambda$ and ocean heat uptake coefficient $\kappa\varepsilon$, using the simple equations $\lambda=-f_{2\times}/ECS$ and $\kappa\gamma= f_{2\times}/TCR - f_{2\times}/ECS$ (e.g., Jiménez-de-la-Cuesta and Mauritsen, 2019); see Chapter 7 for a detailed discussion). The results are displayed in Box 4.1, Figure 1: and are used in the synthesis assessment in Section 4.3.4.

(iv) Model independence diagnosed a priori, based on shared model components for atmosphere, ocean, land surface, and sea ice of CMIP5 models (Boe, 2018). CMIP5 models have been re-sampled assuming that two models sharing either the atmosphere or the ocean component are effectively the same model (Maher et al., 9999b). Downweighting CMIP5 models that share a component with another has substantial influence on diagnosed model agreement on change in ENSO (Maher et al., 9999b), but has negligible influence (much less than 0.1°C) on the ensemble mean and range of GSAT change over the 21st century. No corresponding diagnosis exists yet for CMIP6 models, and no weighting based on a-priori independence is applied here.

(v) Performance in simulating the past and a-posteriori independence based on comparison against observations (Knutti et al., 2017; Abramowitz et al., 2019). This approach has been applied to CMIP6-simulated GSAT and has led to a substantial reduction in model range (Liang et al., 2020, Section 4.3.4). CMIP6-simulated Arctic sea-ice area has been compared to the observed record, and models have been selected whose ensemble range across their individual realizations (Olonscheck and Notz, 2017) includes the observational range of uncertainty. A larger fraction of these selected simulations show an ice-free Arctic in September before 2050, compared to the entire CMIP6 ensemble (SIMIP Community, 2020, Section 4.3.2).

(vi) A linear inverse method (kriging) has combined the entire GSAT record since 1850 with the CMIP6 historical simulations to produce constrained projections for the 21st century; again the reduction in range has been substantial (Ribes et al., 2020, Section 4.3.4).

(vii) Emergent constraints (e.g., Hall and Qu, 2006; Cox et al., 2018), which for the post-1970 warming have been applied to the CMIP5 (Jiménez-de-la-Cuesta and Mauritsen, 2019b) and CMIP6 ensembles (Tokarska et al., 9999) and have likewise led to a substantial reduction in ensemble range (Section 4.3.4).

(viii) Climate predictions initialized from recent observations (e.g., Kirtman et al., 2013) and the Decadal Climate Prediction Project (DCPP) contribution to CMIP6 (Boer et al., 2016; Smith et al., 9999; Sospedra-Alfonso and Boer, 9999). Initialised predictions for the period 2019–2028 exist for three DCPP models and are used here (Box 4.1, Figure 1:, Section 4.4.1). The DCPP results have been drift-removed and referenced to the time-averaged hindcasts for 1995–2014 lead-year by lead-year, following (Kharin et al., 2012; Kruschke et al., 2016).

Box 4.1, Figure 1: shows annual-mean GSAT simulated by CMIP6 models for both the historical period and forced by scenario SSP2-4.5 until 2100, combined with various characterizations of uncertainty. First, internal variability is estimated with the 50-member ensemble simulated with CanESM5. The 5–95% ensemble range for annual-mean GSAT in CanESM5 is slightly below 0.4°C; in other CMIP6 large ensembles this range is about 0.5°C (MIROC6, IPSL-CM6A) and slightly above 0.6°C (S-LENS/EC-Earth3). The CMIP5 large ensemble MPI-GE shows a range of slightly below 0.5°C (Bengtsson and Hodges, 2018), in reasonable agreement with observed variability (Maher et al., 2019). There is thus *high confidence* in the CMIP6-simulated level of internal variability in annual-mean GSAT as displayed in Box 4.1, Figure 1:.

Second, the Section 7.5 *likely* and *very likely* ECS and TCR ranges are converted into GSAT ranges with the EBM as an emulator, using the SSP2-4.5 radiative forcing information (see point (iv) above). Because the ECS and TCR assessments in Section 7.5 are based on multiple lines of evidence and the EBM physics are well understood, there is likewise *high confidence* in the EBM-constrained warming. And third, the initialized-prediction ensembles from three CMIP6 DCPP models are shown in the inset, for the period 2019–2028. During this period, the initialized predictions are broadly consistent, within internal variability, with the EBM-constrained range, further adding to the confidence.

Box 4.1, Figure 1: permits the following assessments for the uncertainty in annual-mean GSAT increase relative to the period 1995–2014, for scenario SSP2-4.5 (see Section 4.3.4). From the mid-term period (2041–2060) onward, the uncertainty characterised by the emulated *very likely* GSAT range (that is, arising from uncertainty in ECS and TCR) is substantially larger than that arising from internal variability (*high confidence*). During the near term (2021–2040), uncertainty in GSAT change relative to 1995–2014 arises in roughly equal measure from internal variability and the uncertainty in ECS and TCR (*high confidence*).

**[START BOX 4.1, FIGURE 1 HERE]**

**Box 4.1, Figure 1:** CMIP6 annual-mean GSAT simulations and various contributions to uncertainty in the projections ensemble. The figure shows anomalies relative to the period 1995–2014 (left y-axis), converted to anomalies relative to 1850–1900 (right y-axis); the difference between the y-axes is 0.86°C (Box 1.2). Shown are historical simulations with 29 CMIP6 models (grey) and projections simulations following scenario SSP2-4.5 (dark yellow). The black curve shows the observations (HadCRUT5, (Morice et al., 9999b)). Light blue shading shows the 50-member ensemble CanESM5, such that the deviations from the CanESM5 ensemble mean have been added to the CMIP6 multi-model mean. The red curves are from the emulator and show the best estimate (solid), *likely* range (dashed), and *very likely* range (dotted) for GSAT. The inset shows a cut-out from the main plot and additionally for the period 2019–2028 in purple, green, and blue the initialised prediction ensembles from three models contributing to DCPP (Boer et al., 2016); solid curves show the ensemble means and shading the range of each prediction system.

**[END BOX 4.1, FIGURE 1 HERE]**

**[END BOX 4.1 HERE]**

## 4.3 Projected Changes in Global Climate Indices in the 21st Century

Here, we assess the latest simulations of representative indicators of global climate change at the surface considered as simple time series and tabulated values over the 21st century and across the main realms of the global climate system. In the atmospheric realm (see Section 4.3.1), we assess simulations of GSAT (see Figure 4.1:a) and global land precipitation (see Figure 4.1:b). Across the cryospheric, oceanic, and biospheric realms (see Section 4.3.2), we assess simulations of Arctic SIA (see Figure 4.1:c), GMSL (see Figure 4.1:d), the AMOC, ocean and land carbon uptake, and pH. In Section 4.3.3 we assess simulations of several indices of climate variability, namely, the indices of the NAM, SAM, and ENSO. Finally, in Section

4.3.4, we assess future GSAT change based on the CMIP6 ensemble in combination with other lines of evidence.

The quantities assessed here comprise a subset of the variables assessed in Chapters 2 and 3; selected so as to illustrate the range of connected changes simulated over the entirety of the 21st century and spanning much of the global climate system (see Figure 4.1:). From the CMIP6 multi-model ensemble we consider historical simulations with observed external forcings to 2014 and extensions to 2100 based on SSP1-1.9 and SSP1-2.6 (sustainable), SSP2-4.5 (middle-of-the-road), SSP3-7.0 (regional rivalry), and SSP5-8.5 (fossil-fuel-rich development). In tabular form, we show ensemble-mean changes and uncertainties for the near-term (2021–2040), mid-term (2041–2060), and the long-term (2081–2100), relative to present-day (1995–2014) and/or the approximation to pre-industrial, 1850–1900. Changes in precipitation over land near 1.5°C, 2.0°C, and 3.0°C of global warming relative to 1850–1900is also assessed.

**[START FIGURE 4.1 HERE]**

**Figure 4.1:** Selected indicators of global climate change from CMIP6 historical and scenario simulations. (a) Global surface air temperature changes relative to the 1995–2014 average (left axis) and relative to the 1850–1900 average (right axis). (b) Global land precipitation changes relative to the 1995–2014 average. (c) September Arctic sea-ice area. (d) Sea level change relative to the 1995–2014 average. Curves with shading are global mean sea level (GMSL) and curves without shading are the contributions due to thermal expansion. (a), (b) and (d) are annual averages, (c) are September averages. In (a)-(c), the curves show averages over the r1 simulations contributed to the CMIP6 exercise, the shadings around the SSP1-2.6 and SSP5-8.5 curves show 5 to 95% ranges (i.e. mean ± standard deviation × 1.645), and the numbers near the top show the number of model simulations.

**[END FIGURE 4.1 HERE]**

Assessments of the regional, and other detailed, manifestations of the changes discussed in this section are undertaken in Section 4.4 (for the near-term) and Section 4.5 (for the mid- to long-term). Detailed physical understanding of the changes documented here are undertaken in Chapters 5 to 11.

## *4.3.1 Atmosphere*

### *4.3.1.1 Surface Air Temperature*

The AR5 assessed from CMIP5 simulations that GSAT will continue to rise over the 21st century if GHGs continue increasing (Collins et al., 2013). The GHG trajectories, or RCPs, considered in the AR5 ranged from RCP2.6 which assumes that GHG emissions peak between 2010 and 2020, with emissions declining substantially thereafter, to RCP8.5 where emissions continue to rise throughout the 21st century. The AR5 concluded that GSAT for 2081–2100, relative to 1986–2005 will *likely* be in the 5–95% range of 0.3°C–1.7°C under RCP2.6 and 2.6°C–4.8°C under RCP8.5. The corresponding ranges for the intermediate emissions scenarios with emissions peaking around 2040 (RCP4.5) and 2060 (RCP6.0) are 1.1°C–2.6°C and 1.4°C–3.1°C, respectively. The AR5 further assessed that GSAT averaged over the period 2081–2100 are projected to *likely* exceed 1.5°C above 1850–1900 for RCP4.5, RCP6.0 and RCP8.5 (*high confidence*), and are *likely* to exceed 2°C above 1850–1900 for RCP6.0 and RCP8.5 (*high confidence*). Global surface temperature changes above 2°C under RCP2.6 were deemed *unlikely* (*medium confidence*).

Here, for continuity's sake, we assess the CMIP6 simulations of GSAT in a fashion similar to the AR5 assessment of the CMIP5 simulations. From each historical and SSP ensemble, we select one simulation (i.e., the "r1" simulation) from each model contributing to that ensemble. From these, we compute anomalies relative to 1995–2014 and display the evolution of ensemble means and 5–95% ranges (see Figure 4.1:). We also use the ensemble mean GSAT difference between 1850–1900 and 1995–2014 to provide an estimate of the changes since 1850–1900 (see the right axis on Figure 4.1:). Finally, we tabulate the ensemble mean

changes between 1995–2014 and 2021–2040, 2041–2060, and 2081–2100 respectively (see Table 4.2:).

Based on results from the CMIP6 models, we conclude that GSAT for 2081–2100, relative to 1995–2014, shows a 5–95% range of 0.5°C–1.7°C under SSP1-2.6 where $CO_2$ concentrations peak between 2040 and 2060 (see Table 4.2:; *high confidence*). The corresponding range under the highest overall emissions scenario (SSP5-8.5) is 2.4°C–5.5°C (*high confidence*). The ranges for the intermediate emissions scenarios (SSP2-4.5 and SSP3-7.0), where $CO_2$ concentrations increase to 2100, but less rapidly than SSP5-8.5, are 1.2°C–3.0°C and 1.9°C–4.3°C, respectively (*high confidence*). The range for the lowest emissions scenario (SSP1-1.9) is 0.2°C–1.3°C (*high confidence*).

**[START TABLE 4.2 HERE]**

**Table 4.2:** CMIP6 annual mean surface air temperature anomalies (°C) from the 1995–2014 reference period for selected time periods, regions and SSPs. The multi-model averages across the individual models and the 5 to 95% ranges (based on multiplying the CMIP6 ensemble standard deviation by 1.645) are given in parentheses.

| Units = °C | | SSP1-1.9 | SSP1-2.6 | SSP2-4.5 | SSP3-7.0 | SSP5-8.5 |
|---|---|---|---|---|---|---|
| Global: | 2021–2040 | 0.7 (0.4, 1.0) | 0.7 (0.4, 1.0) | 0.7 (0.4, 1.1) | 0.7 (0.4, 1.1) | 0.8 (0.5, 1.1) |
| | 2041–2060 | 0.9 (0.4, 1.4) | 1.0 (0.5, 1.5) | 1.3 (0.7, 1.8) | 1.4 (0.8, 2.0) | 1.7 (1.0, 2.4) |
| | 2081–2100 | 0.7 (0.2, 1.3) | 1.1 (0.5, 1.7) | 2.1 (1.2, 3.0) | 3.1 (1.9, 4.3) | 3.9 (2.4, 5.5) |
| Land: | 2081–2100 | 1.0 (0.2, 1.7) | 1.4 (0.6, 2.2) | 2.8 (1.6, 4.0) | 4.1 (2.4, 5.8) | 5.3 (3.1, 7.4) |
| Ocean: | 2081–2100 | 0.6 (0.1, 1.1) | 1.0 (0.4, 1.5) | 1.8 (1.0, 2.6) | 2.7 (1.6, 3.8) | 3.4 (2.0, 4.8) |
| Tropics: | 2081–2100 | 0.6 (0.1, 1.0) | 0.9 (0.4, 1.5) | 1.8 (1.0, 2.6) | 2.7 (1.7, 3.8) | 3.5 (2.1, 4.9) |
| Arctic: | 2081–2100 | 2.6 (-0.4, 5.6) | 3.2 (0.4, 5.9) | 5.8 (2.0, 9.5) | 7.9 (3.7, 12.2) | 10.0 (5.4, 14.7) |
| Antarctic: | 2081–2100 | 0.5 (-0.0, 1.1) | 1.0 (0.2, 1.9) | 2.0 (0.7, 3.3) | 3.0 (1.2, 4.7) | 3.7 (1.5, 5.9) |

**[END TABLE 4.2 HERE]**

With regards to GSAT thresholds of 1.5°C, 2.0°C, and 3.0°C, we note that there is unanimity across all of the CMIP6 model simulations that GSAT change relative to 1850–1900 will rise above: 1) 1.5°C following SSP2-4.5, SSP3-7.0, or SSP5-8.5 (on average around 2029); 2) 2.0°C following either SSP3-7.0 or SSP5-8.5 (on average around 2043), and 3) 3.0°C following SSP5-8.5 (on average around 2062). Under SSP1-1.9, 60% and 40% of the model simulations rise above 1.5°C and 2.0°C, respectively, while for SSP1-2.6 those percentages increase to 90% and 60%, respectively. In summary, we conclude that within the near-term (2021–2040) or mid-term (2041–2060), global temperature rise simulated by the CMIP6 models exceeds 1.5°C relative to 1850–1900 under most of the SSPs considered here, and above 3.0°C under the highest forcing scenario (*high confidence*).

The CMIP6 models project increases in area-weighted land, ocean, tropical (30°S–30°N), Arctic (67.7°N–90°N), and Antarctic (90°S–55°S) surface air temperature (see Table 4.2:). Consistent with the AR5, and earlier assessments, the CMIP6 models project that annual average surface air temperature will warm about 50% more over land than over oceans, and that the Arctic will warm about twice as much as land (see Section 4.5.1). For 2081–2100, relative to 1995–2014, the CMIP6 models show 5–95% ranges of warming over land of 0.2°C–1.7°C and 3.2°C–7.4°C following SSP1-1.9 and SSP5-8.5, respectively (*high confidence*). The corresponding ranges for Arctic surface air temperature change are -0.4°C–5.6°C and 5.4°C–14.6°C, respectively (*high confidence*).

### *4.3.1.2 Precipitation*

The AR5 assessed from the CMIP5 simulations that it would be *virtually certain* that global mean precipitation will increase by more than 0.05 mm day$^{-1}$ (about 2% of global precipitation) and 0.15 mm day$^{-1}$ (about 5% of global precipitation) by the end of the 21st century under the RCP2.6 and RCP8.5 scenarios, respectively (Collins et al., 2013).

Unlike the AR5, our focus here is on land rather than global precipitation because land precipitation has greater societal relevance. As with GSAT, we show results from each CMIP6 model one historical realization from 1950 to 2014 and one scenario realization from 2015 to 2100 for each of the five SSPs considered here. These are displayed as percent changes relative to 1995–2014 (see Figure 4.1:). In tabular form, we also show the percentage global precipitation land change relative to 1995–2014 averages from 2021–2040 (near-term), 2041–2060 (mid-term) and 2081–2100 (long-term). Based on these results, we conclude that global land precipitation is larger during the period 2081–2100 than during the period 1995–2014, under all scenarios considered here (see Table 4.3:; *high confidence*). Global land precipitation for 2081–2100, relative to 1995–2014, shows a 5–95% range of 0.9–4.2% under SSP1-1.9 and 2.5–13.8% under SSP5-8.5, respectively (*high confidence*). The corresponding ranges under the other emissions scenarios are 0.8–5.6% (SSP1-2.6), 1.8–7.7% (SSP2-4.5), and 0.5–10.4% (SSP3-7.0; *high confidence*).

For scenarios where unanimity across all of the model simulations that GSAT change relative to 1850–1900 rises above 1.5°C (SSP2-4.5, SSP3-7.0, or SSP5-8.5), the ensemble-mean change in global land precipitation since 1850–1900 is on average about 1.7% (*high confidence*). For scenarios with unanimous global warming above 2.0°C (SSP2-4.5, SSP3-7.0, or SSP5-8.5) and 3.0°C (SSP3-7.0 or SSP5-8.5), the ensemble-mean increase in global land precipitation is on average about 2.9% and 4.6%, respectively (*high confidence*). Under SSP1-1.9 and SSP1-2.6, global land precipitation for simulations where global warming exceeds 1.5°C and 2.0°C on average will be about 2.1% and 3.5%, respectively (*high confidence*). In summary, we conclude that within the near-term (2021–2040) or mid-term (2041–2060), global land precipitation shows an increase when global temperature rise exceeds 1.5°C relative to 1850–1900 under most of the SSPs considered here, and above 3.0°C under the two scenarios with highest forcings (*high confidence*).

**[START TABLE 4.3 HERE]**

**Table 4.3:** CMIP6 precipitation anomalies (%) relative to averages over 1995–2014 for selected future periods, regions and SSPs. The multi-model averages across the individual models and the 5 to 95% ranges (based on multiplying the CMIP6 ensemble standard deviation by 1.645) are given in parentheses. Also shown are land precipitation anomalies at the time when global increase in GSAT relative to 1850–1900 exceeds 1.5°C, 2.0°C, and 3.0°C, and the percentage of simulations for which such exceedances are true (to the right of the parentheses). Here, the time of GSAT exceedance is determined as the first year at which 11-year running averages of GSAT exceed the given threshold. Land precipitation percent anomalies are then computed as 21-year averages about the year of the first GSAT crossing.

| Units = % | SSP1-1.9 | SSP1-2.6 | SSP2-4.5 | SSP3-7.0 | SSP5-8.5 |
|---|---|---|---|---|---|
| Land: 2021–2040 | 2.6 (0.9, 4.2) | 2.1 (0.6, 3.5) | 1.6 (0.1, 3.0) | 1.1 (-0.6, 2.8) | 1.8 (-0.2, 3.7) |
| 2041–2061 | 2.9 (0.9, 5.0) | 2.7 (0.5, 5.0) | 2.8 (0.7, 4.8) | 2.4 (-0.3, 5.1) | 3.8 (0.7, 6.8) |
| 2081–2100 | 2.7 (0.6, 4.8) | 3.2 (0.7, 5.6) | 4.7 (1.8, 7.7) | 5.5 (0.5, 10.4) | 8.2 (2.5, 13.8) |
| Global: 2081–2100 | 2.2 (0.6, 3.8) | 2.7 (0.9, 4.5) | 4.1 (1.7, 6.4) | 4.8 (1.8, 7.8) | 6.3 (2.6, 10.0) |
| Ocean: 2081–2100 | 2.0 (0.5, 3.6) | 2.5 (0.7, 4.4) | 3.8 (1.3, 6.4) | 4.6 (1.5, 7.6) | 5.8 (1.9, 9.7) |
| Land: $\Delta T > 1.5$°C | 2.1 (-0.4, 4.6) 60 | 2.2 (-1.7, 6.0) 95 | 1.9 (-2.3, 6.1) 100 | 1.3 (-2.8, 5.3) 100 | 1.8 (-2.1, 5.8) 100 |
| $\Delta T > 2.0$°C | 3.9 (1.0, 6.7) 40 | 3.1 (-0.2, 6.4) 64 | 3.1 (-1.5, 7.7) 100 | 2.3 (-2.7, 7.3) 100 | 3.2 (-1.5, 7.9) 100 |
| $\Delta T > 3.0$°C | - (-, -) 0 | - (-, -) 0 | 4.2 (-0.2, 8.6) 67 | 4.3 (-2.3, 10.9) 100 | 4.9 (-1.2, 11.1) 100 |

**[END TABLE 4.3 HERE]**

Relative to 1995–2014, and across all of the scenarios considered here, the CMIP6 models show greater increases in precipitation over land than either globally or over oceans (see Table 4.3:; *medium confidence*). Over the Northern Hemisphere, where the greatest proportion of land resides, the 5–95% changes in global land precipitation between 1995–2014 and 2021–2040 (near-term), 2041–2060 (mid-term), and 2081–2100 (long-term) following SSP5-8.5 are 0.6–4.9%, 1.5–8.8%, and 4.7–17.2%, respectively (Figure 4.2:; *high confidence*). At the other end of scenario spectrum, SSP1-1.9, the corresponding changes are 0.6–5.4%, 0.6–7.3%, and 0.2–7.7%, respectively (*high confidence*). By contrast, over the North Atlantic (NA) subtropics, precipitation decreases by about 10% following SSP3-7.0 and SSP5-8. There is no change in NA subtropical precipitation following SSP1-1.9, SSP1-2.6, or SSP2-4.5 (*high confidence*).

**[START FIGURE 4.2 HERE]**

**Figure 4.2:** CMIP6 annual mean precipitation changes (%) from historical and scenario simulations. (a) Northern Hemisphere (NH) extratropics (30°N–90°N). (b) North Atlantic (NA) subtropics (5°N–30°N, 80°W–0°). Changes are relative to 1995–2014 averages. The curves show averages over the r1 simulations contributed to the CMIP6 exercise. The shadings around the SSP1-2.6 and SSP5-8.5 curves are the 5 to 95% ranges across the ensembles (i.e. mean ± standard deviation × 1.645). The numbers inside each panel are the number of model simulations.

**[END FIGURE 4.2 HERE]**

### *4.3.2 Cryosphere, Ocean, and Biosphere*

#### *4.3.2.1 Arctic Sea Ice*

The AR5 assessed from the CMIP5 simulations that there will be year-round reductions of Arctic sea ice coverage by the end of this century (Collins et al., 2013). These range from between 43% for RCP2.6 and 94% for RCP8.5 in September, and from between 8% for RCP2.6 and 34% for RCP8.5 in March (*medium confidence*). Based on a five-member selection of CMIP5 models, the AR5 further assessed that for RCP8.5, Arctic sea-ice coverage in September will drop below 1 million km$^2$ at some point between 2040 and 2060.

With regards to the model selection in the AR5, model evaluation studies have since identified shortcomings of the CMIP5 models to match the observed distribution of sea-ice thickness in the Arctic (Stroeve et al., 2014; Shu et al., 2015) and the observed evolution of albedo on seasonal scales (Koenigk et al., 2014). It was also found that many models' deviation from observed sea ice cover climatology cannot be explained by internal variability, whereas the models' deviation from observed sea ice cover trend (over the satellite period) can often be explained by internal variability (Olonscheck and Notz, 2017). This hinders a selection of models according to their simulated trends, which additionally has been shown to only have a weak impact on the quality of simulated future trends (Stroeve and Notz, 2015).

Here, we show from each CMIP6 model, one historical realization of September Arctic SIA from 1950–2014 and one scenario realization from 2015–2100 for each considered SSP (see Figure 4.1:). In tabular form we show September and March Arctic SIA averaged over 2021–2040 (near-term), 2041–2060 (mid-term) and 2081–2100 (long-term) for each SSP (see Table 4.4:). The Arctic is considered ice-free with coverage below 1 million km$^2$. Based on results from the CMIP6 models, we conclude that on average the Arctic will become effectively permanently ice-free in September by the end of the 21st century under SSP2-4.5, SSP3-7.0, and SSP5-8.5 (see Figure 4.1: and Table 4.4:; *high confidence*). For those CMIP6 models whose ensemble spread across their individual realizations includes the observational range of uncertainty, the vast majority of simulations show an ice-free Arctic in September before 2050, and before future cumulative anthropogenic $CO_2$ emissions reach 1000 $GtCO_2$ (SIMIP Community, 9999). Finally, in the CMIP6 models,

Arctic SIA in March decreases in the future, but to a much lesser degree than in September (*high confidence*).

**[START TABLE 4.4 HERE]**

**Table 4.4:** CMIP6 Arctic sea ice area for selected months, time periods, and across five SSPs. The multi-model averages across the individual models and the 5–95% ranges (based on multiplying the CMIP6 ensemble standard deviation by 1.645) are given in parentheses.

| Units = $10^6$ km$^2$ | | SSP1-1.9 | SSP1-2.6 | SSP2-4.5 | SSP3-7.0 | SSP5-8.5 |
|---|---|---|---|---|---|---|
| September: | 2021–2040 | 2.4 (-0.4, 5.2) | 2.6 (-0.3, 5.5) | 2.6 (-0.3, 5.4) | 2.9 (-0.1, 5.8) | 2.5 (-0.2, 5.2) |
| | 2041–2060 | 2.0 (-1.1, 5.1) | 1.9 (-1.3, 5.2) | 1.7 (-1.4, 4.8) | 1.6 (-1.5, 4.8) | 1.3 (-1.6, 4.2) |
| | 2081–2100 | 2.2 (-0.7, 5.2) | 1.7 (-1.6, 5.0) | 0.8 (-1.7, 3.4) | 0.6 (-1.4, 2.5) | 0.3 (-1.0, 1.6) |
| March: | 2021–2040 | 12.9 (8.3, 17.5) | 13.2 (9.1, 17.4) | 13.3 (9.4, 17.1) | 13.0 (9.0, 17.1) | 13.1 (9.2, 17.1) |
| | 2041–2060 | 12.7 (8.3, 17.0) | 12.8 (8.7, 16.9) | 12.8 (8.9, 16.6) | 12.3 (8.2, 16.4) | 12.1 (8.1, 16.1) |
| | 2081–2100 | 12.7 (7.9, 17.4) | 12.5 (8.4, 16.7) | 11.5 (7.6, 15.5) | 10.0 (4.9, 15.0) | 8.4 (2.7, 14.1) |

**[END TABLE 4.4 HERE]**

Studies focusing on the relationship of sea ice cover and changes in the external drivers have consistently found a much-reduced likelihood of a near ice-free Arctic Ocean during summer for a global warming compared to pre-industrial levels of 1.5°C compared to 2.0°C (Screen and Williamson, 2017; Jahn, 2018; Niederdrenk and Notz, 2018; Notz and Stroeve, 2018; Sigmond et al., 2018; Olson et al., 2019a). This is shown here in a large initial-condition ensemble of observationally-constrained model simulations where global mean surface temperatures are stabilized at 1.5°C, 2.0°C and 3.0°C warming relative to 1850–1900 in the RCP8.5 scenario (see Figure 4.3:). In these simulations, Arctic sea ice coverage in September is simulated, on average, to drop below 1 million km$^2$ around 2040, consistent with the AR5 models as a group (Sigmond et al., 2018). The individual model simulations, for which there are twenty for each stabilized temperature level, show that the probability of the Arctic becoming ice free (i.e. with area less than 1 million km$^2$) at the end of the 21st century is significantly higher for 2°C warming than for 1.5°C warming above 1850–1900 levels. Estimates, such as these are possibly conservative, as they neglect the possible future reduction in atmospheric aerosol load, which models suggest will contribute to additional future sea-ice loss (Gagné et al., 2015; Wang et al., 2018b).

**[START FIGURE 4.3 HERE]**

**Figure 4.3:** Arctic sea ice extent in September in a large initial-condition ensemble of observationally-constrained simulations of an Earth System Model (CanESM2). The black curve is the average over twenty simulations following historical forcings to 2015 and RCP8.5 extensions to 2100. The coloured curves are averages over twenty simulations each after GSAT has been stabilized at the indicated degree of global mean warming relative to 1850–1900. The bars to the right are the minimum to maximum ranges over 2081–2100 (Sigmond et al., 2018).

**[END FIGURE 4.3 HERE]**

### *4.3.2.2 Global Mean Sea Level*

The AR5 assessed from CMIP5 process-based simulations that it is *very likely* that the rate of GMSL rise during the 21st century will exceed the rate observed during 1971–2010 for all RCP scenarios due to

increases in ocean warming and loss of mass from glaciers and ice sheets (Church et al., 2013). Further, the AR5 concluded that for the period 2081–2100, compared to 1986–2005, GMSL rise is *likely* (*medium confidence*) to be in the 5–95% range of projections from process-based models, which give 0.26–0.55 m for RCP2.6, 0.32–0.63 m for RCP4.5, 0.33–0.63 m for RCP6.0, and 0.45–0.82 m for RCP8.5. For RCP8.5, the rise by 2100 is 0.52–0.98 m with a rate during 2081–2100 of 8–16 mm $yr^{-1}$.

There have been significant modelling advances since the IPCC AR5, with most sea-level projections falling into one of three categories. (1) Central-range projections, combining scenario-conditional probability distributions for the different contributions to estimate a central range under different scenarios. (2) Probabilistic projections, which explicitly consider outcomes for a wide range of probabilities, including low-probability/high-impact outcomes. (3) Semi-empirical projections, based on statistical relationships between past GMSL changes and climate variables, which now calibrate individual contributions and are consistent with physical-model based estimates (Chapter 9 Section 9.6.3.1).

Here, we show annual-mean GMSL anomalies, relative to 1995–2014, for SSP1-2.6, SSP2-4.5, SSP3-7.0, and SSP5-8.5 (see Figure 4.1:). Period average anomalies for the near-term (2021–2040), mid-term (2041–2060), and long-term (2081–2100) are also displayed (see Table 4.5:). The methodologies employed to derive these anomalies are detailed in Chapter 9. Additionally, we show thermosteric contributions to GMSL taken from the CMIP6 models under SSP1-1.9, SSP1-2.6, SSP2-4.5, SSP3-7.0, and SSP5-8.5 (see Figure 4.1: and Table 4.5:). Based on these results, we conclude that under the highest emissions scenario (SSP5-8.5) the 5–95% ranges of GMSL change over the long-term are 0.50 m–1.07 m (see Table 4.5:; *medium confidence*). Under SSP1-2.6, the 5–95% ranges over the long-term are 0.05 m – 0.13 m (*medium confidence*). Over the same time period, the thermosteric contributions to GMSL lead to 5–95% ranges of 0.11 m–0.14 m, 0.12 m–0.17 m, 0.16 m–0.22 m, 0.18 m–0.29 m,, and 0.21 m–0.34 m under SSP1-1.9, SSP1-2.6, SSP2-4.5, SSP3-7.0, and SSP5-8.5, respectively (see Table 4.5:; *high confidence*). In summary, we conclude that under any one of the considered SSPs, there will be a monotonic rise in GMSL through the 21st century with more than a third of that rise accounted for by thermal expansion. (*high confidence*).

**[START TABLE 4.5 HERE]**

**Table 4.5:** Sea level anomalies (m) relative to 1995–2014 for selected time periods. The multi-model mean ± standard deviation × 1.645 range. The multi-model averages across the individual models and the 5 to 95% ranges (based on multiplying the CMIP6 ensemble standard deviation by 1.645) are given in parentheses. Total refers to global mean sea level (GMSL), steric refers to the thermosteric contribution to GMSL. Note that estimates of GMSL under SSP1-1.9 are presently unavailable.

| Units = m | SSP1-1.9 | SSP1-2.6 | SSP2-4.5 | SSP3-7.0 | SSP5-8.5 |
|---|---|---|---|---|---|
| Total: 2021–2040 | - (-, -) | 0.10 (0.08, 0.13) | 0.09 (0.05, 0.12) | 0.09 (0.05, 0.13) | 0.09 (0.05, 0.13) |
| 2041–2060 | - (-, -) | 0.19 (0.17, 0.25) | 0.19 (0.12, 0.28) | 0.19 (0.12, 0.27) | 0.21 (0.13, 0.30) |
| 2081–2100 | - (-, -) | 0.41 (0.29, 0.71) | 0.55 (0.28, 0.89) | 0.65 (0.41, 1.00) | 0.73 (0.50, 1.07) |
| Steric: 2081–2100 | 0.04 (0.03, 0.05) | 0.04 (0.03, 0.05) | 0.04 (0.03, 0.05) | 0.04 (0.03, 0.05) | 0.05 (0.04, 0.06) |
| 2041–2060 | 0.08 (0.06, 0.09) | 0.08 (0.07, 0.09) | 0.09 (0.07, 0.10) | 0.09 (0.07, 0.12) | 0.10 (0.08, 0.12) |
| 2081–2100 | 0.12 (0.11, 0.14) | 0.14 (0.12, 0.17) | 0.19 (0.16, 0.22) | 0.24 (0.18, 0.29) | 0.28 (0.21, 0.34) |

**[END TABLE 4.5 HERE]**

### *4.3.2.3 Atlantic Meridional Overturning Circulation*

The AR5 assessed from the CMIP5 simulations that it is *very likely* that the AMOC will weaken over the 21st century (Collins et al., 2013). Best estimates and ranges for the reduction from CMIP5 are 11% (1–24%) in RCP2.6 and 34% (12–54%) in RCP8.5. As assessed in the AR5, the projected weakening of the

AMOC is consistent with CMIP5 projections of an increase of high-latitude temperature and high-latitude precipitation, with both effects causing the surface waters at high latitudes to become lighter and more stable.

Based on results from a limited number of CMIP6 models that have thus far contributed the required output, we find that the AMOC strength, relative to 1995–2014, and considered across all five SSPs, either decreases significantly, does not change at all, or increases significantly in about 60%, 30%, and 10% of the total number of simulations, respectively (see Figure 4.4:). Based on this analysis, we conclude that on average the CMIP6 models show that the AMOC monotonically weakens over the 21st century (*medium confidence* due to the limited number of model simulations).

**[START FIGURE 4.4 HERE]**

**Figure 4.4:** CMIP6 annual mean AMOC change in historical and scenario simulations. Changes are relative to averages from 1995–2014. The curves show averages over the r1 simulations contributed to the CMIP6 exercise. The shadings around the SSP1-2.6 and SSP5-8.5 curves are the 5–95% ranges across those ensembles (i.e. mean ± standard deviation × 1.645). The circles to the right of the panel show the anomalies averaged from 2081–2100 (long-term) across all of the individual model simulations. The numbers inside the panel are the number of model simulations. Here, the strength of the AMOC is computed as the maximum value of annual-mean ocean meridional overturning mass streamfunction in the Atlantic north of 30°N and below 500 m.

**[END FIGURE 4.4 HERE]**

Based on a large initial condition ensemble of simulations with a CMIP5 model (CanESM2) with emissions scenarios leading to stabilization of global warming, relative to 1850–1900, of 1.5, 2.0°C, or 3.0°C, the AMOC continues to decline for 5-10 years (Sigmond et al., 9999). This is followed by a recovery of the AMOC for about the next 150 years to a level that is approximately independent of the considered stabilization scenario. These results are replicated in simulations in a nearly independent CMIP6 model (CanESM5) with emissions cessation after diagnosed $CO_2$ emissions reach 750 Gt, 1000 Gt, or 1500 Gt. These emissions levels lead to global warming stabilization at 1.5, 2.0°C, or 3.0°C relative to 1850–1900. In summary, in these model simulations the AMOC eventually recovers after the cessation of $CO_2$ emissions (*low confidence* based on the limited number of models considered).

#### *4.3.2.4 Ocean and Land Carbon Uptake*

The AR5 concluded with *very high confidence* that ocean carbon uptake of anthropogenic $CO_2$ will continue under all RCPs through the 21century, with higher uptake corresponding to higher concentration pathways. The future evolution of the land carbon uptake was assessed to be much more uncertain than for ocean carbon uptake, with a majority of CMIP5 models projecting a continued cumulative carbon uptake.

Here, we will show from each CMIP6 model, one historical realization of ocean and land carbon flux and one scenario realization from 2015 to 2100 for SSP1-1.9, SSP1-2.6, SSP2-4.5, SSP3-7.0, and SSP5-8.5 (see Figure 4.5:). Based on results from the CMIP6 models, we conclude that the flux of carbon from the atmosphere into the ocean increases continually through most of 21st century in the highest emissions scenarios (SSP3-7.0 and SSP5-8.5) and decreases continually under the lower emissions scenarios (SSP1-1.9, SSP1-2.6, and SSP2-4.5). In the CMIP6 models, the ensemble-mean ocean carbon flux accumulated from 1850 to 2100 is about 240 PgC, 290 PgC, 380 PgC, 460 PgC, and 530 PgC under SSP1-1.9, SSP1-2.6, SSP2-4.5, SSP3-7.0, and SSP5-8.5, respectively. The flux of carbon from the atmosphere to land shows a similar 21st century behaviour across the scenarios but with much higher year-to-year variation than ocean carbon flux. In the CMIP6 models, the ensemble-mean land carbon flux accumulated from 1850 to 2100 is about 210 PgC, 320 PgC, 400 PgC, 440 PgC, and 570 PgC under SSP1-1.9, SSP1-2.6, SSP2-4.5, SSP3-7.0, and SSP5-8.5, respectively. In summary, we conclude that net ocean and land carbon flux will increase through the 21st century irrespective of the considered emissions scenarios (*high confidence*).

**[START FIGURE 4.5 HERE]**

**Figure 4.5:** CMIP6 carbon uptake in historical and scenario simulations. (a) Net ocean uptake rate (PgC $yr^{-1}$). (b) Net land uptake rate (PgC $yr^{-1}$). The curves show averages over the r1 simulations contributed to the CMIP6 exercise. The shadings around the SSP1-2.6 and SSP5-8.5 curves are the 5–95% ranges across those ensembles (i.e. mean ± standard deviation x 1.645). The numbers inside each panel are the number of model simulations. The land uptake is taken as Net Biome Productivity (NBP) and so includes any modelled net land-use change emissions.

**[END FIGURE 4.5 HERE]**

#### *4.3.2.5 Surface Ocean pH*

The AR5 assessed from the CMIP5 simulations that it is *virtually certain* that increasing storage of carbon by the ocean under all four RCPs through to 2100 will increase ocean acidification in the future (Ciais et al., 2013). Specifically, the AR5 reported that the CMIP5 models project increased ocean acidification globally to 2100 under all RCPs, and that the corresponding model-mean and model-spread in the decrease in surface ocean pH by the end of 21st century would be 0.065 (0.06–0.07) for RCP2.6, 0.145 (0.14–0.15) for RCP4.5, 0.203 (0.20–0.21) for RCP6.0 and 0.31 (0.30–0.32) for RCP8.5.

Here, we show from each CMIP6 model one historical realization of ocean surface pH from 1950 to 2014 and one scenario realization from 2015 to 2100 for SSP2-2.6, SSP2-4.5, SSP3-7.0, and SSP5-8.5 (see Figure 4.6:). Based on results from the CMIP6 models we conclude that, except for the lowest emissions scenario considered here (SSP1-2.6), ocean surface pH decreases monotonically through the 21st century (*high confidence*; Figure 4.6:).

**[START FIGURE 4.6 HERE]**

**Figure 4.6:** Surface ocean pH. The shadings around the SSP1-2.6 and SSP5-8.5 curves are the 5–95% ranges across those ensembles (i.e. mean ± standard deviation x 1.645). The numbers inside each panel are the number of model simulations. Note that surface ocean pH under SSP1-1.9 is currently unavailable from any CMIP6 model.

**[END FIGURE 4.6 HERE]**

### *4.3.3 Modes of Variability*

This subsection summarises the observed changes in the annular modes and El Niño-Southern Oscillation (ENSO) and their attribution assessed in Chapters 2 and 3 and provides an overview of their projected changes from CMIP6 models over the 21st century to set the scene for later assessments. In Sections 4.4.3 and 4.5.3 we compare and assess the salient features of the CMIP6 projected annular modes and ENSO averaged over 2021–2040 (near-term) and 2081–2100 (long-term), respectively.

#### *4.3.3.1 Northern and Southern Annular Modes*

***The NAM***

The NAM is the leading mode of variability in the NH extratropical atmosphere (see Technical Annex VI Section AVI.2). At the surface, the NAM is characterised by opposing fluctuations in zonal mean sea level pressure (SLP) between the northern midlatitudes and high latitudes. Throughout this chapter, we use a simple fixed latitude based NAM index defined as the difference in SLP between 35°N and 65°N (Li and Wang, 2003; Technical Annex VI Section AVI.2). The NAM index computed from the latitudinal gradient in SLP is strongly correlated with variations in the latitudinal position and strength of the midlatitude westerly

jets, and with the spatial distribution of Arctic sea ice (Caian et al., 2018). Projected changes in the position and strength of the midlatitude westerly jets, storm tracks and atmospheric blocking in both hemispheres are assessed in Section 4.5.1.6. The AR5 elected to refer to the NAM, and its synonym the Arctic Oscillation (AO), through its regional counterpart the North Atlantic Oscillation (NAO). Here, we use the term NAM to refer also to the AO and NAO (see Technical Annex VI Section AVI.2).

We first summarise the assessment of past NAM changes and their attribution from Chapters 2 and 3 to put into context the future projections described here. Strong positive trends for the NAM/NAO indices were observed since 1960, which have weakened since the 1990s (*high confidence*; Section 2.4.1.1). The NAO variability in the instrumental record was *likely* not unusual in the millennial and multi-centennial context (Section 2.4.1.1). Climate models simulate the gross features of the NAM with reasonable fidelity, including its interannual variability, but models tend to systematically underestimate the amount of multidecadal variability of the NAM and jet stream compared to observations (Wang et al., 2017b; Bracegirdle et al., 2018; Simpson et al., 2018a); Section 3.7.1), with the caveat of the observational record being relatively short to characterise decadal variability (Chiodo et al., 2019). A realistic simulation of the stratosphere and SST variability in the tropics and northern extratropics are important for a model to realistically capture observed NAM variability. Despite some evidence from climate model studies that anthropogenic forcings influence the NAM, the balance of evidence indicates that there is *little evidence* for a significant role for anthropogenic forcings in driving the observed multidecadal variations of the NAM over the instrumental period (Section 3.7.1).

The AR5 assessed from CMIP5 simulations that the future boreal wintertime NAM is *very likely* to exhibit large natural variations and trends of similar magnitude to that observed in the past and is *likely* to become slightly more positive in the future (Collins et al., 2013). Here, we show from each CMIP6 model, one historical realization of boreal wintertime NAM anomalies from 1950 to 2014 and one scenario realization from 2015 to 2100 for each of the considered SSPs (see Figure 4.7:a). All anomalies are relative to averages from 1995–2014. Based on the CMIP6 model results displayed in Figure 4.7:a, we conclude that the boreal wintertime surface NAM is more positive by the end of the 21st century under SSP3-7.0 and SSP5-8.5. For these high emissions scenarios, the 5–95% range of NAM index anomalies averaged from 2081–2100 are 0.3–3.8 hPa and 0.32–5.2 hPa, respectively. On the other hand, under neither of the lowest emissions scenarios, SSP1-1.9 and SSP1-2.6, does the NAM show a robust change, by the end of the 21st century.

**[START FIGURE 4.7 HERE]**

**Figure 4.7:** CMIP6 simulations of boreal wintertime (DJF) Annular Mode indices: (a) NAM and (b) SAM. The NAM is defined as the difference in zonal mean SLP at 35°N and 65°N (Li and Wang, 2003) and the SAM as the difference in zonal mean SLP at 40°S and 65°S (Gong and Wang, 1999). All anomalies are relative to averages from 1995–2014. The curves show multi-model ensemble averages over the r1 simulations contributed to the CMIP6 exercise. The shadings around the SSP1-2.6 and SSP5-8.5 curves denote the 5 to 95% ranges of the ensembles (i.e. mean ± standard deviation x 1.64). The numbers inside each panel are the number of model simulations.

**[END FIGURE 4.7 HERE]**

Significant progress has been made since the AR5 in understanding the physical mechanisms responsible for changes in the NAM, although large uncertainties remain. It is now clear from the literature that the NAM response, and the closely-related response of the midlatitude storm tracks, to anthropogenic forcing in CMIP5-era climate models is determined by a "tug-of-war" between two opposite processes (Harvey et al., 2014; Shaw et al., 2016; Screen et al., 2018a); 1) Arctic amplification (see Sections 4.5.1.1 and 7.4.4.1), which decreases the low-level meridional temperature gradient, reduces baroclinicity on the poleward flank of the eddy-driven jet, and shifts the storm tracks equatorward and leading to a *negative* NAM (see Box 10.1; Harvey et al., 2015; Hoskins and Woollings, 2015; Peings et al., 2017; Screen et al., 2018a); 2) enhanced warming in the tropical upper-troposphere, due to GHG increases and associated water vapour and lapse rate feedbacks, which increases the upper-level meridional temperature gradient and causes a poleward shift of

the storm tracks and a *positive* NAM (Harvey et al., 2014; Vallis et al., 2015; Shaw, 2019). The large diversity in projected NAM changes in the CMIP5 multi-model ensemble (Gillett and Fyfe, 2013) appears to be at least partly explained by the relative importance of these two mechanisms in particular models (Harvey et al., 2014, 2015; Vallis et al., 2015; McCusker et al., 2017; Oudar et al., 2017). Models that produce larger Arctic amplification also tend to produce larger equatorward shifts of the midlatitude jets and associated negative NAM responses (Barnes and Polvani, 2015; Harvey et al., 2015; Zappa and Shepherd, 2017; McKenna et al., 2018; Screen et al., 2018a; Zappa et al., 2018a).

Another area of progress is understanding the role of cloud radiative effects in shaping the midlatitude circulation response to anthropogenic forcing. Through their non-uniform distribution of radiative heating, cloud changes can modify meridional temperature gradients and alter midlatitude circulation and the annular modes in both hemispheres (Ceppi et al., 2014; Voigt and Shaw, 2015, 2016a; Ceppi and Hartmann, 2016; Ceppi and Shepherd, 2017; Lipat et al., 2018; Albern et al., 2019; Voigt et al., 2019). In addition to the effects of changing upper and lower tropospheric temperature gradients on the NAM, progress has been made since AR5 in understanding the impact of modelled changes in the strength of the stratospheric polar vortex on winter NAM projections (Manzini et al., 2014; Zappa and Shepherd, 2017; Simpson et al., 2018c).

***The SAM***

The SAM is the leading mode of large-scale extratropical atmospheric variability in the SH, which influences climate across many regions including South America, southern African countries, Australia, New Zealand, and Antarctica (see Technical Annex VI Section AVI.3). In its positive phase, the SAM characterizes anomalously low pressure over the polar cap and high pressure in southern mid-latitudes (Marshall, 2003). While there are some zonal asymmetries to the structure of the SAM (see Technical Annex VI Section AVI.3), it is more symmetric than its NH counterpart (Fyfe et al., 1999). Throughout this chapter, we use a simple fixed latitude based SAM index defined as the difference in zonal mean SLP between 40°S and 65°S (Gong and Wang, 1999) (see Technical Annex VI Section AVI.3 for discussion of other SAM indices). Although the SAM is often used as a proxy for the location of the midlatitude westerly wind belt, trends in the SAM can reflect a combination of changes in jet position, width, and strength. The changes in the SH circulation associated with the SAM impact on surface wind stress (Wang et al., 2014) and hence affect the Southern ocean.

Over the instrumental period, there has been a robust positive trend in the SAM index, particularly since 1970 (*high confidence;* Section 2.4.1.2). It is *likely* that the recent trend in the SAM is unprecedented in the past several Centuries (*medium confidence;* Section 2.4.1.2). There is *high confidence* that stratospheric ozone depletion and GHG increases have contributed to the positive SAM trend during the late 20th century, with ozone depletion dominating in austral summer, following the peak of the Antarctic ozone hole in September-October, and GHG increases dominating in other seasons (Section 3.7.2). To capture the effects of stratospheric ozone changes on the SAM, climate models must include a realistic representation of ozone variations (Section 3.7.2). In models that do not explicitly represent stratospheric ozone chemistry, which includes the majority of the CMIP6 model ensemble, an ozone dataset is prescribed. To properly capture the effects of ozone depletion and recovery on the stratosphere and surface climate, the prescribed ozone dataset must realistically capture observed stratospheric ozone trends with sufficiently high temporal resolution (Neely et al., 2014; Young et al., 2014). The CMIP6 experiment protocol recommended the use of a prescribed 4-D monthly mean ozone concentration field for models without stratospheric chemistry (Eyring et al., 2016a).

The AR5 assessed that the positive trend in the austral summer/autumn SAM observed since 1970 (see Section 2.4.1.2) is *likely* to weaken considerably as stratospheric ozone recovers through the mid-21st century, while in other seasons the SAM changes depend on the emissions scenario, with a larger increase in SAM for higher emissions scenarios. Figure 4.7:b shows the SAM index over 1950–2100 from the CMIP6 models, with one historical realization of austral summer SAM (DJF) from 1950 to 2014 and one scenario realization from 2015 to 2100 for each of the core SSPs. In the CMIP6 models, the austral summer SAM is more positive by the end of the 21st century under SSP3-7.0 and SSP5-8.5. On the other hand, under SSP1-1.9 and SSP1-2.6, the SAM is projected be less positive, especially under SSP1-1.9 where the 5–95% ranges

of anomalies relative to 1995–2014 are -3.1 to 0.0 hPa averaged from 2081–2100. In summary, under the highest emissions scenarios in the CMIP6 models, the SAM in the austral summer becomes more positive through the 21st century (see Figure 4.7:b; *high confidence*).

#### *4.3.3.2 El Niño-Southern Oscillation*

The ENSO reflects quasi-periodic fluctuations in SST, wind, and precipitation over the tropical central to eastern Pacific, affecting much of the tropics, subtropics, and beyond. It is the most dominant mode of variability on interannual timescales and also the dominant source of seasonal climate predictability (Timmermann et al., 2018; see Box 11.3 and Technical Annex VI Section AVI.4). The AR5 assessed from CMIP5 simulations that ENSO variability will *very likely* remain the dominant mode of interannual climate variability in the future, and that associated ENSO precipitation variability on regional scales is *likely* to intensify (Christensen et al., 2013a). However, they assessed there was *low confidence* in projected changes in ENSO variability in the 21st century due to a strong component of natural internal variability.

Among a range of indices proposed for representing ENSO, we use the most prominent one, the Niño 3.4 index defined by the average equatorial SST across the central equatorial Pacific (5°S–5°N, 170°W–120°W) (see Technical Annex VI Section AVI.4). Here, we consider the evolution of the amplitude of Niño3.4 index over the 21st century as projected by the CMIP6 models. We show from each CMIP6 model, one historical realization of annual-mean Niño3.4 index amplitude from 1950 to 2014 and one scenario realization from 2015 to 2100 for each of the considered SSPs (see Figure 4.8:). To separate ENSO variability from long-term tropical Pacific warming, each model realization is regressed against a third-order polynomial fit to the multi-model ensemble mean, and this time series is then removed from the original Niño3.4 index. ENSO amplitude is then defined as the multi-model standard deviation in each year. Note that the different number of models available for each SSP scenario affects the relative variance of each time series. The results for ENSO amplitude in CMIP6 models from 1950–2100 are displayed in Figure 4.8:. From these results, it is *very likely* that the amplitude of ENSO variability does not robustly change over the 21st century (*high confidence*). This conclusion is broadly consistent with results from CMIP5 models (Christensen et al., 2013b), and other large initial condition ensemble experiments (Maher et al., 2018).

**[START FIGURE 4.8 HERE]**

**Figure 4.8:** CMIP6 simulations of the annual amplitude of the ENSO index. Here, the amplitude is defined as the standard deviation across the individual model Niño3.4 index values in a given year and each historical and SSP simulation. To account for potential background changes in the Niño3.4 index, the model average Niño 3.4 index is fitted to a third-order polynomial and then removed from each model by linear regression. The curves show averages over the r1 simulations contributed to the CMIP6 exercise. The numbers inside the panel are the number of model simulations.

**[END FIGURE 4.8 HERE]**

### *4.3.4 Synthesis Assessment of GSAT*

The AR5 assessment of the long-term change in GSAT was based exclusively on the output from the multi-model CMIP5 ensemble (Collins et al., 2013). As for almost all quantities, one realization per model per scenario was picked and defined the ensemble. The 5–95% ensemble range was used to characterize the uncertainty, but the 5–95% ensemble range was interpreted as the 17–83% (*likely*) uncertainty range, taking into account potential uncertainty not represented by the model range. In contrast to the long-term assessment, the AR5 near-term GSAT assessment contained additional uncertainty quantification based on recent observations (Kirtman et al., 2013). While this addition was necessary and justified, it created an inconsistency in the transition from near-term to long-term GSAT assessment in the AR5. Furthermore, the CMIP5-based uncertainty characterization for ECS was distinct from the *likely* range assessed for ECS

(Collins et al., 2013), although the CMIP5 range in ECS and the AR5 ECS *likely* range did not differ much.

In the AR6, GSAT change is assessed throughout using multiple lines of evidence in addition to the CMIP6 projection simulations, for all time horizons out to year 2100 (for the display of the projection results, see Sections 4.3.1 for the entire 21st century and 4.4.1.1 for the near term). Recent research (see BOX 4.1:, Section 7.5) has made it possible to provide both tighter and more confident constraints on GSAT change, conditioned as before on specific scenarios. The assessment combines the CMIP6 projections driven by the SSP scenarios with observational constraints on past simulated warming (Jiménez-de-la-Cuesta and Mauritsen, 2019; Liang et al., 2020; Ribes et al., 2020; Tokarska et al., 2020, Figure 4.9:a,b), as well as the AR6-updated assessment of ECS and TCR in Section 7.5. The combination is formed such that first the average of the constrained CMIP6 results is formed (Figure 4.9:c). Then, an emulator based on a two-layer energy balance model is used (e.g., Held et al., 2010). The emulator is driven by the Chapter 7-derived ERF, and its parameters are chosen such that the best estimate, lower bound of the *very likely* range, and upper bound of the *very likely* range of climate feedback parameter and ocean heat uptake coefficient take the values that map onto the corresponding combination of ECS (3°C, 2°C, and 5°C, respectively) and TCR (1.8°C, 1.2°C, and 2.4°C, respectively) of Section 7.5 (see BOX 4.1:). As a final step, the mean is taken of the constrained-CMIP6 and emulator-based values (Figure 4.9:d; Table 4.6:). Note that not all constrained projections are available for all scenarios and all time periods.

Averaged over the period 2081–2100, GSAT is *very likely* to be higher than in the recent past (1995–2014) by 0.3°C–0.9°C in the low-emission scenario SSP1-1.9 and by 2.6°C–4.7°C in the high-emission scenario SSP5-8.5. For the scenarios SSP1-2.6, SSP2-4.5, and SSP3-7.0, the corresponding *very likely* ranges are 0.6°C–1.4°C, 1.3°C–2.5°C, and 2.0°C–3.8°C, respectively (Figure 4.9:, Table 4.6:). Because the different approaches used for long-term GSAT change produce consistent results (Figure 4.9:), there is *high confidence* in this assessment. GSAT change averaged over the mid-term period 2041–2060 shows a nearly complete separation of the *very likely* ranges between SSP1-1.9 and SSP5-8.5 (Table 4.6:, *high confidence*, see also Section 4.3.1).

The CMIP6 multi-model 5–95% ensemble range of projected warming by the end of the 21st century, relative to the period 1995–2014, is approximately 20% larger than the CMIP5 range (Section 4.3.1). The range has increased mainly because the upper end of the projected warming range has increased, due to models with higher ECS in CMIP6, compared to CMIP5 (Zelinka et al., 2020b; Meehl et al., 9999; Meinshausen et al., 9999; Tokarska et al., 9999) (*high confidence*). The higher warming rates simulated by the more sensitive CMIP6 models are assessed *unlikely* to occur but cannot be excluded (*medium confidence*); the implications of these *unlikely* warming rates can currently be assessed for only a few climate quantities besides GSAT (see Sections 4.5.1 and 4.8), owing to insufficient available literature on other quantities.

**[START FIGURE 4.9 HERE]**

**Figure 4.9:** Multiple lines of evidence for GSAT changes for the long-term period, 2081–2100, relative to the average over 1995–2014. The unconstrained CMIP6 5–95% ranges (coloured bars) in (a) differ slightly because different authors used different subsamples of the CMIP6 archive. The constrained CMIP6 5–95% ranges (coloured bars) in (b) are smaller than the unconstrained ranges in (a) and differ because of different samples from the CMIP6 archive and because different observations and methods are used. In (c), the average of the ranges in (b) is formed (grey bars). Green bars in (c) show the emulator ranges, defined such that the best estimate, lower bound of the *very likely range*, and upper bound of the *very likely* range of climate feedback parameter and ocean heat uptake coefficient take the values that map onto the corresponding values of ECS and TCR of Section 7.5 (see BOX 4.1:). The table in (d) is constructed by taking the average of the constrained CMIP6 estimates (grey bars in c) and the emulator estimates (green bars in c).

**[END FIGURE 4.9 HERE]**

The same information underpinning the assessment of GSAT change for certain periods can also be used to

assess the time when certain levels of GSAT increase are reached (Table 4.6:). Here, the most policy-relevant change is that relative to the mean GSAT over the period 1850–1900, which is taken as an approximation for pre-industrial temperatures, consistent with the IPCC AR5 (Stocker et al., 2013) and the IPCC SR1.5 (Masson-Delmotte et al., 2018b) (see Box 1.2). We note that the recent reference period 1995–2014 was warmer than the period 1850–1900 by 0.86°C, based on the new HadCRUT5 dataset (Morice et al., 9999a) (see Box 1.2). This value is approximately 0.1°C higher than diagnosed in AR5 and SR1.5, due to dataset updates alone (Section 2.3.1); this difference matters a great deal for the assessment of when a warming level of 1.5°C is reached. Because of the additional uncertainty that arises when referencing to a period in the more distant past and because only the emulator (Ribes et al., 9999) have produced the time series that allow the diagnosis of times when GSAT thresholds are crossed, there is only *medium confidence* in the individual timing entries in (Table 4.6:). Note that Ribes et al. (2020) only used scenarios SSP1-2.6, SSP2-4.5, and SSP5-8.5; the mean and confidence ranges for these scenarios are calculated by averaging over the emulator results (Ribes et al., 9999). For SSP1-1.9 and SSP3-7.0, Table 4.6: lists the emulator results; these entries can therefore not be compared directly to the entries for the other scenarios. For the near term, initialized predictions constitute another line of evidence over the period 2019–2028 (see BOX 4.1:, Section 4.4.1.1). The predictions are consistent with the GSAT *very likely* range from the emulator (BOX 4.1:), further adding to the confidence in the near-term assessment.

A warming level of 1.5°C in GSAT, relative to the period 1850–1900, is, in the near-term period 2021–2041, *very likely* to be reached in scenarios SSP3-7.0 and SSP5-8.5, *likely* to be reached in scenarios SSP1-2.6 and SSP2-4.5, and *more likely than not* to be reached in Scenario SSP1-1.9 (*high confidence*, Table 4.6:*)*. The best estimate for reaching a global warming level of 1.5°C – neglecting the influence of natural internal variability – is around year 2030, across all scenarios assessed here (*medium confidence*, Table 4.6:). There is *medium confidence* that an ECS/TCR combination near the lower end of the assessed *very likely* range delays reaching 1.5°C to later than during the near-term for scenario SSP2-2.6 and avoids it altogether for scenario SSP1-1.9 (Table 4.6:). This broader assessment of when 1.5°C is reached under which condition encompasses the SR1.5 assessment of 1.5°C *likely* being reached in the period 2030–2052, with year 2040 as the best estimate, assuming that the current warming rate continues. However, the best estimate for when a global warming level of 1.5°C relative to 1850–1900 will be reached is assessed here in Chapter 4 to be about ten years earlier than the best estimate of the SR1.5 (*medium confidence*). The dominant cause of this re-assessment is the provision of enhanced estimates of the historical observational record (see Section 2.3.1).

A warming level of 2°C in GSAT, relative to the period 1850–1900, is *very likely* to be reached in the mid-term period 2041–2060 or before under SSP5-8.5, *likely* to be reached in the mid-term period under SSP3-7.0 and SSP2-4.5, *more likely than not*, not to be reached in the mid-term period or thereafter under SSP1-2.6, and *very unlikely* to be reached during the 21st century under SSP1-1.9.

**[START TABLE 4.6 HERE]**

**Table 4.6:** Assessment results for GSAT change, based on multiple lines of evidence. The change is displayed in °C relative to the 1995–2014 reference period for selected time periods (near term 2021–2040, mid-term 2041–2060, and long-term 2081–2100), and as the time when certain temperature thresholds are crossed, relative to the period 1850–1900. The timing of crossing a threshold does not include the uncertainty arising from natural internal variability. The entries give both the best estimate and, in parentheses, the *very likely* (5–95%) range. There is *high confidence* in the changes over the twenty-year periods relative to 1995–2014, which combine constrained CMIP6 projections and emulator results. There is *medium confidence* in the timings when certain global warming levels are reached, which are based on a combination of emulator results and (Ribes et al., 9999) for SSP1-2.6, SSP2-4.5, and SSP5-8.5 but solely on emulator results for SSP1-1.9 and SSP3-7.0. An entry n.a. means that the global warming level is not attained during the period 2021–2100.

| | SSP1-1.9 | SSP1-2.6 | SSP2-4.5 | SSP3-7.0 | SSP5-8.5 |
|---|---|---|---|---|---|
| Near term, 2021–2040, relative to 1995–2014 | 0.7 (0.4, 0.9) | 0.6 (0.4, 0.8) | 0.7 (0.4, 0.9) | 0.7 (0.4, 0.9) | 0.7 (0.5, 1.0) |
| Mid-term, 2041–2060, relative to 1995–2014 | 0.8 (0.5, 1.1) | 0.9 (0.6, 1.2) | 1.1 (0.8, 1.5) | 1.3 (0.9, 1.8) | 1.6 (1.1, 2.0) |
| Long-term, 2081–2100, relative to 1995–2014 | 0.6 (0.3, 0.9) | 1.0 (0.6, 1.4) | 1.9 (1.3, 2.5) | 2.9 (2.0, 3.8) | 3.6 (2.6, 4.7) |
| 1.5°C, relative to 1850–1900 | 2028 (2022, n. a.) | 2033 (2024, 2053) | 2031 (2024, 2042) | 2029 (2023, 2038) | 2028 (2022, 2036) |
| 2°C, relative to 1850–1900 | n.a. (n.a., n.a.) | n.a. (2047, n.a.) | 2050 (2040, 2073) | 2046 (2036, 2060) | 2042 (2035, 2051) |
| 3°C, relative to 1850–1900 | n.a. (n.a., n.a.) | n.a. (n.a., n.a.) | n.a. (2074, n.a.) | 2074 (2058, 2098) | 2064 (2054, 2078) |
| 4°C, relative to 1850–1900 | n.a. (n.a., n.a.) | n.a. (n.a., n.a.) | n.a. (n.a., n.a.) | 2100 (2079, n.a.) | 2082 (2069, 2100) |

**[END TABLE 4.6 HERE]**

## 4.4 Near-term Global Climate Changes

This section assesses near-term projections of changes in large-scale climate over the period 2021–2040 and includes information from both initialised decadal predictions and near-term climate model projections. The assessment covers near-term information for GSAT, spatial patterns of surface air temperature and precipitation, and global monsoon precipitation and circulation. The sensitivity of the projected quantities to following a particular emissions scenario will be assessed, including for the likelihood of exceeding global temperature targets in the near-term, together with the influence of internal variability.

### *4.4.1 Atmosphere*

#### *4.4.1.1 Global Surface Air Temperature*

The AR5 assessed that it is *likely* that GSAT will increase in the range 0.3°C–0.7°C over the period 2016–2035 relative to 1986–2005 (*medium confidence*), and that there were not large differences in the GSAT change among different RCPs in this period. The AR5 further assessed that it is *more likely than not* that the mean GSAT for the period 2016–2035 will be more than 1°C above the mean for 1850–1900, and it is *very unlikely* that it will be more than 1.5°C above the 1850–1900 mean (*medium confidence*). It was shown that in the period 2016–2035, differences in GSAT across RCP scenarios for a single climate model are typically smaller than differences between climate models under a single RCP scenario, indicating that model structural uncertainty is larger than scenario uncertainty over that period (Hawkins and Sutton, 2009).

Here, we assess how GSAT is projected to evolve over the near term (2021–2040) under the different core SSPs using the CMIP6 models and a simple climate model emulator (see BOX 4.1:). The AR5 showed that the near-term GSAT is relatively insensitive to the particular RCP emissions scenario. Here we assess the robustness of this result under different SSP scenarios. We further assess the likelihood of exceeding 1.5°C and 2°C global warming above 1850–1900 levels, respectively, during the near-term under a given scenario.

***Near-term projections***

Near-term GSAT projections exhibit only minor dependence on the SSP scenario chosen, consistent with the AR5 assessment (Table 4.6:). Averaged over the near term and viewed across all scenarios, GSAT is *very*

*likely* to be higher than over the reference period 1995–2014 by 0.4°C–1.0°C, with most of the uncertainty arising from that in ECS and TCR (Table 4.6:, e.g., Lehner et al., 2020). Uncertainty in near-term projections of annual-mean GSAT arises in roughly equal measure from internal variability and model uncertainty (*high confidence,* BOX 4.1:). Predictions initialized from recent observations simulate GSAT changes for the period 2019–2028 relative to the recent past that are consistent with the assessed *very likely* range in annual-mean GSAT (Figure 4.10:, Table 4.6:, *high confidence*). A detailed assessment of the performance and skill of initialized decadal predictions is given in Section 4.2.3. All assessments for GSAT assume that there will be no large volcanic eruption in the near term. Section 4.4.4 assesses the impact a large volcanic eruption could have on near-term climate.

A warming level of 1.5°C in GSAT, relative to the period 1850–1900, is in the near-term period 2021–2041 *very likely* to be reached in scenarios SSP3-7.0 and SSP5-8.5, *likely* to be reached in scenarios SSP1-2.6 and SSP2-4.5, and *more likely than not* to be reached in Scenario SSP1-1.9 (*high confidence,* Table 4.6:). The best estimate for reaching a global warming level of 1.5°C – neglecting the influence of natural internal variability – is around year 2030, across all scenarios assessed here (*medium confidence*, Table 4.6:). A detailed assessment of internal variability and its effect on near-term temperature trends, including the potential to detect in the near-term the effects of mitigation actions, is given in Section 4.6.3. There is *medium confidence* that an ECS/TCR combination near the lower end of the assessed *very likely* range delays reaching 1.5°C to beyond the year 2040 for scenario SSP2-2.6 and avoids it altogether for scenario SSP1-1.9 (Table 4.6:).

A warming level of 2°C in GSAT, relative to the period 1850–1900, will in the near-term period 2021–2041 *very unlikely* be reached under SSP1-1.9, *unlikely* be reached under SSP2-2.6, SSP2.4-5, and SSP3-7.0, and *more likely than not,* not be reached under SSP5-8.5 (Table 4.6:).

**[START FIGURE 4.10 HERE]**

**Figure 4.10:** CMIP6 annual-mean GSAT simulations for the recent past and the near term. The figure shows anomalies relative to the period 1995–2014 (left y-axis), converted to anomalies relative to 1850–1900 (right y-axis); the difference between the y-axes is 0.86°C (BOX 1.2). Shown are historical simulations with 29 CMIP6 models (grey) and projections simulations with the same models, following scenario SSP2-4.5 (dark yellow). For the other scenarios, the projections would look similar, apart from the contribution by internal variability (see Section 4.6.3). The black curve shows the observations (HadCRUT5, (Morice et al., 9999a)). Light blue shading shows the 50-member ensemble CanESM5, such that the deviations from the CanESM5 ensemble mean have been added to the CMIP6 multi-model mean. The red curves are from the emulator and show the best estimate (solid), likely range (dashed), and very likely range (dotted) for GSAT (BOX 4.1:). Forecasts for the period 2019–2028 from three prediction systems contributing to DCPP (Boer et al., 2016) are shown in purple, green, and blue. The DCPP results have been drift-removed and referenced to the time-averaged hindcasts for 1995–2014 lead-year by lead-year, following (Kharin et al., 2012; Kruschke et al., 2016), and have then been ensemble-averaged for each prediction system (solid); the shading shows the ensemble range for each prediction system.

**[END FIGURE 4.10 HERE]**

### *4.4.1.2 Spatial Patterns of Surface Warming*

Figure 4.11: shows maps of seasonal mean surface air temperature changes in the near term (2021–2040) in the SSP1-2.6 and SSP5-8.5 scenarios. Consistent with the findings of the AR5 and earlier assessments, these show that the largest warming occurs at high latitudes, particularly in winter in the Arctic (see Section 4.5.1.1), and larger warming over land than over the oceans in both winter and summer seasons (see also Section 4.5.1.1). In both scenarios, the increase in seasonal mean surface temperatures over many NH land regions exceeds 1°C relative to 1995–2014. In the near-term, the two scenarios show surface temperature changes that are similar in magnitude. The projected trajectories for well-mixed GHGs, and as a

consequence the effective radiative forcing, in the scenarios have not yet diverged that much (O'Neill et al., 2016; Riahi et al., 2017). Based on the currently available CMIP6 models, regions that do not show robust warming in the near-term include the northern North Atlantic, parts of India, parts of North America and Eurasia in winter, and the subtropical eastern Pacific in the Southern Hemisphere.

**[START FIGURE 4.11 HERE]**

**Figure 4.11:** CMIP6 multi-model mean change (°C) in (top) DJF and (bottom) JJA near-surface air temperature in 2021–2040 from SSP1-2.6 and SSP5-8.5 relative to 1995–2014 based on 22 models. Stippling indicates regions where the multi-model mean change exceeds two standard deviations of pre-industrial internal variability and where at least 90% of the models agree on the sign of change, as a measure of robustness. Hatching indicates regions where the multi-model mean signal is less than one standard deviation of internal variability.

**[END FIGURE 4.11 HERE]**

The pattern of ERF from aerosols and well-mixed GHGs are distinct (Chapter 7). When comparing scenarios, one question therefore concerns the dependence of patterns of near-surface warming on the precise mix of forcing agents in the scenarios. The spatial efficacies – the change in surface temperature per unit ERF – for $CO_2$, sulphate and black carbon aerosols and solar forcing have been recently evaluated in climate models (Modak et al., 2016, 2018a; Duan et al., 2018; Modak and Bala, 2019; Richardson et al., 2019). It has been found that, on average, the spatial patterns of near-surface warming are largely similar for different external drivers (Xie et al., 2013; Samset et al., 2018b; Richardson et al., 2019), despite the patterns of forcing being different and large spread across different models (Richardson et al., 2019).

Internal variability in near-surface temperature change is large in many regions, particularly in mid-latitudes and polar regions (Hawkins and Sutton, 2012). Projections from individual realizations can therefore exhibit divergent regional responses in the near-term in areas where the amplitude of a forced signal is relatively small compared to internal variability (Deser et al., 2012b, 2014, 2016).

#### *4.4.1.3 Precipitation*

The near-term changes are largely uncertain, and much of the non-robustness in near-term projections is attributable to natural internal variability. The magnitude of projected changes in mean precipitation in the near term is considerably small compared to the magnitude of natural internal variability (Hawkins and Sutton, 2011, 2016; Hoerling et al., 2011; Deser et al., 2012b; Power et al., 2012). The other sources of uncertainty, model uncertainty and scenario uncertainty, are generally small compared to internal variability (Hawkins and Sutton, 2011; Thompson et al., 2015; Lehner et al., 9999). Considering the uncertainty in near-term projections, internal variability contributes to more than 80% of total uncertainty in precipitation in the first decades and remained more than 50% at the end of the century (Hingray and Saïd, 2014). Based on large ensembles of climate change experiments, it was shown that on regional scales, anthropogenic changes in decadal precipitation mean state are distinguishable, outside the range expected from natural variability (Zhang and Delworth, 2018).

In addition to the response to GHG forcing, forcing from natural and anthropogenic aerosols exert impacts on regional patterns of precipitation (Ramanathan et al., 2005; Bollasina et al., 2011; Polson et al., 2014; Krishnan et al., 2016; Liu et al., 2018a; Shawki et al., 2018). In contrast to the GHG changes, aerosol changes induce a drying in the SH tropical band compensated by wetter conditions in the NH counterpart (Acosta Navarro et al., 2017). The spatially uneven distribution of the aerosol forcing may also induce changes in tropical precipitation caused by shifts in the mean location of the intertropical convergence zone (ITCZ) (Hwang et al., 2013; Ridley et al., 2015; Voigt et al., 2017). Because of the large uncertainty in the aerosol radiative forcing, there is *low to medium confidence* in the impacts of aerosols on near-term projected changes in precipitation.

**[START FIGURE 4.12 HERE]**

**Figure 4.12:** CMIP6 multi-model mean change (%) in (top) DJF and (bottom) JJA precipitation from SSP1-2.6 (21 models) and SSP5-8.5 (22 models) in 2021–2040 relative to 1995–2014. Stippling indicates regions where the multi-model mean change exceeds two standard deviations of pre-industrial internal variability and where at least 90% of the models agree on the sign of change, as a measure of robustness. Hatching indicates regions where the multi-model mean signal is less than one standard deviation of internal variability.

**[END FIGURE 4.12 HERE]**

Figure 4.12 shows maps of seasonal mean precipitation change in the near term in the SSP1-2.6 and SSP5-8.5 scenarios. Consistent with the findings of the AR5 and earlier assessments, projected changes of seasonal mean precipitation in the near term will *likely* increase at high latitudes, especially over oceanic regions and in wet regions (over the tropics) and decrease in dry regions (including large parts of the subtropics). However, large uncertainties in the sign of projected change were seen especially in regions located on the borders between regions of increases and regions of decreases. Precipitation changes in the near term show seasonal amplification, precipitation increase in the rainy season and decrease in the dry season (Fujita et al., 2019).

#### *4.4.1.4 Global Monsoon Precipitation and Circulation*

The global monsoon as a system comprises a hierarchy of regional and local monsoons, including the Asian-Australian monsoon, the African monsoon, and the North and South American monsoons (see Chapter 8 Section 8.3.2.4 and Figure 8.12). The global monsoon concept helps to dissect the mechanisms and controlling factors of monsoon variability at various temporal-spatial scales (Wang and Ding, 2008; Wang et al., 2017c). Since the AR5, there has been considerable progress in understanding the factors that affect the decadal changes of GM. Decadal variability of the global monsoon precipitation from 1901 to 2014, in particular over the NH, is rooted primarily in the north-south hemispheric thermal contrast modulated by the phase of AMV and an east-west thermal contrast in the Pacific modulated by the Interdecadal Pacific Oscillation (IPO) (Wang et al., 2018a). The global monsoon precipitation has shown an enhanced trend during the satellite era (Lin et al., 2014), and can be explained by the phase change of AMV (Wang et al., 2013; Deng et al., 2018) (see Section 2.3.1.4.2). Chapter 2 assesses it *likely* that global monsoon precipitation, linked to circulation intensity, has increased over the last 40 years (*medium confidence*). It has been shown that both the IPO and AMV contribute to natural internal variability in the global monsoon (see Section 3.3.3.2). Since the forcing uncertainty is generally negligible for near-term projections, internal variability including the contributions of IPO and AMV is the most important source of uncertainty for global monsoon projection.

In the AR5, there was no specific assessment on global monsoon changes in the near term, but information can be derived from the AR5 projections of the spatial patterns of precipitation change. While the basic pattern of wet regions including global monsoon regions tending to get wetter and dry regions tending to get drier is apparent, large response uncertainty is evident in the substantial spread in the magnitude of projected change simulated by different climate models, highlighting the large amplitude of the natural internal variability of mean precipitation. Over the global land monsoon regions (South Asia, East Asia, West Africa, Australia, North and South America), near-term projected multi-model mean precipitation changes are almost everywhere smaller than the estimated standard deviation of natural internal variability (Figure 4.12:).

**[START FIGURE 4.13 HERE]**

**Figure 4.13:** (a) Global land monsoon precipitation index anomalies (Unit: %) defined as the area-weighted mean precipitation rate in the global land monsoon domain defined by Wang et al. (2013) for the CMIP6 historical simulation and five SSPs. (b) Anomalies in Northern Hemisphere summer monsoon (NHSM)

circulation index (Unit: m/s), defined as the vertical shear of zonal winds between 850 and 200 hPa averaged in a zone stretching from Mexico eastward to the Philippines (0°–20°N, 120°W–120°E) (Wang et al., 2013) in the CMIP6 historical simulation and five SSPs. One realization is averaged from each model. Anomalies are shown relative to the present-day (1995–2014) mean. The number of models included in each simulation is given in the legend.

**[END FIGURE 4.13 HERE]**

The global land monsoon precipitation index, defined as the area-weighted precipitation rate in the global land monsoon domain, tends to increase by 1-4% in the near term under all five core SSPs (Figure 4.13:a), but the changes are small compared to the intermodel spread in the historical period. The tropical monsoon circulation index, defined as the vertical shear of zonal winds between 850 and 200 hPa averaged in a zone stretching from Mexico eastward to the Philippines (0°–20°N, 120°W–120°E), tends to decrease under four of the five SSP scenarios (Figure 4.13:b), potentially associated with the weak increase of monsoon precipitation, but again the projected changes in the global monsoon circulation are weak relative to natural internal variability and structural differences across models. In summary, we assess that near-term changes in global monsoon precipitation and circulation are *likely* to be dominated by the effects of natural internal variability.

### *4.4.2 Cryosphere, Ocean, and Biosphere*

#### *4.4.2.1 Arctic Sea Ice*

The AR5 assessed that for RCP8.5, Arctic sea-ice coverage in September will drop below 1 million km$^2$ at some point between 2040 and 2060 (Collins et al., 2013). Since the AR5, there has been substantial progress in understanding the response of Arctic sea ice to near-term changes in external forcing. In particular, it is *very likely* that different trajectories of the near-term evolution of anthropogenic forcing cause distinctly different likelihood ranges for very low sea-ice coverage to occur over the next two decades (see Figure 4.1: and Section 4.3.2). This is most directly described in terms of the range of cumulative anthropogenic $CO_2$ emissions over the period 2020–2040, which ranges from about 500 Gt $CO_2$ in RCP2.6 to more than 1000 Gt $CO_2$ in RCP 8.5. This results in an *unlikely* drop of September Arctic sea-ice coverage to below 1 million km$^2$ before 2040 for RCP 2.6, and a *likely* drop of September Arctic sea-ice coverage to below 1 million km$^2$ before 2040 for RCP 8.5 (*medium confidence*), based on a single study (Notz and Stroeve, 2018) but consistent with estimates from temperature-based studies cited below. These estimates are derived from an observed loss of about 3 m$^2$ of September sea-ice area per tonne of $CO_2$ emissions (Notz and Stroeve, 2016) and an estimated internal variability of standard deviation < 0.5 million km$^2$ of September sea-ice coverage as given by CMIP5 simulations and the observational record (Notz and Marotzke, 2012; Olonscheck and Notz, 2017). The much higher likelihood of a virtually sea-ice free Arctic Ocean during summer before 2040 in RCP8.5 compared to RCP2.6 is consistent with related studies that find a substantially increased likelihood of an ice-free Arctic Ocean for 2.0°C mean global warming relative to pre-industrial levels compared to 1.5°C mean global warming relative to pre-industrial levels (Screen and Williamson, 2017; Jahn, 2018; Niederdrenk and Notz, 2018; Sigmond et al., 2018; Olson et al., 2019b).

An assessment of September Arctic sea ice area changes in the mid- to long-term is provided in Section 4.3. Here, we display 5–95% ranges of September Arctic sea ice area trends across the CMIP6 historical simulations with SSP1-1.9, SSP1-2.6, SSP2-4.5, SSP3-7.0, and SSP5-8.5 extensions, and for all 10-year, 20-year, and 30-year periods ending in the near-term (2021–2040; see Figure 4.14:). Despite the substantial importance of anthropogenic forcing on the evolution of Arctic sea-ice cover, internal variability may mask its impact over the near-term. Based on results from the CMIP6 models, we conclude that Arctic SIA will decrease in September in the near-term given 10-year, 20-year, or 30-years trends ending in 2021–2040, respectively (*high confidence*; see Figure 4.14:).

**[START FIGURE 4.14 HERE]**

**Figure 4.14:** CMIP6 linear trends in September Arctic sea ice area (106 km$^2$ per decade) for 10-year, 20-year, and 30-year periods ending in 2021–2040 following five SSPs. Plotted are the 5–95% ranges (i.e. mean ± standard deviation × 1.64) across the r1 simulations contributed to the CMIP6 exercise. The numbers at the top of the plot are the number of model simulations in each SSP ensemble. The numbers near the bottom of the plot indicate the SSP-average percentage of simulated trends that are negative (i.e. indicating decreasing sea ice area).

**[END FIGURE 4.14 HERE]**

#### *4.4.2.2 Ocean and Land Carbon Uptake*

Ocean carbon uptake is both a key feature of the physical ocean in mitigating the rise of atmospheric $CO_2$ and a driver of changes in the ocean biosphere, including changes in ocean acidity. The AR5 assessed, with *high confidence*, that all CMIP5 models project continued ocean carbon uptake through the 21st century, with higher uptake in those RCPs with higher concentration pathways (Ciais et al., 2013). On the other hand, the AR5 determined that the future evolution of land carbon uptake is much more uncertain and gave only *medium confidence* on the magnitude of simulated future land carbon changes. (Ciais et al., 2013). The AR5 did not assess near-term changes in ocean or land carbon uptake.

Here, we display 5–95% ranges of ocean and land carbon uptake trends across the CMIP6 simulations for five SSPs, and for all 10-, 20-, and 30-year periods ending in 2021–2040 (see Figure 4.15:). Based on results from the CMIP6 models, we conclude that SSP2-4.5, SSP3-7.0, and SSP5-8.5 all lead to positive 10-, 20-, and 30-year period trends in ocean carbon uptake over the near-term. Positive trends in ocean carbon uptake are less obvious in the lower emissions scenarios for 10- and 20-year periods, but very apparent for 30-year periods. Ensemble-mean trends in land carbon uptake over the near term are generally positive, but in association with large uncertainties. In summary, it is *very likely* that ocean carbon uptake will increase in the near-term under the higher emissions scenarios (*high confidence*).

**[START FIGURE 4.15 HERE]**

**Figure 4.15:** CMIP6 trends in carbon uptake (PgC yr$^{-1}$ per decade) for 10-year, 20-year, and 30-year periods ending in 2021–2040 following five SSPs. (a) Ocean carbon uptake. (b) Land carbon uptake. Plotted are the 5–95% ranges (i.e. mean ± standard deviation × 1.64) across the r1 simulations contributed to the CMIP6 exercise. The numbers at the top of the plot are the number of model simulations in each SSP ensemble. The numbers near the bottom of the plot indicate the SSP-average percentage of simulated trends that are positive (i.e. indicating increasing carbon flux from the atmosphere into the ocean or land).

**[END FIGURE 4.15 HERE]**

### *4.4.3 Modes of Variability*

This subsection assesses the near-term evolution (2021–2040) of the large-scale modes of climate variability and their associated teleconnections. Discussions of the physical mechanisms and the individual feedbacks involved in the future change of each mode are provided in Chapters 8–10.

#### *4.4.3.1 Northern and Southern Annular Modes*

***The NAM***

The AR5 assessed from CMIP5 simulations that there is only *medium confidence* in near-term projections of a northward shift of NH storm track and westerlies, and an associated increase in the NAM index, because of

the large response uncertainty and the potentially large influence of internal variability. In general, the projected near-term multi-model mean change in the NAM is weak in magnitude compared to the inter-model and/or multi-realization variability within the ensemble (Figure 4.16:, and Deser et al., 2012; Barnes and Polvani, 2015). On such short timescales, it is apparent that any forced signal of change in the NAM, which will be subject to considerable model uncertainty arising from imperfect representation of the physical processes described above, is expected to be of comparable magnitude to interannual or decadal variability in the NAM that is unrelated to anthropogenic forcing (Li et al., 2018a). A tendency to a near-term change towards a more positive NAM during the boreal winter is apparent in Figure 4.16:, where the near-term (2021–2040) changes in the NAM, relative to present-day (1995–2014), from the CMIP6 ensemble for five SSPs are shown.

**[START FIGURE 4.16 HERE]**

**Figure 4.16:** CMIP6 Annular Mode index change (hPa) from 1995–2014 (present-day; as an average) to 2021–2040 (near-term; as an average). (a) NAM and (b) SAM. The NAM is defined as the difference in zonal mean sea-level pressure (SLP) at 35°N and 65°N (Li and Wang, 2003) and the SAM as the difference in zonal mean SLP at 40°S and 65°S (Gong and Wang, 1999). The shadings are the 5 to 95% ranges (i.e. mean ± standard deviation × 1.64). The numbers near the top of each panel are the numbers of model simulations in each SSP ensemble. The numbers near the bottom of the panels are the SSP-averaged percentage of simulations with positive anomalies.

**[END FIGURE 4.16 HERE]**

On seasonal to interannual timescales, there is new evidence since AR5 that initialised predictions show lower potential predictability for the boreal winter NAO than the correlation skill with respect to observations (Eade et al., 2014; Baker et al., 2018; Scaife and Smith, 2018). This has been referred to in the literature as a "signal-to-noise paradox" and means that very large ensembles of predictions are needed to isolate the predictable component of the NAO. While the processes that contribute to predictability of the winter NAO on seasonal timescales are distinct from the processes that drive multi-decadal trends, there is emerging evidence that initialised predictions also underrepresent the predictability of the winter NAO on decadal timescales (Smith et al., 2019c). Post-processing and aggregation of initialised predictions may therefore reveal significant skill for predicting the winter NAO on decadal timescales (Smith et al., 9999).

***The SAM***

The AR5 assessed that it is *likely* that increases in GHGs and the projected recovery of the Antarctic ozone hole will be the principal drivers of future SAM trends. They further concluded that the positive trend in austral summer/autumn SAM observed over the past several decades (Section 2.4.1.2) is *likely* to weaken considerably as stratospheric ozone recovers through to the mid-21st century. The effects of ozone depletion and recovery on the SH circulation primarily occur in austral summer, while GHGs influence the SH circulation year round (Gillett and Fyfe, 2013; Grise and Polvani, 2014b) and are therefore *likely* to be the dominant driver of projected circulation changes outside of austral summer (Gillett and Fyfe, 2013; Barnes et al., 2014; Solomon and Polvani, 2016). Based on current scenarios specifying future atmospheric decline of ozone depleting substances (World Meteorological Organisation, 2010), the Antarctic ozone hole in October is projected by chemistry-climate models to recover by around 2060 (Dhomse et al., 2018; World Meteorological Organisation, 2014, 2019). Observational evidence since AR5 shows the onset of healing of the Antarctic ozone hole (World Meteorological Organisation, 2019; Solomon et al., 2016), which has been connected using detection and attribution methods to a pause in the summer SAM trend since 2000 (Banerjee et al., 9999). In austral summer, ozone recovery and increasing GHGs will have opposing effects on the SAM over the next several decades (Barnes et al., 2014).

Since the AR5, there have been advances in understanding the role of internal climate variability for projected near-term SH circulation trends (Solomon and Polvani, 2016). A large initial condition ensemble experiment following the RCP4.5 emissions scenario shows a monotonic positive SAM trend in JJA. In DJF,

the SAM trend over the first half of the 21st century is weaker compared to the strongly positive trend observed and simulated over the late 20th century. In that model, the number of realizations required to identify a significant change in decadal mean austral winter SAM index from a year 2000 reference state decreased to below five by around 2025–2030 (Solomon and Polvani, 2016). However, in DJF the same criterion is not met until the second half of the 21st century, owing to the near-term opposing effects of ozone recovery and GHGs on the summer SAM.

Figure 4.16:b shows seasonal mean near-term (2021–2040) changes in the SAM index relative to present-day (1995–2014) from the CMIP6 ensemble for the five core SSPs. These results show a weak tendency in the near-term towards a more positive SAM index (<1 hPa) in all seasons except austral summer. In austral summer, the central estimates of near-term SAM index anomalies are close to zero for all the core SSPs except SSP1-1.9, though less than half to number of realizations are included for SSP1-1.9 compared to the other four SSPs. In all seasons, the differences between the central estimates of the change in SAM index for each SSP are much smaller than the inter-model ensemble spread. The CMIP6 ensemble spread is largest in austral winter, consistent with the large internal variability in the SH atmospheric circulation (Garfinkel et al., 2015). However, despite the number of CMIP6 realizations in Figure 4.16:b being larger than the suggested threshold of five realizations needed to detect a significant near-term change in decadal mean austral winter SAM index for a single CMIP5 model (Solomon and Polvani, 2016), the 5–95% intervals on the CMIP6 spread encompass zero for all core SSPs. This suggests both internal variability and model uncertainty contribute to the CMIP6 ensemble spread in near-term SAM index changes.

An influence of forcing agents other than stratospheric ozone and GHGs, such as anthropogenic aerosols, on SAM changes over the historical period has been reported in some climate models (Rotstayn, 2013), but the response across a larger set of CMIP5 models is not robust (Steptoe et al., 2016) and depends on the details of the tropospheric temperature response to aerosols (Choi et al., 2019). This gives *low confidence* in the potential influence of anthropogenic aerosols on the SAM in the future.

#### *4.4.3.2 El Niño-Southern Oscillation and its Teleconnections*

The AR5 assessed that it is *very likely* that the ENSO will remain the dominant mode of interannual variability in the future, but did not specify its change in near term. A subset of CMIP5 models that simulate the ENSO Bjerknes index most realistically show an increase of ENSO SST amplitude in the near-term future and decline thereafter (Kim et al., 2014). However, a detection of robust near-term changes of ENSO SST variability in response to anthropogenic forcing is difficult to achieve due to pronounced unforced low-frequency modulations of ENSO (Wittenberg, 2009; Maher et al., 2018). Figure 4.8: in 4.3.3.2 using CMIP6 models also shows no robust change in ENSO SST variability in near term.

**[START FIGURE 4.17 HERE]**

**Figure 4.17:** Multi-model mean (thick line) of changes in amplitude of ENSO rainfall variability from CMIP6 historical simulation from 1950 to 2014 and four SSPs from 2015 to 2100. Shading is the 10–90% range across CMIP6 models for historical simulation (grey), SSP1-2.6 (mid blue) and SSP5-8.5 (pink), respectively. The amplitude of ENSO rainfall variability is defined as the standard deviation of the Niño3-area averaged rainfall index over 30-year running windows. The standard deviation in every single model is normalized by each model's present-day standard deviation averaged from 1950 to 1999. The number of available model is listed in parentheses.

**[END FIGURE 4.17 HERE]**

While there is no strong model consensus on the change in amplitude of ENSO SST variability, the amplitude of ENSO-associated rainfall variability *likely* increases (Power et al., 2013; Cai et al., 2015). Analysis of CMIP6 models shows a slight increasing trend in amplitude of rainfall variability over Niño3.4 region in near term attributable to mean moisture increase regardless of changes in ENSO SST variability

(Figure 4.17:Figure 4.8:). However, there is no distinguishable changes in the rainfall variability among four SSPs with significant model spread in the near term. From these results, it is *likely* that there is no robust change in amplitude of ENSO SST and rainfall variability in the near term although the rainfall variability slightly increases (*medium confidence*).

#### *4.4.3.3 Pacific Decadal Variability*

Climate variability of the Pacific Ocean on decadal and interdecadal timescales is described in terms of a number of quasi-oscillatory SST patterns such as the Pacific Decadal Oscillation (PDO) (Mantua et al., 1997) and the Interdecadal Pacific Oscillation (IPO) (Folland, 2002), which are referred to as the Pacific Decadal Variability (PDV) (Newman et al., 2016b). PDV comprises an inter-hemispheric pattern that varies at decadal-to-interdecadal timescales (see Chapter 3, Figure 3.35). One important feature of PDV is indeed the strong covariance between the tropics and extratropics (Liu, 2012), which has proved difficult to simulate accurately by climate models (Newman et al., 2016b). However, although the spatial domains to derive the IPO and PDO indices differ, and uncertainty applies to trend removal and time-filtering (Newman et al., 2016b; Tung et al., 2019), the IPO and PDO are highly correlated in time and they will be assessed together as the PDV (see Technical Annex AVI.7).

The AR5 assessed that near-term predictions of PDV (then referred to as PDO or IPO) were largely model dependent (Mochizuki et al., 2012; van Oldenborgh et al., 2012), not robust to sampling of initialization start-dates, overall not statistically significant, and worse than persistence (Doblas-Reyes et al., 2013), although some studies showed positive skill for PDV (Mochizuki et al., 2010; Chikamoto et al., 2013). Consistently, the CMIP5 decadal-prediction ensemble yielded no prediction skill of SST over the key PDV centres of action in the Pacific Ocean, both at 2–5 year and 6–9 year forecast averages (Doblas-Reyes et al., 2013; Guemas et al., 2013a).

Since the AR5, the processes causing the multi-decadal variability in the Pacific Ocean have become better understood (Newman et al., 2016a; Henley, 2017). However, the relative importance of tropical and extratropical processes underlying PDV remains unclear; although it seems to be stochastically driven rather than self-excited (Liu, 2012; Liu and Di Lorenzo, 2018).

Because PDV represents not one, but many dynamical processes, it represents a challenge as a target for near-term climate predictions and projections. The new generation of decadal forecast systems keeps showing poor (Shaffrey et al., 2017) to moderate (Smith et al., 2019c) multi-year prediction skill for PDV, although there is the potential for forecasting capabilities in case studies (Meehl and Teng, 2012; Meehl et al., 2014a). For the near-term, a transition of PDV from the negative phase (1999-2012) towards a positive phase is predicted in the coming years (2013-2022) (Meehl et al., 2016).

The PDV has been shown to influence the pace of global warming (Meehl et al., 2011, 2016; Kosaka and Xie, 2013; England et al., 2014; Watanabe et al., 2014; Cai et al., 2015; Dai et al., 2015; Douville et al., 2015); but the extent to which PDV is externally forced or internally generated and how it will evolve in a future climate remain open questions (Deser and Phillips, 2017).

#### *4.4.3.4 Indian Ocean Basin and Dipole Modes and their Teleconnections*

Important modes of interannual climate variability with pronounced climate impacts in the Africa-Indo-Pacific areas of the globe are the Indian Ocean Dipole (IOD), which is closely related to- and often coincides with ENSO phases (Stuecker et al., 2017), and the Indian Ocean Basin (IOB) mode, which is often described as a capacitor effect in response to ENSO (Xie et al., 2009; Du et al., 2013) (IOD and IOB are extensively described in Technical Annex AVI.5)

The projected climate mean state changes in the tropical Indian Ocean resemble a positive IOD state, with faster warming in the west compared to the east. This mean state change will potentially lead to a reduction

in the amplitude difference between positive and negative IOD events, however with no robust change in IOD frequency (Cai et al., 2013). Currently, no new studies and evidence exist that would suggest a cessation of IOD variability and robust change in the IOB mode in the near-term to long-term future. This means that we can also expect that the ENSO-IOD and connection with phenomena of important climate implications like the Afro-Asian monsoons alongside other Indian Ocean Basin relationships observed in the current climate to persist in the near-term future.

#### *4.4.3.5 Atlantic Multidecadal Variability*

The Atlantic Multi-decadal Variability (AMV) is a large-scale climate mode accounting for the main fluctuations in North Atlantic SST on multi-decadal time scales (Technical Annex AVI.8). The AMV influences air temperatures and precipitation over adjacent and remote continents, and its undulations can partially explain the observed variations in the NH mean temperatures (Steinman et al., 2015). The origin of this variability is still uncertain. Ocean dynamics (e.g., changes in the AMOC), external forcing, and local atmospheric forcing all seem to play a role (Menary et al., 2015; Ruprich-Robert and Cassou, 2015; Brown et al., 2016; Cassou et al., 2018; Wills et al., 2019).

The AR5 assessed with *high confidence* that initialized predictions can improve the skill for temperature over the North Atlantic, in particular in the sub-polar branch of AMV, compared to the projections, for the first five years (see WG1 AR5 Figures 11.3 and 11.4). However, non-initialized predictions showed positive correlation over the same time-range as well, consistent with the notion that part of this variability is caused by external forcing.

Since the AR5, near-term initialized predictions, both multi-model (Bellucci et al., 2015a; García-Serrano et al., 2015; Smith et al., 2019c) and single-model ensembles (Marotzke et al., 2016; Simpson et al., 2018b; Yeager et al., 2018a), confirm substantial skill in hindcasting North-Atlantic SSTs anomalies on a time range of 8–10 years. Yet, skill in predicting the AMV is not always translated into equally successful predictions of temperature and precipitations over the nearby land. This might be related to systematic model errors in the simulation of the spatial and temporal structure of the AMV and too weak associated teleconnections (see Section 3.7.7), and also to the higher noise in regional land variables compared to the AMV index. However, as shown in (Simpson et al., 2019b), AMV predictions can be used as proxies to predict other variables (March precipitation over Western Europe in Simpson et al., (2019b)) whose relationship with North Atlantic SST is robust in observations, but not well captured in climate models. Encouraging results about the prediction of land precipitation linked to the warm AMV phase (see Chapter 3 section 3.7.7 and Figure AVI.9) on a 2-9 year time scale are reported in the multi-model study by Smith et al. (2019c). Positive correlations with observations are found in the Sahel, South America, the Maritime Continent. Analyses from large-ensemble decadal prediction systems such as the Community Earth System Model decadal prediction large ensemble (CESM-DPLE) (Yeager et al., 2018a) show an improvement with respect to the CMIP5 decadal hindcasts (Martin and Thorncroft, 2014b) in forecasting Sahel precipitation over three to seven years, which is consistent with the current understanding of AMV impact over Africa (Mohino et al., 2016; Smith et al., 2019c). CESM-DPLE predicts drought conditions over the Sahel through 2020, which is compatible with a shift towards a negative phase of AMV as a result of a weakening of the AMOC, advocated by a number of studies (Hermanson et al., 2014; Robson et al., 2014b; Yeager et al., 2015).

However, since the AMOC-AMV relationship varies considerably from model to model in terms of amplitudes, spatial properties, preferred time scales, and associated teleconnections (Ruiz-Barradas et al., 2013; Ba et al., 2014; Peings et al., 2016), and recent studies have even argued about the active role of ocean dynamics in generating the AMV, that could be consequently attributed to random atmospheric forcing (Clement et al., 2015; O'Reilly et al., 2016; Zhang et al., 2016; Cane et al., 2017), the *confidence* in the predictions of AMV impacts is *low*. On the other hand, there is *high confidence* that the AMV skill over 5–8-year lead time is improved by using initialized predictions (compared to non-initialized ones).

#### *4.4.3.6 Tropical Atlantic Modes and their Teleconnections*

Interannual variability of the tropical Atlantic can be described in terms of two main climate modes: the Atlantic Equatorial Mode and the Atlantic Meridional Mode (AMM) (Technical Annex AVI.6). The Atlantic Equatorial Mode, also commonly referred to as the Atlantic Niño or Atlantic Zonal Mode, is associated with SST anomalies near the equator, peaking in the eastern basin, while the AMM is characterized by an inter-hemispheric gradient of SST and wind anomalies. Both modes are associated with changes in the ITCZ and related winds and exert a strong influence on the climate in adjacent and remote regions.

Despite considerable improvements made in CMIP5 with respect to CMIP3, most CMIP5 models have difficulties in simulating the mean climate of the tropical Atlantic (Mohino et al., 2019) and are not able to correctly simulate the main aspects of Tropical Atlantic Variability (TAV) and associated impacts. This is presumably the main reason why there is a lack of specific studies dealing with near-term changes in tropical Atlantic modes. Nevertheless, the AR5 reported that the ocean is more predictable than continental areas at the decadal timescale. In particular, the predictability in tropical oceans is mainly associated with decadal variations of the external forcing component. Since the AMV affects the tropical Atlantic, near-term variations of the AMV can modulate the Equatorial Mode and the AMM as well as associated impacts. The AR5 reported with *high confidence* that the skill of predicting the AMV index increases with initialization for the early forecast ranges.

There are no specific studies focusing on near-term changes in tropical Atlantic modes; nevertheless, decadal predictions show that although the North Atlantic stands out in most CMIP5 models as the primary region where skill might be improved because of initialization, encouraging results have also been found in the tropical Atlantic (Meehl et al., 2014a). The impact of the initialization in the tropical Atlantic is not only visible in surface temperature but also in the subsurface ocean (Corti et al., 2015). In particular, initialization improves the skill via remote ocean conditions in the North Atlantic subpolar gyre and tropical Pacific, which influence the tropical Atlantic through atmospheric teleconnections (Dunstone et al., 2011; Vecchi et al., 2014; García-Serrano et al., 2015). Improvements of some aspects of climate prediction systems (initialization techniques, large ensembles, increasing model resolution) have also led to skill improvements over the tropical Atlantic (Pohlmann et al., 2013; Monerie et al., 2017; Yeager and Robson, 2017).

Recent studies have shown that the AMV can modulate not only the characteristics of the Atlantic Niños, but also their inter-basin teleconnections (Indian and Pacific). In particular, the Atlantic Niño–ENSO relationship is strongest during negative AMV phases (Martín-Rey et al., 2014; Losada and Rodríguez-Fonseca, 2016) when equatorial Atlantic SST variability is enhanced (Martín-Rey et al., 2017; Lübbecke et al., 2018).

Based on CMIP5 and available CMIP6 results, we conclude that there is a clear lack of studies on the near-term evolution of TAV and associated teleconnections. However, some studies show that despite severe model biases there are skilful predictions in the mean state of tropical Atlantic surface temperature several years ahead (*medium confidence*), though skill in simulated variability has not been assessed yet.

Decadal changes in the Atlantic Niño spatial configuration and associated teleconnections might be modulated by the AMV, but there is *low confidence* in these results.

### *4.4.4 Response to Short-Lived Climate Forcers and Volcanic Eruptions*

Mitigation of long-lived GHGs is also associated with mitigation of short-lived climate forcers (SLCF) (methane, aerosols, ozone) (see also Sections 6.6.3 and 6.6.4). The AR5 assessed that emission reductions aimed at decreasing local air pollution could have a near-term impact on climate (*high confidence*) (Kirtman et al., 2013). Because of their shorter lifetimes, early action on SLCF species including black carbon, methane and hydrofluorocarbons mainly influences near-term surface warming rates (Chalmers et al., 2012; Shindell et al., 2017; Shindell and Smith, 2019a) and has a modest influence on warming levels by mid-century up to a few tenths of a degree Celsius (Smith and Mizrahi, 2013; Stohl et al., 2015; Hienola et al.,

2018). However, SLCF mitigation has a limited role in limiting maximum warming relative to comparable reductions taking place later (Hienola et al., 2018; Rogelj et al., 2014). Samset et al. (2020) find that strong mitigation policies targeting black carbon (BC) emissions would have a rapid, discernible impact on GSAT trends, but a small net effect in the longer term. Mitigation of $CH_4$ combines rapid effects on surface temperature with long term gains, while mitigation of $CO_2$ stands out as the most efficient, both in the short and longer term, although very strong mitigation is required to have clearly detectible effect in the near-term. Rapid elimination of sulphate aerosols ($SO_2$), which contributes a negative radiative forcing in the present day (Section 7.3.3), would *likely* cause an increase in GSAT of a few tenths of a degree (Matthews and Zickfeld, 2012; Gillett and Von Salzen, 2013; Samset et al., 2018b; Lelieveld et al., 2019), but this could be tempered by reductions in methane emissions (*high confidence*) (Rogelj et al., 2018b).

A complete phase-out of all anthropogenic $SO_2$, black carbon, and organic carbon is expected to lead to additional surface warming for a climate stabilization scenario (0.5°C–1.1°C; *low confidenc*e) (Samset et al., 2018b). However, more realistic scenarios for current air quality legislation targets and the maximum feasible reduction of SLCFs from anthropogenic sources based on current technological options indicate combined climate and air quality benefits on decadal and longer timescales (Shindell and Smith, 2019b). The estimated additional warming for scenarios of increasing anthropogenic methane and black carbon emissions by mid-century, compared to a scenario for maximum technical reduction, is much lower than an earlier estimate (UNEP, 2011; Shindell et al., 2012). Figure 4.18: shows GSAT evolution in CMIP6 models for the SSP3-7.0-lowNTCF experiment (Collins et al., 2017b) which reduces concentrations of short-lived climate forcers relative to the SSP3-7.0 scenario. The results show that the projected multi-model mean GSAT anomaly is increased by a few tenths of a degree by mid-century, but this difference is smaller than the *likely* GSAT range of the SSP3-7.0 projections based on the CMIP6 model spread.

Distinguishing the role of SLCFs for climate from that of long-lived GHGs is complicated by the fact that many short-lived species are co-emitted with $CO_2$ through combustion; hence policies aimed at reducing carbon emissions implicitly capture some SLCF reductions. For example, considering SLCFs separately from long-lived GHG emissions artificially inflates the potential control that SLCFs can exert on climate under ambitious mitigation and stabilization strategies (Rogelj et al., 2014). In scenarios consistent with meeting the 2°C target, additional measures to reduce anthropogenic black carbon emissions have little effect, because the key emissions are already ruled out through the implicit $CO_2$ controls. Nevertheless, other approaches may aim to tackle poor air quality through legislation, which would influence the abundance of SLCFs (Shindell et al., 2017).

**[START FIGURE 4.18 HERE]**

**Figure 4.18:** Global surface air temperature change relative to the 1995–2014 average (left axis) and relative to the 1850–1900 average (right axis). The comparison is for CMIP6 models for the AerChemMIP (Collins et al., 2017b) SSP3-7.0-lowNTCF experiment, where concentrations of short-lived species are reduced compared to reference SSP3-7.0 scenario. The curves show averages over the r1 simulations contributed to the CMIP6 exercise, the shadings around the SSP3-7.0 curve shows 5 to 95% ranges (i.e. mean ± standard deviation x 1.645), and the numbers near the top show the number of model simulations.

**[END FIGURE 4.18 HERE]**

Since the AR5, there have been advances in the physical understanding of the climate system response to SLCFs. The GSAT response to an idealised, large change in black carbon has been shown to be relatively weak in climate models owing to rapid adjustments that contribute to the effective radiative forcing and partly offset the stronger, positive instantaneous radiative forcing (Stjern et al., 2017). There may be a larger sensitivity of surface temperatures to aerosol emissions in northern mid-latitudes and over land (*low confidence*). The additional warming at high northern latitudes associated with projected reductions in aerosol emissions over the 21st century, as compared to a reference scenario that assumes no reduction in SLCFs, is expected to have knock-on effects on other parts of the climate system, including a more rapid reduction in Arctic sea ice extent (Gagné et al., 2015). Furthermore, a removal of anthropogenic aerosols

could increase global mean precipitation (2–4.6%; *low confidence*; Richardson et al., 2018; Samset et al., 2018; Takahashi et al., 2018). Future tropospheric ozone radiative forcing is *likely* to be determined by an interplay between changes to tropospheric ozone precursor emissions, changes to stratosphere-to-troposphere exchange of ozone, future methane emissions, and changes to lightning-$NO_x$ production of ozone (Banerjee et al., 2018; Finney et al., 2018a; Iglesias-Suarez et al., 2018).

The main uncertainties in the climate impacts of SLCFs in the future come from: (i) the uncertainty in anthropogenic aerosol ERF and the rapid adjustments that affect ERF for other SLCFs (Chapter 7); (ii) uncertainty in the relative emissions of different SLCFs that have warming and cooling effects in the current climate (Chapter 7); and (iii) physical uncertainty including the efficacy of the climate response to SLCFs compared to long-lived GHGs (Marvel et al., 2016; Richardson et al., 2019). One example of physical uncertainty is that the shortwave radiative forcing from methane was underestimated in previous calculations (Etminan et al., 2016; Collins et al., 2018), which affects understanding of present day and future methane effective radiative forcing (ERF) (Modak et al., 2018a). Another example of physical uncertainty is projected changes in lightning-$NO_x$ production, which contributes to future ozone radiative forcing (Banerjee et al., 2014, 2018; Finney et al., 2018b). Methane levels have continued to rise since the AR5, and the current trajectory for methane lies between the RCP4.5 and RCP8.5 scenarios (Nisbet et al., 2019). If the recent observed growth in methane emissions were to continue until 2100, it would add an additional 0.5 $Wm^{-2}$ radiative forcing by 2100 compared to the RCP2.6 scenario, with the latter being broadly consistent with the Paris Agreement global temperature goal (Nisbet et al., 2019).

Another factor that could substantially alter projections in the near term would be the occurrence of a large explosive volcanic eruption, or even a decadal to multi-decadal sequence of small-to-moderate volcanic eruptions as witnessed over the early 21st century (Santer et al., 2014). An eruption similar to the last large tropical eruption, Mount Pinatubo in the Philippines in June 1991, is expected to cause substantial Northern Hemisphere (NH) cooling, peaking between 0.09°C and 0.38°C and lasting for three to five years, as indicated by climate model simulations over the past millennium (e.g., Jungclaus et al., 2010). The phase 3 of Paleoclimate Modelling Intercomparison Project (PMIP3)/CMIP5 models simulated a significant Northern Hemisphere (NH) cooling in response to individual volcanic events (peaks between 0.1°C and 0.5°C depending on model during the first year after the eruption), and that lasts for three to five years. The response to changes in multi-decadal volcanic forcing shows similar cooling in both simulations and reconstructions of NH temperature. Volcanic eruptions generally result in decreased global precipitation for up to a few years following the eruption (Iles and Hegerl, 2014, 2015; Man et al., 2014), with climatologically wet regions drying and climatologically dry regions wetting (*medium confidence*), which is opposite to the response under global warming (Held and Soden, 2006; Iles et al., 2013).

In the AR5, uncertainty due to future volcanic activity was generally not considered in the assessment of the CMIP5 21st-century climate projections (Taylor et al., 2012; O'Neill et al., 2016). Since the AR5, there has been considerable progress in quantifying the impacts of volcanic eruptions on decadal climate prediction and longer-term climate projections (Meehl et al., 2015; Timmreck et al., 2016; Bethke et al., 2017). By exploring 60 possible volcanic futures under RCP4.5, it has been demonstrated how the inclusion of volcanic forcing may enhance climate variability on annual-to-decadal timescales (Bethke et al., 2017). The interannual uncertainty range in annual-mean GSAT is about 50% higher (from 0.3°C to 0.5°C) in simulations with volcanoes relative to simulations without volcanoes (Figure 4.19:). Consistent with a tropospheric cooling response, the change in ensemble spread in the volcanic cases is skewed towards lower GSAT relative to the non-volcanic cases (see Figure 4.19:). In these simulations with multiple volcanic forcing futures there is: 1) an increase in the frequency of extremely cold individual years; 2) an increased likelihood of decades with negative GSAT trend; and 3) later anthropogenic signal emergence (*high confidence*).

**[START FIGURE 4.19 HERE]**

**Figure 4.19:** Annual-mean GSAT. a, Ensemble mean (solid) of VOLC (blue), VOLC-CONST (magenta) and NO-VOLC (red/orange) with 5–95% range (shading) and ensemble minima/maxima (dots) for VOLC and

NO-VOLC; evolution of the most extreme member (black). b, Probability density function (PDF) of the 2016–2035 mean relative to pre-industrial (PI), with 5–95% bootstrap confidence bounds. c, PDF of the time when GSAT change relative to PI (20-year running average) exceeds 1.5°C. d, PDF of annual anomalies with anthropogenic trend removed. The spread of VOLC-CONST is linearly shifted relative to NO-VOLC, and therefore not shown in a–c. These calculations are based on three 21st-century simulation ensembles with the Norwegian Earth System Model (NorESM), which use the same mid-range anthropogenic forcing scenario RCP4.5 but differ in their volcanic forcing: a 60-member ensemble using plausible stochastic volcanic forcing (VOLC); a 60-member reference ensemble using zero volcanic forcing (NO-VOLC); and a 20-member ensemble using 1850–2000 averaged volcanic forcing (VOLC-CONST). [This figure is adapted from (Bethke et al., 2017).]

**[END FIGURE 4.19 HERE]**

El Nino-like warming appears after large volcanic eruptions that is seen in both observations (Adams et al., 2003; McGregor et al., 2010; Khodri et al., 2017a) and climate model simulations (Ohba et al., 2013; Pausata et al., 2015; Stevenson et al., 2016; Khodri et al., 2017b; Predybaylo et al., 2017) (see Figure 4.20:). The impact of northern, tropical, and southern volcanic eruptions on Pacific sea surface temperature (SST), and the different response mechanisms arising due to differences in the volcanic forcing structure, have been investigated using the Community Earth System Model Last Millennium Ensemble (CESM-LME) (Zuo et al., 2018). The Pacific features a significant El Niño-like SST anomaly five to ten months after northern and tropical eruptions, with a weaker tendency after southern eruptions. The Niño3 index peaks with a lag of 1.5 years after northern and tropical eruptions. Two years after all three types of volcanic eruptions, a La Niña–like SST anomaly pattern over the equatorial Pacific is simulated, forming an ENSO-like cycle (Zuo et al., 2018). Large tropical eruptions are associated with co-occurring El Niño and positive Indian Ocean Dipole (IOD) events in the ensemble mean that peak 6–12 months after the volcanic forcing maximum, marking a significant increase in the likelihood of each event occurring in the SH spring/summer following the eruption (Maher et al., 2015). Such responses in tropical variability are expected to follow future volcanic eruptions, too.

**[START FIGURE 4.20 HERE]**

**Figure 4.20:** (a) Evolution of the composite Niño-3 index with zonal mean removed (units: °C) after northern eruptions (blue line), tropical eruptions (red line), and southern eruptions (green line). The spreads of the individual volcanic eruptions are denoted by the blue, red, and green shading, respectively. (b) The lead–lag correlation between the Niño-3 index (5°S–5°N, 150°–90°W) and the 850-hPa zonal wind in the western-to-central equatorial Pacific (5°S–5°N, 110°E–150°W) following northern (blue line), tropical (red line), and southern eruptions (green line). The positive value of the horizontal axis indicates that the Niño-3 index lags the 850-hPa zonal wind. [This figure is adapted from Zuo et al. (2018).]

**[END FIGURE 4.20 HERE]**

## 4.5 Mid- to Long-term Global Climate Change

### *4.5.1 Atmosphere*

This section assesses how the global atmospheric indicators discussed in Section 4.3 manifest themselves in large-scale spatial patterns of atmospheric change in the mid-term (2041-2060) and long-term (2081–2100). The patterns of change in any given future period represent a combination of unforced internal variability and a forced response (Deser et al., 2016). The role of internal variability is much larger at the local to regional scale than in the global mean projections. We here assess multi-model mean patterns, which represent an estimate of the forced response. It is important to note that this estimate of the forced response is a more homogeneous pattern than the 20-yr mean change patterns in any individual model realization (Knutti et al., 2010). The forced response is put into the context of internal variability by hatching the areas where

the signal is smaller than 2 standard deviations of 20-year means in local variability (see Section 4.2.5 for details).

#### *4.5.1.1 Near-Surface Air Temperature*

Patterns of near-surface air temperature changes show wide-spread warming by 2041–2060 and 2081–2100 (Figure 4.21:) for all SSPs with respect to 1995–2014. The area fraction experiencing warming increases with the level of global mean warming. As GSAT continues to increase, it is *very likely* that by the middle and the end of the 21st century most of the global land and ocean areas will be warmer than in 1995–2014 (*high confidence*) (see also Section 4.3.1.1).

**[START FIGURE 4.21 HERE]**

**Figure 4.21:** Multi-model mean change in annual mean near-surface air temperature (°C) in 2041–2060 and 2081–2100 in (top) SSP1-2.6 and (bottom) SSP5-8.5 relative to 1995–2014. Stippling indicates regions where the multi-model mean change exceeds two standard deviations of pre-industrial internal variability and where at least 90% of the models agree on the sign of change, as a measure of robustness. Hatching indicates regions where the multi-model mean signal is less than one standard deviation of internal variability.

**[END FIGURE 4.21 HERE]**

The temperature change pattern in any given model can be interpreted as a combination of unforced internal variability of the coupled climate system acting at synoptic to multi-decadal time scales and forced response pattern to forcings such as changes in atmospheric GHG and aerosol concentrations or in land use or land management (Deser et al., 2012b, 2016). The higher the level of global warming and the longer the period averaged across, the more the sign of the regional temperature change is dominated by the forced response. Figure 4.21: illustrates the CMIP6 multi-model mean estimate of this forced response for two different SSPs. Note that the global average of the pattern shown in Figure 4.21: correspond to CMIP6 multi-model mean GSAT warming (see Section 4.3.1) and are thus somewhat higher than the mean of the assessed GSAT range assessed in Section 4.3.4. However, the multi-model mean pattern shows some robust key characteristics that are independent of the exact GSAT level, such as a land-ocean warming contrast or amplified warming over the Arctic region assessed below. Changes in aerosol concentrations and land use and land management can furthermore have a direct imprint on the regional warming pattern (Bright et al., 2017; Kasoar et al., 2018).

***Land-Ocean Warming Contrast***

It is *virtually certain* that average warming will be higher over land than over the ocean. This so-called land-ocean warming contrast is a striking feature of observed trends (Lambert and Chiang, 2007; Byrne and O'Gorman, 2018) and projected changes in surface-air temperature (Sutton et al., 2007; Joshi and Gregory, 2008; Dong et al., 2009; Lambert et al., 2011; Drost et al., 2012; Bayr and Dommenget, 2013; Byrne and O'Gorman, 2013b; Izumi et al., 2013; Joshi et al., 2013). Between 1979 and 2016, average temperature over continents increased by 42% more than over oceans (Byrne and O'Gorman, 2018); a similar warming contrast is found in CMIP5 projections though with large differences across models and latitudes (Sutton et al., 2007; Drost et al., 2012; Byrne and O'Gorman, 2013b; Joshi et al., 2013). The land-ocean warming contrast is typically quantified as an amplification factor defined as the ratio of land-to-ocean warming: $A = \delta T_{\text{Land}} / \delta T_{\text{Ocean}}$ (Byrne and O'Gorman, 2013a). The amplification factor is greater than one for almost all regions and is larger for dry subtropical continents (about 1.5) than for moist regions in the tropics and mid-latitudes (about 1.2) (Byrne and O'Gorman, 2013a), suggesting a link between the land-ocean warming contrast and surface dryness.

It has long been recognized that the warming contrast is not primarily caused by the differences in effective heat capacity between land and ocean (e.g., Sutton et al., 2007). However, only since the AR5 a robust

physical understanding of the warming contrast has been developed. A simple theory based on atmospheric dynamics and moisture transport shows that surface-air temperature and relative humidity over land are strongly coupled, and demonstrates that the warming contrast occurs because air over land is drier than over oceans (Joshi et al., 2008; Byrne and O'Gorman, 2013a, 2013b, 2018). The warming contrast causes land relative humidity to decrease (Byrne and O'Gorman, 2016, 2018; Chadwick et al., 2016) and this feeds back on and strengthens the warming contrast. Decomposing the mechanisms controlling the tropical land-ocean warming contrast (Byrne and O'Gorman, 2013b), it is found that for the median CMIP5 model approximately 40% of the warming contrast is due to continents being drier, the feedback due to decreases in land relative humidity under global warming accounts for another 40%, and the remaining contribution comes from modest increases in near-surface ocean relative humidity (Schneider et al., 2010). Differences in land relative humidity responses across models are the primary cause of uncertainty in the land-ocean warming contrast (Byrne and O'Gorman, 2013b). These land relative humidity changes are ultimately controlled by moisture transport between the land and ocean boundary layers (Byrne and O'Gorman, 2016; Chadwick et al., 2016) and are also sensitive to characteristics of land surfaces that are challenging to model, including stomatal conductance and soil moisture (Berg et al., 2016).

***Polar Amplification***

It is *very likely* that under all SSPs the warming in the Arctic will be more pronounced than on global average over the 21st century (*high confidence*). Since the AR5 the understanding of the physical mechanisms driving the Arctic Amplification has improved.

The Arctic surface is projected to warm by more than the global average over the 21st century, with annual-average Arctic warming of about 3°C (SSP1-2.6) to 12°C (SSP5-8.5) by 2081–2100 (Figure 4.21:). This phenomenon, known as polar or Arctic amplification, is a ubiquitous feature of the response to GHG forcing simulated by climate models (Manabe and Wetherald, 1975, 1980; Manabe and Stouffer, 1980; Robock, 1983; Hansen et al., 1984; Manabe et al., 1991; Holland and Bitz, 2003; Winton, 2006; Pithan and Mauritsen, 2014) and has been observed over recent decades concurrent with Arctic sea-ice loss (Serreze and Barry, 2011) (Chapter 2). Based on robust scientific understanding and agreement across multiple lines of evidence (Section 7.6), there is *high confidence* that warming will continue to be Arctic amplified over the 21st century on timescales longer than several decades.

A variety of mechanisms contribute to Arctic amplification (see Chapter 7 Section 7.6.2). While surface-albedo feedbacks associated with the loss of sea ice and snow have long been known play important roles (Arrhenius, 1896; Manabe and Stouffer, 1980; Robock, 1983; Hall, 2004), it is now recognized that temperature (lapse-rate and Planck) feedbacks also contribute substantially to Arctic amplification with longwave radiative damping to space with warming being less efficient at high latitudes (Winton, 2006; Pithan and Mauritsen, 2014; Goosse et al., 2018). Changes in poleward atmospheric and oceanic heat transports are thought to contribute to Arctic warming (Holland and Bitz, 2003; Bitz et al., 2006; Lee et al., 2011, 2017, Marshall et al., 2014, 2015a; Woods and Caballero, 2016; Nummelin et al., 2017; Singh et al., 2017; Oldenburg et al., 2018), but the primary drivers of polar amplification within models appear to be polar feedback processes rather than heat transport changes (Pithan and Mauritsen, 2014; Stuecker et al., 2018). However, quantifying the role of individual factors in the coupled climate system is complicated by interactions between polar climate feedbacks and heat transports and between the different climate feedbacks (Section 7.6.2). Projected reduction in the strength of the AMOC over the 21st century is expected to reduce Arctic warming, but even a strong AMOC reduction would not eliminate Arctic amplification entirely (Liu et al., 2017, 2018c; Wen et al., 2018) (*medium confidence*).

There remains substantial uncertainty in the magnitude of projected Arctic amplification with the Arctic warming by a factor of two to four times the global average in models (Holland and Bitz, 2003; Nummelin et al., 2017). This uncertainty primarily stems from different representations of polar surface-albedo, lapse-rate, and cloud feedbacks, and from different projected poleward energy transport changes (Holland and Bitz, 2003; Crook et al., 2011; Mahlstein and Knutti, 2011; Pithan and Mauritsen, 2014; Bonan et al., 2018). The magnitude of Arctic amplification may also depend on the mix of radiative forcing agents (Najafi et al., 2015; Sand et al., 2016), with tropospheric aerosol emissions reducing simulated Arctic warming over the

middle of the 20th century (Gagné et al., 2017) and with aerosol emission reductions enhancing simulated Arctic warming over recent and future decades (Gagné et al., 2015; Acosta Navarro et al., 2016; Wobus et al., 2016; Wang et al., 2018b).

Climate models project weakly polar amplified warming in the SH under transient warming (Figure 4.21:). Model simulations (Hall, 2004; Danabasoglu and Gent, 2009; Li et al., 2013) and paleoclimate proxies indicate polar amplification in both hemispheres near equilibrium, but generally with less warming in the Antarctic than the Arctic (Section 7.6). The primary driver of delayed warming of the southern high latitudes is the upwelling of unmodified water from depth in the Southern Ocean and associated ocean heat uptake that is then transported away from Antarctica by northward flowing surface waters (Froelicher et al., 2015; Marshall et al., 2015a; Armour et al., 2016a; Liu et al., 2018b) (Section 7.2; Section 7.6.2; Section 9.2). Changes in westerly surface winds over the Southern Ocean have the potential to affect the rate of sea-surface warming, but there is currently *low confidence* in even the sign of the effect based on a diverse range of climate model responses to wind changes (Marshall et al., 2014; Ferreira et al., 2015; Kostov et al., 2017). A substantial increase in freshwater input to the ocean from the Antarctic ice sheet could further slow the emergence of SH polar amplification by cooling the Southern Ocean surface (Bronselaer et al., 2018; Schloesser et al., 2019), but this process is not represented in current climate models which lack dynamic ice sheets. Thus, while there is *high confidence* that the SH high latitudes will warm by more than the tropics on centennial timescales, there is *low confidence* that such a feature will emerge this century (Section 7.6).

***Seasonal Warming Patterns***

The warming pattern also shows distinct seasonal characteristics. The majority of models show a stronger hemispheric winter than summer warming over land poleward of about 55°N, and likewise, poleward of 55°S around Antarctica (Figure 4.22:) and thereby a reduced amplitude of the temperature cycle (Dwyer et al., 2012; Donohoe and Battisti, 2013). On the other hand over most of the subtropics and mid-latitudinal land regions except for parts of Asia, models project stronger warming in hemispheric summer than winter (Donohoe and Battisti, 2013; Sanchez and Simon, 2018; Santer et al., 2018), leading to an amplification of the seasonal cycle. This phenomenon that has been studied particularly in the case of the amplified summer warming over the Mediterranean region (Seager et al., 2014a; Kröner et al., 2017; Brogli et al., 2019).

**[START FIGURE 4.22 HERE]**

**Figure 4.22:** Multi-model mean difference in projected warming in JJA minus warming in DJF in 2081–2100 relative to 1995–2014 for (left) SSP1-2.6 and (right) SSP5-8.5. Particularly over the extratropics the warming difference is a simple approximation for the change in the amplitude of the seasonal cycle.

**[END FIGURE 4.22 HERE]**

***Changes in Temperature Variability***

It has long been recognized that along with mean temperatures also variance and skewness of the temperature distribution may be changing (Gregory and Mitchell, 1995; Mearns et al., 1997). By amplifying or dampening changes in the tail of temperature distribution such changes are potentially highly relevant extremes and pose a serious challenge to adaptation measures. Changes in temperature variability can occur from diurnal to multi-decadal time scales and from the local to the global scale.

Changes in GSAT variability are poorly understood. Based on model experiments it has been suggested that unforced variability of global mean temperatures tend to decrease in a warmer world as a result of reduced albedo variability in high latitudes resulting from melting snow and sea ice (Huntingford et al., 2013; Brown et al., 2017), but *confidence* remains *low*. An assessment of changes in global temperature variability is inherently challenging due to the interplay of unforced internal variability and forced changes.

Changes in tropical temperature variability may arise from changes in the amplitude of the El Niño Southern

Oscillation (ENSO) (Section 4.3.3.2). However, even the sign of the changes in ENSO amplitude remains inconsistent across models (Zheng et al., 2016). Large single-model initial-condition ensembles cover most of the range of changes in ENSO variance found in CMIP5 (Maher et al., 2018; Zheng et al., 2018), suggesting that internal variability accounts for most of the uncertainty. However, even if the forced response in ENSO amplitude is derived as the average of these large ensembles, the sign of the changes remain inconsistent (Maher et al., 2018).

Over the extratropics, several studies have identified robust large-scale patterns of changes in variability of annual and particularly seasonal mean temperature, including (a) a reduction in high latitudinal winter temperature variability and (b) an increase in summer temperature variability over land in tropics and subtropics (Huntingford et al., 2013; Holmes et al., 2016) as shown in Figure 4.23:. There is growing evidence that year-to-year and daily temperature variability decreases in winter over mid- to high-latitudes (Fischer et al., 2011; De Vries et al., 2012; Screen, 2014; Holmes et al., 2016; Borodina et al., 2017), which implies that the lowest temperatures rise more than the respective seasonal mean temperatures. Reduced high-latitude temperature variability may result from disproportionally large warming in source region of cold-air advection due to Arctic amplification and land-sea contrast (De Vries et al., 2012; Screen, 2014; Holmes et al., 2016). It has further been argued that a reduction in snow and sea-ice coverage from partly to completely snow- and ice-free ocean and land surface would substantially reduce cold-season temperature variability (Gregory and Mitchell, 1995; Fischer et al., 2011; Borodina et al., 2017).

**[START FIGURE 4.23 HERE]**

**Figure 4.23:** Relative change in variability of (left) JJA and (right) DJF mean temperature in three large initial condition ensembles. Changes are shown as percentage changes of standard deviation across local seasonal mean temperatures calculated as the average standard deviation across members of the large ensembles for every given year. Changes are shown for MPI 100-member grand ensemble by 2081–2100 (Maher et al., 2019), CanESM2 50-member ensemble (Kirchmeier-Young et al., 2017) and NCAR-CESM 30-member ensemble (Kay et al., 2015) for RCP8.5.

**[END FIGURE 4.23 HERE]**

On the other hand, enhanced summer temperature variability is projected over some land regions in the mid-latitudes and subtropics. In particular an increase in daily to interannual summer temperature variability has been projected over central Europe as a result of larger year-to-year variability in soil moisture conditions varying between a wet and dry regime and leading to enhanced land-atmosphere interaction (Seneviratne et al., 2006; Fischer et al., 2012b; Holmes et al., 2016). Furthermore, the amplified warming in the source region of warm-air advection due to land-ocean warming contrast and amplified Mediterranean warming (Seager et al., 2014a; Brogli et al., 2019), may lead to disproportionally strong warming of the hottest days and summers and thereby increased variability.

### *4.5.1.2 Annual Mean Atmospheric Temperature*

Section 12.4.3.2 of the IPCC AR5 assessed there was *high confidence* in the overall pattern of projected end of 21st century tropospheric temperature change and it is *very likely* that some of the greatest warming will occur in the northern high latitudes. They further assessed that relatively large warming is *likely* in the tropical upper troposphere, but with *medium confidence* owing to the relatively large observational uncertainties and contradictory analyses regarding model accuracy in simulating tropical upper tropospheric temperature trends.

**[START FIGURE 4.24 HERE]**

**Figure 4.24:** Change in annual and zonal mean atmospheric temperature (°C) in 2081–2100 in (left) SSP1-2.6 and

(right) SSP5-8.5 relative to 1995–2014 for 21 CMIP6 models.

**[END FIGURE 4.24 HERE]**

Figure 4.24: shows annual and zonal mean temperature changes in the long-term (2081–2100) relative to present-day (1995–2014) in the CMIP6 multi-model mean for SSP1-2.6 and SSP5-8.5. The changes are based on the raw model ensemble (i.e. without any weighting or emergent constraints applied). These can be compared to Figure 12.12 in (Collins et al., 2013). The projections show warming throughout the troposphere by the end of this century and a mix of warming and cooling in the stratosphere depending on the emissions scenario. The patterns of tropospheric temperature changes are highly consistent with those derived from earlier generations of climate models as discussed in AR5, AR4 and TAR. In SSP1-2.6, the multi-model mean tropospheric warming remains below 2°C everywhere in the troposphere except near the surface in the Arctic; this is similar to the findings based on CMIP5 models in AR5 for RCP2.6. In SSP5-8.5, the zonal mean tropospheric warming is also largest in the tropical upper troposphere and near the surface in the Arctic. In those regions, the largest temperature changes are about 1°C higher than in AR5 for RCP8.5. Therefore, the larger increase in GSAT in the unconstrained CMIP6 model ensemble for SSP5-8.5 compared to CMIP5 for RCP8.5 also translates into stronger warming in these regions. This is expected based on the theory for polar amplification discussed in Sections 4.5.1.1 and 7.4.4.1 and at low latitudes is consistent with the temperature dependence of moist adiabats. The latter point is also consistent with Section 3.3.1.2 which assesses with *medium confidence* that the CMIP5 and CMIP6 models overestimate tropical upper tropospheric warming since 1979 and that this is caused by an overestimate of the SST trend during this period.

Projected stratospheric temperature trends are determined by a balance between the major radiative drivers from ozone recovery, rising $CO_2$ and other greenhouse gases (including stratospheric water vapour), as well as future changes in the Brewer Dobson circulation which can alter the latitudinal pattern of stratospheric temperature trends. In the lower stratosphere, models project a weak cooling in the inner tropics in SSP1-2.6 and warming at other latitudes. There is enhanced warming over the Antarctic pole owing to the effects of ozone hole recovery on polar temperatures. The projected strengthening of the Brewer Dobson circulation in the future also affects stratospheric temperature trends, with adiabatic cooling at low latitudes and warming in middle and high latitudes. In SSP5-8.5, there is widespread cooling across much of the stratosphere, as expected from the higher GHG emissions, with a smaller warming in the Antarctic lower stratosphere. Owing to the importance of ozone recovery for the radiative balance of the stratosphere, future global and local stratospheric temperature trends do not scale with projected GSAT change.

In summary, new results since AR5 do not materially alter the understanding of projected zonal mean atmospheric temperature changes. We assess that there is *high confidence* in the overall pattern of projected tropospheric temperature changes given its robustness across many generations of climate models. We further assess that it is *very likely* that projected long-term tropospheric warming will be larger than the global mean in the Arctic lower troposphere and near surface (*high confidence)*. It is *very likely* that global mean stratospheric cooling will be larger for scenarios with higher atmospheric $CO_2$ concentrations (*high confidence*). It is *likely* that tropical upper tropospheric warming will be larger than at the tropical surface, however with an uncertain magnitude owing to discrepancies between modelled and observed temperature trends (see Section 3.3.1.2).

### *4.5.1.3 Near-Surface Humidity*

The relative humidity (RH) is expected to remain approximately constant on climatological time scales and planetary space scales, as indicated from modelling studies prior to the AR5. The AR5 noted the regional differences in long-term changes in RH, particularly on the contrast between land and ocean. Based on assessments from CMIP5 models, the AR5 concluded with *medium confidence* that 'reductions in near-surface RH over many land areas are *likely*'. The decrease in RH over most land areas is primarily contributed by the larger warming rates over land than over the ocean and is termed the last-saturation-

temperature constraint, as explained in the AR5.

Since the AR5, significant effort has been devoted to understanding the mechanisms for the decrease in land RH under global warming, and the relevance of the RH changes for land-sea warming contrast and water cycle. For the land RH decrease, both the moisture transport from the ocean and land-atmosphere feedback processes contribute. For specific humidity and its changes over land, the oceanic contribution is dominant while the role of evapotranspiration is secondary. However, the changes in land RH are also strongly influenced by evapotranspiration, which is suppressed by the drying soils under climate change (Byrne and O'Gorman, 2015; Berg et al., 2016; Chadwick et al., 2016). The combination of both oceanic and continental influences can explain the spatially diverse trends in RH over land in the observations for the recent decades, with a generally dominant negative trend at the global scale (Vicente-Serrano et al., 2018). The changes of land RH and temperature are not independent. There is a strong feedback between the land RH decrease and land-ocean warming contrast under future warming projections (see Section 4.5.1.1).

Changes in land RH can modulate the response of the water cycle to global warming (Chadwick et al., 2013; Byrne and O'Gorman, 2015). Most CMIP5 models project high precipitation associated with high near-surface RH and temperature under climate change (Lambert et al., 2017). Over land, the spatial gradients of fractional changes in RH contribute to a drying tendency in precipitation minus evapotranspiration with warming, which partly explains why the 'wet-gets-wetter, dry-gets-drier' principle does not hold over land (Byrne and O'Gorman, 2015). Terrestrial aridity is projected to increase over land, as manifested by a decrease in the ratio of precipitation to potential evapotranspiration, in which the decrease in land RH has a contribution of about 35% according to CMIP5 models under doubling $CO_2$ forcings (Fu and Feng, 2014). The aridity can be further amplified by the feedbacks of projected drier soils on land surface temperature, RH and precipitation (Berg et al., 2016).

The CMIP6 multi-model ensemble projects general decreases in near-surface relative humidity over most land areas, but moderate increases over the oceans (Figure 4.25:). The absolute change is weak and only on the order of a few percent. A season-dependence of the response is projected. During boreal winter, significant decreases relative to natural variability are projected in the high latitudes of the NH, subtropical Eurasian continent, Amazonia, southern Africa and Europe. During boreal summer, significant decreases relative to natural variability are projected in the tropical and subtropical Eurasian continent, North America, South America, South Africa and Australia. Significant decrease is projected in the mid-latitude SH.

**[START FIGURE 4.25 HERE]**

**Figure 4.25:** Multi-model mean change (%) in seasonal (top) DJF and (bottom) JJA mean near-surface relative humidity in 2041–2060 and 2081–2100 relative to 1995–2014, for (left) SSP1-2.6 and (right) SSP5-8.5. 16 and 17 CMIP6 models are used for SSP1-2.6 and SSP5-8.5, respectively. Stippling indicates regions where the multi-model mean change exceeds two standard deviations of pre-industrial internal variability and where at least 90% of the models agree on the sign of change, as a measure of robustness. Hatching indicates regions where the multi-model mean signal is less than one standard deviation of internal variability..

**[END FIGURE 4.25 HERE]**

The AR5 assessed an increase in projected heat stress, dominated by increasing temperatures in spite of local decreases in RH. The AR5 identified hotspots of future heat stress increases in areas with abundant atmospheric moisture availability and high present-day temperatures, such as Mediterranean coastal regions.

Since the AR5, more comprehensive assessments on the future changes in heat stress have been conducted, concerning spatial variability (Pal and Eltahir, 2016; Kang and Eltahir, 2018), diurnal cycle (Buzan et al., 2015; Li et al., 2018b), extreme events (Pal and Eltahir, 2016), and different global warming targets (Russo et al., 2017; Schwingshackl et al., 9999). The detection of historical changes provides a sound physical basis for future projections. Already in the observed records, there is a detectable increase in wet-bulb globe

temperature globally and over land regions since the 1970s that is attributable to human induced GHG emissions (Knutson and Ploshay, 2016; Li et al., 2017).

Continued increases in heat stress are expected over all land regions along with rising temperatures, as consistently projected by global (including CMIP5) and regional climate models based on different heat stress metrics (Fischer and Knutti, 2013; Li et al., 2017; Russo et al., 2017). The projections of heat stress indices are relatively robust across models, with smaller uncertainty than would be expected from temperature and humidity individually, because the projected greater warming is usually accompanied by larger decreases in RH in models (Fischer and Knutti, 2013). While multiple heat stress indicators are used in future projections, the uncertainty in projected changes in heat stress is to a larger extent induced by different climate models compared to that from different choices of indices (Zhao et al., 2015).

There is spatial variability of the heat stress responses. On the regional scale, extreme wet-bulb temperatures are expected to approach and even exceed the physiologic threshold for human adaptability (35°C) in hotspots such as southwest Asia and North China Plain in the late 21st century under RCP8.5, with possible interactions between humid coastal air masses and hot interior ones (Pal and Eltahir, 2016; Kang and Eltahir, 2018). These severe heat-related conditions located in low-elevation areas close to water bodies are consistent with those projected for southern Europe and Mediterranean coasts (Fischer and Schär, 2010). The exposure to humid heat waves is also expected to be high in some of the most densely populated regions, such as the Eastern United State and China (Russo et al., 2017). There is an urban amplification in heat stress changes compared to neighbouring rural areas directly related to the urban heat island effect, although weakly offset by the urban humidity deficit (Fischer et al., 2012a).

Due to the co-occurrence of temperature, humidity and wind speed conditions, the heat index will increase at a faster rate than atmospheric temperature alone (Horton et al., 2016; Li et al., 2018b). The increase in apparent temperature (referred to as heat index) is 0.17°C (0.12°C–0.25°C) per decade faster than that in air temperature under RCP8.5 projections from CMIP5 models throughout the 21st century, and is more remarkable in summer daytime than winter night-time (Li et al., 2018b). The elevated heat stress consequently results in future increases in heat-related morbidity and mortality (Li et al., 2018b) and reductions in labour capacity especially in peak months of heat stress (Dunne et al., 2013).

The CMIP6 multi-model ensemble projects robust increases in the mean wet-bulb temperature over land areas with distinct regional and seasonal characteristics (Figure 4.26:). Spatially, the increases in wet-bulb globe temperature are largest in the northern high latitudes, related to the polar amplification in atmospheric warming. The forced climate change signal is significantly different from the internal variability over nearly all land regions under SSP5-8.5 in the mid- and long-term.

**[START FIGURE 4.26 HERE]**

**Figure 4.26:** Multi-model mean change (°C) in seasonal (left) DJF and (right) JJA mean simplified wet-bulb globe temperature in 2081–2100 in SSP1-2.6 and SSP5-8.5 relative to 1995–2014 based on 10 and 11 CMIP6 models, respectively. The data is based on seasonal averages of daily values calculated in Schwingshackl et al. (2020).

**[END FIGURE 4.26 HERE]**

#### *4.5.1.4 Precipitation*

The AR5 assessed that changes in average precipitation in a warmer world will exhibit substantial spatial variation and the contrast of annual mean precipitation between dry and wet regions and that the contrast between wet and dry seasons will increase over most of globe as temperature increase. The AR5 assessed that the general pattern of change indicates that high latitude land masses are *likely* to experience greater amounts of precipitation due to the increased specific humidity of the warmer troposphere as well as

increased transport of water vapour from the tropics by the end of this century under the RCP8.5 scenario. Many mid-latitude and subtropical arid and semi-arid regions will *likely* experience less precipitation and many moist mid-latitude regions will *likely* experience more precipitation by the end of this century under the RCP8.5 scenario.

Since the AR5, significant progress has been achieved in understanding changes in patterns and rates of precipitation with GSAT rise. The projected precipitation changes can be decomposed into a part that is related to atmospheric circulation referred to as dynamical component and a part related to water vapour changes, the thermodynamic component. There is *high confidence*, based on understanding and modelling (Fläschner et al., 2016; Samset et al., 2016), that global mean precipitation increases approximately 1–3% per °C of GSAT warming. The increase in atmospheric water vapour is a robust change under global warming, the magnitude of precipitation increase is less than the increase of water vapour concentrations (Held and Soden, 2006). Global energy balance places a strong constraint on the global-mean rainfall (Allen and Ingram, 2002; Pendergrass and Hartmann, 2014; Myhre et al., 2018b). Regional precipitation changes are dominated by transport of water vapour and dynamical processes. Assessment of the processes controlling global and regional precipitation changes are discussed in Chapter 8, Section 8.2.

The thermodynamic response to global warming is associated with a wet-get-wetter mechanism, with enhanced moisture flux leading to subtropical dry regions getting drier and tropical and midlatitude wet regions getting wetter (Held and Soden, 2006; Chou et al., 2009). Over the twenty-first century, significant rate of precipitation change is associated with a spatial stabilization and intensification of moistening and drying patterns (Chavaillaz et al., 2016). Precipitation changes on a regional scale are more complex and show poor agreement among climate models (Turner and Annamalai, 2012; Knutti et al., 2013b; Ramesh and Goswami, 2014; Madsen et al., 2017). Model projections of circulation-related fields show a wide range of possible outcomes, which are primarily controlled by dynamics and exert a strong control on regional climate (Shepherd, 2014). The tropical circulation slows down with moisture and stratification changes, connecting to a poleward expansion of the Hadley cells and storm tracks (Frierson et al., 2007; Lu et al., 2007; Foltz et al., 2018).

Climate models provide very diverse values in hydrological sensitivity, changes per degree Celsius of surface warming (Knutti et al., 2013b; Liu et al., 2014; Fläschner et al., 2016; Watanabe et al., 2018). Precipitation response to fast adjustments and slow temperature-driven responses are discussed in detail in Section 8.1.1. of Chapter 8. Rapid adjustments account for large regional differences in hydrological sensitivity across multiple drivers (Samset et al., 2016; Myhre et al., 2017). The rapid regional precipitation response to increased $CO_2$ is robust among models, implying that the uncertainty in long-term changes is mainly associated with the response to SST-mediated feedbacks (Richardson et al., 2016).

Most of the projected changes exhibit a sharp contrast between land and ocean, with surface temperature-driven (slow) sensitivity reaching 3–5% $°C^{-1}$ over the ocean and only 0–2% $°C^{-1}$ over land (Samset et al., 2018a). Temperature-driven intensification of land-mean precipitation during the twentieth century has been masked by fast precipitation responses to anthropogenic sulphate and volcanic forcing (Allen and Ingram, 2002; Richardson et al., 2018b). As projected sulphate forcing decreases and warming continues, land-mean precipitation is expected to increase more rapidly and may become clearly observable by the mid-21st century (Richardson et al., 2018b). The processes that govern large-scale changes in precipitation are discussed in Chapter 8.

There has been considerable progress in understanding the factors contributing to changes in patterns of precipitation. Precipitation changes were interpreted as a wet-get-wetter and dry-get-drier pattern with a moistening trend in high latitudes and tropics and a drying trend in subtropics to middle latitudes (Held and Soden, 2006). Recent studies suggest that the dry-get-drier argument might not hold, especially over land regions (Greve et al., 2014; Feng and Zhang, 2015). In the tropics, weakening of circulation leads to wet-gets-drier and dry-gets-wetter pattern (Chadwick et al., 2013). Climate model agreement for precipitation change in the tropics is lower than for other regions, with large areas of little model consensus on the sign and magnitude of change (Knutti et al., 2013b; McSweeney and Jones, 2013). Sources of inter-model uncertainty in regional tropical rainfall projections arise from circulation changes (Kent et al., 2015;

Chadwick, 2016), spatial shifts in convection and convergence, associated with SST pattern change and land–sea thermal contrast change (Kent et al., 2015; Chadwick et al., 2017) with a secondary contribution from the response to direct $CO_2$ forcing (Chadwick, 2016). Factors governing changes in large-scale precipitation patterns are discussed in detail in Chapter 8.

The tropospheric energy budget exerts a strong control on mean precipitation (Allen and Ingram, 2002; O'Gorman et al., 2012). Tropospheric radiative cooling constrains global precipitation (Pendergrass and Hartmann, 2014), leading to a slow SST-dependent response due to radiative feedbacks and a forcing dependent rapid adjustment. Fast precipitation changes are most sensitive to strongly absorbing drivers like $CO_2$ and black carbon (Richardson et al., 2018b). The sensitivity of global precipitation change to warming is smaller (2% $°C^{-1}$) as compared to the sensitivity of water vapour concentration change (7% $°C^{-1}$). Reduced convective mass flux as part of weakening atmospheric circulation strength is one way in which the atmosphere adjusts in reconciling the water vapour and precipitation changes (Bony et al., 2013; Vecchi and Soden, 2007).

Precipitation changes exhibit strong seasonal characteristics, and, in many regions, the sign of the precipitation changes varies with season. Seasonal mean rainfall follows a warmer-get-wetter pattern (Sobel and Camargo, 2011; Huang et al., 2013; Putnam and Broecker, 2017), and projections of seasonal mean precipitation anomalies provide a robust signal (Huang et al., 2013; Lee et al., 2013). Precipitation variability is projected to increase over a majority of global land area in response to warming (Pendergrass et al., 2017).

Consistent with the findings of the AR5, a gradual increase in global precipitation is projected over the 21st century with change exceeds 0.05 mm $day^{-1}$ (about 2% of global precipitation) and 0.15 mm $day^{-1}$ (about 5% of global precipitation) by 2100 in SSP1-2.6 and SSP5-8.5, respectively. Global maps of the percentage change in seasonal precipitation (JJA and DJF) based on CMIP6 models in the long-term (2081–2100) from SSP1-2.6 and SSP5-8.5 are presented in Figure 4.27:. Precipitation is projected to increase in the CMIP6 models, especially in monsoon regions, tropical oceans and high latitudes. Mediterranean and larger parts of the subtropics precipitation are projected to decrease.

**[START FIGURE 4.27 HERE]**

**Figure 4.27:** Multi-model mean change (%) in (top) DJF and (bottom) JJA mean precipitation in 2081–2100 relative to 1995–2014, for (left) SSP1-2.6 and (right) SSP5-8.5. 21 and 22 CMIP6 models are used for SSP1-2.6 and SSP5-8.5, respectively. Stippling indicates regions where the multi-model mean change exceeds two standard deviations of pre-industrial internal variability and where at least 90% of the models agree on the sign of change, as a measure of robustness. Hatching indicates regions where the multi-model mean signal is less than one standard deviation of internal variability..

**[END FIGURE 4.27 HERE]**

Based on the assessment of CMIP6 models, we conclude that it is *virtually certain* that, in the long term, global precipitation will increase with GSAT rise (*high confidence*). It will *likely* increase by 1–3% per °C GSAT warming (*high confidence*). It is virtually certain that the pattern of projected precipitation change will exhibit substantial regional and seasonal contrast in response to global warming (high confidence). Precipitation will increase in large parts of monsoon region, tropics and high latitude but decrease in Mediterranean and large parts of the subtropics in response to GHG-induced warming (*high confidence*).

### *4.5.1.5 Global Monsoon Precipitation and Circulation*

In the AR5, the changes of the global monsoons were assessed in the context of long-term trends across the 21st century and the change by the end (2081–2100) of the 21st century. The AR5 showed growing evidence of improved skill of climate models in reproducing the climatological features of the global monsoon. Taken together with identified model agreement on future changes, the global monsoon precipitation, aggregated

over all regional monsoon regions, is *likely* to strengthen in the 21st century with increases in its area and intensity, while the monsoon circulation weakens. Monsoon onset dates are *likely* to become earlier or not to change much and monsoon retreat dates are *likely* to be delayed, resulting in lengthening of the monsoon seasons in many monsoon regions. In CMIP5 models, the global monsoon area (GMA), the global monsoon total precipitation (GMP), and the global monsoon precipitation intensity (GMI) are projected to increase by the end of the 21st century (2081–2100). In all RCP scenarios, GMA is *very likely* to increase, and GMI is *likely* to increase, resulting in a *very likely* increase in GMP, by the end of the 21st century (2081–2100) (Kitoh et al., 2013).

Since the AR5, there has been considerable progress in understanding the physical reasons governing the projected changes in precipitation. The multi-model ensemble of the four best CMIP5 models for simulating GM properties projects that under the RCP4.5 scenario the NH monsoon precipitation is projected to increase much larger than the SH counterpart due to increase in temperature difference between the NH and SH, significant enhancement of the Hadley circulation, and atmospheric moistening, against stabilization of troposphere (Lee and Wang, 2014). It has been suggested that the dynamic effect plays more important role on regional differences in projected precipitation change among different monsoon regions than the thermodynamic effect. In the Asian monsoon regions, the monsoon circulation slows down at a much lower rate than in the other monsoon regions (Endo and Kitoh, 2014). Under the RCP4.5 scenario, the CMIP5 models project enhanced global monsoon activity, with the increases of GMA, GMP, and GMI by 1.9%, 3.2%, and 1.3%, respectively, per degree Celsius of surface warming. The increase in GMP is primarily attributed to the increase of moisture convergence, which comes mainly from the increase of water vapour concentration but is partly offset by the convergence effect (Hsu et al., 2013). Under RCP4.5, the interannual variability of monsoon rainfall is projected to intensify mainly over land, and the relationship between monsoon and El Niño is projected to strengthen (Hsu et al., 2013).

By using CMIP6 models, it is also suggested that land monsoon precipitation sensitivity slightly increase with the level of GHG forcing, whereas the ocean monsoon precipitation has no sensitivity. The global monsoon land precipitation sensitivity has a median of 0.8% per 1°C GSAT in SSP2-4.5 and a median of 1.4% per 1°C GSAT in SSP5-8.5 (Wang et al., 2019).

Based on the projections of changes in precipitation from CMIP6 under the four SSPs, the global monsoon precipitation, aggregated over all monsoon systems, is *likely* to strengthen in the 21st century with increases in its intensity, while the monsoon circulation weakens (Figure 4.13:). Over the period of 2021–2040, the increase of precipitation for SSP1-2.6 is generally stronger than that of SSP5-8.5, while over the long-term period (2081–2100), the increase of monsoon precipitation under SSP5-8.5 is far stronger than that of SSP1-2.6. In the long-term period (2081–2100), the global monsoon precipitation index projected to increase by 0.9–1.7 % per 1°C GSAT rise (5–95% range of the available projections), but the global monsoon circulation index is projected to decrease by 10.4– 19.4 % per 1°C GSAT rise, based on all of the SSPs (*medium confidence*).

In Figure 4.13:, the robust patterns in monsoon rainfall changes in the mid- to long-term include the north-south asymmetry characterized by more increase in the NH than the Southern Hemisphere and the east-west asymmetry characterized by enhanced Asian-African monsoons and weakened North American monsoon (*high confidence*) (Lee and Wang, 2014; Mohtadi et al., 2016; Wang et al., 9999a, 9999b).

#### *4.5.1.6 Sea Level Pressure, Large-scale Atmospheric Circulation, Storm Tracks and Blocking*

In this subsection, we assess projected long-term changes in aspects of the large-scale atmospheric circulation including sea level pressure patterns, zonal wind changes, storm track density and blocking. Here we provide a global overview of these features that is complementary to the regional assessment of links to the hydrological cycle in section 8.4.2, and assessment of the connections to extreme events in section 11.7.2.

***Sea level pressure***

The AR5 assessed that mean sea level pressure is projected to decrease in high latitudes and increase in mid-latitudes. Such a pattern is associated with a poleward shift in the storm track and an increase in the annular mode index. Figure 4.28: shows seasonal mean sea level pressure changes for 2081–2100 in a low GHG emission scenario (SSP1-2.6) and a high GHG emission scenario (SSP5-8.5). The broad pattern of increasing sea level pressure in mid-latitudes and decreasing pressure over polar regions is most pronounced for the high GHG forcing scenario. In SSP1-2.6, an opposite response is found at southern high latitudes, which in austral summer can be attributed to the relatively more important role of ozone recovery for the circulation in the absence of a larger global warming signal.

**[START FIGURE 4.28 HERE]**

**Figure 4.28:** Multi-model mean change in (top) DJF and (bottom) JJA mean sea level pressure (hPa) in 2081–2100 relative to 1995-2014, for (left) SSP1-2.6 and (right) SSP5-8.5 based on 22 CMIP6 models. Stippling indicates regions where the multi-model mean change exceeds two standard deviations of pre-industrial internal variability and where at least 90% of the models agree on the sign of change, as a measure of robustness. Hatching indicates regions where the multi-model mean signal is less than one standard deviation of internal variability..

**[END FIGURE 4.28 HERE]**

***Zonal wind and westerly jets***

Storm tracks and mid-latitude westerly jets are dynamically related aspects of mid-latitude circulation. The AR5 assessed that a poleward shift of the Southern Hemisphere (SH) westerlies and storm track is *likely* by the end of the 21st century in the RCP8.5 scenario (*medium confidence*). In contrast, *low confidence* was assessed for the storm-track response in the Northern Hemisphere (NH).

Figure 4.29: shows changes in annual and zonal mean zonal wind at the end of the century (2081–2100) for the SSP1-2.6 and SSP5-8.5 scenarios. In both scenarios there is a strengthening and lifting of the subtropical jets in both hemispheres, consistent with the response to large-scale tropospheric warming found in earlier generations of climate models (Collins et al., 2013). In the SH, there is on average a weak equatorward shift of the mid-latitude jet in SSP1-2.6. This annual mean perspective masks the fact that changes in the SH mid-latitude jet are expected to show a seasonal variation owing to the relative importance of ozone recovery and GHGs as a driver of circulation changes in different seasons (Bracegirdle et al., 9999). This relative balance is further evident when examining the SSP5-8.5 scenario in Figure 4.29:, which shows a stronger poleward shift in the SH mid-latitude jet compared to the weak equatorward shift in SSP1-2.6 (Barnes and Polvani, 2013; Bracegirdle et al., 9999). In the NH, the changes in lower tropospheric zonal mean zonal winds by the end of the century are smaller than found in the SH and reflect an average over potentially divergent regional wind changes particularly over the major NH ocean basins (Simpson et al., 2014).

**[START FIGURE 4.29 HERE]**

**Figure 4.29:** Multi-model mean change in annual and zonal mean zonal wind (m $s^{-1}$) in 2081–2100 in (left) SSP1-2.6 and (right) SSP5-8.5 relative to 1995–2014 based on 21 CMIP6 models. The 1995–2014 climatology is shown in contours with spacing 10 m $s^{-1}$. Stippling indicates regions where the multi-model mean change exceeds two standard deviations of pre-industrial internal variability and where at least 90% of the models agree on the sign of change, as a measure of robustness. Hatching indicates regions where the multi-model mean signal is less than one standard deviation of internal variability..

**[END FIGURE 4.29 HERE]**

CMIP5 models show a strong seasonal and regional dependence in the response to climate change of NH

westerlies (Barnes and Polvani, 2013; Grise and Polvani, 2014b; Simpson et al., 2014; Zappa et al., 2015). CMIP5 projections indicate a poleward shift of the westerlies in the North Atlantic in summer, and in both the North Pacific and North Atlantic in Autumn (Barnes and Polvani, 2013; Simpson et al., 2014). The shift of the westerlies is more uncertain in the other seasons, particularly in the North Atlantic in winter (Zappa and Shepherd, 2017). A poleward shift of the jets and storm tracks is expected in response to an increase in the atmospheric stratification and in the equator-to-pole meridional temperature gradient (Harvey et al., 2014; Shaw et al., 2016). Simulations indicate that most of the changes in winter storminess over the Euro-Atlantic regional will occur only after exceeding the 1.5 degree warming level (Barcikowska et al., 2018). Progress since the AR5 has better highlighted how different climate change aspects can drive different, and potentially opposite, responses in the mid-latitude jets and storm tracks. Potential drivers include the patterns in sea surface warming (Mizuta et al., 2014; Langenbrunner et al., 2015; Ceppi et al., 2018), land-sea contrast (Shaw and Voigt, 2015), the loss of sea ice (Deser et al., 2015; Harvey et al., 2015; Screen et al., 2018b; Zappa et al., 2018b), and changes in the strength of the stratospheric polar vortex (Manzini et al., 2014; Grise and Polvani, 2017; Simpson et al., 2018c; Ceppi and Shepherd, 2019). From an energetics perspective, the uncertainty in the response of the jet streams depends on the response of clouds, their non-spatially uniform radiative feedbacks shaping the meridional profile of warming (Ceppi and Hartmann, 2016; Voigt and Shaw, 2016b; Ceppi and Shepherd, 2017; Lipat et al., 2018; Albern et al., 2019; Voigt et al., 2019). The influence from competing dynamical drivers and the absence of observational evidence suggests there is at most *medium confidence* on a poleward shift of the NH low-level westerlies in autumn and summer and *low confidence* in the other seasons.

**[START FIGURE 4.30 HERE]**

**Figure 4.30:** Multi-model mean change in winter (NH DJF, SH JJA) zonal wind at 850 hPa (*u850*) in 2081–2100 in (left) SSP1-2.6 and (right) SSP5-8.5 relative to 1995–2014. The 1995–2014 climatology is shown in contours with spacing 5 m $s^{-1}$. Stippling denotes where at least 90% of models agree on the sign of change.

**[END FIGURE 4.30 HERE]**

The anthropogenic forced signal in extratropical atmospheric circulation may be small compared to natural internal variability (Deser et al., 2012b, 2014) and, as assessed in the AR5, there is generally low agreement across models in many aspects of regional atmospheric circulation change particularly in the NH (Shepherd, 2014). The latter point means that, in some regions, a multi-model average perspective of atmospheric circulation change, like that shown in Figure 4.30:, represents a small residual after averaging over large intermodel spread (evident from the general lack of stippling in Figure 4.30:). This is in strong contrast to thermodynamic aspects of climate change, such as surface temperature change, for which model results are generally highly consistent (see e.g., Figure 4.21:). Furthermore, models share systematic biases in some aspects of extratropical atmospheric circulation such as midlatitude jets, which can have complex implications for understanding forced changes (Simpson and Polvani, 2016). Given these issues, an emerging field of research since AR5 has focused on the development of "storylines" for regional atmospheric circulation change (Shepherd, 2019). A storyline may be defined as "a physically self-consistent unfolding of past events, or of plausible future events or pathways" (Shepherd et al., 2018). The storyline approach is grounded in the identification of a set of physical predictors of atmospheric circulation change, such as those described above (e.g., Harvey et al., 2014; Manzini et al., 2014), which act together to determine a specific outcome in the form of projected atmospheric circulation change. The consequences of multi-model spread in the physical predictors of atmospheric circulation change can be investigated, conditioned on a specified level of global warming (Zappa and Shepherd, 2017; Zappa, 2019; Mindlin et al., 9999). A complementary approach is to use atmospheric circulation analogues based on past observed events or modes of natural internal variability while accounting for changes to the background mean climate (Hazeleger et al., 2015; Deser et al., 2017). The storyline approach does not attempt to a priori assign a likelihood to a specific storyline but may provide useful examples for assessing tolerance and stress testing of weather and climate sensitive systems (see also Sections 1.4.4, 4.8.1 and 10.5.3).

***Extratropical cyclones***

As stated in the AR5, the number of extratropical cyclones (ETC) composing the storm tracks is projected to decline in the future projections, but by no more than a few percent. The reduction is mostly located on the equatorward flank of the storm tracks, which is associated with the Hadley cell expansion and a poleward shift in the mean genesis latitude of ETCs (Tamarin-Brodsky and Kaspi, 2017). Furthermore, the poleward propagation of individual ETCs is expected to increase with warming (Graff and LaCasce, 2014; Tamarin-Brodsky and Kaspi, 2017), thus contributing to a poleward shift in the mid-latitude transient-eddy kinetic energy. The increased poleward propagation results from the strengthening of the upper tropospheric jet and increased cyclone-associated precipitation (Tamarin-Brodsky and Kaspi, 2017), which are robust aspects of climate change.

The number of ETCs associated with intense surface wind speeds and undergoing explosive pressure deepening are projected to strongly decrease in the NH winter (Seiler and Zwiers, 2016; Kar-Man Chang, 2018). There are, however, regional exceptions such as in the northern North Pacific, where explosive and intense ETCs are projected to increase in association with the poleward shift of the jet and increased upper-level baroclinicity (Seiler and Zwiers, 2016). The weakening of surface winds of ETCs in the NH is attributed to the reduced low-level baroclinicity from SST and sea ice changes (Harvey et al., 2014; Seiler and Zwiers, 2016; Wang et al., 2017a). Eddy kinetic energy and intense cyclone activity is also projected to decrease in the NH summer in association with a weakening of the jet (Lehmann et al., 2014; Chang et al., 2016). However, it remains unclear how important a future increase in mesoscale latent heating could be for the dynamical intensity of ETCs (Li et al., 2014; Pfahl et al., 2015; Willison et al., 2015; Michaelis et al., 2017). Because mesoscale heating is presumably not properly represented at the spatial resolution of CMIP5 climate models, there is only *medium confidence* in the projected decrease in the frequency of intense NH ETCs. Over the North Pacific, the CMIP6 models show a northward shift of winter ETC density by the end of century (2081–2100) under the SSP5-8.5 scenario (Figure 4.31:a).

In contrast to the NH, CMIP5 models indicate that the frequency of intense ETCs will increase in the SH (Chang, 2017). The wind speeds associated with ETCs are therefore expected to intensify in the SH storm track for high emission scenarios (*high confidence*). These changes in intensity are accompanied by an overall southward shift of the SH winter storm track due to the poleward shift in the upper level jet and the increase in the meridional SST gradient linked to the slower warming of the Southern Ocean (Grieger et al., 2014). The southward shift in the SH winter storm track is also seen in CMIP6 models for the long-term (2081–2100) under the SSP5-8.5 scenario (Figure 4.31:b).

Regardless of dynamical intensity changes, the number of ETC associated with extreme precipitation is projected to greatly increase with warming (*high confidence*), due to the increase moisture-loading capacity of the atmosphere (Yettella and Kay, 2017; Hawcroft et al., 2018).

**[START FIGURE 4.31 HERE]**

**Figure 4.31:** Multi-model mean change of extratropical storm track density in winter (NH DJF and SH JJA) in 2081-2100 in SSP5-8.5 relative to 1995-2014 based on 5 CMIP6 models. [Figure will be updated with further CMIP6 models and uncertainty assessment as additional models provide high frequency output].

**[END FIGURE 4.31 HERE]**

***Atmospheric blocking***

Blocking is associated with a class of quasi-stationary high-pressure weather systems in the middle and high latitudes that disrupt the prevailing westerly flow. These events can persist for extended periods, such as a week or longer, and can cause long-lived extreme weather conditions, from heat waves in summer to cold spells in winter (see section 11.7.2 for a detailed discussion of these features and sections 3.3.3.3 and 10.3.3.4 for the assessment of blocking biases in models simulations). The AR5 assessed with *medium confidence* that the frequency of blocking would not increase under enhanced GHG concentrations, while

changes in blocking intensity and persistence remained uncertain.

CMIP5 projections suggest that the response of blocking frequency to climate change might be quite complex (Dunn-Sigouin et al., 2013; Masato et al., 2013). An eastward shift of winter blocking activity in the NH is indicated (Masato et al., 2013; Kitano and Yamada, 2016; Lee and Ahn, 2017; Matsueda and Endo, 2017) while during boreal summer, blocking frequency tends to decrease in mid-latitudes (Matsueda and Endo, 2017), with the exception of the eastern Europe-western Russia region (Masato et al., 2013). The projected increase of blocking in boreal summer partially contrasts with the observed increase in Greenland blocking (Hanna et al., 2018; Davini and D'Andrea, 2019). However, as shown in (Woollings et al., 2018), the spatial distribution and the magnitude of the suggested changes are sensitive to the blocking detection methods (Schwierz et al., 2004; Barriopedro et al., 2010; Davini et al., 2012). In the SH, blocking frequency is projected to decrease in the Pacific sector during austral spring and summer. However, seasonal and regional changes are not totally consistent across the models (Parsons et al., 2016), and, as extensively discussed in section 10.3.3.4, models biases might affect their response.

To better understand the uncertainty in future blocking activity, a process-oriented approach has been proposed that aims to link blocking responses to different features of the global warming pattern. The upper-level tropical warming might be the key factor leading to a reduced blocking, because of the strengthening of zonal winds (Kennedy et al., 2016). The more controversial influence of near-surface Arctic warming might lead to an increased blocking frequency (Mori et al., 2014; Francis and Vavrus, 2015) (see Box 10.1).

Figure 4.32: illustrates the CMIP6 multi-model mean estimate of the wintertime blocking frequencies over three regions with large blocking activity for four different SSPs. The multi-model mean shows a remarkable decrease in blocking activity over Greenland and North Pacific for SSP7.0 and SSP8.5. The large differences among models and the large sensitivity to the blocking detection methods suggest that there is at most *medium confidence* in a shift of the major centres of blocking activities, with a decrease of winter blocking frequency in those regions with the largest frequencies during the historical period.

**[START FIGURE 4.32 HERE]**

**Figure 4.32:** Box plot showing wintertime (December to March) present-day (historical simulations, 1995–2014) and future climate (SSP simulations, 2081–2100) atmospheric blocking frequencies over (a) the Central European region (20°W–20°E, 45°N–65°N), (b) the Greenland region (65°W–20°W, 62.5°N–72.5°N), (c) the North Pacific region (130°E–150°W, 60°N–75°N). Values show the percentage of blocked days per season following the (Davini et al., 2012) index. Median values are the black horizontal bar. The numbers below each bar report the number of models included. Observationally-based values are obtained as the average of the ERA-Interim Reanalysis, the JRA-55 Reanalysis and the NCEP/NCAR Reanalysis. Adapted from (Davini and D'Andrea, 2019)

**[END FIGURE 4.32 HERE]**

## *4.5.2 Ocean*

### *4.5.2.1 Ocean Temperature*

There is *high confidence* that over 90% of the excess heat accumulated in the climate system between 1971 and 2010 has been stored in the global ocean (Chapter 7 Section 7.2.2.2, Chapter 9 Section 9.2.3.1). There is *high confidence* that the upper (0-700m), intermediate (700–2000m), and deep ocean (2000-6000m) contributes to approximately 60%, 30%, and 10% of the global ocean warming since 1971, respectively (Section 2.3.3.1). It is *very likely* that the anthropogenic forcing has made a substantial contribution to the ocean heat content increase that extends to the deeper ocean (Chapter 3 Section 3.5.1.2). There is *high confidence* that the ocean upper few hundred meters is becoming more stably stratified as a result of global surface ocean warming and high-latitude freshening (Chapter 9 Section 9.2.3.3).

The redistribution of heat to the ocean interior is governed by a collection of complicated processes. Much of the heat uptake appears to track what one would expect from the uptake of a passive tracer (Marshall et al., 2015b; Armour et al., 2016b; Zanna et al., 2019). Changes in different processes can either warm or cool the ocean. In the 70-year idealized $4\times CO_2$ experiments performed by three climate models, it is found that convective and mixed-layer processes, as well as eddy-related processes, tend to cool the subsurface ocean, whereas advective and diapycnically diffusive processes tend to warm the ocean interior (Exarchou et al., 2015). The Southern Ocean plays a dominant role in the global ocean heat uptake. CMIP5 model simulation shows that during the period 1861–2005, about 75% ocean heat uptake occurs in the Ocean south of 30°S (Froelicher et al., 2015). The observed warming of the Southern Ocean since 1950s is primarily attributed to increase in GHGs, and the effect of stratospheric ozone depletion is much smaller (Swart et al., 2018). It is *likely* that the Southern Ocean will continue playing a major role in the ocean heat uptake (Chapter 9 Section 9.2.3.1).

#### *4.5.2.2 Ocean acidification*

The long-term trend of surface ocean acidification is largely determined by the pathways of atmospheric $CO_2$ with weak dependence on future climate change (Section 4.3.2.4) (Hurd et al., 2018). It is *virtually certain* that continued penetration of anthropogenic $CO_2$ from the surface to the deep ocean will acidify the ocean interior (Chapter 5 Section 5.3.3). The continued acidification of the deep ocean can be demonstrated by the shoaling of the saturation horizon of calcium carbonate, which represents the interface below which seawater is undersaturated with calcium carbonate. At present, the calcium carbonate saturation horizon is much shallower in the subarctic Pacific and the Southern Ocean, compared to that of the North Atlantic (Feely et al., 2004). Undersaturation with respect to calcium carbonate mineral will start to occur in high latitude oceans. Under RCP 8.5 scenario, aragonite (a mineral form of calcium carbonate) undersaturation is projected across ~20% of the Southern Ocean surface by 2060, across ~60% of the surface by 2080 and >80% of the surface by 2100 (Negrete-García et al., 2019). The long-term trend of ocean acidification is modulated at interannual and seasonal timescales (Chapter 5 Section 5.3.3).

### *4.5.3 Modes of Variability*

This subsection assesses the mid- to long-term evolution of the large-scale climate modes of variability and their associated teleconnections. Assessments of the physical mechanisms and the individual feedbacks involved in the future change of each mode are provided in Chapters 8–10.

#### *4.5.3.1 Northern and Southern Annular Modes*

***The NAM***

The AR5 assessed from CMIP5 simulations that the future boreal wintertime NAM is *very likely* to exhibit natural variability and forced trends of similar magnitude to that observed in the historical period and is *likely* to become slightly more positive in the future. Considerable uncertainty existed related to physical mechanisms to explain the observed and projected changes in the NAM, but it was clear that NAM trends are closely connected to projected shifts in the mid-latitude jets and storm tracks.

NAM projections from climate models analysed since the AR5 reveal broadly similar results to the AR5 for the late 21st century, showing a positive trend with a comparable magnitude to the multi-model or multi-realization variability. A tendency to towards a more positive NAM index is apparent in Figure 4.33:a, where the long-term (2081–2100) changes in the NAM, relative to present-day (1995–2014), from the CMIP6 ensemble for the five core SSPs are shown. The NAM generally becomes more positive by the end of the century except in the boreal summer (JJA) when there is no change in the NAM in these simulations. In boreal winter (DJF) under SSP5-8.5, the central estimate for the NAM is almost 3 hPa higher in 2081–2100 (on average) compared to 1995–2014 (on average).

***The SAM***

The AR5 assessed it is *likely* that the evolution of the SAM over the 21st century will be primarily determined by the interplay between the effects of ozone recovery and changing greenhouse gas concentrations and that these will act to push the SAM in opposite directions. Owing to the relative effects of these two drivers, CMIP5 model SAM and SH circulation projections differed markedly across forcing scenarios and across seasons (Barnes and Polvani, 2013; Barnes et al., 2014). The CMIP5 models simulated a weak negative SAM trend in austral summer for the RCP4.5 scenario by the end of the century (Zheng et al., 2013a), while for a higher GHG forcing scenario (RCP8.5) they simulated a weak positive SAM trend in austral summer (Zheng et al., 2013a). A substantial fraction of the spread in CMIP5 projections of the end of century SH summer jet shift under a high forcing scenario (RCP8.5) may be attributable to differences in the simulated change in break-up of the stratospheric polar vortex, with models that produce a later break-up date showing a larger summertime poleward jet shift (Ceppi and Shepherd, 2019). For a low GHG emissions scenario (RCP2.6) the effect of ozone recovery on the SAM may dominate over that of GHGs in austral summer (Eyring et al., 2013). In austral winter, the poleward shift of the SH circulation in CMIP5 models, and the associated increase in the SAM index, tends to be larger, on average, in higher forcing scenarios though with substantial inter-model spread (Barnes et al., 2014). New research since the AR5 shows that the previous theory for the apparent relationship across models between the annual mean climatological SH jet position and the amplitude of forced SH jet shift (Kidston and Gerber, 2010) does not hold at seasonal timescales (Simpson and Polvani, 2016).

Figure 4.33:b shows the long-term (2081–2100) changes, relative to present-day, in the SAM index. In most seasons the SAM becomes more positive by the end of the century relative to 1995–2014 in the highest forcing SSPs (SSP2-4.5, SSP3-7.0 and SSP5-8.5). Conversely, in the lower forcing SSPs (SSP1-1.9 and SSP1-2.6), in most seasons the SAM index does not show a robust change compared to present-day. The greatest differences in the SAM amongst the scenarios are found in austral summer, where the CMIP6 models show a central estimate of an increase in SAM index of 2.5 hPa in SSP5-8.5 and a decrease of about 1.5 hPa in SSP1-1.9. In austral winter and spring, the central estimate for the increase in SAM is more than four times larger than over the near-term 2021–2040 (see Section 4.4.3.1). In austral autumn and winter, the increase in SAM is larger by about a factor of three to four compared to the projected near-term changes (see Section 4.4.3.1).

**[START FIGURE 4.33 HERE]**

**Figure 4.33:** CMIP6 Annular Mode index change from 1995–2014 (as an average) to 2081–2100 (as an average): (a) NAM and (b) SAM. The NAM is defined as the difference in zonal mean SLP at 35°N and 65°N (Li and Wang, 2003) and the SAM as the difference in zonal mean SLP at 40°S and 65°S (Gong and Wang, 1999). The shadings are the 5 to 95% ranges (i.e. mean ± standard deviation x 1.64). The numbers near the top are the numbers of model simulations in each SSP ensemble. The numbers near the bottom are the SSP-averaged percentage of simulations with positive anomalies.

**[END FIGURE 4.33 HERE]**

### *4.5.3.2 El Niño-Southern Oscillation and its Teleconnections*

The AR5 assessed that it is *very likely* that the ENSO will remain the dominant mode of interannual variability in the future. Moreover, due to increased moisture availability the associated precipitation variability on regional scales was assessed to *likely* intensify. An eastward shift in the patterns of temperature and precipitation variations in the North Pacific and North America related to El Niño and La Niña teleconnections was projected with *medium confidence*. The stability of teleconnections to other regional implications including those in Central and South America, the Caribbean, Africa, most of Asia, Australia and most Pacific Islands were assessed to be uncertain (Christensen et al., 2013b).

While pronounced low-frequency modulations of ENSO exist in unforced control simulations (Wittenberg, 2009), there is potential for anthropogenically forced changes in both ENSO SST variability and climate

impacts in the mid-term to long-term future (Cai et al., 2015). While a subset of CMIP5 models that simulate linear ENSO stability realistically exhibit a decrease in ENSO amplitude by the latter half of the 21st century (Figure 4.16:), there is no strong consensus among models on long-term Niño 3.4 SST changes when considering all models (Cai et al., 2015). However, an increase of Eastern Pacific (EP)-ENSO SST variance has been shown when taking into account the biases in the ENSO pattern simulation by different models (Cai et al., 2018a).

The ENSO characteristics depend on the climate mean state of the tropical Pacific; however, ENSO can also change the mean state through nonlinear processes (Cai et al., 2015; Timmermann et al., 2018). The response of the tropical Pacific mean state to anthropogenic forcing is characterized by a faster warming on the equator compared to the off-equatorial region, a faster warming of the eastern equatorial Pacific compared to the central tropical Pacific, and a weakening of the Walker circulation in most models. These changes are associated with enhanced precipitation on the equator, especially in the eastern part of the basin (Watanabe et al., 2012; Cai et al., 2015).

While there is no strong model consensus on how these mean state changes affect ENSO SST variability, consensus exists that these changes are conducive to an increase in extreme ENSO-associated rainfall even if ENSO SST variability itself remains unchanged in CMIP5 models (Power et al., 2013; Cai et al., 2015). Moreover, there is an indication that tropical cyclones will become more frequent during future El Niño events (and less frequent during future La Niña events) by the end of the 21st century (Chand et al., 2017), thus contributing to the projected increase in ENSO-associated hydroclimate impacts. These projected changes of ENSO impacts depend, however, critically on the projected climate mean state changes. For instance, one CMIP5 model that warms less in the eastern than in the western Pacific exhibits a pronounced decrease in extreme ENSO events (Kohyama and Hartmann, 2017). This example highlights the importance of constraining tropical Pacific mean state changes in order to enhance confidence in the projected response of Pacific climate variability, such as ENSO. However, it has been also suggested that historical model biases over the equatorial Pacific cold tongue in CMIP5 may lead to the greater precipitation mean change and amplification of extreme ENSO-associated rainfall in CMIP5 (Stevenson et al., 2019).

Here we assess the mid- to long-term changes in amplitude of ENSO SST and rainfall variability in CMIP6 models. Overall, there is no robust change in ENSO SST amplitude in the mid- and long-term period across all four SSPs (Figure 4.8:). In contrast, the robust increase in ENSO rainfall amplitude is found particularly in SSP2-4.5, SSP3-7.0, and SSP5-8.5 (Figure 4.17:) attributable to the increase in mean SST and moisture (Cai et al., 2014; Kim et al., 2014; Huang and Xie, 2015). The changes in ENSO rainfall amplitude in the long-term future (2081–2100) relative to the recent past (1995–2014) are statistically significant at the 95% confidence based on F-test. Thus, the change in ENSO SST variability is highly uncertain in CMIP5 and CMIP6 models (*medium confidence*) but it is *very likely* that ENSO-related rainfall variability will increase significantly (*high confidence*) regardless of ENSO amplitude changes in mid- and long-term future.

#### *4.5.3.3 Pacific Decadal Variability*

The AR5 assessed that there is *low confidence* in projections of future changes in Pacific decadal variability (PDV) due to the inability of CMIP5 models to satisfactory represent the connection between PDV and Indo-Pacific SST variations. Because the PDV appears to encompass the combined effects of different dynamical processes operating at different timescales, representation of PDV in CMIP5 climate models remains a challenge and its long-term evolution under climate change uncertain.

In addition to uncertainty from the future evolution of the mechanisms that determined the PDV, it is also unclear how the background state in the Pacific Ocean will change due to time-varying radiative forcing, and how this change will interact with variability at interannual and low-frequency timescales (Fedorov et al., 2019). Recent research suggests that PDV would have a weaker amplitude and higher frequency with global warming (Zhang and Delworth, 2016; Xu and Hu, 2017; Geng et al., 2019). The former appears to be associated with a decrease in SST variability and the meridional gradient over the Kuroshio-Oyashio region, and with a reduction in North Pacific wind stress and the meandering of the subpolar/subtropical gyre

interplay (Zhang and Delworth, 2016). The latter is hypothesized to rely on the enhanced ocean stratification and shallower mixed layer of a warmer climate, which would increase the phase speed of the westward-propagating oceanic waves, hence shortening the decadal-interdecadal component (Goodman and Marshall, 1999; Zhang and Delworth, 2016; Xu and Hu, 2017). The weakening of the PDV in a warmer climate may reduce the internal variability of global mean surface temperature, to which PDV seems associated (Zhang et al., 1997; Kosaka and Xie, 2016). Thus, a weaker and more frequent PDV could reduce the disturbance of the internal variability to the global warming trend and eventually lead to a reduced probability of global warming hiatus events.

Concerning secular variations, a multi-model projection suggests the PDV shift into a negative phase, particularly towards the end of the century for which the trend becomes statistically significant, although not absent of model diversity and uncertainty (Lapp et al., 2012). The influence of anthropogenic climate change on the PDV, however, is still unclear (Liu and Di Lorenzo, 2018)

On the basis of recent studies conducted using CMIP5 models, there is still low *confidence* on how PDV would change under global warming.

#### *4.5.3.4 Indian Ocean Basin and Dipole Modes and their Teleconnections*

In the mid- to long-term period, the projected climate mean state changes in the tropical Indian Ocean resemble a positive IOD state, with faster warming in the west compared to the east (Cai et al., 2013; Zheng et al., 2013b). However, it was argued that this projected mean state change could be due to the large mean state biases in the simulated current climate and potentially not a realistic expectation (Li et al., 2016a). If the mean state change will indeed resemble a positive IOD state however, this would lead to a reduction in the amplitude difference between positive and negative IOD events, but with no robust change in IOD frequency (Cai et al., 2013). For a small subset of CMIP5 models that simulate IOD events best, a slight increase in IOD frequency was found under the CMIP5 RCP4.5 scenario (Chu et al., 2014) .

However, it was also found that the frequency of extreme positive IOD events, which exhibit the largest climate impacts, might increase by a factor of about three under the CMIP5 RCP8.5 scenario (Cai et al., 2014). An approximate doubling of these extreme positive IOD events was still found for global warming of 1.5 °C warming above pre-industrial levels, without a projected decline thereafter (Cai et al., 2018b). These results depend however on how realistic the projected mean state change is in the Indian Ocean and could thus potentially turn out to be spurious (Li et al., 2016a).

For a small subset of CMIP5 models that simulate Indian Ocean Basin mode (IOB), a considerable decrease in IOB frequency was found under the CMIP5 RCP4.5 scenario (Chu et al., 2014). For a different subset of models however, it was found that ENSO-related IOB warming increases under the same CMIP5 RCP4.5 scenario (Tao et al., 2015).

Given the results that ENSO events in general (Cai et al., 2018a) and extreme El Niño events (Cai et al., 2014) are projected to increase in response to greenhouse warming, and given the close relationship between ENSO-IOD (Stuecker et al., 2017) and ENSO-IOB (Xie et al., 2009; Du et al., 2013), ENSO-related IOD and IOB variability might increase. Currently, no new studies and evidence exist that would suggest a disappearance of either IOD or IOB variability in the mid-term to long-term future. This means that we also expect that the ENSO-IOD and ENSO-IOB relationships observed in the current climate will persist in the future (*high confidence*).

#### *4.5.3.5 Atlantic Multidecadal Variability*

Based on paleoclimate reconstructions and model simulations, the AR5 assessed that AMV is *unlikely* to change its behaviour in the future. However, AMV fluctuations over the coming decades are *likely* to influence regional climate, enhancing or offsetting some of the effects of global warming.

Recent proxy-derived reconstructions of AMV-related signals show persistent multi-decadal variability over the last three centuries (Kilbourne et al., 2014; Svendsen et al., 2014; Moore et al., 2017), up to the last millennium (Chylek et al., 2011; Zhou et al., 2016; Wang et al., 2017b) and beyond (Knudsen et al., 2011). This implies that in the past AMV properties were little affected by large climatic excursions.

The AMV long-term changes under future warming scenarios have been so far scarcely investigated. A study on the CMIP5 multi-model simulations under RCP8.5 scenario by (Villamayor et al., 2018) found no substantial differences in the simulated SST patterns (and in the related tropical rainfall response) when RCP8.5, historical and piControl simulations are compared. Such results suggest that the AMV and its teleconnections are not expected to change under global warming. However, since a superposition of multiple processes control the AMV, as extensively discussed in Tech Annex AVI.8, and in Chapter 3 (Section 3.7.7) and Chapter 9 (Section 9.2.3.1), the length of the RCP8.5 simulations might be not sufficient to properly evaluate the respective weight and interplay of internal components and influences from external forcing on AMV projections.

On the basis of paleoclimate reconstructions and CMIP5 model simulations AMV *is unlikely* to change in the future, however there is clearly a knowledge gap on long-term changes of the AMV under global warming.

#### *4.5.3.6 Tropical Atlantic Modes and their Teleconnections*

In spite of remarkable progress made in CMIP5 with respect to CMIP3, climate models were generally not able to correctly simulate the main aspects of Tropical Atlantic variability (TAV) and associated impacts. This is *likely* the main reason why in the AR5 there are very few studies dealing with long-term changes in TAV. The models that best represent the Atlantic meridional mode (AMM) show a weakening for future climate conditions. However, model biases in the Atlantic Niños are too strong to properly assess changes. Nevertheless, there is robust evidence over multiple generations of models of a warming in the mean state of the Tropical Atlantic basin, though the impact of climatological changes on the variability is quite uncertain.

Long-term changes in TAV modes and associated teleconnections are expected as a result of global warming, but large uncertainties exist (Lübbecke et al., 2018; Cai et al., 2019). Observational analyses show large discrepancies in SST and trade winds strength (Servain et al., 2014; Mohino and Losada, 2015). Single-model sensitivity experiments show that Atlantic Niño characteristics at the end of twenty firsts century remain equal to those of the twentieth century, though changes in the climatological SSTs can lead to changes in the associated teleconnections (Mohino and Losada, 2015).

The weakening of the AMOC expected from global warming (e.g., (Robson et al., 2014a; Caesar et al., 2018) has been suggested to have an influence on the mean background state of tropical-Atlantic surface conditions, thereby enhancing equatorial Atlantic variability and resulting in a stronger tropical Atlantic–ENSO teleconnection (Svendsen et al., 2014) (see Chapter 3 Section 3.7.5 for a detailed discussion). But again, based on CMIP5 and CMIP6 results, we conclude that there is a clear lack of model studies investigating the long-term evolution of TAV and associated teleconnections. Most of studies rely on a single model, and hence a large uncertainty exists. The strong model biases together with limitations in the observational record might explain this lack of progress.

## 4.6 Implications of Climate Policy

### *4.6.1 Patterns of Climate Change for Specific Levels of Global Warming*

This subsection provides an assessment of changes in climate at 1.5°C, 2°C, 3°C, and 4°C of global warming relative to the period 1850–1900 (see Chapter 1 Section 1.6.2), including a discussion of the regional patterns of change in temperature (Section 4.6.1.1), precipitation (Section 4.6.1.2) and aspects of atmospheric circulation (Section 4.6.1.3). An assessment of changes in extreme weather events as a function of different levels of global warming is provided in Chapter 11, whilst corresponding analyses of regional

climate change are provided in Chapter 12 and in the Atlas. This section builds upon assessments from the AR5 WGI report (Bindoff et al., 2013; Christensen et al., 2013b; Collins et al., 2013; Hartmann et al., 2013) and Chapter 3 of the IPCC Special Report on Global Warming of 1.5°C (SR1.5; Hoegh-Guldberg et al., 2018), as well as a substantial body of new literature related to projections of climate at 1.5°C, 2°C, and higher levels of global warming above pre-industrial levels. Such analyses are of direct relevance in terms of assessing the benefits of restricting global warming to the thresholds specified by the Paris Agreement on Climate Change and to understand the risks associated with exceeding these thresholds.

Several methodologies have been applied to estimate the spatial patterns of climate change associated with a given level of global warming. These include performing model simulations under stabilisation scenarios designed to achieve a specific level of global warming (e.g. Dosio et al., 2018; Kjellström et al., 2018; Mitchell et al., 2017), the analysis of epochs identified within transient simulations that systematically exceed different thresholds of global warming (e.g. Hoegh-Guldberg et al., 2018), and analysis based on statistical methodologies that include empirical scaling relationships (ESR) (e.g., Dosio and Fischer, 2018; Schleussner et al., 2017; Seneviratne et al., 2018) and statistical pattern scaling (e.g., Kharin et al., 2018). These different methodologies are discussed in some detail in Section 4.2.5 (see also James et al., 2017) and generally provide qualitatively consistent results regarding changes in the spatial patterns of temperature and rainfall means and extremes at different levels of global warming.

In this subsection, we present the projected patterns of climate change obtained following the epoch approach (also called the time-shift method, see Section 4.2.4) under the Tier 1 SSPs (SSP1-2.6, SSP2-4.5, SSP3-7.0 and SSP5-8.5). For each model simulation considered under each of these SSPs, 20-year moving averages of the global average atmospheric surface temperature are first constructed, and this time series is used to detect the first year during which global warming exceeds the 1.5°C, 2°C, 3°C and 4°C thresholds with respect to the 1850–1900 GSAT. The temperature thresholds are not exceeded in all the model simulations across the Tier 1 SSPs, that is, decreasing numbers of simulations are available for the analysis of patterns of change as the temperature threshold increases. For each simulation within which a given temperature threshold is exceeded, a 20-year global climatology is subsequently constructed to represent that level of global warming, centred on the year for which the threshold was first exceeded. The composite of all such climatologies across the Tier 1 SSPs and model simulations constitute the spatial patterns of change for a given temperature threshold. Some of the complexities of scaling patterns of climate change with different levels of global warming are also discussed in the following sections. These include overshoot vs. stabilization scenarios and limitations of pattern scaling for strong mitigation and stabilization scenarios (Tebaldi and Arblaster, 2014). At least for the case of annual temperature and precipitation, strong evidence exists that even for strong mitigation and stabilization scenarios, patterns of change at lower levels of warming scale similarly to those reconstructed from transient simulations using either standard pattern-correlation or time-shift methodologies (Tebaldi and Knutti, 2018b).

Pattern scaling performance based on scenario experiments is generally better for near-surface temperature than for precipitation (Ishizaki et al., 2013). For precipitation, rapid adjustments due to different forcing agents must be accounted for (Richardson et al., 2016). Also important are possible non-linear responses to different forcing levels (Good et al., 2015, 2016). Pattern scaling does not work as well at high forcing levels (Osborn et al., 2018). It is also important to distinguish the forced response from internal variability when comparing similar warming levels (Suarez-Gutierrez et al., 2018). The purpose of this section is not to repeat the analysis for all the variables considered in Sections 4.4 and 4.5, but rather to show a selected number of key variables that are important from the perspective of understanding the response of the physical climate system to different levels of warming.

#### *4.6.1.1 Temperature*

Global warming of 1.5°C implies higher mean temperatures compared to the preindustrial levels across the globe, with generally higher warming over land compared to ocean areas (*virtually certain*) and larger warming in high latitudes compared to low latitudes (Figure 4.34:). In addition, global warming of 2°C versus 1.5°C results in robust increases in the mean temperatures in almost all locations, both on land and in

the ocean (*virtually certain*), with subsequent further warming at all locations at higher levels of global warming (*virtually certain*). For each particular level of global warming, relatively larger mean warming is projected for land regions (*virtually certain*, see Figure 4.34:, also see (Christensen et al., 2013b; Collins et al., 2013; Seneviratne et al., 2016a). The projected changes at 1.5°C and 2°C global warming are consistent with observed historical global trends in temperature and their attribution to anthropogenic forcing (see Chapter 3), as well as with observed changes under the recent global warming of 0.5°C (SR1.5; Hoegh-Guldberg et al., 2018; Schleussner et al., 2017). That is, spatial patterns of temperature changes associated with the 0.5°C difference in GMST warming between 1991–2010 and 1960–1970 (Schleussner et al., 2017; SR1.5) are consistent with projected changes under 1.5°C and 2°C of global warming.

The largest increase in mean annual temperature is found in the high latitudes of the Northern Hemisphere (NH) across all levels of global warming (*virtually certain*; Figure 4.34:). This phenomena peaks in the Arctic and is known as Arctic amplification, with the underlying physical mechanisms discussed in detail in Section 4.5.1. For the CMIP6 ensemble average considered here, Arctic annual mean temperatures warm by a factor of 2.3, 2.5, 2.4 and 2.4 for 1.5°C, 2°C, 3°C and 4°C of global warming, respectively. That is, Arctic warming scales linearly with GSAT. Generally, when Arctic amplification is considered across individual constituting models, warming occurs at a factor of 2-4 times the global level of warming. Polar amplification is also projected to occur over Antarctica across all levels of global warming (Figure 4.34:), but with a reduced amplitude compared to the Arctic (*high confidence*). The underlying physical mechanisms that reduce the amplitude of polar amplification over Antarctica are discussed in some detail in Section 4.5.1. In the Southern Hemisphere robust patterns of relatively high rates of warming are projected for the subtropical continental areas of South America, southern Africa and Australia (*high confidence*). The relatively strong warming in subtropical southern Africa may be attributed to strong soil-moisture–temperature coupling and projected increased dryness under enhanced subsidence (Engelbrecht et al., 2015; Vogel et al., 2017). Across the globe, in the tropics, subtropics and mid- to high latitudes, temperature tend to scale linearly with the level of increase in GSAT and is largely scenario independent *(high confidence)*.

**[START FIGURE 4.34 HERE]**

**Figure 4.34:** Projected spatial patterns of changes in annual mean temperature (°C) at 1.5°C, 2°C, 3°C, and 4°C of global warming compared to the period 1850–1900 (top), and the spatial differences of temperature change between 2°C, 3°C, and 4°C of global warming relative to 1.5°C of global warming (bottom). Stippling indicates regions where the multi-model mean change exceeds two standard deviations of pre-industrial internal variability and where at least 90% of the models agree on the sign of change, as a measure of robustness. Hatching indicates regions where the multi-model mean signal is less than one standard deviation of internal variability.. Values were assessed from a 20-year period at a given warming level, based on model simulations under the Tier 1 SSPs of CMIP6.

**[END FIGURE 4.34 HERE]**

### *4.6.1.2 Precipitation*

It is *virtually certain* that global mean precipitation will increase with increased global mean surface temperature. The AR5 assessment based on CMIP5 simulations showed that global-mean precipitation will increase with global temperature change across a range from 1% to 3% $°C^{-1}$. Percentage precipitation change at different levels of global warming based on an ensemble of CMIP6 models composited from SSP1-2.6, SSP2-4.5, SSP3-7.0 and SSP5-8.5 are shown in Figure 4.35:. While precipitation increase with increase in global mean temperature, patterns of precipitation change do not scale linearly with surface air temperature increase. A number of recent studies have demonstrated that global hydrological sensitivity, the relative change of global-mean precipitation per degree of global warming, shows large diversity among models (Samset et al., 2016, 2018a; Myhre et al., 2017). The response of global mean precipitation to warming is constrained by global energy balance (O'Gorman et al., 2012; Pendergrass and Hartmann, 2014; Richardson et al., 2018b). The overall precipitation response can be considered as a sum of fast and slow responses: the fast response due to atmospheric adjustment to forcing correlates with radiative forcing associated with

atmospheric absorption, whereas the slower response caused by changes in surface temperature correlates with radiative forcing at the top of the atmosphere (Samset et al., 2016). Differences in how the fast adjustment processes are represented within models are expected to explain a large fraction of the present model spread in the precipitation projections (Myhre et al., 2017). Hydrological sensitivity and energy budget constraints on global precipitation changes are discussed in Section 4.5 and also in Section 8.1.1 and 8.1.2 of Chapter 8. The fast response are forcing-dependent and the slow response are forcing-independent and scale with the change in GSAT. Section 4.2.4 discusses the pattern scaling and points out that temperature change patterns conform better to pattern scaling approximations than precipitation patterns (Tebaldi and Arblaster, 2014). Regional changes are more contrained by forcings, and may be expected to amplify as a function of increasing degrees of global warming (Good et al., 2016).

**[START FIGURE 4.35 HERE]**

**Figure 4.35:** Projected spatial patterns of changes in annual precipitation (expressed as a % change) at 1.5°C, 2°C, 3°C and 4°C of global warming compared to the period 1850–1900. Stippling indicates regions where the multi-model mean change exceeds two standard deviations of pre-industrial internal variability and where at least 90% of the models agree on the sign of change, as a measure of robustness. Hatching indicates regions where the multi-model mean signal is less than one standard deviation of internal variability.. Values were assessed from a 20-year period at a given warming level, composited from SSP1-2.6, SSP2-4.5, SSP3-7.0 and SSP5-8.5 in CMIP6.

**[END FIGURE 4.35 HERE]**

Global warming of 1.5°C–2°C will result in increases in precipitation over most high-latitude regions, as well as in the tropics (*high confidence*) (Figure 4.35:). These increases are projected to amplify under higher levels of global warming *(high confidence*). Across the Southern Hemisphere subtropics, decreases in precipitation are robustly projected across lower levels of global warming, amplifying over higher levels of global warming (*high confidence*) (Figure 4.35:). These changes occur in conjunction with patterns of relatively large increases in near-surface temperature over the subtropical continental areas in the Southern Hemisphere (Figure 4.35:). Increases in extreme precipitation events under different levels of global warming are discussed in Chapter 11.

Recent studies have also shown that 1.5 °C and 2.0 °C global warming have regional implications; summer rainfall over the Asian monsoon regions will increase in both means and the extremes. Based on CMIP5 projections, area and population exposures to dangerous extreme precipitation events was shown to increase with warming over the global land monsoon regions (Zhang et al., 2018). The SR1.5 stated *low confidence* regarding changes in global monsoons at 1.5°C versus 2°C of global warming, as well as differences in monsoon responses at 1.5°C versus 2°C. Recent studies (Vautard et al., 2014; Jacob et al., 2018; Kjellström et al., 2018) have shown that 2°C of global warming was associated with a robust increase in mean precipitation over central and northern Europe in winter, but only over northern Europe in summer, and with decrease in mean precipitation in central/southern Europe in summer. For statistically significant changes in regional annual average precipitation, a global mean warming of 2.5°C–3°C is required (Tebaldi et al., 2015). It may also be noted that over the winter rainfall regions of south-western South America, South Africa and Australia, projected decreases in mean annual rainfall show high agreement across models and a strong climate change signal even under 1.5°C of global warming, with further amplification of the signal at higher levels of global warming (*high confidence*). This is a signal evident in observed rainfall trends over these regions (see Chapter 3).

**[START FIGURE 4.36 HERE]**

**Figure 4.36:** Area fraction (% change) with significant precipitation increase (left-hand side) and decrease (right-hand side) in the projected annual precipitation change at 1.5°C, 2°C, 3°C and 4°C of global warming compared to the period 1850–1900. Values were assessed from a 20-year period at a given warming level from SSP1-2.6, SSP3-7.0 and SSP5-8.5 in CMIP6. The solid line illustrates the CMIP6-multi model

mean and the shaded band is the 5-95% range across models that reach a given level of warming.

**[END FIGURE 4.36 HERE]**

It is *virtually certain* that average warming will be higher over land than over the ocean. Precipitation variability in most climate models increase over most of the global land area in response to warming (Pendergrass et al., 2017). The global average of the 20-year return value of the annual maximum daily precipitation increase with temperature increase, but with large regional variations (Westra et al., 2013; Kitoh and Endo, 2016). It is also *very likely* that with increased warming, a larger land area is projected to experience statistically significant increase or decrease in precipitation. The increase of area fraction with significant precipitation increase is larger in land than ocean, but the increase of area with significant precipitation decrease is larger in ocean than land (Figure 4.36:).

In summary, based on the assessment of CMIP6 models, it is *virtually certain* that global precipitation will increase with increased global mean surface temperature. Precipitation increase on land will be higher at 3°C and 4°C compared to 1.5°C 2˚C of warming and it is *very likely* that with increase warming, a larger land area is projected to experience statistically significant increase or decrease in precipitation (*high confidence*)

### *4.6.1.3 Atmospheric Circulation*

The AR5 reported that the application of pattern scaling to extract information on variables other than surface temperature and precipitation was relatively under explored. Since the AR5, new studies have examined the relationship between projections of midlatitude atmospheric circulation and GSAT both in terms of interpreting spread in responses across the CMIP5 multi-model ensemble (Grise and Polvani, 2014a, 2016) and to investigate variations in the circulation response as a function of GSAT change over time within a given forcing experiment (Grise and Polvani, 2017; Ceppi et al., 2018).

At a fixed time horizon, the CMIP5 multi-model spread in GSAT explains only a small fraction of the spread in the shift of the Northern hemisphere midlatitude circulation due to an abrupt quadrupling in $CO_2$ (Grise and Polvani, 2016). The fraction of model spread explained by GSAT in the shift of the SH circulation is larger, but still fairly small (Grise and Polvani, 2014a, 2016). At a fixed time horizon and for a given emissions scenario, CMIP5 multi-model spread in storm track shifts, and the closely related midlatitude jets, can be better explained by multi-model spread in lower and upper level meridional temperature gradients than by GSAT (Harvey et al., 2014; Grise and Polvani, 2016).

The transient response of the midlatitude jets to forcing in the North Atlantic, North Pacific and Southern Hemisphere behaves nonlinearly with GSAT (Grise and Polvani, 2017; Ceppi et al., 2018). This is a consequence of the time-dependence of the relationship between radiative forcing and GSAT and the temporal evolution of SST patterns (Ceppi et al., 2018), with a potential seasonal component in the SH associated with polar stratospheric temperature changes (Grise and Polvani, 2017). Consequently, the epoch approach applied to a transient simulation of the 21st century will overestimate the midlatitude circulation response in a stabilized climate. Dedicated time slice experiments simulating stabilized climates are therefore required to assess differences in midlatitude circulation at given levels of global warming (Li et al., 2018a). A further complication in the Southern Hemisphere is the competing influences of ozone recovery and increasing greenhouse gas concentrations on the summertime midlatitude circulation during the first half the 21st century (Barnes and Polvani, 2013; Barnes et al., 2014). Using transient 21st century experiments to diagnose changes in SH midlatitude circulation at different levels of warming therefore confounds the effects of ozone recovery and GHG increases (Ceppi et al., 2018). Given these various limitations, we do not apply epoch analysis to assess midlatitude atmospheric circulation changes and related annular modes of variability.

### *4.6.2 Climate Goals, Path-Dependence, and Overshoot*

This subsection assesses deviations from pattern scaling that may be due to non-linearity of climate change in response to radiative forcing or differing response to non-$CO_2$ forcing in affecting patterns of climate change at levels of global warming. Reversibility of climate due to temporary overshoot of global mean temperature levels during the 21st century will also be assessed.

The AR5 presented the concept of TCRE – the transient climate response to cumulative carbon emissions. This allows climate goals to be determined in terms of global total carbon budgets as global temperature increase is near-linear with cumulative emissions (this is assessed further in chapter 5). Research since the AR5 has shown that the concept of near-linearity of climate change to cumulative carbon emissions holds for measures other than just GSAT, such as regional climate (Leduc et al., 2016) or extremes (Harrington et al., 2016; Seneviratne et al., 2016b). As such, TCRE remains a valuable concept to define climate goals and how to achieve them.

It has long been known that the climate response to increasing forcing is approximately linear in terms of global metrics and some patterns of surface change (e.g., Stouffer and Manabe, 1999). This "pattern scaling" approach means we can generalise patterns of climate change at levels of global warming across a range of scenarios (Section 4.6.1). However, there is evidence that not all aspects do so. It has been shown that the first 2°C of warming does not have the same characteristics as the second 2°C under idealized $CO_2$ simulations (Good et al., 2016). Climate sensitivity has been found to be state dependent (nonlinear) under different levels of forcing (Andrews et al., 2012; Knutti and Rugenstein, 2015) and new millennial-length simulations with ESMs has shown how climate feedbacks and adjustments change over long time periods and become progressively less stabilising (Rugenstein et al., 2019b).

In addition to the sensitivity of the climate response to the rate and magnitude of increasing $CO_2$ concentration, the climate response can vary regionally due to non-$CO_2$ components of forcing (Samset et al., 2016; Richardson et al., 2018b, 2018a).

Figure 4.37: shows deviation of patterns of climate change at a common level of warming achieved by two different pathways. Over many land areas, especially northern mid to high latitudes, SSP5-8.5 has more warming than SSP1-2.6 for the same global GSAT change of 2 degrees. Differences in rainfall are mainly over ocean areas although some tropical land areas appear drier in SSP5-8.5 than SSP1-2.6.

**[START FIGURE 4.37 HERE]**

**Figure 4.37:** Projected changes in the global pattern of near-surface temperature (top row) and precipitation (second row) associated with a 2°C increase in global temperature achieved by different pathways from 15 CMIP6 ESMs. Panels show temperature and precipitation changes averaged over 20-year period when GSAT reaches 2 degrees above 1850–1900 for two scenarios; SSP5-8.5 and SSP1-2.6. The bottom row and right-hand panels show differences (SSP5-8.5 minus SSP1-2.6) in the temperature and precipitation changes due to path dependence.

**[END FIGURE 4.37 HERE]**

IPCC SR1.5 assessed the challenges to achieve low climate goals such as 1.5 or 2 degrees. While emissions reductions to achieve them are still possible (Kriegler et al., 2018), it is also of interest to quantify the implications of overshoot – here meaning the resultant climate change if GSAT temporarily exceeds a warming level before reducing again.

We assess results from the SSP5-34-OS overshoot scenario in which $CO_2$ peaks at 571 ppm in the year 2062 and reverts to 497 ppm by 2100 – approximately the same level as in 2040. We show that GSAT, land precipitation, September Arctic sea-ice extent and steric sea level are not reversible by 2100 under this

reversal of $CO_2$ concentration (Figure 4.38:). Changes in quantities for 2081–2100 relative to a 20-year period of the same average $CO_2$ are: 0.36±0.34 K; 0.05±0.02 mm/day; -0.46±0.34 million $km^2$; 12±0.5 cm respectively. There is *low confidence* in knowledge of the extent of reversibility of climate patterns following overshoot of a global temperature level. While global mean temperature is expected to decline approximately reversibly with reducing $CO_2$ (Section 4.7.2) regional patterns may differ after overshoot.

**[START FIGURE 4.38 HERE]**

**Figure 4.38:** Simulated changes in climate, plotted against atmospheric $CO_2$ concentration, for SSP5-34-OS from $CO_2$ concentration of 480 up to 571 and back to 500 by 2100. (a) Global temperature change; (b) Global land precipitation change; (c) September Arctic sea ice extent; (d) Global steric sea level. Plotted changes are relative to the 2034–2053 mean which has same $CO_2$ as 2080–2100 mean (shaded grey bar). Red lines denote changes during the period up to 2062 when $CO_2$ is rising, blue lines denote changes after 2062 when $CO_2$ is decreasing again.

**[END FIGURE 4.38 HERE]**

### *4.6.3 Climate Response to Mitigation, Carbon Dioxide Removal, and Solar Radiation Modification*

Anthropogenic climate change can be limited by both mitigation through reduced emissions of GHGs and intentional large-scale interventions in the climate system referred to as geoengineering, climate engineering, or climate intervention (e.g., Royal Society, 2009; National Research Council, 2015a, 2015b). Two categories of fundamentally different climate intervention have been proposed: carbon dioxide removal (CDR) and solar radiation modification (SRM). CDR refers to anthropogenic activities that remove $CO_2$ from the atmosphere and durably store it in geological, terrestrial or ocean reservoirs, or in products (SR1.5, Glossary). SRM refers to intentional modification of the Earth's shortwave radiation budget to reduce surface warming (SR1.5, Glossary). As in SR1.5, use of the term "geoengineering" is avoided here because of inconsistencies in the literature, which uses this term to refer to SRM, CDR or both, whereas CDR and SRM are explicitly differentiated here. While there is some overlap between mitigation and CDR, as in SR1.5, they are treated separately here to distinguish between activities that reduce the emissions of greenhouse gases (mitigation) and those that reduce $CO_2$ concentrations already in the atmosphere (CDR). Most strong-mitigation scenarios assume CDR in addition to emissions reductions; for example, RCP2.6 explicitly includes direct CDR from around 2025 onward and achieves net negative emissions by 2070 through a combination of bioenergy and carbon capture and storage (van Vuuren et al., 2011a). Similarly, the emission scenario of SSP1-1.9 is characterized by a rapid decline to zero and a long period of negative emissions for $CO_2$ (O'Neill et al., 2016; Rogelj et al., 2018a).

Here, only the climate system response to mitigation and suggested methods of climate intervention is assessed; the risks, governance and ethics are assessed as part of the Working Group III Sixth Assessment Report (AR6). While the SRM methods are briefly discussed in section 4.6.3.3, the CDR methods are discussed in detail in Chapter 5.

#### *4.6.3.1 Climate Response to Mitigation*

Mitigation through reduced GHG emissions would slow and limit the degree of climate change relative to high emissions scenarios such as SSP5-8.5 (*very high confidence*). Because peak warming depends on the cumulative carbon emissions (Allen et al., 2009; Meinshausen et al., 2009; Frame et al., 2014; Matthews et al., 2018), mitigation that reaches net-zero emission by 2100 would avoid crossing more severe warming thresholds while late mitigation could lead to their exceedance.

Because of the long atmospheric lifetime of $CO_2$, under scenarios of decreasing emissions there would be a substantial lag between a peak in $CO_2$ emissions and peak in atmospheric $CO_2$ concentration, and because of

the thermal inertia of the climate system, there would be a further lag in peak temperature on the order of decades (*high confidence*) (Matthews, 2010; Ricke and Caldeira, 2014; Zickfeld and Herrington, 2015).

Mitigation would reduce $CO_2$ emissions, but atmospheric $CO_2$ concentrations would continue to increase as long as emissions exceed removal by sinks (Millar et al., 2017). Because of thermal inertia, temperatures would continue to increase even when emissions are compensated by sinks and atmospheric $CO_2$ is stabilized *(high confidence*). Even if anthropogenic greenhouses-gas emissions were halted now, the radiative forcing due to long-lived GHGs concentrations, and consequently surface temperatures, would decrease only slowly in the future, at a rate determined by the lifetime of the gas (Collins et al., 2013). The zero emissions commitment (ZEC) is the amount of warming projected to occur following a subsequent complete cessation of emissions (4.7.2.2). There is *low confidence* in the amount of this "committed" warming after cessation of $CO_2$ emissions. Simulated ZEC by Earth system models following cessation of $CO_2$ emission after 1000 PgC is emitted varies, in terms of sign and magnitude, substantially across models (see section 4.7.2.2) (Jones et al., 2019b).

In the AR5 (Collins et al., 2013) and in this assessment (Section 4.3), a consistent and robust feature across climate models is a continuation of global warming in the 21st century for all scenarios. However, GSAT for 2081–2100, relative to 1995–2014, increases by 0.5°C–1.7°C and 2.4°C–5.5°C under SSP1-2.6 and SSP5-8.5 (5–95% range; see Table 4.2:), respectively, clearly demonstrating the potential benefit of mitigation policies. CMIP6 model simulations indicate that the Arctic will become permanently ice-free in September by the end of the 21st century under SSP2-4.5, SSP3-7.0, and SSP5-8.5, but not in SSP1-1.9 and SSP1-2.6 (see Table 4.4:). In the SR1.5 report (Masson-Delmotte et al., 2018b), robust differences in regional climate characteristics between present-day and global warming of 1.5°C, and between 1.5°C and 2°C above pre-industrial levels are reported. These differences include increases in mean temperature in most land and ocean regions (*high confidence*), hot extremes in most inhabited regions (*high confidenc*e), heavy precipitation in several regions *(medium confidence*), and the probability of drought and precipitation deficits in some regions (*medium confidenc*e).

The benefits of mitigation on extremes have been much more clearly identified in model simulations as the magnitude of extremes scales approximately linearly with simulated global mean warming (*high confidence;* Chapter 11) (Aerenson et al., 2018). An analysis of a suite of extreme indices in simulations that stabilize temperature at 1.5 and 2ºC warming show that even for scenarios that are separated by only half of a degree in global average temperature, the statistics of extremes are significantly different (Aerenson et al., 2018). Sanderson et al. (2017b) find that the exceedance of historical record temperature occurs with 60% greater frequency in the 2°C climate than in a 1.5°C climate aggregated globally, and extreme precipitation intensity is significantly higher in a 2.0°C climate than a 1.5°C climate. Further, several studies have assessed the differences in impacts between the RCP4.5 and RCP8.5 scenarios using large ensembles. Clear benefits of mitigation have been found in the case of extremes in temperatures and precipitation (O'Neill et al., 2016; Fix et al., 2018; Lehner et al., 2018; Oleson et al., 2018; Sanderson et al., 2018). Using large ensembles, Tebaldi and Wehner (2018) found that statistically significant differences between RCP4.5 and RCP8.5 in extreme temperatures over all land areas become pervasive over the globe by 2050. Reduction in the frequency of extreme precipitation events associated with tropical cyclones is also possible through mitigation from RCP8.5 to RCP4.5 (Bacmeister et al., 2018). The increase in the magnitude of extremes as a function of global mean temperature change is discussed in detail in Chapter 11.

An important conclusion of the AR5 (Collins et al., 2013; Kirtman et al., 2013) and in this assessment (see Sections 4.3 and 4.4) is that near-term climate projections are not very sensitive to emission pathways, that is, in the near term, different scenarios give rise to similar magnitudes and patterns of climate change. For instance, temperature increases are almost the same for all the SSP scenarios during 2021–2040 (see Table 4.2:). However, on longer time scales, the warming rate begins to depend more on the specified GHG concentration pathway, being highest (3.9°C ± 1.6°C by 2081–2100) in the highest emission scenario SSP5-8.5 and significantly lower in SSP1-1.9 (0.7°C ± 0.6°C). A multi-model ensemble analysis of warm-season temperatures in the RCP2.6 and RCP8.5 scenarios (Ciavarella et al., 2017) found that for many regions, it takes about 20 years of emissions reductions for extreme seasonal warmth to reduce by more than half following initiation of mitigation. (Sanderson et al., 2018) reach similar conclusions using single-model

ensembles for the RCP4.5 and RCP8.5 scenarios: while internal variability is a significant component of uncertainty for periods before 2050, the period 2061–2080 sees largely separate joint distributions of annual mean temperature and precipitation in most regions. Hence, for the latter portion of the 21st century, the range of regional climatic states that might be expected in the RCP8.5 scenario is significantly and detectably further removed from today's climate state than the RCP4.5 scenario is from today's climate even in the presence of internal variability (*high confidence*).

An important new development since the AR5 is quantification of the role of internal variability in masking the climate response to mitigation and the estimation of the "detection timescale" for "mitigation benefits" using large initial-condition ensembles (see Sections 4.2.1 and 4.2.5, BOX 4.1: and FAQ 4.2:). Detecting the climate response to mitigation is non-trivial, partly because internal variability strongly affects trends on decadal scales, and partly because once mitigation in in place, it is no longer possible to know what the climate would have been without mitigation. The lag due to inertia in the system also affects the timescale of detection of mitigation effects. The detection timescale for mitigation benefits was first investigated by (Tebaldi and Friedlingstein, 2013), analysing five CMIP5 models and a three-member initial-condition ensemble for each model. The $CO_2$ emissions in the "counterfactual" scenarios RCP4.5 and RCP8.5 depart from the mitigation scenario RCP2.6 in 2020 and 2010, respectively, but the median time of detection for departure of $CO_2$ concentration in the RCP4.5 and RCP8.5 scenarios from the RCP2.6 scenario is about 10 years later after the emission paths separate. For global mean temperature, because of the thermal lags in the climate system, the median detection time of mitigation was about 25-30 years (Tebaldi and Friedlingstein, 2013), which translates into detection of a mitigation signal by 2035 (RCP8.5) or 2045 (RCP4.5). The difference in detection time between $CO_2$ concentration and global mean temperature is related to the difference in signal-to-noise ratio between $CO_2$ and temperature (*high confidence*).

The time of detection of mitigation depends on the seasons and the regions (Tebaldi and Friedlingstein, 2013). Generally, winter temperatures are more challenging for detection, adding a decade to the detection time *(high confidence*), whereas detection times for summer averages are similar to the annual temperature averages. This is mainly due to larger variability in winter temperatures. Detection happens later at the regional scale, with a median detection time of 30–45 years after emission paths separate (Tebaldi and Friedlingstein, 2013). A stricter requirement (of 95% confidence level) induces a delay of several decades, bringing detection time toward the end of the 21st century at regional scales. There are also large uncertainties in detection times that result from uncertainty in climate sensitivity and internal variability (*high confidence*). Currently, there is no literature on reducing the uncertainty in detection time using observational constraints, and such constraints could make the response to mitigation more detectable than is implied by unconstrained multi-model ensembles.

The quantification of the role played by internal variability in masking the effects of mitigation in the near term has been conducted by several recent studies (Marotzke, 2019; Maher et al., 9999a; Samset et al., 9999; Spring et al., 9999). Marotzke (2019) uses a large initial condition ensemble (100 members) from a single model to quantify the irreducible uncertainty due to internal variability. The ensemble mean surface temperature in both RCP 2.6 and RCP 4.5 scenarios in Marotzke (2019) increases by ~0.5 between 2005 and 2035 and the difference between ensemble means stay below one ensemble standard deviation until 2035, indicating that the climate response to RCP2.6 and RCP4.5 is nearly indistinguishable in the near term, 2005–2035. The trends in global mean temperature are higher over the period 2021–2035 than over 2006–2020 in one-third of all realizations in the mitigation scenario RCP2.6, suggesting that the temperature would rise at a faster rate with a probability of as much as one third in a mitigation scenario. The probability was about one-half in the RCP4.5 scenario.

The time of emergence of a detectable, significant change from curbing emissions of a broad range of long and short lived climate forcers relative to a higher emission scenario has been also studied (Samset et al., 9999). By combining reduced complexity and earth system modelling, Samset et al. (2020) found that the global mean temperatures in the future scenarios RCP2.5, RCP4.5 and RCP8.5 differ from each other in a statistically significant manner only 25-35 years after the emissions start to diverge. A detailed assessment of the climate response to short lived climate forcers is provided in Section 4.4.4.

Maher et al. (2020a) uses six single model initial-condition large ensembles (SMILES) to quantify the role of internal variability in surface temperature trends in the short-term (15-year) and mid-term (30-year). This study finds that surface temperature trend projections are dominated by internal variability in the short-term, with little influence of structural model differences or warming pathway, and this finding is independent of the model-dependent estimate of the magnitude of internal variability. In agreement with the AR4 and AR5, in the mid-term, structural model differences and scenario uncertainties play a larger role in controlling surface temperature trend projections than they do on the shorter timescales. Further, in all models, in the short term, a lack of warming, or even a cooling trend can occur at all individual points on the globe, even under the largest greenhouse gas emissions (Figure 4.39:). Even out to thirty years, parts of the globe could still experience no detectable warming trend due to internal variability.

These conclusions on the role of internal variability in masking the global mean temperature trends are also applicable to atmospheric $CO_2$ concentration, as the atmospheric $CO_2$ growth rate on inter-annual time scales is largely controlled by the response of the land and ocean carbon sinks to climate variability. (Spring et al., 9999), using the same 100-member large ensemble used by Marotzke (2019), show that certainty regarding the effect of mitigation on $CO_2$ growth rate is achieved only after 10-15 years. Because the detection time for $CO_2$ concentration is much shorter than that for physical climate quantities, the absence of early detectability of the climate effects of mitigation is mainly due to the inertia and internal variability of the physical climate system rather than the global carbon cycle (Tebaldi and Friedlingstein, 2013; Marotzke, 2019; Maher et al., 9999a; Samset et al., 9999; Spring et al., 9999) (*high confidence*).

These recent results and our improved understanding indicate that in the near term, global mean temperature might rise at a faster rate than before with or without emissions reductions (*medium confidence*). Larger differences in the climate responses between scenarios are, however, projected to occur in the mid to long-term (Section 4.5). Therefore, assessments of the benefits of mitigation in the near term are contingent on quantitatively estimating internal variability.

**[START FIGURE 4.39 HERE]**

**Figure 4.39:** Near-term (2021–2040) maximum (top row) and minimum (middle row) trends in the initial condition ensemble from MPI (left and centre columns), and CESM (right column) models in the RCP2.6 (left column) and RCP8.5 scenarios (centre and right columns). The percentage of ensemble members which show a warming trend in the near-term is shown in the bottom panels. The panels in the middle row clearly indicate that in the near term in both mitigation (RCP2.6) and non-mitigation (RCP8.5) scenarios, a cooling trend is possible at any individual point on the globe, though not everywhere simultaneously. Modified from (Maher et al., 9999a).

**[END FIGURE 4.39 HERE]**

### *4.6.3.2 Climate Response to Carbon Dioxide Removal*

***Introduction***

Chapter 6 in WG1 AR5 and Chapter 5 in AR6 discuss the different CDR options and their implications for global biogeochemical cycles. The potential, cost, co-benefits and side effects of these approaches are assessed in SR1.5 (SR1.5, Chapter 4). In this sub-section, only the physical climate system response to CDR is assessed. CDR is also referred to as 'negative emissions'; the term 'net emissions' refers to the difference between anthropogenic carbon emissions and removal by CDR options, and net negative emissions imply a scenario where $CO_2$ removal exceeds emissions. All CDR options would lead to a reduction in net emissions and hence lower global mean temperature compared to a scenario without CDR; however, the maximum potential of CDR varies (*high confidence*; see Chapter 5). There could be a significant delay between deployment of CDR and net emissions to turn negative (van Vuuren et al., 2011a). The implication is that a mere deployment of CDR would not cause a reduction in atmospheric $CO_2$ levels, and net emissions should be less than land and ocean $CO_2$ sinks for $CO_2$ levels in the atmosphere to decrease. Hence, deployment of CDR is expected to precede net negative emissions and the consequent cooling of global mean temperature.

Thus, CDR could play a different, but an important role in the period before reaching net-zero emissions. However, it should be cautioned that none of the CDR proposals has been proven to work in reality, especially at large scale, and their overall lifecycle emission balance raises questions about their carbon negativity.

In the AR5, emission pathways that were assessed with a 66% or better chance of limiting global warming to 2°C by 2100 included CDR – typically about 10 $GtCO_2$ $yr^{-1}$ in 2100 or about 200–400 $GtCO_2$ over the course of the century (Smith et al., 2016; van Vuuren et al., 2016). The assessment in SR1.5 was consistent with the AR5: all analysed pathways limiting warming to 1.5°C by 2100 with no or limited overshoot include the use CDR to some extent to neutralize emissions from anthropogenic activities (SR1.5, Chapter 2) (Rickels et al., 2018). Unless affordable and environmentally and socially acceptable CDR becomes feasible and available at scale well before 2050, 1.5°C-consistent pathways will be difficult to realize, especially in overshoot scenarios (SR1.5, Chapter 4). The required scale of removal by CDR can vary from couple of $GtCO_2$ per year from 2050 onwards to as much as 20 $GtCO_2$ per year (Waisman et al., 2019). Thus, CDR plays a pivotal role in reducing climate warming in the low emission scenarios.

However, as CDR approaches are inherent in scenarios that limit warming to 1.5 or 2°C (SR1.5), the assessment of climate response to CDR approaches in earth system models is usually performed on high emission scenarios such as RCP8.5 (Keller et al., 2014; González et al., 2018), and these modelling studies typically find limited cooling from CDR as the effectiveness depends on the background emission scenario – the effectiveness of a specified amount of $CO_2$ removal is small for large background $CO_2$ concentrations as $CO_2$ radiative forcing scales with the logarithm of $CO_2$ concentration. As there is little consensus on the climate impacts and atmospheric $CO_2$ reduction efficacy of the different types of proposed CDR (Chapter 5), the Carbon Dioxide Removal Model Intercomparison Project (or CDRMIP) has been recently initiated to explore the potential of impacts, potential and challenges of CDR (Keller et al., 2018). The first results from idealized CDRMIP simulations where $CO_2$ concentrations are specified to increase at 1% per annum and subsequently to decrease at 1% per annum are used to assess the CDR-induced lag in this section and climate "reversibility" in 4.7.2. The CDRMIP result assessed here is also equally applicable to mitigation as the $CO_2$ ramp down could be due to mitigation or CDR or a combination of both.

**[START FIGURE 4.40 HERE]**

**Figure 4.40:** Multi-model simulated response in global and annual mean climate variables against for a ramp up followed by ramp down of $CO_2$. Atmospheric $CO_2$ increases from pre-industrial level at a rate of 1% $yr^{-1}$ to 4×$CO_2$, then decrease at the same rate to pre-industrial level and then remains constant. a) normalized ensemble mean anomaly of key variables as a function of year, including atmospheric $CO_2$, surface air temperature, precipitation, sea level rise, global sea-ice area, Northern Hemisphere sea ice area in September, and Atlantic meridional overturning circulation (AMOC); b) surface air temperature; c) precipitation; d) Arctic September sea ice area; e) AMOC; f) thermostatic sea level; 5-year running means are shown for all variables except the sea level rise ; In b-f, red lines represent the phase of $CO_2$ ramp up, blue lines represent the phase of $CO_2$ ramp down, brown lines represent the period after $CO_2$ has returned to pre-industrial level, and black lines represent multi-model mean. For all of the segments in b-f, the solid coloured lines are CMIP6 models and the dashed lines are other models (i.e., EMICs, CMIP5 era models). Vertical dashed lines indicate peak $CO_2$ and when $CO_2$ again reaches pre-industrial value. The number of CMIP6 and non-CMIP6 model results used in each panel is indicated in each panel. The time series for the multi-model means (b-f) and the normalized anomalies (a) is terminated when data from all models are not available in order to avoid the discontinuity in the time series.

**[END FIGURE 4.40 HERE]**

***Lag in climate response to CDR***

Because of the timescales of the carbon cycle and thermal inertia in the climate system, the atmospheric $CO_2$ and the physical climate system response (e.g. changes in temperature and precipitation) are expected to lag behind the deployment of CDR (*high confidence*). Figure 4.40: illustrates the first results from CDRMIP

(Keller et al., 2018) that shows the climate response to idealized CDR deployment in which atmospheric $CO_2$ increases from pre-industrial level at a rate of 1% yr-1 to 4×$CO_2$ and then decrease at the same rate to pre-industrial level. As illustrated in Figure 4.40:, changes in key climate variables, including surface air temperature, precipitation, the sea-ice area, the AMOC, and sea level substantially lag behind the deployment of CDR. In particular, notwithstanding a decline in atmospheric $CO_2$, global mean thermosteric sea level would continue to rise. When atmospheric $CO_2$ returns to pre-industrial level, global sea level is higher than its value at peak $CO_2$ (Figure 4.40:), and it is *likely* that global sea level would not return to pre-industrial levels for over 1000 years after atmospheric $CO_2$ is restored to the pre-industrial concentration (Tokarska and Zickfeld, 2015; Ehlert and Zickfeld, 2018). Therefore, sea level rise will not be reversed by CDR on human timescales and land that is lost to sea level rise will not be retrieved (*high confidence*). In the case of AMOC, there is uncertainty: a comparison of different global models show agreement (weakening) during the ramp up phase of $CO_2$, but the results are model dependent during the ramp down phase (Sgubin et al., 2015) – continued weakening in some models, strengthening, but not reaching the initial state in some, and strengthening with a overshoot in others.

Global mean precipitation would increase initially in response to an abrupt $CO_2$ reduction (Cao et al., 2015b). This is related to the fast adjustments (directly related to radiative forcing changes) in the climate system (Chapter 7) before global mean surface temperature increases substantially. Several studies (Bala et al., 2010; Cao et al., 2012; Richardson et al., 2016; Myhre et al., 2018a) have shown that when $CO_2$ in the atmosphere is abruptly increased, global mean precipitation is initially reduced before it starts to increase in response to global mean surface temperature increase. Hence, an initial increase in precipitation is simulated for a CDR-related decline in $CO_2$.

The relationship between cumulative carbon emissions and surface temperature change becomes nonlinear during periods of net negative emissions owing to the delayed response of the deep ocean to previously increasing $CO_2$ (Zickfeld et al., 2016). When corrected for this lagged response, or if the $CO_2$ decline is applied after the system has equilibrated with the previous $CO_2$ increase, the relationship between temperature change and cumulative carbon emissions is again close to linear during periods of net negative $CO_2$ emissions. The transient climate response to cumulative carbon emissions (TCRE, Chapter 5) is found to be larger when $CO_2$ is ramped up than on the downward $CO_2$ trajectory in simulations with a symmetric 1% per year increase and decrease in atmospheric $CO_2$ (Zickfeld et al., 2016). The cooling effectiveness of negative $CO_2$ emissions is also found to be less if applied at higher $CO_2$ concentration because of the logarithmic dependence of radiative forcing on $CO_2$ concentration (Chapter 7).

***CDR cooling potential and side effects***

As discussed earlier, the potential of CDR to mitigate anthropogenic warming would depend on the background $CO_2$ emission scenario and the strength of mitigation prior to CDR deployment. Higher near-term mitigation decreases the need for larger CDR deployment (Waisman et al., 2019). The role that CDR will play in high emission scenarios is *very likely* to be limited. Even when applied continuously and at scales as large as currently deemed possible, under a high $CO_2$ emission scenario (e.g. RCP 8.5), the widely discussed CDR options such as afforestation, ocean iron fertilization and surface ocean alkalinisation are individually either expected to be relatively ineffective, with limited (8%) warming reductions relative to a scenario with no CDR option, or they have potential side effects (Keller et al., 2014) (*medium confidence*). The biogeophysical effect of local warming and availability of land in the case of afforestation, acidification in fertilized region in the case of ocean iron fertilization, and mining and the related impacts on terrestrial ecosystems in the case ocean alkalisation are some of the side effects. The challenges involved in comparing the effects of various CDR options has been also recognized in recent studies (Sonntag, 2018; Mengis et al., 2019). For instance, due to compensating processes such as biogeophysical effects of afforestation (warming from albedo decrease when forests are converted to cropland) more carbon is expected to be removed from the atmosphere by afforestation than by ocean alkalinisation to reach the same reduction in global mean temperature.

***Climate response to termination of CDR***

The literature on the termination effects of CDR is limited and assessments of CDR termination have mostly

considered scenarios where CDR implementation does not result in net negative emissions (Keller et al., 2014; González et al., 2018). The climate effect of CDR termination is *likely* to be dependent on the background $CO_2$ emission scenarios. With higher ongoing emissions when termination occurs, warming trend after termination is *likely* to be higher. In simulations where CDR is applied at scales as large as currently deemed possible, the increase in global mean warming rates following termination are too small when CDR is terminated (Keller et al., 2014). González et al. (2018) simulated an ocean alkalinisation scenario that stabilizes atmospheric $CO_2$ at RCP 4.5 levels under RCP 8.5 emissions. A termination of this large-scale CDR application could cause some regions to warm at a rate similar to those caused by termination of SRM.

#### *4.6.3.3 Climate Response to Solar Radiation Modification*

***Introduction***

SRM refers to the intentional modification of the Earth's shortwave radiative budget with the aim of reducing GHG-induced warming (AR5, SR1.5, Glossary) (Caldeira et al., 2013). A ~2% decrease in net solar radiation budget at the top of the atmosphere would be sufficient to offset all of the warming from a doubling of $CO_2$ (Royal Society, 2009). Several SRM options, their efficacy, uncertainties related to our current understanding of SRM climate processes, side effects such as reduction in global precipitation and depletion of stratospheric ozone and associated potential risks such as abrupt termination were discussed in Chapter 7 of AR5. A short summary that updates a subset of the SRM options whose climate response have been studied using climate models is listed in Table 4.7:. All approaches, except for cirrus cloud thinning, aim to cool the Earth by deflecting more solar radiation to space. Cirrus cloud thinning aims to cool the planet through increasing the longwave emission to space, which could be achieved by reducing the amount of high clouds in the climate system (Mitchell and Finnegan, 2009; Storelvmo et al., 2014). However, as in SR1.5, the terminology of SRM is used in this report to refer to all direct interventions on the planetary radiation budget, including both shortwave and longwave modification. Potential tropospheric and surface-based approaches such as injection of sulphate aerosols into the troposphere and surface albedo enhancements for moderating regional warming have been also suggested (MacCracken, 2016; Field et al., 2018).

**[START TABLE 4.7 HERE]**

**Table 4.7:** A brief summary of the various SRM approaches

| SRM scheme | Proposed mechanism of the SRM approach | Potential for countering a warming from a doubling of $CO_2$ (RF=3.5 W $m^{-2}$) | Key side effects | References |
|---|---|---|---|---|
| Stratospheric Aerosol Injection (SAI) | Injection of aerosols or their precursors into the stratosphere which scatter sunlight back to space; sulphates, calcium carbonate or tin oxide have been proposed; radiative forcing could be nearly uniform for a global implementation; large uncertainties in efficiency (cooling per unit injected mass of aerosols) associated with aerosol microphysics, radiative properties, injection location and transport | Achievable with 20-25 Mt S per year injection (equivalent to ~3-4 Mt. Pinatubo eruptions each year). The exact amount would depend on the latitude, altitude, and season of injection | Decrease in direct and increase in diffuse sunlight at the surface; Changes to stratospheric chemistry; potential delay in ozone hole recovery and increase in surface UV radiation; potential decrease in crop yields; potential disruption to monsoon rainfall; | (Pitari et al., 2014; Niemeier and Timmreck, 2015; Ferraro and Griffiths, 2016) (Tilmes et al., 2017) (Tilmes et al., 2018a) (World Meteorological Organization, 2018) (Proctor et al., 2018) |
| Marine cloud | Injection of sea salt aerosols to | Achievable if | Large changes to | (Latham et al., |

| | | | | |
|---|---|---|---|---|
| brightening (MCB) | increase the albedo of marine stratocumulus clouds; heterogeneous radiative forcing; effectiveness is ambiguous; large uncertainties associated with aerosol–cloud-radiation interactions. | nearly 75 % of ocean area is seeded but there are large uncertainties in the magnitude of the responses. | local circulations; Uncertain regional changes in precipitation patterns; sea salt deposition on land | 2012; Stjern et al., 2018) |
| Whitening the roofs | Painting the roof of buildings to increase the reflectivity; heterogeneous radiative forcing | Not achievable; max potential RF about -0.1 W $m^{-2}$ | Potential changes to urban climate | (Seneviratne et al., 2018a) |
| Lightening the colour of the crops | Genetically modify the colour of crops to increase sunlight reflection; heterogeneous radiative forcing | Not achievable; max potential RF about -0.5 W $m^{-2}$ | Uncertain changes to regional precipitation, photosynthetic activity, carbon uptake and biodiversity | (Seneviratne et al., 2018a) |
| Ocean albedo increase | Add reflecting particles on the ocean surface or create microbubbles by stirring the ocean surface; heterogeneous radiative forcing; land-sea radiative forcing contrast | RF of several $Wm^{-2}$ is achievable | Effect on ocean circulation and biology; regional hydrological cycle change | (Kravitz et al., 2013b; Gabriel et al., 2017) (Cvijanovic et al., 2015) (Mengis et al., 2016) (Kravitz et al., 2018) |
| Cirrus cloud thinning (CCT) | Inject ice nuclei in the upper troposphere to reduce the amount of cirrus clouds to allow more longwave radiation to escape to space; heterogeneous radiative forcing; large uncertainties in feasibility because of lack of understanding of cirrus cloud formation processes, as well as ice microphysical processes | Uncertain | Changes in regional hydrological cycle | (Storelvmo et al., 2014; Gasparini and Lohmann, 2016) (Jackson et al., 2016b) |
| Space sunshades | Place mirrors or reflecting particles in space between sun and earth to reflect sunlight back to space; nearly uniform radiative forcing | Blocking of about 2 % of the incoming solar radiation | Decrease in sunlight for photosynthesis. Less intense global hydrological cycle | (Kravitz et al., 2013a; Kalidindi et al., 2015) |

**[END TABLE 4.7 HERE]**

***Assessment of SRM in AR5***

The main assessment in the AR5 on the climate system response to SRM is that the compensation between GHG warming and SRM cooling would be imprecise (*high confidence*). SRM would not produce a future climate identical to the present (or pre-industrial) climate. However, a climate with SRM and high atmospheric GHG levels would be closer to that of the unperturbed climate than a world with elevated GHG concentrations and no SRM. There are large uncertainties in understanding of SRM-related climate processes. There is *high confidence* that the millennial timescale for the lifetime of $CO_2$ in the atmosphere (Chapter 5) will necessitate a long-term deployment of SRM if it is used in the absence of mitigation (Section 4.6.3.1) and CDR (Section 4.6.3.2) to offset climate change. There is also *high confidence* that SRM will not mitigate the problem of ocean acidification associated with increasing atmospheric $CO_2$ concentration. A sudden termination of SRM would cause a rapid increase in surface temperatures (within a decade or two) to values that are consistent with the high GHG forcing (*high confidence*).

***Assessment of SRM in SR1.5***

At the time of the AR5, SRM modelling research was in its infancy, and the assessment was mainly based on highly idealized simulations that used solar constant reductions. Since then, several modelling studies have

examined the climate response to less idealized SRM options, such as stratospheric aerosol injection (SAI) (Tilmes et al., 2018b), marine cloud brightening (MCB) (Stjern et al., 2018b) and cirrus cloud thinning (CCT) (Gasparini et al., 2017). SRM-specific impacts on climate variables and human natural ecosystems for the SRM options, SAI, MCB, CCT and ground-based albedo modification (GBAM), their governance, institutional and technological challenges and economic feasibility, ethics and social acceptability were assessed in SR1.5. SRM was primarily assessed in terms of its potential to limit warming below 1.5°C in temporary overshoot scenarios as a way to reduce elevated temperatures. The overall assessment was that the combined uncertainties surrounding the various SRM approaches, including technological maturity, physical understanding, potential impacts, challenges of governance, legality, and potential impacts on sustainable development could render SRM economically, socially and institutionally undesirable. Against this background, the existing literature only supports SRM as a supplement to deep mitigation, for example in overshoot scenarios to limit global warming below specific thresholds such as 1.5°C warming (SR1.5) (Tilmes et al., 2016; MacMartin et al., 2018). SRM was discussed in the context of short-term action to complement strong concurrent emissions reductions and aid staying below short-term global temperature levels (Keith and MacMartin, 2015; Sugiyama et al., 2018) such as limiting warming to 1.5°C using an 'adaptive SRM' approach (SR1.5) where SRM implementation could span only a few decades to hold warming to 1.5°C (Keith and MacMartin, 2015; MacMartin et al., 2018).

***Scope of SRM assessment in AR6***

This subsection assesses the global and large-scale physical climate system response to widely-studied SRM approaches. Chapter 5 assesses the biogeochemical implications of SRM and Chapter 8 assesses the abrupt water cycle changes in response to initiation or termination of SRM. The risks, governance and ethics associated with SRM are assessed in Chapter 14 of the WG3 Report.

Since the AR5, more climate modelling studies have assessed the climate response to different SRM options, including those in the Geoengineering Model Intercomparison Project (GeoMIP (Kravitz et al., 2011) (Kravitz et al., 2015)), which started at the time of the AR5 (Kravitz et al., 2013a). Data from the second phase of GeoMIP (Kravitz et al., 2015), as part of CMIP6, is becoming available at the time writing this report. However, results from the analysis of GeoMIP6 data are limited and the assessment on climate response to SRM here is derived mostly from GeoMIP literature and several other studies which have used single models. The most-studied SRM approach using climate models since the AR5 is the SAI, which is simulated by a variety of models with different complexities of SAI representation. Other aerosol-based SRM approaches such as MCB and CCT have also been widely studied, but less extensively compared to SAI. New findings in these three relatively well-studied aerosol-based approaches since the AR5 are assessed here. The feasibility of meeting multiple temperature and precipitation goals by intentionally designing targeted geoengineering approaches and the detection of climate response to SRM deployment are also assessed.

***Efficacy of SRM forcings***

There is *high confidence* that the SRM required to offset a $CO_2$-induced global mean temperature increase is larger than the $CO_2$-induced radiative forcing (Schmidt et al., 2012; Russotto and Ackerman, 2018). This is because the efficacy of solar forcing is less than one (~0.8) (Modak et al., 2016) (meaning that the global mean warming is less than that due to an equivalent CO2 effective radiative forcing ) (See Chapter 7). This has been explained on the basis of differing vertical profile of radiative forcing (Modak et al., 2016) and photochemically induced stratospheric ozone changes that modulate surface solar radiation (G. Chiodo, 2016). The efficacy of stratospheric sulphate aerosol forcing has also been shown to be less than one, but the efficacy is larger than one for CCT, and is close to one for MCB (Duan et al., 2018; Krishna-Pillai Sukumara-Pillai et al., 2019) (*medium confidence*). The difference in efficacy can be attributed to different base climate states established after fast adjustment (Modak et al., 2018b) and to different spatial patterns of change in sea surface temperature during slow feedback (Rugenstein et al., 2016; Andrews and Webb, 2018).

***Climate Response to SRM***

As assessed in the AR5, one of the key features of SRM is that it has the potential to cool the planet rapidly; in highly idealised scenarios that abruptly introduce SRM the cooling occurs with an e-folding time of only ~5 years (Matthews and Caldeira, 2007). A more realistic approach would be a slow ramp up of SRM to offset further warming (MacCracken, 2016). Idealized modelling studies have also consistently shown that SRM has the potential to markedly and rapidly diminish the effect of increasing GHG on global and regional climate (Irvine et al., 2016; Kravitz et al., 2017b). However, there could be substantial residual climate change at the regional scale (*high confidence*) (Kravitz et al., 2014); it is *virtually certain* that none of the SRM approaches are able to completely reverse GHG-induced anthropogenic climate change at global and regional scales. There are also large uncertainties in important SRM-related climate processes such as aerosol microphysics and aerosol-cloud-radiation interaction and hence the level of understanding is low. These uncertainties also affect climate change projections. Different SRM options can produce the same amount of global mean cooling, but with substantially different responses in the spatial pattern of temperature and precipitation. The spatial patterns of temperature and precipitation change relative to the corresponding high-$CO_2$ world for highly idealized scenarios of space sunshading, stratospheric aerosol injection, and marine cloud brightening are shown in (Figure 4.41:). By design, each SRM approach is able to offset the same amount of $CO_2$-induced global mean warming, but with differences in spatial pattern of temperature and precipitation change, which is also different from that of unperturbed, low-$CO_2$ world (Figure 4.41:). Also, the patterns of climate response would depend on the design choice used for SRM (*high confidence*) (MacMartin and Kravitz, 2019).

**[START FIGURE 4.41 HERE]**

**Figure 4.41:** Multi-model response per degree global mean cooling in temperature (left) and precipitation (right). Top row shows the response to a $CO_2$ decrease, calculated as the difference between piControl and abrupt4x$CO_2$ (11 model average); second row shows the response to a solar reduction, calculated as the difference between GeoMIP experiment G1 and abrupt4x$CO_2$ (11 model average); third row shows the response to stratospheric sulphate aerosol injection, calculated as the difference between GeoMIP experiment G4 and RCP4.5 (6 model average); and bottom row shows the response to marine cloud brightening, calculated as the difference between GeoMIP experiment G4cdnc and RCP4.5 (8 model average). All differences (average of years 11-50 of simulation) are normalized by the global mean cooling in each scenario, averaged over years 11-50. Stippling in the right panels shows regions where 75% of the models agree on the sign of the precipitation response. The values of correlation represent the spatial correlation of each SRM-induced temperature and precipitation change pattern with that of low-$CO_2$ induced change pattern (top row). RMS (root mean square) is calculated based on the fields shown in the maps (normalized by global mean cooling).

**[END FIGURE 4.41 HERE]**

There is *high confidence* that there is a trade-off between reversing temperature and precipitation change through SRM (Kravitz et al., 2013a; Irvine et al., 2016; Muri et al., 2018a), because precipitation change responds differently to GHG and SRM ERFs (Andrews et al., 2009; Bala et al., 2010; Jackson et al., 2016b; Duan et al., 2018). If SRM was used to fully offset GHG-induced global mean warming, this would over-compensate the GHG-induced increase in global mean precipitation (Irvine et al., 2016) and cause a substantial reduction in rainfall in the tropical monsoonal regions (Robock et al., 2008; Tilmes et al., 2013). Furthermore, regional SRM approaches such as aerosol injections into the Arctic stratosphere are expected to have a remote influence on tropical monsoon precipitation by shifting the mean position of the ITCZ (Nalam et al., 2018). This shift can be counteracted by simultaneously cooling the Southern Hemisphere (MacCracken et al., 2013; Kravitz et al., 2016; Nalam et al., 2018). The large-scale response of precipitation minus evaporation (P-E), which is more relevant to freshwater availability, is found to be smaller than that of precipitation because of reduction in both precipitation and evaporation (Tilmes et al., 2013; Nalam et al., 2018; Irvine et al., 2019). $CO_2$-induced changes in extremes in temperature and precipitation and tropical cyclone intensity are also *likely* to be reduced by SRM (Curry et al., 2014; Aswathy et al., 2015; Muthyala et al., 2018b, 2018a; Irvine et al., 2019).

Idealized model simulations suggest that by offsetting GHG-induced global mean warming, reduced solar irradiance could return Arctic sea ice to pre-industrial or present-day levels (Moore et al., 2014; Tilmes et al., 2014). In a scenario where aerosol injection is used to limit radiative forcing at year 2020 levels, September sea ice extent still decreases from 2020 to 2070, because of the high-latitude residual warming, but not as quickly as in the simulation without SRM (Berdahl et al., 2014). If aerosol injection is used to stabilize global mean temperature at 1.5°C above pre-industrial levels, Arctic sea ice loss is also stabilized (Jones et al., 2018). It has been found that SRM could stabilize the strength of AMOC under high-$CO_2$ scenarios over timescales from a few decades to thousands of years (Cao et al., 2016; Hong et al., 2017). However, the AMOC response to SRM is highly uncertain, and residual changes can be substantial. For instance, if SAI is used to simultaneously stabilize global mean temperature, the equator-to-pole temperature gradient, and the interhemispheric temperature gradient, the hydrological responses over the North Atlantic Ocean would lead to an acceleration of the AMOC and to continued warming of the deep and polar oceans, particularly in the vicinity of southern Greenland (Fasullo et al., 2018).

Typically, modelling studies have used SRM to offset all of $CO_2$ -induced warming. It is found that by offsetting only half of the GHG-induced global warming, relative to an assumed high-GHG world, most regions would experience less extreme temperature, precipitation, water availability shortages, and tropical cyclone intensity (*low confidence*) (Irvine et al., 2019).

***Stratospheric aerosol injection (SAI)***

One of the most-studied SRM approaches to offset climate warming is SAI (Table 4.7:), which is expected to have several side effects such as reduction of stratospheric ozone and disruption to monsoon rainfall. The natural analogue for SAI is major volcanic eruptions (Chapter 1) such as Mt. Pinatubo of 1991, which injected about 20 Tg $SO_2$ into the stratosphere (Bluth et al., 1992; Niemeier and Timmreck, 2015) and caused a global mean cooling of about 0.5°C in 1992 (Soden et al., 2002). While volcanic eruptions are not perfect analogues for SAI (Robock et al., 2013; Plazzotta et al., 2018; Duan, 2019), studies on the local/regional impacts of past volcanic eruptions can inform on the potential impact of stratospheric aerosol injection. Emergent constraints (see Chapter 1 and 5) that relate the climate system response to volcanic eruptions and SAI can be used to constrain the land surface temperature response to SAI, and a recent study shows that CMIP5 models overestimate the land surface warming per unit change in surface solar radiation by ~20% (Plazzotta et al., 2018). The SAI approach involves large uncertainties relating to aerosol microphysics, transport, sedimentation, aerosol radiative properties and cloud responses (Kashimura et al., 2017; Visioni et al., 2017; Krishna-Pillai Sukumara-Pillai et al., 2019). It is *likely* that the efficacy of SAI, expressed as the ratio between sulphate aerosol forcing and injection rate, which is sensitive to the location of injection, decreases with injection rate of $SO_2$ as larger particle concentrations in the background leads to larger size particles and lower efficiency (Niemeier and Timmreck, 2015; Kleinschmitt et al., 2018).

Stratospheric aerosol injections are expected to warm the lower stratosphere because of absorption of near-infrared solar and terrestrial longwave radiation by the aerosols. This aerosol-induced warming is expected to alter the stratospheric ozone and water vapour concentrations, thereby changing stratospheric and tropospheric circulation (Niemeier and Schmidt, 2017; Krishna-Pillai Sukumara-Pillai et al., 2019). For instance, model simulations indicate stronger polar jets and weaker storm tracks and poleward shift of the tropospheric mid-latitude jets in response to stratospheric sulphate injections in the tropics (Ferraro et al., 2015; Richter Jadwiga et al., 2018), as the meridional temperature is increased in the lower stratosphere by the aerosol-induced heating.The aerosol-induced warming would also offset some of the GHG-induced stratospheric cooling (*medium confidence*).

***Marine cloud brightening (MCB)***

SRM approaches such as MCB, which use a highly heterogeneous radiative forcing to cool the climate system, are expected to cause large changes in regional precipitation patterns (Stjern et al., 2018a) (*high confidence*) (Figure 4.41:). Because of the high level of uncertainty associated with cloud processes and cloud radiative responses to aerosol changes, the climate response to MCB is highly uncertain. Recent studies suggest that the direct scattering effect of sea salt aerosol might play an important role in the cooling

potential of MCB through sea spay injection. Regional applications of MCB has been suggested for offsetting severe impacts from tropical cyclones whose genesis is associated warmer sea surface temperatures (MacCracken, 2016). However, such regional approaches also involve large uncertainties in the magnitude of the responses and side effects.

***Cirrus Cloud Thinning (CCT)***

Cirrus clouds trap more outgoing thermal radiation than they reflect incoming solar radiation and thus have an overall warming effect on the climate system (Mitchell and Finnegan, 2009; Gasparini and Lohmann, 2016). Hence, the objective of CCT is to decrease cirrus clouds amount by increasing the heterogeneous nucleation via seeding cirrus clouds with ice nucleating particles, which would cause larger ice crystals and rapid fallout resulting in reduced lifetime and coverage of cirrus clouds (Muri et al., 2014), (Gasparini et al., 2017; Lohmann and Gasparini, 2017; Gruber et al., 2019). The maximum cooling potential of CCT achieved by removing all cirrus clouds is estimated to be about 5 W $m^{-2}$ (Gasparini and Lohmann, 2016). However, for the optimal seeding concentration and globally nonuniform seeding strategy, a net negative cloud forcing of only about 2 W $m^{-2}$ is estimated (Storelvmo et al., 2014). However, a few studies find that no seeding strategy achieves a significant cooling effect due to complex microphysical mechanisms limiting the climate responses (Penner et al., 2015; Gasparini and Lohmann, 2016). A higher than optimal concentration of ice nucleating particles could result in over-seeding that could have the deleterious effect of prolonging cirrus lifetime and contributing to global warming (Storelvmo et al., 2013). In contrast to SAI and MCB that acts on shortwave radiation, CCT, by acting on longwave radiation, is *likely* to cause an increase in global precipitation relative to the unperturbed low-$CO_2$ climate state (Jackson et al., 2016b; Muri et al., 2018a). The increase of precipitation in response to CCT is due to enhanced radiative cooling of the troposphere, which is opposite to the effect of increased $CO_2$ concentrations (Kristjánsson et al., 2015). Despite its reduced side effects on the hydrological cycle and the stratospheric Ozone, CCT is associated with large uncertainties related to ice nucleation in cirrus clouds and its representation in climate models (Penner et al., 2015).

***Strategically designed SRM***

Since the AR5, a few modelling studies have designed SRM approaches aiming at influencing surface temperature not only in the global mean. For example, in the Geoengineering Large Ensemble Project (GLENS), by interactively adjusting the rate of sulphate aerosol injection at different latitudes, global mean temperature, the interhemispheric temperature gradient, and the equator-to-pole temperature gradient are maintained at the year-2020 level under the RCP 8.5 scenario (Kravitz et al., 2017a; MacMartin et al., 2017; Tilmes et al., 2018a). Desired meridional radiative forcing profiles can also be achieved by linearly combining sulphate aerosol injections at different latitudes, altitudes, and seasons (Dai et al., 2018). However, large regional and seasonal residual climate change is still found in the GLENS simulations (Fasullo et al., 2018; Cheng et al., 2019; Jiang et al., 2019; Simpson et al., 2019a).

While SAI or MCB forcings cause a decrease in global mean precipitation when fully offsetting $CO_2$-induced warming, CCT, which causes cooling by increasing longwave radiation to space, is *likely* to increase the precipitation (Kristjánsson et al., 2015; Cao et al., 2017; Muri et al., 2018b). Recent modelling work suggested that changes in global mean temperature and precipitation can be simultaneously offset by combining stratospheric aerosol injection and cirrus cloud thinning (Cao et al., 2017). However, there is *low confidence* in the applicability of this result to the real world owing to the large uncertainty in simulating aerosol forcing and the complex cirrus microphysical processes. There are also large uncertainties in the potential of CCT to cool the climate system (Gasparini and Lohmann, 2016). The interaction and potential side effects of combining different SRM approaches to cool the Earth is also largely unknown.

***Detectability of climate response to SRM***

Internal variability could mask the forcing-related change in the near term (see section 4.6.3.1). Hence, a full test of the climate system response to SRM will *very likely* require a SRM forcing of the size produced by the 1991 Mount Pinatubo eruption which produced global mean cooling of about 0.5 K (Robock et al.,

2010). The effect of SRM on global temperature and precipitation has been found to be detectable after one to two decades (Bürger and Cubasch, 2015b; Lo et al., 2016) which is similar to the timescale for the detection of mitigation effects (Section 4.6.3.1). An analysis using GLENS simulation (MacMartin et al., 2019) shows that for many regions the differences in temperature, precipitation change and precipitation minus evaporation at grid-scale between a climate state with GHG-induced 1.5° C global mean temperature change and another climate state with the same global mean temperature under RCP4.5 emissions and a limited deployment of SRM are not detectable by the end of this century. However, for higher emissions scenarios (the RCP8.5 scenario) and correspondingly larger SRM deployment for maintaining the same global mean temperature change of 1.5°C, the regional differences are detectable readily before the end of the century.

***Climate response to termination of SRM***

As assessed in AR5, a hypothetical, sudden and sustained termination of SRM would cause a rapid increase in global temperature, precipitation and sea level rise, and rapid reduction in sea ice area and Atlantic meridional overturning circulation (Matthews and Caldeira, 2007; Robock et al., 2008; Jones et al., 2013; McCusker et al., 2014; Crook et al., 2015; Muri et al., 2018a) (*high confidence*). The warming rates would be especially larger for an SRM implementation in a world with large emissions for a substantial period (McCusker et al., 2014). This is because the sudden removal of large SRM-induced negative radiative forcing subjects the climate system to a high GHG forcing scenario, causing larger rates of warming for several years following termination. Sudden and sustained termination of SRM would increase both land and ocean temperature and precipitation at a rate that far exceeds (> an order of magnitude) that predicted for future climate change without SRM (McCusker et al., 2014; Crook et al., 2015). Average 5-year summer precipitation trends on land is negative indicating general drying that would exacerbate the effects of rapid warming (McCusker et al., 2014). A gradual phase-out of SRM combined with mitigation and CDR is *likely* to avoid the large warming rates from sudden SRM termination (Keith and MacMartin, 2015; Tilmes et al., 2016) and simple policies could prevent SRM termination (Parker and Irvine, 2018). As discussed earlier, all conclusions in the literature have been drawn from highly idealized scenarios and hence there are large uncertainties surrounding SRM deployment and termination. The large warming rates due to the sudden and sustained termination effect in a high-$CO_2$ world is *likely* to increase land and ocean temperature velocities to unprecedented speed and pose great threats to biodiversity (Trisos et al., 2018). A sudden and sustained termination of SRM also weaken carbon sinks, accelerating atmospheric $CO_2$ accumulation and warming (Matthews and Caldeira, 2007; Tjiputra et al., 2016).

## 4.7 Climate Change Beyond 2100

This section assesses changes in climate beyond 2100. An advance since AR5 is the availability of Earth system model results for scenarios beyond 2100 and for much longer stabilisation simulations compared with analysis predominantly on Earth system models of intermediate complexity (EMICs) at the time of AR5 (e.g. Eby et al., 2013; Zickfeld et al., 2013). However, because of the long timescales required for performing simulations, this section will also draw on EMICs as fewer simulations by fully complex GCMs and ESMs have been performed.

On multi-century timescales it is common to explore changes that are due to some long-term commitment. Here we differentiate between:

- Committed emissions due to infrastructure. Even in the presence of climate policy, infrastructure that causes greenhouse gas emissions cannot be changed straight away. There is therefore a commitment from existing infrastructure that some emissions will continue for a number of years into the future (Davis and Socolow, 2014; Smith et al., 2019a). Shindell and Smith (2019) show that this limits the sudden warming from aerosol reduction that has been postulated in the event of a cessation of anthropogenic emissions. Further consideration of this aspect of commitment will be assessed by WG3.
- Climate response to constant emissions. Some of the scenario extensions beyond 2100 make assumptions about constant emissions (either positive or negative). Section 4.7.1 will assess changes

in climate under scenario extensions beyond 2100.

- Committed climate change to constant composition. There is widespread literature on how the climate continues to change after stabilisation of radiative forcing. This includes diagnosing the long-term climate response (equilibrium climate sensitivity) to a doubling of $CO_2$. Since the AR5 more GCMs have run stabilised forcing simulations for many centuries allowing new insights into their very long-term behaviour. Section 4.7.2 will assess GSAT response to constant composition and committed changes to various components (e.g. ice sheets, AMOC) given a constant forcing.
- Committed response to zero emissions. How much climate change has our past activity committed us? There is a need to know how climate would continue to evolve if all emissions ceased. SR15 assessed changes in climate if emissions of all greenhouse gases and aerosols ceased. Section 4.7.2 assesses new results considering cessation of $CO_2$-only emissions which forms a significant term in calculating remaining carbon budgets.
- Irreversibility. Some changes do not revert if the forcing is removed, leaving a committed change to the system. Section 4.7.2 will assess changes in the Earth system which may be irreversible.
- Abrupt changes. If a tipping point in the climate system is passed, then some elements may continue to respond if the forcing which caused them is removed. Section 4.7.3 will assess the potential for abrupt changes in the Earth system.

### *4.7.1 Change in Global Climate Indices Beyond 2100*

This subsection assesses changes in global climate indices out to 2300 using extensions of the RCP scenarios. Although scenarios of climate forcing exist beyond 2100, the long timescales mean they are less based on attempts at realistic socio-economic storylines and make more simplifying assumptions about future changes in climate forcing. Results will be drawn from CMIP5 extension scenarios to 2300 and beyond (ECPs, Meinshausen et al., 2011). Newer CMIP6 simulations from SSP extensions (Meinshausen et al., 2019b) are not yet widely available.

Meinshausen et al. (2011) describe the extensions to the RCP scenarios. These involved a mix of constant emissions, constant concentration or simplified changes to emissions:

- ECP2.6: constant (negative) emissions after 2100, which result in $CO_2$ reducing to approximately 370ppm (approximately 1.5 $Wm^{-2}$) by 2300.
- ECP4.5/ECP6.0: constant concentration of greenhouse gases, although the pathway is smoothed to avoid a discontinuity at 2100, so concentrations become constant after 2150.
- ECP8.5: constant emissions during the period 2100–2150, followed by a linear reduction during 2150-2250, and then constant concentration thereafter. This scenario reaches almost 2000ppm (approx. 12 $Wm^{-2}$) and corresponds to approximately 5000 PgC cumulative $CO_2$ emissions. Most analyses of ESM extensions beyond 2100 have focussed on this scenario.

Changes in climate at 2300 have impacts and commitments beyond this timeframe. Randerson et al. (2015) showed increasing importance on carbon cycle feedbacks of slow ocean processes, Mahowald et al. (2017) showed the long-lasting legacy of land-use effects and Moore et al. (2018) show how changes in Southern Ocean winds affect nutrients and marine productivity well beyond 2300. Clark et al. (2016) show that physical and biogeochemical impacts of 21st century emissions have a potential committed legacy of at least 10,000 years.

**[START FIGURE 4.42 HERE]**

**Figure 4.42:** Simulated climate changes up to 2300 from the CMIP5 multi-model ensemble under the four RCP scenarios. (a) projected GSAT change (b) global land precipitation change (c) September Arctic sea-ice extent (millions square km) (d) thermal steric sea level rise. Coloured numbers denote the number of models included in each panel for each scenario. Models used: CanESM2, bcc-csm1-1, GISS-E2-R, GISS-E2-H, IPSL-CM5A-LR, IPSL-CM5A-MR, CNRM-CM5 MPI-ESM-LR, CESM1-CAM5, CCSM4, CSIRO-Mk3-6-0, HadGEM2-ES, MIROC5, MIROC-ESM.

**[END FIGURE 4.42 HERE]**

#### *4.7.1.1 Global Surface Air Temperature*

It is *very likely* that GSAT will exceed 1.5°C–2°C above that of the period 1850–1900 at the year of 2300 in all extended RCP scenarios except for the RCP2.6 (*high confidence*; Figure 4.42:). Caesar et al., (2013) showed for the HadGEM2-ES model that under the extended RCP2.6, where $CO_2$ concentration and radiative forcing continue to decline beyond 2100, GSAT stabilised during the 21st century before decreasing and remaining below 2°C until 2300. This is also reflected in the multi-model ensemble where the mean projection under the RCP2.6 peaks at 1.85°C relative to preindustrial and returns to 1.5°C by 2300. The high-emission scenario RCP8.5 shows continuous increase in GSAT, with a multi-model ensemble-mean of 9.8°C temperature rise relative to preindustrial and a range of 5.7°C–14.2°C at 2300. Under the high RCP8.5 scenario, regional temperature changes above 20 degrees have been reported in multiple models over high latitude land areas (Caesar et al., 2013; Randerson et al., 2015). Randerson et al., (2015) found that 1.6 degrees of warming by 2300 came from non-$CO_2$ forcing alone in RCP8.5.

Compared with EMIC results from Zickfeld et al. (2013) ESMs tend to show higher warming by 2300 although this is for a small set of models so not necessarily a systematic difference between these classes of model. Tokarska et al. (2016) examined 4 ESMs and 7 EMICs and also found greater warming in the ESMs. Tokarska et al. (2016) also showed ESMs maintain a more closely linear relationship (TCRE) between cumulative carbon emissions and warming up to approximately 5000 PgC implying that the concept of carbon budgets was applicable over a greater temperature range than previously thought.

#### *4.7.1.2 Global Land Precipitation*

Caesar et al. (2013) showed that under the CMIP5 extension simulations, HadGEM2-ES projected global land precipitation to remain roughly the same in RCP2.6, to increase by about 4% in RCP4.5 and to increase by about 7% in RCP8.5. Precipitation changes over land showed larger variability and a less clear signal than global total precipitation. Their results showed global precipitation increasing linearly with temperature while radiative forcing increases, but then more quickly if forcing is stabilised or reduced. This backs up findings of (Wu et al., 2010) that accumulation of ocean heat leads to an intensification of the hydrological cycle after stabilisation. Figure 4.42: shows that global land precipitation increases in the ensemble mean for all scenarios up to 2300.

#### *4.7.1.3 Arctic Sea Ice*

It was shown that under the CMIP5 extension simulations, most models minimum (September) Arctic sea ice extent began to recover under RCP2.6 out to 2300, while RCP4.5 and RCP8.5 extensions became ice free in September (Hezel et al., 2014). They also found that under the RCP8.5 extension, the Arctic became ice-free nearly year-round by 2300. Figure 4.42: shows partial sea ice recovery by 2300 in RCP2.6 in line with GSAT and continued decline in the other scenarios with RCP6.0 as well as RCP8.5 becoming ice-free in September.

#### *4.7.1.4 Global Mean Sea Level*

The AR5 and the SROCC assessed long-term GMSL. By using CMIP5 models out to 2100 and a model emulator out to 2300 to estimate the steric GMSL due to warming, it was found that even under the RCP2.6 extension, GMSL continued to rise out to 2300 (Palmer et al., 2018). Under the RCP4.5 extension, the steric component of GMSL rose from approximately 0.2 m at 2100 to 0.3–0.7 m by 2300. Under the RCP8.5 extension, the steric component of GMSL rose from approximately 0.3 m at 2100 to 0.8–1.6 m by 2300. Using CMIP5 ESM projections, Figure 4.42: shows the steric component of global sea level above that of

the period 1850–1900 of 0.24 m (0.16-0.32); 0.49 m (0.43-0.60) and 1.27 m (1.11-1.35) for RCPs 2.6, 4.5 and 8.5 respectively.

#### *4.7.1.5 Atlantic Meridional Overturning Circulation*

The AR5 assessed a small number of CMIP5 model simulations of the AMOC beyond 2100 and assessed that once radiative forcing is stabilized, the AMOC begins to recover, but in some models towards less than its pre-industrial level. This assessment was supported in simulations of EMICs following the same ECPs (Zickfeld et al., 2013). AMOC in the CMIP5 (CMIP6) model simulations following the RCP (SSP) extensions past 2100 generally recovers to less than its pre-industrial level once warming ceases (e.g. Sigmond et al., 2020).

### *4.7.2 Climate-change Commitment and Irreversibility*

#### *4.7.2.1 Climate change under constant forcing*

Equilibrium climate sensitivity (ECS) is defined as the change in GSAT under constant $CO_2$ concentration held at double pre-industrial levels. Because it is not tractable to run complex atmosphere-ocean coupled general circulation models (AOGCMs) to full equilibrium, it is often quantified in shorter century-scale (often 150 years) simulations with results extrapolated to estimate the long-term warming – termed *effective* climate sensitivity (see Chapter 7 Section 7.5.1, and Box 7.1). ECS has been shown to correlate more closely with 21$^{st}$ century warming than transient climate response to steady growth of $CO_2$ concentrations (TCR) (Grose et al., 2018). For the first time, a coordinated collection of millennial length simulations with AOGCMs has been assembled and analysed (LongRunMIP; Rugenstein et al., 2019). Because AOGCMs have more detailed process representation of feedback processes, especially clouds, which are central to climate sensitivity, the LongRunMIP allows new insights into how these feedbacks and adjustments change over long time periods. While patterns of near-surface air temperature appear robust across models, with polar amplification and land-sea contrast declining, but not disappearing over millennia, cloud radiative effects are not consistent in sign between models nor for a single model response to different levels of forcing. This means that caution is required interpreting studies using a single, or small subset, of models to explore very long-term effects. Analysis has shown that very long runs give a best estimate equilibration warming 10-30% higher than extrapolation after 150 years (Rugenstein et al., 2019b). Time varying fast feedbacks become progressively less stabilising first in the tropics and then in mid-latitudes on centennial to millennial timescales.

#### *4.7.2.2 Climate change following zero emissions*

The constant composition commitment is defined as the unrealized warming that results from constant atmospheric greenhouse gas and aerosol concentrations (Meehl et al., 2007), and has been interpreted as meaning that additional 'warming in the pipeline' was the result of past greenhouse gas emissions. However, the constant composition commitment rather results primarily from the future $CO_2$ and other emissions that are required to maintain stable atmospheric concentrations over time (Matthews and Weaver, 2010; Matthews and Solomon, 2013).

The zero emissions commitment (ZEC) is the change in GSAT projected to occur following a subsequent complete cessation of emissions. Assessment of remaining carbon budgets requires an assessment of ZEC as well as of the Transient Climate Response to cumulative carbon Emissions (TCRE). It has been shown that there is an offset of continued warming following cessation of emissions by continued $CO_2$ removal by natural sinks (e.g. Joos et al., 2013; Matthews and Caldeira, 2008; Solomon et al., 2009).

#### *4.7.2.2.1 Global Surface Air Temperature*

Some models continue the warming by up to 0.5°C after emissions cease at 2°C of warming (Frölicher et al., 2014a; Frölicher and Paynter, 2015; Williams et al., 2017), while others simulate little to no additional warming (Nohara et al., 2015). In the recent assessment of ZEC in the SR1.5, the available evidence indicated that past $CO_2$ emissions do not commit to substantial further warming (Allen et al., 2018). A ZEC close to zero was thus applied for the computation of the remaining carbon budget for the SR1.5 (Rogelj et al., 2018b). However, the available literature consisted of simulations from a small number of models using a variety of experimental designs, with some simulations showing a complex evolution of temperature following cessation of emissions (e.g. Frölicher et al., 2014a; Frölicher and Paynter, 2015).

Here we draw on new simulations (Jones et al., 2019a) to provide an assessment of ZEC using multiple ESMs and EMICs (MacDougall et al., submitted). Figure 4.43: shows results from 15 models that simulate the evolution of $CO_2$ and the GSAT response following cessation of emissions after 1000 PgC is emitted following a 1% per year $CO_2$ increase. All simulations show a strong reduction in atmospheric $CO_2$ concentration following cessation of $CO_2$ emissions in agreement with previous studies and basic theory that natural carbon sinks will persist. Therefore, we assess that it is *very likely* that atmospheric $CO_2$ concentrations will decline for decades if $CO_2$ emissions cease. Temperature evolution in the 100 years following cessation of emissions varies strongly by model, with some models showing declining temperature, others having ZEC close to zero, and others showing continued warming following cessation of emissions (Figure 4.43:). The response of GSAT depends on the balance of carbon sinks and ocean heat uptake as analysed in MacDougall et al. (2020). The 20-year average GSAT change 50 years after the cessation of emissions ($ZEC_{50}$) is summarised in Table 4.8:. Values of $ZEC_{50}$ range from -0.36 to 0.29ºC with a model ensemble mean of -0.04ºC and median of 0.01ºC. There is no strong relationship between $ZEC_{50}$ and modelled climate sensitivity (neither ECS nor TCR; MacDougall et al., 2020). We therefore assess *low confidence* in the sign of ZEC on 50-year timescales, but its magnitude is *likely* less than 0.18ºC. Chapter 5 will assess the implications of this for remaining carbon budgets (Chapter 5 Section 5.5.2).

#### *4.7.2.2.2 Global Land Precipitation and Arctic Sea Ice*

Global land precipitation and Arctic Sea Ice changes past 2100 closely mirror temperature changes, with little change in either metric under conditions of temperature stabilization. The global precipitation response may delay the SST response by a few decades depending on severity of the trajectory to ZEC and aerosol interactions (Tsutsui et al., 2007; Cao et al., 2011; Boucher et al., 2012; Wu et al., 2015).

#### *4.7.2.2.3 Global Mean Sea Level*

As discussed in the SR1.5 and SROCC, global mean sea level continues to rise under ZEC and surface temperature stabilization (Caesar et al., 2013; Palter et al., 2018; Sigmond et al., 2020). Moreover, sea level continues to rise even with strong negative emissions (Wigley, 2018).

#### *4.7.2.2.4 North Atlantic Meridional Circulation*

AMOC generally overshoots when emissions are terminated (Wu et al., 2011; Jackson et al., 2014; Sigmond et al., 2020) (see Section 4.3), followed by recovery to less than its pre-industrial level. Averaged over the period from 2400–2600, the strength of AMOC in CanESM5 is indistinguishable between individual realizations following the 1.5°C and 2.0°C global warming stabilization (Sigmond et al., 9999). On the other hand, following 3.0°C global warming stabilization, each individual simulation settles to a level less than any of the 1.5°C and 2.0°C stabilization simulations (Sigmond et al., 9999). These results raise the issue of the detectability of the long-term impact of different emissions scenarios (Marotzke, 2019).

**[START FIGURE 4.43 HERE]**

**Figure 4.43:** Zero Emissions Commitment (evolution of GSAT) (panel a) and change in atmospheric $CO_2$ concentration (panel b) following cessation of emissions under the experiment where 1000 PgC was

emitted following the 1% experiment (A1; Jones et al., 2019). ZEC is the temperature anomaly relative to the estimated temperature at the year of cessation. $ZEC_{50}$ is the 20-year mean GSAT change centred on 50 years after the time of cessation (see Table 4.8:). Multi-model mean shown as thick black line, individual model simulations in grey.

**[END FIGURE 4.43 HERE]**

**[START TABLE 4.8 HERE]**

**Table 4.8:** Temperature anomaly relative to the year emissions cease averaged over a 20-year time window centred about the 50th year following cessation of $CO_2$ emissions ($ZEC_{50}$) for the A1 (1000 PgC 1% experiment; Jones et al., 2019). Seven ESMs (top half) and 8 EMICs (bottom half) performed this simulation.

| MODEL | $ZEC_{50}$ ($^{O}C$) |
|---|---|
| ACCESS-ESM1.5 | 0.01 |
| CANESM5 | -0.13 |
| CNRM-ESM2-1 | 0.06 |
| GFDL-ESM2M | -0.27 |
| MIROC-ES2L | -0.08 |
| MPI-ESM1.2-LR | -0.27 |
| UKESM1-0-LL | 0.28 |
| BERN3D-LPX | 0.01 |
| DCESS1.0 | 0.06 |
| CLIMBER-2 | -0.07 |
| IAPRAS | 0.29 |
| LOVECLIM | -0.21 |
| MESM | 0.01 |
| PLASM-GENIE | -0.36 |
| UVIC ESCM 2.9PF | 0.07 |

**[END TABLE 4.8 HERE]**

### *4.7.2.3 Irreversible climate change*

This report defines a perturbed state of a dynamical system as irreversible on a given timescale (in this context, a century), if the recovery time scale from this state due to natural processes is substantially longer than the time it takes for the system to reach this perturbed state. Understanding of reversibility of climate system components has advanced since the AR5. Some aspects of the physical climate changes induced by GHG warming have been demonstrated to be reversible (Boucher et al., 2012; Tokarska and Zickfeld, 2015). Others such as sea-level rise or terrestrial ecosystems continue to respond on long timescales (Clark et al., 2016; Zickfeld et al., 2017; Pugh et al., 2018). Reversibility has been defined both in terms of the response to $CO_2$ and the response to GSAT. The latter is reversible in models with respect to $CO_2$ with a several year lag. Reversibility with respect to other climate forcers is less commonly examined.

As described in Table 4.9:, reversal of climate indicators in response to decline in forcing in the available literature begins with land surface and air temperature with a lag of several years, followed by ocean surface and land temperature along with sea ice with a lag of a few decades. Precipitation over ocean, North Atlantic and Southern Ocean Meridional Overturning Circulation follow SST with a further lag of a few decades (Sgubin et al., 2014; Sigmond et al., 9999). However, AMOC in some studies experiences overshoot or irreversibility depending on salinity supply from the subtropics (Jackson et al., 2016a) and freshwater forcing by glacier melt (Rahmstorf and Ganopolski, 1999), respectively. Land precipitation changes are inconsistent among models. Ocean heat content experiences long time scales of response while ocean mixed layer depths tend to overshoot as the legacy of deep-ocean warming. Land carbon stores and frozen soil are *likely* reversible with a long lag while loss of permafrost carbon is *likely* irreversible. Upper ocean carbon stores are similarly reversible with a long lag in the upper ocean while changes to deep ocean stores are irreversible

on a centennial time scale. Ice sheet changes are largely irreversible. ENSO responses are variable, but tend to decrease amplitude under warming on millennial timescales (Callahan et al., 9999), and to overshoot towards a more ENSO -like mean state during cooling (Ohba et al., 2014; Luo et al., 2017), particularly in models that experience excessive Equatorial warming (Zheng et al., 2016).

The Carbon Dioxide Removal Model Intercomparison Project (CDR-MIP) (Keller et al., 2018) comprises a set of 1% ramp-down simulations aimed at establishing a multi-model assessment of reversibility of Earth system components. Preliminary results from CDRMIP are presented in Section 4.6.3. Results from the SSP5-3.4-Overshoot scenario and other quantities of climate change at the same $CO_2$ level before and after overshoot are assessed in section 4.6.2.

**[START TABLE 4.9 HERE]**

**Table 4.9:** Synthesis table of components of the climate system which exhibit reversibility.

| quantity | Linearly reversible with lag | Overshoots | Irreversible |
|---|---|---|---|
| Global Land Surface/air Temperature | Follows forcing with few year delay (Held et al., 2010; Boucher et al., 2012) | | |
| Global Ocean Surface/air Temperature | Decades delay (Cao et al., 2011; Boucher et al., 2012) | | |
| Global Mean Surface/Air Temperature | Combination of land and ocean responses (Nakashiki et al., 2006; Tsutsui et al., 2007; Boucher et al., 2012; Zickfeld et al., 2013, 2016; Andrews and Ringer, 2014) | | |
| Sea Ice | Follows SST (Armour et al., 2011; Boucher et al., 2012) | | |
| Global Ocean Precipitation | Decades delay relative to SST (Boucher et al., 2012) | | |
| Global Land Precipitation | Some models (Boucher et al., 2012) *Likely* reversible with lag and undershoot (Wu et al., 2015) | | |
| Global Mean Precipitation | Decades delay relative to SST (Tsutsui et al., 2007; Cao et al., 2011;Boucher et al., 2012;Wu et al., 2015) | | |
| AMOC | In some models (Nakashiki et al., 2006;Sgubin et al., 2014;Palter et al., 2018) | Under salinification of subtropical surface ocean (Wu et al., 2011; Jackson et al., 2014; Sigmond et al., 9999) | Under extreme Greenland ice melt (Rahmstorf and Ganopolski, 1999; Jackson and Wood, 2018) |
| Ocean heat content and sea level rise | | | Long timescale of response (Nakashiki et al., 2006; Tsutsui et al., 2007; Zickfeld et al., 2013, 2016; Ehlert and Zickfeld, 2018) |
| Mixed layer depth | | Increased mixing with interior warming (Nakashiki et al., 2006; John et al., 2015) | |
| El Niño Southern Oscillation | | El Niño-like pattern emerges (Held et al., 2010; Ohba et al., 2014; Luo et al., 2017) | |
| Southern MOC | *Likely* reversible (Ehlert and Zickfeld, 2018) | | |

| | | | |
|---|---|---|---|
| Monsoon | *Likely* reversible with lag and undershoot (Wu et al., 2015) | | |
| Tropical Forest | *Likely* reversible with lag (Jones et al., 2009) | | |
| Boreal Forest | | | |
| Land carbon store | Long lag of soil/vegetation carbon stores (Boucher et al., 2012) | | |
| permafrost | *Likely* reversible soil freezing (Boucher et al., 2012) | | Irreversible loss of decomposed carbon (MacDougall, 2013) |
| Ocean Carbon Store | Long lag in upper ocean (Cao and Caldeira, 2010; Zickfeld et al., 2013, 2016) | | Long timescale of response (Cao and Caldeira, 2010; Zickfeld et al., 2013, 2016) |
| Ocean Biogeochemistry | Upper ocean acidification (Frölicher et al., 2014b) | Surface alkalinity, nitrogen cycle (John et al., 2015) | Deep ocean acidification (Frölicher et al., 2014a) and $O_2$ (Mathesius et al., 2015), silica cycle (John et al., 2015) |
| Ice sheets | | | Irreversible melt (Rahmstorf and Ganopolski, 1999; Ganopolski and Rahmstorf, 2001; Ridley et al., 2010) |

**[END TABLE 4.9 HERE]**

### *4.7.3 Potential for Abrupt Climate Change*

The AR6 adopts the definition of a 'tipping point' (Kopp et al., 2016) as a level of change in system properties beyond which a system reorganizes, often abruptly, and does not return to the initial state even if the drivers of the change are abated. For the climate system, it refers to a critical threshold when global or regional climate changes from one stable state to another stable state. The term abrupt refers to changes that occur faster than the rate of change of forcing (Alley et al., 2003). This definition includes shifts from one equilibrium state to another (tipping points), but also other responses of the climate system to external forcing (see Section 1.2.4.2 in Chapter 1). For example, (Drijfhout et al., 2015) provided an assessment of 13 regional mechanisms of abrupt change, finding abrupt changes in sea ice, oceanic flows, land ice, and terrestrial ecosystem response, although with little consistency among the models. The potential for abrupt changes in ice sheets, the Atlantic meridional overturning circulation (AMOC), tropical forests and ecosystem responses to ocean acidification were also recently reviewed by (Good et al., 2018). They found that some degree of irreversible loss of the West Antarctic Ice Sheet (WAIS) may have already begun, that tropical forests are adversely affected by drought, and rapid development of aragonite undersaturation at high latitudes affecting calcifying organisms.

Abrupt changes in the climate system are assessed across multiple chapters. This section provides a synthesis, in an update to the AR5 Table 12.4. Classic examples of potential abrupt climate changes include AMOC, Greenland and Antarctic ice sheets, permafrost carbon, methane clathrates, tropical and boreal forests, sea ice, and hydrological cycles/monsoon circulations. New since AR5 (Table 4.10:) (e.g., Drijfhout et al., 2015) is the recognition that tropical and boreal forest abrupt responses are fundamentally different, with tropical forest dieback driven by the increased potential for drought (Drijfhout et al., 2015) while boreal forest response includes both thermal and hydrological factors (Drijfhout et al., 2015). The relatively robust abruptness of Southern ocean Meridional Overturning Circulation shutdown has also been recently appreciated (de Lavergne et al., 2014; Ehlert and Zickfeld, 2018).

**[START TABLE 4.10 HERE]**

**Table 4.10:** Summary table of components in the Earth system that have been proposed as susceptible to abrupt or irreversible change.

| Earth System Component | Tipping Point? | Irreversible? | Projected 21st century change | See chapter/section |
|---|---|---|---|---|
| Arctic Sea Ice | Yes | No | *High confidence* in severe summer and moderate winter declines | 9.3.1 |
| Antarctic Sea Ice | Yes | No | *Low confidence* in moderate winter and summer declines | 9.3.2 |
| Snow cover | No | No, for seasonal cover. Possible for permanent cover due to snow albedo feedbacks | *Virtually certain* Northern Hemisphere snow cover extent and duration decrease | 9.5.3<br>See also 8.6.2.3 |
| Permafrost Ice | Yes. Via thermokarst | No | *Virtually certain* near-surface permafrost extent will shrink | 9.5.2 |
| Ice Sheets | No | Yes | *Likely* to continue to lose mass | 9.4.2 |
| Glaciers | Yes | Yes | *High confidence* in substantial global mass loss | 9.5.1 |
| Ocean Heat Content | No | No for upper ocean, yes for deep ocean | *Very high confidence* oceans will continue to warm | 9.2.2 |
| Sea Level Rise | No | Yes | *Very high confidence* sea level will continue to rise | 9.6.3 |
| AMOC | Possible collapse | No | *Very likely* to decrease in strength | 9.2.3.1 |
| Southern MOC | Possible collapse | No | *High confidence* in decrease in strength | 9.2.3.2 |
| Monsoon | No | No | *Likely* poleward extension | |
| El Niño Southern Oscillation | No | El Niño-like pattern emerges (Held et al., 2010)(Ohba et al., 2014)(Luo et al., 2017) | Variable results | |
| Permafrost Carbon | No | Yes | Gradual decline | (Ch 5) |
| Methane Clathrates | Possible $CH_4$ release from clathrates | Yes | *Extremely unlikely* large scale release | 5.4.8.2, 5.4.8.3 |
| Ocean Carbon Sink | No, gradual wind-induced reduction in Southern ocean carbon sink | No for upper ocean, yes for deep ocean | Not yet assessed | 5.4.8.4 |
| Ocean Biogeochemistry | Aragonite undersaturation, hypoxia | No for upper ocean, yes for deep ocean | Polar undersaturation | (Ch 5) |

| | | | | |
|---|---|---|---|---|
| Tropical Forest Dieback | Possible if climate threshold crossed | Postulated via feedbacks on rainfall | Partial loss of Amazon forest | 5.4.8.1 |
| Boreal Forest | Possible if climate threshold crossed | Postulated via feedbacks on temperature, albedo and snow cover | Poleward extension | (Ch 5) |
| Land Carbon | Possible if climate threshold crossed for forest ecosystems | Yes | Soil carbon loss | (Ch 5) |

**[END TABLE 4.10 HERE]**

It has been postulated that ESMs may be prone to being too stable (Valdes, 2011), given palaeo-evidence of abrupt events (Dakos et al., 2008; Klus et al., 2018; Sime et al., 2019). However, the CMIP5 archive did contain evidence of abrupt changes simulated by these models (Drijfhout et al., 2015).

## 4.8 Low-Probability High-Warming Storylines

Previous IPCC assessments have primarily assessed the projected *likely* range of changes (e.g., Collins et al., 2013, see also BOX 1.1). The focus on the *likely* range partly results from the design of model intercomparison projects that are not targeted to systematically assess the upper and lower bounds of projections, which in principle would require a systematic sampling of structural and parametric model uncertainties. The upper and lower bounds of model projections may further be sensitive to the missing representation of processes and to deep uncertainties about the model representation of the climate system (Box 1.1).

However, an integrated risk assessment requires taking into account also high potential levels of warming whose probability is low, but potential impacts on society and ecosystems are high (Xu and Ramanathan, 2017; Sutton, 2018). Risk to human and natural systems results from the interactions of climate-related hazards, with exposure to and vulnerability to those hazards (Chapter 1 Section 1.2.3.2, Cross-chapter Box 1.1). The climate-related risks have been argued to increase with increasing levels of global warming (O'Neill et al., 2017) even if their probability decreases. Thus, it has recently been argued that an assessment that is too narrowly focused on the *likely* range potentially ignores the changes in the physical climate system that are associated with the highest risks (Sutton, 2018).

Given that the CMIP experiments can be considered ensembles of opportunity that are not designed for probabilistic assessments of the tails of the distribution, alternative approaches such as physically plausible high-impact scenario (PPHIS) (Sutton, 2018) or storylines have been suggested (Lenderink et al., 2014; Zappa and Shepherd, 2017; Kjellström et al., 2018; Shepherd et al., 2018) (see Chatper 1 Section 1.4.3). Such storylines can be used for risk assessment and adaptation planning in order to test how well adaptation strategies would cope if the impacts of climate change turned out to be more severe than suggested by the *likely* model range (see Chapter 1 Section 1.4.3). Note that by definition the lower bound of the *likely* model range (see BOX 4.1:) is equally probable, but are not specifically emphasized in this section due to its focus on storylines associated with highest risks. This section further focuses on storylines of high global warming levels along with their manifestation in global patterns of temperature and precipitation changes. However, this does not account for the largest potential changes at regional levels, which would require taking into account storylines of regional changes dependent on changes in atmospheric circulation, land-atmosphere interactions and regional to local feedbacks.

This section adapts an approach suggested in Sutton (2018). Since changes in temperature and precipitation tend to increase with the level of warming in most places (Section 4.6.1), a low-probability high-warming storyline is here illustrated for a level of warming consistent with the upper bound of the assessed *very likely* range (see Section 4.3.4).

The warming consistent with the upper bound of the assessed *very likely* range corresponds to a warming of 4.6°C in 2081–2100 relative 1995–2014 for SSP5-8.5 and 1.4°C for SSP1-2.6, respectively (Section 4.3.4). Figure 4.44: illustrates different lines of evidence of changes in annual mean temperature patterns consistent with this low-probability high-warming storyline next to the multi-model mean (Figure 4.44:, first row). The first estimate (Figure 4.44:, second row) is based on the assumption that the multi-model mean temperature pattern (Figure 4.44:, second row) linearly scales with global mean warming. While linear has been shown to provide an appropriate approximation for changes in temperatures patterns at lower levels of warming (Section 4.2.4), this assumption cannot be easily tested for an extrapolation to higher levels of warming. Thus, a second estimate (Figure 4.44:, third row) is based on the average of the 5 models that simulate a GSAT warming most consistent with the upper bound of the assessed *very likely* range (see BOX 4.1: and Section 4.3.4). The two estimates for the annual mean temperature pattern for a low-probability high-warming storyline are consistent.

Both estimates show a warming pattern that substantially exceeds the multi-model mean warming in all regions for both SSP1-2.6 and SSP5-8.5 scenarios. Even for SSP1-2.6, a high-warming storyline shows 2-3°C warming over much of Eurasia and North America and more than 4°C warming relative to present-day over the Arctic. For SSP5-8.5 a high-warming storyline is associated with wide-spread warming of more than 6°C over most extra-tropical land regions and even over the Amazon. Over large parts of the Arctic annual mean temperatures increase by more than 10°C relative to present-day in such a high-warming storyline.

Individual models (Figure 4.44:, bottom row) project even stronger warming over extratropical land regions, but their projected GSAT warming exceeds the assessed *very likely* 5–95% range and thus correspond to an *extremely unlikely* (<5% probability) storyline. While both models tend to overestimate the observed warming trend over the historical period (Tokarska et al., 9999), they show a good representation of several aspects of the present-day climate (Andrews et al., 2019; Sellar et al., 2019; Swart et al., 2019) that falls within the range of models (chapter 3). While this assessment is limited to temperature and precipitation, such a high-warming storyline would manifest itself also in other climate variables (Sanderson et al., 2011) assessed in this chapter such as Arctic sea ice, atmospheric circulation changes, and sea level rise (Ramanathan and Feng, 2008; Xu and Ramanathan, 2017; Steffen et al., 2018). Storylines of high changes in sea level rise may substantially exceed the range shown in Figure 4.1: (see Chapter 9 Box 9.3).

**[START FIGURE 4.44 HERE]**

**Figure 4.44:** Changes in annual mean temperature in 2081–2100 relative to 1995–2014 in (left) SSP1-2.6 and (right) SSP5-8.5. (a,b) Multi-model mean changes consistent as in section 4.5.1. (c-h) Estimates for annual mean warming pattern consistent with a storyline representing a physically plausible high-global-warming storyline for 2081–2100. (c,d) Pattern-scaled multi-model mean warming to the GSAT of the upper bound of the assessed *very likely* range (scaled from CMIP6 multi-model mean of 3.9°C for SSP5-8.5 and 1.1°C for SSP1-2.6, see section 4.3.1, to 95% of assessed range 4.61°C for SSP5-8.5 and 1.4°C for SSP1-2.6, see section 4.3.4). (e,f) Average of five models with GSAT warming nearest to the upper estimate of the *very likely* range (CESM2, CNRM-CM6-1, EC-Earth3, EC-Earth3-Veg, IPSL-CM6A-LR for SSP1-2.6 and CESM2, CESM2-WACCM, CNRM-CM6-1, EC-Earth3, EC-Earth3-Veg for SSP5-8.5), (g,h) Average of two models (CanESM5 and UKESM) projecting warming exceeding the *very likely* range.

**[END FIGURE 4.44 HERE]**

Furthermore, high-warming storylines are *very likely* also associated with substantial changes in the hydrological cycle due to strong thermodynamic changes that are potentially amplified or offset by dynamical changes (Emori and Brown, 2005; Seager et al., 2014b; Chavaillaz et al., 2016; Kröner et al., 2017; Chen et al., 2019). Here the assessment of the hydrological cycle in high-warming storylines is limited to changes in annual mean precipitation.

Quantifying precipitation changes associated with high-warming storylines is challenging since models show

increasing and decreasing precipitation over different regions (Section 4.5.1 and 4.6.1). In some areas models project opposing signals in different seasons or a combination of decreasing mean and increasing extreme precipitation (Kendon et al., 2014; Ban et al., 2015; Giorgi et al., 2016; Pendergrass et al., 2017). Models with the most pronounced GSAT warming are not necessarily associated with the strongest precipitation response in all regions, particularly due to potential changes in atmospheric dynamics (Madsen et al., 2017; Zappa and Shepherd, 2017; Li et al., 2018a).

Different alternative estimates of changes in annual mean precipitation patterns consistent with high-warming levels are compared here. The first estimate (Figure 4.45:b) is based on a linear pattern scaling of the multi-model mean precipitation pattern for SSP5-8.5 (Figure 4.45:a) to be consistent with the upper bound of the assessed *very likely* GSAT range (see above). This estimate is reasonably consistent with the average response of the five models with GSAT warming most consistent with the upper bound of the *very likely* warming range. (Figure 4.45:c). Both estimates show pronounced increases in annual mean precipitation of more than 30% in many regions north of 50°N and over parts of the tropics. Around the Mediterranean and other parts of the subtropics of the northern and southern subtropics a high-warming storyline is projected to be associated with a reduction in annual mean precipitation of 30% and more, which is even more pronounced depending on the season.

It is important to note that the multi-model mean response pattern, as well as the pattern-scaled response show a smoother pattern than the outcome of changes in 20-yr averages in individual simulations (Tebaldi and Knutti, 2007; Knutti et al., 2010). This is because (a) it is an estimate of the forced response, i.e. the response pattern in absence of internal variability, and (b) model differences in the location of the largest changes tend to cancel each other. Individual model simulations show opposing signs in precipitation changes e.g. substantial increases or decreases over Australia, the west coast of North America, parts of West Africa or around the Persian Gulf (Figure 4.45:d), which tend to offset each other in the multi-model mean response. The spatial probability distribution of precipitation changes shows that areas of strong precipitation increase and drying occur in all models (Figure 4.45:g, see also 4.6.1). However, due to the spatial smoothing the multi-model mean response shows a lower area fraction of drying than most of the models (Tebaldi and Knutti, 2007; Knutti et al., 2010). The five models with GSAT warming consistent with a high-warming storyline and the two models projecting GSAT warming exceeding the *very likely* GSAT warming range show a much larger area fraction of drying and tend to project a somewhat larger fraction of strong precipitation increases than the multi-model mean.

The high-warming storyline shown in Figure 4.45:bc does not correspond to an upper or lower estimate of annual precipitation increase and decrease over individual locations, which in many regions may differ in the sign of the response (Figure 4.45:ef) due to differences in the model response and internal variability (Madsen et al., 2017). Figure 4.45:ef illustrates upper and lower local estimates corresponding to the 5–95% model range of local uncertainties as opposed to the global-warming storylines. Note however, that Figure 4.45:ef does not show a physically plausible global precipitation response pattern because information at the different grid points is simulated by different model simulations.

Again, the manifestation of changes in the hydrological cycle for a high-warming storyline is not limited to precipitation, but would substantially affect other variables such as soil moisture, runoff, atmospheric humidity, evapotranspiration and many other variables. The changes are also not limited to annual mean precipitation but may be stronger or weaker for individual seasons and for heavy precipitation and dry spells.

**[START FIGURE 4.45 HERE]**

**Figure 4.45:** Changes in annual mean precipitation in 2081–2100 relative to 1995–2014 in SSP5-8.5. (a) Multi-model mean changes consistent as in section 4.5.1. (b,c) Estimates for annual mean precipitation changes consistent with a storyline representing a physically plausible high-global-warming storyline for 2081–2100. (b) Pattern-scaled multi-model mean precipitation to the GSAT of the upper bound of the *very likely* range (scaled from CMIP6 multi-model mean of 3.9°C, see section 4.3.1, to 95% of assessed range see section 4.3.4). (c) Average of five models with GSAT warming nearest to the upper bound of the *very likely* range (CESM2, CESM2-WACCM, CNRM-CM6-1, EC-Earth3, EC-Earth3-Veg) (d) Annual mean

precipitation changes in four individual model simulations with high GSAT warming showing. (e,f) Local upper estimate (95% quantile across models) and lower estimate (5% quantile across models) at each grid point. Information at individual grid points comes from different model simulations and illustrates local uncertainty range but should not be interpreted as a pattern. (g) Area fraction of changes in annual mean precipitation 2081–2100 relative to 1995–2014 for individual model simulations (thin black lines) and models with high GSAT warming (thin red lines). The grey range illustrates the 5–95% range across CMIP6 models for each and the solid black line the area fraction of the multi-model mean pattern shown in (a).

**[END FIGURE 4.45 HERE]**

## 4.9 Limitations to the Assessment

1) Every projection assessment is conditioned on a particular scenario, and while the differences between climate responses to different scenarios can be and are assessed here, it is usually not possible to combine responses to individual scenarios into an overall probabilistic statement about expected future climate. The fundamental reason for this is a lack of probabilities that can be assigned to scenarios (Schneider, 2001); the scenarios do not come with statements about real-world attainability to the extent that it depends on political and social processes (e.g., O'Neill et al., 2016). Exceptions to this limit in the assessment are possible only under special circumstances, such as for some statements about near-term changes that are largely independent of the scenario chosen (e.g., Section 4.4.1).

2) By definition, it is impossible to assess the effects of 'unknown unknowns' – no uncertainty can be assessed if its very existence is not known.

**Frequently Asked Questions**

## FAQ 4.1: What Can We Say about How the Climate Will Change over the Next Twenty Years?

*Many aspects of the climate system, including global average temperatures, Arctic sea ice cover, and sea levels, have shown clear increasing or decreasing trends in recent decades, and we expect most of these trends to continue for at least the next twenty years. Our confidence in that conclusion derives from the expectation that radiative forcing from greenhouse gases will continue to increase as a result of continued emissions, from our understanding of the physics of the climate system, and from our confidence in model simulations of the global-scale changes that will result from the increase in radiative forcing. However, estimates of the magnitude of these near-term changes are much more uncertain, mainly because natural internal variability can in the near term mask – and for some quantities even overwhelm – the response of the climate to increased radiative forcing.*

There is a clearly recognized societal need for information about climate change over the near term, defined here as the next twenty years. When providing this information, however, we must distinguish between two different contributions to the changes we expect to see. The first contribution is the expected response of the climate system to the increase in radiative forcing implied by the continued emissions of greenhouse gases over the next twenty years in virtually all available scenarios. A second contribution arises from the natural internal variability caused by chaotic processes in the atmosphere and the ocean, ranging from localized weather systems to larger-scale patterns and oscillations that change over months, years, or decades. In the near term, natural internal variability plays a major role relative to the response to increased radiative forcing, so time averages or trends calculated over twenty years contain a substantial chaotic element.

Natural internal variability can be predicted to some extent, provided that model simulations are started from accurate observations of the current state of the climate system. Near-term climate predictions do not attempt to forecast individual weather events, but instead provide information such as how much warmer or colder future years will be on average, compared to the year just passed. Forecast quality or 'skill' is achieved because some elements of the climate system, primarily the oceans, vary on long time scales such as years to decades. Current climate models have some skill in predicting these slow variations, such that useful statements about the future state of natural internal variability can be made out to about ten years ahead. However, looking ahead for twenty years, there are indications that for most quantities of interest, natural internal variability will never be predictable. This implies that natural internal variability causes some uncertainty that can at best be quantified accurately but that cannot be reduced.

FAQ 4.1, Figure 1 illustrates the near-term interplay between natural internal variability and the expected response to further increased radiative forcing for two important indicators of global climate change, the globally averaged surface air temperature and the Arctic sea ice area in September. The figure shows projected changes relative to the time-average over the period 1995–2014 for simulations with different climate models and one low-emission and one high-emission scenario. Viewed over all simulations, the global temperature tends to increase, and the sea-ice area tends to decrease, but each individual simulation shows the large influence of natural internal variability. One source of uncertainty, however, is not pronounced over the next twenty years. The choice of emissions scenario has little impact on the results – in stark contrast to simulation results for the end of the 21st century shown by the bars to the right of the figure. This reduced dependence on the scenario arises because virtually all scenarios assume that greenhouse gas emissions will continue over the next twenty years, leading to increased greenhouse gas concentrations and hence increased radiative forcing over the near term.

Since the period 1995–2014 has been warmer than the period 1850–1900 by about 0.9°C, we notice from FAQ 4.1 Figure 1 that a global warming of 1.5°C above the pre-industrial level may well occur within the next twenty years.

**[START FIGURE FAQ 4.1, FIGURE 1 HERE]**

**FAQ 4.1, Figure 1:** Simulations over the period 1995–2040, encompassing the recent past and the near-term future, of two important indicators of global climate change, (a) globally averaged surface air temperature, and (b), the area of Arctic sea ice in September. Both quantities are shown as deviations from the average over the period 1995–2014. The grey curves are for the historical period ending in 2014; the colours refer to one low- and one high-emission SSP scenario as shown in the inlet. In (a), the bars to the right show the range of simulated values for year 2100. In (b), some models simulate an ice-free Arctic in September already in the near term, which is why they show no further decrease. [Placeholder figure, based on eleven currently available CMIP6 models. To be updated with other CMIP6 models and, possibly, shading for indicating uncertainty.]

**[END FIGURE FAQ 4.1, FIGURE 1 HERE]**

## FAQ 4.2: How Quickly Would We See the Effects of Reducing Greenhouse Gas Emissions?

*Over many decades, reductions in greenhouse gas emissions would limit the amount of surface warming and changes in many other aspects of the climate system. In the first few decades after emissions reductions begin, however, the effects on the climate system will be difficult to diagnose, both because the climate system takes some time to respond to the emissions reduction and because natural internal variability will mask the climate system response to the reductions. Emissions reductions are expected to leave a discernible fingerprint on atmospheric $CO_2$ concentrations after about ten years and on global surface temperature after about 20–30 years. An effect of mitigation on regional precipitation trends is expected only later in the 21st century.*

Reducing emissions of $CO_2$ – the most important greenhouse gas – would slow down the increase in atmospheric $CO_2$ concentrations; however, concentrations will only begin to decrease when emissions approach zero. This delay in response is a manifestation of the very long lifetime of $CO_2$ in the atmosphere. As a consequence, the radiative forcing will first also continue to increase, although at a detectably smaller rate after about ten years. This smaller rate of increase in radiative forcing is expected to lead to a smaller rate of global surface warming. But this reduction in the rate of warming will be overlain by natural internal variability, which is caused by chaotic processes in the atmosphere and the ocean, such as the ever-changing weather. Detecting whether surface warming has indeed slowed down will thus be difficult in the decades right after emissions reductions begin.

There has been some recent research on this detection problem, but not enough for a broad quantitative consensus to have emerged. A number of issues need to be considered. For example, there is no unambiguous definition of a no-mitigation emissions pathway against which emissions reductions can be defined. Furthermore, this detection problem – which is analogous to detecting human-induced climate change in the observed record of the past – becomes more difficult on the regional scale and for many quantities other than temperature.

FAQ 4.2 Figure 1 illustrates when the benefits of mitigation may be detectable for globally averaged surface air temperature for two scenarios: one where emissions begin to fall after 2020 (SSP1-2.6) and one without mitigation (SSP3-7.0). For each year from 1995 to 2100, the figure shows the temperature trend over the preceding twenty years. The uncertainty arising from natural internal variability in the climate system is represented by simulating each scenario fifty times with the same climate model but starting from slightly different initial states in 1850; for each scenario, the differences between individual simulations are caused entirely by simulated natural internal variability. The average over all fifty simulations represents the expected climate response for a given scenario. The climate history that will actually unfold under each scenario would consist of this expected response combined with the contribution from natural internal variability.

Diagnosing the time of detection of mitigation benefit depends on the criterion applied: how certain does one want to be? For the model chosen here, which is relatively sensitive to higher greenhouse gas concentrations and therefore shows a relatively large difference between scenarios, it takes a bit over twenty years before detection is certain. Certain detection is displayed in FAQ 4.2 Figure 1 by the lack of overlap between the ranges of each scenario. Less-than-certain detection can be diagnosed earlier. With the same level of natural internal variability but smaller differences in the responses to different scenarios, detection would occur later than displayed here.

Detection of a discernible effect of $CO_2$ emissions reductions on atmospheric $CO_2$ concentrations is expected earlier than for temperature, after about ten years assuming reductions as in Scenario SSP1-2.6. A detectable effect of mitigation on regional precipitation trends is expected only later in the 21st century under the same scenario. In summary, the benefits of mitigation are clearly discernible in crucial climate variables such as global temperature only after a delay of a few decades – a delay that might cause a substantial communication challenge.

**[START FIGURE FAQ 4.2, FIGURE 1 HERE]**

**FAQ 4.2, Figure 1:** Illustrating when the benefits of emissions reduction might become detectable in globally averaged surface air temperature. The figure shows twenty-year linear trends, and the time axis is defined such that in each year, the trend over the preceding twenty years is displayed. Shown are the results from a single CMIP6 model, CanESM5, run under one scenario that can be considered to represent no mitigation (SSP3-7.0) and one scenario that represents mitigation (SSP1-2.6). For each scenario, the model is run fifty times with very slightly different conditions for the year 1850 (each scenario simulation starts from the end of a historical simulation ending in 2014). Differences between individual runs are caused by simulated natural internal variability and can be considered an uncertainty that cannot be reduced. The figure shows the average of all fifty simulations as full-drawn lines and the individual simulations as shaded lines. Three time periods are highlighted, by showing the distribution of simulated twenty-year trends for each scenario, calculated retrospectively in years 2040 (trend over the near-term period), 2060 (trend over the mid-term period), and 2100 (trend over the long-term period). The filled circle shows the average over all fifty simulations, and the bars show the ranges of simulations in each scenario.

**[END FIGURE FAQ 4.2, FIGURE 1 HERE]**

## FAQ 4.3: At a Given Level of Global Warming, What are the Spatial Patterns of Climate Change?

*As the planet warms, climate change does not unfold uniformly across the globe, but some patterns of regional change show clear and direct relationships to increases in global average temperature. For example, the Arctic warms more than other regions, land areas warm more than the oceans, and the Northern Hemisphere warms more than the Southern Hemisphere. In cases like these, we can infer the direction and magnitude of some regional changes – particularly temperature changes – for any given level of global warming.*

There are two main advantages to identifying a robust pattern of regional change – one for which there is *high confidence* based on strong evidence and a good understanding of the physical process involved – for a given level of global warming. First, such a pattern enables us to make statements about expected regional change that are largely independent of the various future scenarios used to project global temperature changes. As long as different scenarios result in the same global warming level, irrespective of the time when this level is attained in each scenario, we can with *high confidence* specify the expected regional change that would result from this warming. Second, we can reliably make projections for warming levels that have not been directly analysed or simulated explicitly. For example, if a change pattern per degree Celsius of global surface warming is identified reliably, the expected regional change can be calculated for any global warming level by simple multiplication ('scaling') of the pattern. This approach can be highly efficient for studies of climate impacts at regional scales. When patterns of changes are robust, impact assessments can readily be performed for all levels of global warming, for all future time periods, and for all scenarios.

Pattern scaling has some well-known strengths and weaknesses. It yields robust estimates for temperature changes at a given level of global warming, but there are limitations in areas of high natural internal variability that become particularly evident at low levels of warming and for seasonal changes, for areas with strong feedbacks due to melting snow or sea ice, and for areas with large differences between transient and very-long-term changes. Patterns are less robust for precipitation changes, for reasons that are likewise quite well understood. Global and regional changes in precipitation depend not only on changes in globally averaged temperatures but also on human influences on regional climate, such as emissions of particulate matter (known as aerosols) and land-use changes. Furthermore, regional precipitation changes are more strongly influenced by natural internal variability in the atmosphere, meaning that any given surface warming level can result in quite different spatial changes in precipitation. Pattern scaling can still be applied to precipitation changes, but the uncertainties are larger than for temperature changes.

Finally, there are climate variables for which pattern scaling is not appropriate. For example, robust patterns cannot be established for changes in snow or sea ice cover, because both snow and ice vanish completely if certain temperature thresholds are crossed. If snow cover in an area melts completely, there can be no further melting, and the simple proportionality lying behind pattern scaling no longer applies. Changes in these bounded variables are better described by whether a threshold is crossed or not.

**[START FAQ 4.3 FIGURE 1 HERE]**

**FAQ 4.3, Figure 1:** Example for a robust warming pattern, which is presented here as the average of fourteen CMIP6 models using the scenario SSP3-7.0. Surface warming relative to 1850–1900 is shown for time periods over which the globally averaged surface warming is 1.5°C, 2°C, and 3°C, respectively. We recognise the strong warming over the Arctic, generally stronger warming over land than over the ocean, generally stronger warming in the Northern Hemisphere than in the Southern Hemisphere, and less warming over the central subpolar North Atlantic.

**[END FIGURE FAQ 4.3, FIGURE 1 HERE]**

## References


Abramowitz, G., Herger, N., Gutmann, E., Hammerling, D., Knutti, R., Leduc, M., et al. (2019). ESD Reviews: Model dependence in multi-model climate ensembles: weighting, sub-selection and out-of-sample testing. *Earth Syst. Dynam.* 10, 91–105. doi:10.5194/esd-10-91-2019.

Acosta Navarro, J. C., Ekman, A. M. L., Pausata, F. S. R., Lewinschal, A., Varma, V., Seland, Ø., et al. (2017). Future Response of Temperature and Precipitation to Reduced Aerosol Emissions as Compared with Increased Greenhouse Gas Concentrations. *J. Clim.* 30, 939–954. doi:10.1175/JCLI-D-16-0466.1.

Acosta Navarro, J. C., Varma, V., Riipinen, I., Seland, Ø., Kirkevåg, A., Struthers, H., et al. (2016). Amplification of Arctic warming by past air pollution reductions in Europe. *Nat. Geosci.* 9, 277–281. doi:10.1038/ngeo2673.

Adams, J. B., Mann, M. E., and Ammann, C. M. (2003). Proxy evidence for an El Niño-like response to volcanic forcing. *Nature* 426, 274–278. doi:10.1038/nature02101.

Aerenson, T., Tebaldi, C., Sanderson, B., and Lamarque, J. F. (2018). Changes in a suite of indicators of extreme temperature and precipitation under 1.5 and 2 degrees warming. *Environ. Res. Lett.* 13. doi:10.1088/1748-9326/aaafd6.

Ahlm, L., Jones, A., Stjern, C. W., Muri, H., Kravitz, B., and Kristjánsson, J. E. (2017). Marine cloud brightening – as effective without clouds. *Atmos. Chem. Phys.* 17, 13071–13087. doi:10.5194/acp-17-13071-2017.

Albern, N., Voigt, A., and Pinto, J. G. (2019). Cloud-Radiative Impact on the Regional Responses of the Midlatitude Jet Streams and Storm Tracks to Global Warming. *J. Adv. Model. Earth Syst.* 11, 1940–1958. doi:10.1029/2018MS001592.

Allen, M. R., Dube, O. P., Solecki, W., Aragón-Durand, F., Cramer, W., Humphreys, S., et al. (2018). "Framing and Context," in *Global Warming of 1.5°C. An IPCC Special Report on the impacts of global warming of 1.5°C above pre-industrial levels and related global greenhouse gas emission pathways, in the context of strengthening the global response to the threat of climate change,* eds. V. Masson-Delmotte, P. Zhai, H.-O. Pörtner, D. Roberts, J. Skea, P. R. Shukla, et al. (In Press).

Allen, M. R., Frame, D. J., Huntingford, C., Jones, C. D., Lowe, J. A., Meinshausen, M., et al. (2009). Warming caused by cumulative carbon emissions towards the trillionth tonne. *Nature* 458, 1163–1166. doi:10.1038/nature08019.

Allen, M. R., and Ingram, W. J. (2002). Constraints on future changes in climate and the hydrologic cycle. *Nature* 419, 224–232. Available at: http://dx.doi.org/10.1038/nature01092.

Alley, R. B., Marotzke, J., Nordhaus, W. D., Overpeck, J. T., Peteet, D. M., Jr., R. A. P., et al. (2003). Abrupt Climate Change. *Science (80-. ).* 299, 2005–2010.

Amann, M., Klimont, Z., and Wagner, F. (2013). Regional and global emissions of air pollutants: recent trends and future scenarios. *Annu. Rev. Environ. Resour.* 38, 31–55.

Andrews, T., Andrews, M. B., Bodas-Salcedo, A., Jones, G. S., Kulhbrodt, T., Manners, J., et al. (2019). Forcings, feedbacks and climate sensitivity in HadGEM3-GC3.1 and UKESM1. *Submitt. to J. Adv. Model. Earth Syst.* doi:10.1029/2019MS001866.

Andrews, T., and Forster, P. M. (2010). The transient response of global-mean precipitation to increasing carbon dioxide levels. *Environ. Res. Lett.* 5, 1–6. doi:10.1088/1748-9326/5/2/025212.

Andrews, T., Forster, P. M., and Gregory, J. M. (2009). A surface energy perspective on climate change. *J. Clim.* 22, 2557–2570. doi:10.1175/2008JCLI2759.1.

Andrews, T., Gregory, J. M., Webb, M. J., and Taylor, K. E. (2012). Forcing, feedbacks and climate sensitivity in CMIP5 coupled atmosphere-ocean climate models. *Geophys. Res. Lett.* 39, L09712. doi:10.1029/2012GL051607.

Andrews, T., and Ringer, M. A. (2014). Cloud feedbacks, rapid adjustments, and the forcing--response relationship in a transient CO2 reversibility scenario. *J. Clim.* 27, 1799–1818.

Andrews, T., and Webb, M. J. (2018). The dependence of global cloud and lapse rate feedbacks on the spatial structure of tropical pacific warming. *J. Clim.* 31, 641–654. doi:10.1175/JCLI-D-17-0087.1.

Annan, J. D., and Hargreaves, J. C. (2017). On the meaning of independence in climate science. *Earth Syst. Dyn.* 8, 211–224. doi:10.5194/esd-8-211-2017.

Armour, K. C., Eisenman, I., Blanchard-Wrigglesworth, E., McCusker, K. E., and Bitz, C. M. (2011). The reversibility of sea ice loss in a state-of-the-art climate model. *Geophys. Res. Lett.* 38, n/a-n/a. doi:10.1029/2011GL048739.

Armour, K. C., Marshall, J., Scott, J. R., Donohoe, A., and Newsom, E. R. (2016a). Southern Ocean warming delayed by circumpolar upwelling and equatorward transport. *Nat. Geosci.* 9, 549–554. doi:10.1038/ngeo2731.

Armour, K. C., Marshall, J., Scott, J. R., Donohoe, A., and Newsom, E. R. (2016b). Southern Ocean warming delayed by circumpolar upwelling and equatorward transport. *Nat. Geosci.* 9, 549–554. doi:10.1038/ngeo2731.

Arrhenius, S. (1896). On the influence of carbonic acid in the air upon the temperature of the ground. *Philos. Mag. J. Sci.* 41, 237–276.

Aswathy, V. N., Boucher, O., Quaas, M., Niemeier, U., Muri, H., Mülmenstädt, J., et al. (2015). Climate extremes in multi-model simulations of stratospheric aerosol and marine cloud brightening climate engineering. *Atmos. Chem. Phys.* 15, 9593–9610. doi:10.5194/acp-15-9593-2015.

Ba, J., Keenlyside, N. S., Latif, M., Park, W., Ding, H., Lohmann, K., et al. (2014). A multi-model comparison of

Atlantic multidecadal variability. *Clim. Dyn.* 43, 2333–2348. doi:10.1007/s00382-014-2056-1.
Bacmeister, J. T., Reed, K. A., Hannay, C., Lawrence, P., Bates, S., Truesdale, J. E., et al. (2018). Projected changes in tropical cyclone activity under future warming scenarios using a high-resolution climate model. *Clim. Change* 146, 547–560. doi:10.1007/s10584-016-1750-x.
Baker, L. H., Shaffrey, L. C., Sutton, R. T., Weisheimer, A., and Scaife, A. A. (2018). An Intercomparison of Skill and Overconfidence/Underconfidence of the Wintertime North Atlantic Oscillation in Multimodel Seasonal Forecasts. *Geophys. Res. Lett.* 45, 7808–7817. doi:10.1029/2018GL078838.
Bala, G., Caldeira, K., and Nemani, R. (2010). Fast versus slow response in climate change: Implications for the global hydrological cycle. *Clim. Dyn.* 35, 423–434. doi:10.1007/s00382-009-0583-y.
Balaji, V., Taylor, K. E., Juckes, M., Lautenschlager, M., Blanton, C., Cinquini, L., et al. (2018). Requirements for a global data infrastructure in support of CMIP6. *Geosci. Model Dev. Discuss.* 11, 3659–3680. doi:10.5194/gmd-2018-52.
Ban, N., Schmidli, J., and Schär, C. (2015). Heavy precipitation in a changing climate: Does short-term summer precipitation increase faster? *Geophys. Res. Lett.* doi:10.1002/2014GL062588.
Banerjee, A., Archibald, A. T., Maycock, A. C., Telford, P., Abraham, N. L., Yang, X., et al. (2014). Lightning NOx, a key chemistry-climate interaction: Impacts of future climate change and consequences for tropospheric oxidising capacity. *Atmos. Chem. Phys.* 14, 9871–9881. doi:10.5194/acp-14-9871-2014.
Banerjee, A., Fyfe, J. C., M., P. L., Waugh, D., and Chang, K.-L. (9999). A pause in Southern Hemisphere circulation trends due to the Montreal Protocol. *Nature*, (submitted).
Banerjee, A., Maycock, A. C., and Pyle, J. A. (2018). Chemical and climatic drivers of radiative forcing due to changes in stratospheric and tropospheric ozone over the 21st century. *Atmos. Chem. Phys.* 18, 2899–2911. doi:10.5194/acp-18-2899-2018.
Barcikowska, M. J., Weaver, S. J., Feser, F., Russo, S., Schenk, F., Stone, D. A., et al. (2018). Euro-Atlantic winter storminess and precipitation extremes under 1.5\,{\degree}C vs. 2\,{\degree}C warming scenarios. *Earth Syst. Dyn.* 9, 679–699. doi:10.5194/esd-9-679-2018.
Barnes, E. A., Barnes, N. W., and Polvani, L. M. (2014). Delayed southern hemisphere climate change induced by stratospheric ozone recovery, as projected by the CMIP5 models. *J. Clim.* 27, 852–867. doi:10.1175/JCLI-D-13-00246.1.
Barnes, E. A., and Polvani, L. (2013). Response of the Midlatitude Jets, and of Their Variability, to Increased Greenhouse Gases in the CMIP5 Models. *J. Clim.* 26, 7117–7135. doi:10.1175/JCLI-D-12-00536.1.
Barnes, E. A., and Polvani, L. M. (2015). CMIP5 projections of arctic amplification, of the North American/North Atlantic circulation, and of their relationship. *J. Clim.* 28, 5254–5271. doi:10.1175/JCLI-D-14-00589.1.
Barriopedro, D., García-Herrera, R., and Trigo, R. M. (2010). Application of blocking diagnosis methods to General Circulation Models. Part I: a novel detection scheme. *Clim. Dyn.* 35, 1373–1391. doi:10.1007/s00382-010-0767-5.
Baumberger, C., Knutti, R., and Hirsch Hadorn, G. (2017). Building confidence in climate model projections: an analysis of inferences from fit. *Wiley Interdiscip. Rev. Clim. Chang.* 8, e454. doi:10.1002/wcc.454.
Bayr, T., and Dommenget, D. (2013). The Tropospheric Land-Sea Warming Contrast as the Driver of Tropical Sea Level Pressure Changes. *J. Clim.* 26, 1387–1402.
Bellucci, A., Haarsma, R., Bellouin, N., Booth, B., Cagnazzo, C., Hurk, B., et al. (2015a). Advancements in decadal climate predictability: The role of nonoceanic drivers. *Rev. Geophys.* 53, 165–202. doi:10.1002/2014RG000473.
Bellucci, A., Haarsma, R., Gualdi, S., Athanasiadis, P. J., Caian, M., Cassou, C., et al. (2015b). An assessment of a multi-model ensemble of decadal climate predictions. *Clim. Dyn.* 44, 2787–2806. doi:10.1007/s00382-014-2164-y.
Bengtsson, L., and Hodges, K. I. (2018). Can an ensemble climate simulation be used to separate climate change signals from internal unforced variability? *Clim. Dyn.* doi:10.1007/s00382-018-4343-8.
Berdahl, M., Robock, A., Ji, D., Moore, J. C., Jones, A., Kravitz, B., et al. (2014). Arctic cryosphere response in the geoengineering model intercomparison project G3 and G4 scenarios. *J. Geophys. Res.* 119, 1308–1321. doi:10.1002/2013JD020627.
Berg, A. M., Findell, K., Lintner, B. R., Giannini, A., Seneviratne, S. I., van den Hurk, B., et al. (2016). Land-atmosphere feedbacks amplify aridity increase over land under global warming. *Nat. Clim. Chang.* 6, 869–874.
Berner, J., Achatz, U., Batté, L., Bengtsson, L., Cámara, A. de la, Christensen, H. M., et al. (2017). Stochastic Parameterization: Toward a New View of Weather and Climate Models. *Bull. Am. Meteorol. Soc.* 98, 565–588. doi:10.1175/BAMS-D-15-00268.1.
Bethke, I., Outten, S., Otterå, O. H., Hawkins, E., Wagner, S., Sigl, M., et al. (2017). Potential volcanic impacts on future climate variability. *Nat. Clim. Chang.* 7, 799–805. doi:10.1038/nclimate3394.
Bindoff, N. L., Stott, P. A., AchutaRao, K. M., Allen, M. R., Gillett, N., Gutzler, D., et al. (2013). "Detection and Attribution of Climate Change: from Global to Regional," in *Climate Change 2013: The Physical Science Basis. Contribution of Working Group I to the Fifth Assessment Report of the Intergovernmental Panel on Climate Change*, eds. T. F. Stocker, D. Qin, G.-K. Plattner, M. Tignor, S. K. Allen, J. Boschung, et al. (Cambridge, United Kingdom and New York, NY, USA: Cambridge University Press), 867–952.

Bitz, C. M., Gent, P. R., Woodgate, R. A., Holland, M. M., and Lindsay, R. (2006). The influence of sea ice on ocean heat uptake in response to increasing CO2. *J. Clim.* 19, 2437–2450. doi:10.1175/JCLI3756.1.

Bluth, G. J. S., Doiron, S. D., Schnetzler, C. C., Krueger, A. J., and Walter, L. S. (1992). Global tracking of the SO2 clouds from the June, 1991 Mount Pinatubo eruptions. *Geophys. Res. Lett.* 19, 151–154. doi:10.1029/91GL02792.

Boe, J. (2018). Interdependency in multimodel climate projections: Component replication and result similarity. *Geophys. Res. Lett.* 45, 2771–2779. doi:10.1002/2017gl076829.

Boer, G. J., Kharin, V. V., and Merryfield, W. J. (2013). Decadal predictability and forecast skill. *Clim. Dyn.* 41, 1817–1833. doi:10.1007/s00382-013-1705-0.

Boer, G. J., Smith, D. M., Cassou, C., Doblas-Reyes, F., Danabasoglu, G., Kirtman, B., et al. (2016). The Decadal Climate Prediction Project (DCPP) contribution to CMIP6. *Geosci. Model Dev.* 9, 3751–3777. doi:10.5194/gmd-9-3751-2016.

Bollasina, M. A., Ming, Y., and Ramaswamy, V. (2011). Anthropogenic Aerosols and the Weakening of the South Asian Summer Monsoon. *Science (80-. ).* 334, 502–505. doi:10.1126/science.1204994.

Bonan, D. B., Armour, K. C., Roe, G. H., Siler, N., and Feldl, N. (2018). Sources of Uncertainty in the Meridional Pattern of Climate Change. *Geophys. Res. Lett.* 45, 9131–9140. doi:10.1029/2018GL079429.

Bony, S., Bellon, G., Klocke, D., Sherwood, S., Fermepin, S., and Denvil, S. (2013). Robust direct effect of carbon dioxide on tropical circulation and regional precipitation. *Nat. Geosci.* 6, 447–451. doi:10.1038/ngeo1799.

Borodina, A., Fischer, E. M., and Knutti, R. (2017). Emergent constraints in climate projections: A case study of changes in high-latitude temperature variability. *J. Clim.* 30, 3655–3670. doi:10.1175/JCLI-D-16-0662.1.

Boucher, O., Halloran, P. R., Burke, E. J., Doutriaux-Boucher, M., Jones, C. D., Lowe, J., et al. (2012). Reversibility in an Earth System model in response to CO 2 concentration changes. *Environ. Res. Lett.* 7, 024013. doi:10.1088/1748-9326/7/2/024013.

Bracegirdle, T. J., Lu, H., Eade, R., and Woollings, T. (2018). Do CMIP5 Models Reproduce Observed Low‐Frequency North Atlantic Jet Variability? *Geophys. Res. Lett.* 45, 7204–7212. doi:10.1029/2018GL078965.

Bracegirdle, T., Krinner, G., Tonneli, M., Haumann, F., Naughten, K., Rackow, T., et al. (9999). Twenty first century changes in Antarctic and Southern Ocean surface climate in CMIP6. *Atmos. Sci. Lett.* (submitted.

Branstator, G., and Teng, H. Y. (2010). Two limits of initial-value decadal predictability in a CGCM. *J. Clim.* 23, 6292–6311. doi:10.1175/2010jcli3678.1.

Bright, R. M., Davin, E., O'Halloran, T., Pongratz, J., Zhao, K., and Cescatti, A. (2017). Local temperature response to land cover and management change driven by non-radiative processes. *Nat. Clim. Chang.* doi:10.1038/nclimate3250.

Brogli, R., Kröner, N., Sørland, S. L., Lüthi, D., and Schär, C. (2019). The Role of Hadley Circulation and Lapse-Rate Changes for the Future European Summer Climate. *J. Clim.* 32, 385–404. doi:10.1175/JCLI-D-18-0431.1.

Bronselaer, B., Stouffer, R. J., Winton, M., Griffies, S. M., Hurlin, W. J., Russell, J. L., et al. (2018). Change in future climate due to Antarctic meltwater. *Nature* 564, 55–58. doi:10.1038/s41586-018-0712-z.

Brown, P. T., Lozier, M. S., Zhang, R., and Li, W. (2016). The necessity of cloud feedback for a basin-scale Atlantic Multidecadal Oscillation. *Geophys. Res. Lett.* 43, 3955–3963. doi:10.1002/2016GL068303.

Brown, P. T., Ming, Y., Li, W., and Hill, S. A. (2017). Change in the magnitude and mechanisms of global temperature variability with warming. *Nat. Clim. Chang.* 7, 743–748. doi:10.1038/nclimate3381.

Bürger, G., and Cubasch, U. (2015a). The detectability of climate engineering. *J. Geophys. Res.* 120, 11,404-11,418. doi:10.1002/2015JD023954.

Bürger, G., and Cubasch, U. (2015b). The detectability of climate engineering. *J. Geophys. Res.* 120, 11,404-11,418. doi:10.1002/2015JD023954.

Buzan, J. R., Oleson, K., and Huber, M. (2015). Implementation and comparison of a suite of heat stress metrics within the Community Land Model version 4.5. *Geosci. Model Dev.* 8, 151–170. doi:10.5194/gmd-8-151-2015.

Byrne, M. P., and O'Gorman, P. A. (2013a). Land-ocean warming contrast over a wide range of climates: Convective quasi-equilibrium theory and idealized simulations. *J. Clim.* 26, 4000–4016.

Byrne, M. P., and O'Gorman, P. A. (2013b). Link between land-ocean warming contrast and surface relative humidities in simulations with coupled climate models. *Geophys. Res. Lett.* 40, 5223–5227. doi:10.1002/grl.50971.

Byrne, M. P., and O'Gorman, P. A. (2015). The Response of Precipitation Minus Evapotranspiration to Climate Warming: Why the "Wet-Get-Wetter, Dry-Get-Drier''' Scaling Does Not Hold over Land." *J. Clim.* 28, 8078–8092.

Byrne, M. P., and O'Gorman, P. A. (2016). Understanding decreases in land relative humidity with global warming: conceptual model and GCM simulations. *J. Clim.* 29, 9045–9061.

Byrne, M. P., and O'Gorman, P. A. (2018). Trends in continental temperature and humidity directly linked to ocean warming. *Proc. Natl. Acad. Sci.* 115, 4863–4868. doi:10.1073/pnas.1722312115.

Caesar, J., Palin, E., Liddicoat, S., Lowe, J., Burke, E., Pardaens, A., et al. (2013). Response of the HadGEM2 Earth System Model to future greenhouse gas emissions pathways to the year 2300. *J. Clim.* 26, 3275–3284.

Caesar, L., Rahmstorf, S., Robinson, A., Feulner, G., and Saba, V. (2018). Observed fingerprint of a weakening Atlantic Ocean overturning circulation. *Nature* 556, 191–196. doi:10.1038/s41586-018-0006-5.

Cai, W., Santoso, A., Wang, G., Weller, E., Wu, L., Ashok, K., et al. (2014). Increased frequency of extreme Indian Ocean Dipole events due to greenhouse warming. *Nature* 510, 254–258.
Cai, W., Santoso, A., Wang, G., Yeh, S.-W., An, S.-I., Cobb, K. M., et al. (2015). ENSO and greenhouse warming. *Nat. Clim. Chang.* 5, 849–859. Available at: http://dx.doi.org/10.1038/nclimate2743.
Cai, W., Wang, G., Dewitte, B., Wu, L., Santoso, A., Takahashi, K., et al. (2018a). Increased variability of eastern Pacific El Niño under greenhouse warming. *Nature* 564, 201–206. doi:10.1038/s41586-018-0776-9.
Cai, W., Wang, G., Gan, B., Wu, L., Santoso, A., Lin, X., et al. (2018b). Stabilised frequency of extreme positive Indian Ocean Dipole under 1.5 °C warming. *Nat. Commun.* 9, 1419. doi:10.1038/s41467-018-03789-6.
Cai, W., Wu, L., Lengaigne, M., Li, T., McGregor, S., Kug, J.-S., et al. (2019). Pantropical climate interactions. *Science (80-. ).* 363, eaav4236. doi:10.1126/science.aav4236.
Cai, W., Zheng, X. T., Weller, E., Collins, M., Cowan, T., Lengaigne, M., et al. (2013). Projected response of the Indian Ocean Dipole to greenhouse warming. *Nat. Geosci.* 6, 997–1007. doi:10.1038/ngeo2009.
Caian, M., Koenigk, T., Döscher, R., and Devasthale, A. (2018). An interannual link between Arctic sea-ice cover and the North Atlantic Oscillation. *Clim. Dyn.* 50, 423–441. doi:10.1007/s00382-017-3618-9.
Caldeira, K., Bala, G., and Cao, L. (2013). The science of geoengineering. *Annu. Rev. Earth Planet. Sci.* 41, 231–256. doi:10.1146/annurev-earth-042711-105548.
Callahan, C. W., Chen, C., Rugenstein, M., Bloch-Johnson, J., Yang, S., and Moyer, E. J. (9999). Robust decrease in ENSO amplitude under long-term warming. *Nat. Clim. Chang.* (submitted.
Cane, M. A., Clement, A. C., Murphy, L. N., and Bellomo, K. (2017). Low-Pass Filtering, Heat Flux, and Atlantic Multidecadal Variability. *J. Clim.* 30, 7529–7553. doi:10.1175/JCLI-D-16-0810.1.
Cao, L., Bala, G., and Caldeira, K. (2011). Why is there a short-term increase in global precipitation in response to diminished CO2 forcing? *Geophys. Res. Lett.* 38. doi:10.1029/2011GL046713.
Cao, L., Bala, G., and Caldeira, K. (2012). Climate response to changes in atmospheric carbon dioxide and solar irradiance on the time scale of days to weeks. *Environ. Res. Lett.* 7, 034015. doi:10.1088/1748-9326/7/3/034015.
Cao, L., Bala, G., Zheng, M., and Caldeira, K. (2015a). Fast and slow climate responses to CO2 and solar forcing: A linear multivariate regression model characterizing transient climate change. *J. Geophys. Res.* 120, 12,037-12,053. doi:10.1002/2015JD023901.
Cao, L., Bala, G., Zheng, M., and Caldeira, K. (2015b). Fast and slow climate responses to CO2 and solar forcing: A linear multivariate regression model characterizing transient climate change. *J. Geophys. Res. Atmos.* 120, 12,12-37,53. doi:10.1002/2015JD023901.
Cao, L., and Caldeira, K. (2010). Atmospheric carbon dioxide removal: long-term consequences and commitment. *Environ. Res. Lett.* 5, 024011. doi:10.1088/1748-9326/5/2/024011.
Cao, L., Duan, L., Bala, G., and Caldeira, K. (2016). Simulated long-term climate response to idealized solar geoengineering. *Geophys. Res. Lett.* 43, 2209–2217. doi:10.1002/2016GL068079.
Cao, L., Duan, L., Bala, G., and Caldeira, K. (2017). Simultaneous stabilization of global temperature and precipitation through cocktail geoengineering. *Geophys. Res. Lett.* 44, 7429–7437. doi:10.1002/2017GL074281.
Caron, L.-P., Hermanson, L., Dobbin, A., Imbers, J., Lledó, L., and Vecchi, G. A. (2017). How Skillful are the Multiannual Forecasts of Atlantic Hurricane Activity? *Bull. Am. Meteorol. Soc.* 99, 403–413. doi:10.1175/BAMS-D-17-0025.1.
Cassou, C., Kushnir, Y., Hawkins, E., Pirani, A., Kucharski, F., Kang, I.-S., et al. (2018). Decadal Climate Variability and Predictability: Challenges and Opportunities. *Bull. Am. Meteorol. Soc.* 99, 479–490. doi:10.1175/BAMS-D-16-0286.1.
Ceppi, P., and Hartmann, D. L. (2016). Clouds and the Atmospheric Circulation Response to Warming. *J. Clim.* 29, 783–799. doi:10.1175/JCLI-D-15-0394.1.
Ceppi, P., and Shepherd, T. G. (2017). Contributions of Climate Feedbacks to Changes in Atmospheric Circulation. *J. Clim.* 30, 9097–9118. doi:10.1175/JCLI-D-17-0189.1.
Ceppi, P., and Shepherd, T. G. (2019). The Role of the Stratospheric Polar Vortex for the Austral Jet Response to Greenhouse Gas Forcing. *Geophys. Res. Lett.* 46, 6972–6979. doi:10.1029/2019GL082883.
Ceppi, P., Zappa, G., Shepherd, T. G., and Gregory, J. M. (2018). Fast and slow components of the extratropical atmospheric circulation response to CO2forcing. *J. Clim.* 31, 1091–1105. doi:10.1175/JCLI-D-17-0323.1.
Ceppi, P., Zelinka, M. D., and Hartmann, D. L. (2014). The response of the Southern Hemispheric eddy-driven jet to future changes in shortwave radiation in CMIP5. *Geophys. Res. Lett.* doi:10.1002/2014GL060043.
Chadwick, R. (2016). Which aspects of CO2forcing and SST warming cause most uncertainty in projections of tropical rainfall change over land and ocean? *J. Clim.* 29, 2493–2509. doi:10.1175/JCLI-D-15-0777.1.
Chadwick, R., Boutle, I., and Martin, G. (2013). Spatial Patterns of Precipitation Change in CMIP5: Why the Rich Do Not Get Richer in the Tropics. *J. Clim.* 26, 3803–3822. doi:10.1175/JCLI-D-12-00543.1.
Chadwick, R., Douville, H., and Skinner, C. B. (2017). Timeslice experiments for understanding regional climate projections: applications to the tropical hydrological cycle and European winter circulation. *Clim. Dyn.* 49, 3011–3029. doi:10.1007/s00382-016-3488-6.
Chadwick, R., Good, P., and Willett, K. M. (2016). A simple moisture advection model of specific humidity change over land in response to SST warming. *J. Clim.* 29, 7613–7632.

Chalmers, N., Highwood, E. J., Hawkins, E., Sutton, R., and Wilcox, L. J. (2012). Aerosol contribution to the rapid warming of near-term climate under RCP 2.6. *Geophys. Res. Lett.* 39, 2–7. doi:10.1029/2012GL052848.

Chand, S. S., Tory, K. J., Ye, H., and Walsh, K. J. E. (2017). Projected increase in El Niño-driven tropical cyclone frequency in the Pacific. *Nat. Clim. Chang.* 7, 123–127. doi:10.1038/nclimate3181.

Chang, E. K. M. (2017). Projected Significant Increase in the Number of Extreme Extratropical Cyclones in the Southern Hemisphere. *J. Clim.* 30, 4915–4935. doi:10.1175/JCLI-D-16-0553.1.

Chang, E. K. M., Ma, C.-G., Zheng, C., and Yau, A. M. W. (2016). Observed and projected decrease in Northern Hemisphere extratropical cyclone activity in summer and its impacts on maximum temperature. *Geophys. Res. Lett.* 43, 2200–2208. doi:10.1002/2016GL068172.

Chavaillaz, Y., Joussaume, S., Bony, S., and Braconnot, P. (2016). Spatial stabilization and intensification of moistening and drying rate patterns under future climate change. *Clim. Dyn.* 47, 951–965. doi:10.1007/s00382-015-2882-9.

Chen, G., Norris, J., David Neelin, J., Lu, J., Ruby Leung, L., and Sakaguchi, K. (2019). Thermodynamic and dynamic mechanisms for hydrological cycle intensification over the full probability distribution of precipitation events. *J. Atmos. Sci.* doi:10.1175/JAS-D-18-0067.1.

Cheng, W., MacMartin, D. G., Dagon, K., Kravitz, B., Tilmes, S., Richter, J. H., et al. (2019). *Soil moisture and other hydrological changes in a stratospheric aerosol geoengineering large ensemble*. doi:10.1029/2018jd030237.

Chikamoto, Y., Kimoto, M., Ishii, M., Mochizuki, T., Sakamoto, T. T., Tatebe, H., et al. (2013). An overview of decadal climate predictability in a multi-model ensemble by climate model MIROC. *Clim. Dyn.* 40, 1201–1222. doi:10.1007/s00382-012-1351-y.

Chikamoto, Y., Timmermann, A., Widlansky, M. J., Balmaseda, M. A., and Stott, L. (2017). Multi-year predictability of climate, drought, and wildfire in southwestern North America. *Sci. Rep.* 7, 6568. doi:10.1038/s41598-017-06869-7.

Chiodo, G., Oehrlein, J., Polvani, L. M., Fyfe, J. C., and Smith, A. K. (2019). Insignificant influence of the 11-year solar cycle on the North Atlantic Oscillation. *Nat. Geosci.* 12, 94–99. doi:10.1038/s41561-018-0293-3.

Choi, J., Son, S. W., and Park, R. J. (2019). Aerosol versus greenhouse gas impacts on Southern Hemisphere general circulation changes. *Clim. Dyn.* 52, 4127–4142. doi:10.1007/s00382-018-4370-5.

Chou, C., Neelin, J. D., Chen, C.-A., and Tu, J.-Y. (2009). Evaluating the "Rich-Get-Richer" Mechanism in Tropical Precipitation Change under Global Warming. *J. Clim.* 22, 1982–2005. doi:10.1175/2008JCLI2471.1.

Christensen, H. M., and Berner, J. (2019). From reliable weather forecasts to skilful climate response: A dynamical systems approach. *Q. J. R. Meteorol. Soc.* 145, 1052–1069. doi:10.1002/qj.3476.

Christensen, H. M., Berner, J., Coleman, D. R. B., and Palmer, T. N. (2017). Stochastic parameterization and El Niño-southern oscillation. *J. Clim.* 30, 17–38. doi:10.1175/JCLI-D-16-0122.1.

Christensen, J. H., Kumar, K. K., Aldrian, E., An, S.-I., Cavalcanti, I. F. A., and M. de Castro, W. Dong, P. Goswami, A. Hall, J.K. Kanyanga, A. Kitoh, J. Kossin, N.-C. Lau, J. Renwick, D.B. Stephenson, S.-P. X. and T. Z. (2013a). "Climate Phenomena and their Relevance for Future Regional Climate Change," in *Climate Change 2013 - The Physical Science Basis*, eds. T. F. Stocker, D. Qin, G.-K. Plattner, M. Tignor, S. K. Allen, J. Boschung, et al. (Cambridge: Cambridge University Press), 1217–1308. Available at: https://www.cambridge.org/core/product/identifier/CBO9781107415324A036/type/book_part.

Christensen, J. H., Kumar, K. K., Aldrian, E., An, S.-I., Cavalcanti, I. F. A., and M. de Castro, W. Dong, P. Goswami, A. Hall, J.K. Kanyanga, A. Kitoh, J. Kossin, N.-C. Lau, J. Renwick, D.B. Stephenson, S.-P. X. and T. Z. (2013b). "Climate Phenomena and their Relevance for Future Regional Climate Change," in *Climate Change 2013 - The Physical Science Basis*, eds. T. F. Stocker, D. Qin, G.-K. Plattner, M. Tignor, S. K. Allen, J. Boschung, et al. (Cambridge: Cambridge University Press), 1217–1308.

Christensen, P., Gillingham, K., and Nordhaus, W. (2018). Uncertainty in forecasts of long-run economic growth. *Proc. Natl. Acad. Sci. U. S. A.* doi:10.1073/pnas.1713628115.

Chu, J.-E., Ha, K.-J., Lee, J.-Y., Wang, B., Kim, B.-H., and Chung, C. E. (2014). Future change of the Indian Ocean basin-wide and dipole modes in the CMIP5. *Clim. Dyn.* 43, 535–551. doi:10.1007/s00382-013-2002-7.

Church, J. a., Clark, P. U., Cazenave, a., Gregory, J. M., Jevrejeva, S., Levermann, a., et al. (2013). Sea level change. *Clim. Chang. 2013 Phys. Sci. Basis. Contrib. Work. Gr. I to Fifth Assess. Rep. Intergov. Panel Clim. Chang.* doi:10.1017/CB09781107415315.026.

Chylek, P., Folland, C., Dijkstra, H., Lesins, G., and Dubey, M. (2011). Ice-core data evidence for a prominent near 20 year time-scale of the Atlantic Multidecadal Oscillation. *Geophys. Res. Lett. - Geophys RES LETT* 38. doi:10.1029/2011GL047501.

Ciais, P., Sabine, C., Bala, G., Bopp, L., Brovkin, V., Canadell, J., et al. (2013). Carbon and Other Biogeochemical Cycles 6. *Clim. Chang. 2013 - Phys. Sci. Basis*. doi:10.1017/CBO9781107415324.015.

Ciavarella, A., Stott, P., and Lowe, J. (2017). Early benefits of mitigation in risk of regional climate extremes. *Nat. Clim. Chang.* 7. doi:10.1038/NCLIMATE3259.

Clark, P. U., Shakun, J. D., Marcott, S. A., Mix, A. C., Eby, M., Kulp, S., et al. (2016). Consequences of twenty-first-century policy for multi-millennial climate and sea-level change. *Nat. Clim. Chang.* 6, 360–369. doi:10.1038/nclimate2923.

Claussen, M., Mysak, L. A., Weaver, A. J., Crucifix, M., Fichefet, T., Loutre, M. F., et al. (2002). Earth system models of intermediate complexity: closing the gap in the spectrum of climate system models. *Clim. Dyn.* 18, 579–586. doi:10.1007/s00382-001-0200-1.

Clement, A., Bellomo, K., Murphy, L. N., Cane, M. A., Mauritsen, T., Radel, G., et al. (2015). The Atlantic Multidecadal Oscillation without a role for ocean circulation. *Science (80-. ).* 350, 320–324. doi:10.1126/science.aab3980.

Collins, J. W., Lamarque, J.-F. J. F., Schulz, M., Boucher, O., Eyring, V., Hegglin, I. M., et al. (2017a). AerChemMIP: Quantifying the effects of chemistry and aerosols in CMIP6. *Geosci. Model Dev.* 10, 585–607. doi:10.5194/gmd-10-585-2017.

Collins, M., Booth, B. B. B., Bhaskaran, B., Harris, G. R., Murphy, J. M., Sexton, D. M. H., et al. (2011). Climate model errors, feedbacks and forcings: a comparison of perturbed physics and multi-model ensembles. *Clim. Dyn.* 36, 1737–1766.

Collins, M., Knutti, R., Arblaster, J., Dufresne, J.-L.-L., Fichefet, T., Friedlingstein, P., et al. (2013). "Long-term Climate Change: Projections, Commitments and Irreversibility," in *Climate Change 2013: The Physical Science Basis. Contribution of Working Group I to the Fifth Assessment Report of the Intergovernmental Panel on Climate Change*, eds. T. F. Stocker, D. Qin, G.-K. Plattner, M. Tignor, S. K. Allen, J. Boschung, et al. (Cambridge, United Kingdom and New York, NY, USA: Cambridge University Press). doi:10.1017/CBO9781107415324.024.

Collins, W. D., Feldman, D. R., Kuo, C., and Nguyen, N. H. (2018). Large regional shortwave forcing by anthropogenic methane informed by Jovian observations. *Sci. Adv.* 4, 1–10. doi:10.1126/sciadv.aas9593.

Collins, W. J., Lamarque, J.-F., Schulz, M., Boucher, O., Eyring, V., Hegglin, M. I., et al. (2017b). AerChemMIP: quantifying the effects of chemistry and aerosols in CMIP6. *Geosci. Model Dev.* 10, 585–607. doi:10.5194/gmd-10-585-2017.

COP21 (2015). Adoption of the Paris Agreement. Conference of the Parties Available at: https://unfccc.int/resource/docs/2015/cop21/eng/l09r01.pdf.

Corti, S., Palmer, T., Balmaseda, M., Weisheimer, A., Drijfhout, S., Dunstone, N., et al. (2015). Impact of initial conditions versus external forcing in decadal climate predictions: A sensitivity experiment. *J. Clim.* 28, 4454–4470. doi:10.1175/JCLI-D-14-00671.1.

Corti, S., Weisheimer, A., Palmer, T. N., Doblas-Reyes, F. J., and Magnusson, L. (2012). Reliability of decadal predictions. *Geophys. Res. Lett.* 39, L21712. doi:10.1029/2012GL053354.

Cox, P. M., Huntingford, C., and Williamson, M. S. (2018). Emergent constraint on equilibrium climate sensitivity from global temperature variability. *Nature* 553, 319–322. Available at: http://dx.doi.org/10.1038/nature25450.

Cox, P., and Stephenson, D. (2007). A Changing Climate for Prediction. *Science (80-. ).* 317, 207–208. Available at: http://science.sciencemag.org/content/317/5835/207.abstract.

Crook, J. A., Forster, P. M., and Stuber, N. (2011). Spatial patterns of modeled climate feedback and contributions to temperature response and polar amplification. *J. Clim.* 24, 3575–3592. doi:10.1175/2011JCLI3863.1.

Crook, J. A., Jackson, L. S., Osprey, S. M., and Forster, P. M. (2015). A comparison of temperature and precipitation responses to different earth radiation management geoengineering schemes. *J. Geophys. Res.* 120, 9352–9373. doi:10.1002/2015JD023269.

Curry, C. L., Sillmann, J., Bronaugh, D., Alterskjaer, K., Cole, J. N. S., Ji, D., et al. (2014). A multimodel examination of climate extremes in an idealized geoengineering experiment. *J. Geophys. Res. Atmos.* 119, 3900–3923. doi:10.1002/2013JD020648.

Cvijanovic, I., Caldeira, K., and MacMartin, D. G. (2015). Impacts of ocean albedo alteration on Arctic sea ice restoration and Northern Hemisphere climate. *Environ. Res. Lett.* 10, 44020. doi:10.1088/1748-9326/10/4/044020.

Dai, A., Fyfe, J. C., Xie, S. P., and Dai, X. (2015). Decadal modulation of global surface temperature by internal climate variability. *Nat. Clim. Chang.* 5, 555–559. doi:10.1038/nclimate2605.

Dai, Z., Weisenstein, D. K., and Keith, D. W. (2018). Tailoring Meridional and Seasonal Radiative Forcing by Sulfate Aerosol Solar Geoengineering. *Geophys. Res. Lett.* 45, 1030–1039. doi:10.1002/2017GL076472.

Dakos, V., Scheffer, M., Nes, E. H. van, Brovkin, V., Petoukhov, V., and Held, H. (2008). Slowing down as an early warning signal for abrupt climate change. *Proc. Natl. Acad. Sci.* 105, 14308–14312. doi:10.1073/PNAS.0802430105.

Danabasoglu, G., and Gent, P. R. (2009). Equilibrium climate sensitivity: Is it accurate to use a slab ocean model? *J. Clim.* 22, 2494–2499. doi:10.1175/2008JCLI2596.1.

Davini, P., Cagnazzo, C., Gualdi, S., and Navarra, A. (2012). Bidimensional Diagnostics, Variability, and Trends of Northern Hemisphere Blocking. *J. Clim.* 25, 6496–6509. doi:10.1175/JCLI-D-12-00032.1.

Davini, P., and D'Andrea, F. (2019). From CMIP-3 to CMIP-6 : Northern Hemisphere atmospheric blocking simulation in present and future climate. *J. Clim.*

Davini, P., Von Hardenberg, J., Corti, S., Christensen, H. M., Juricke, S., Subramanian, A., et al. (2017). Climate SPHINX: Evaluating the impact of resolution and stochastic physics parameterisations in the EC-Earth global climate model. *Geosci. Model Dev.* 10, 1383–1402. doi:10.5194/gmd-10-1383-2017.

Davis, S. J., and Socolow, R. H. (2014). Commitment accounting of CO2emissions. *Environ. Res. Lett.* 9, 84018. doi:10.1088/1748-9326/9/8/084018.
Dawson, A., and Palmer, T. N. (2015). Simulating weather regimes: impact of model resolution and stochastic parameterization. *Clim. Dyn.* 44, 2177–2193. doi:10.1007/s00382-014-2238-x.
de Lavergne, C., Palter, J. B., Galbraith, E. D., Bernardello, R., and Marinov, I. (2014). Cessation of deep convection in the open Southern Ocean under anthropogenic climate change. *Nat. Clim. Chang.* 4, 278–282. doi:10.1038/nclimate2132.
De Vries, H., Haarsma, R. J., and Hazeleger, W. (2012). Western European cold spells in current and future climate. *Geophys. Res. Lett.* 39, L04706. doi:10.1029/2011GL050665.
Deng, K., Yang, S., Ting, M., Tan, Y., and He, S. (2018). Global Monsoon Precipitation: Trends, Leading Modes, and Associated Drought and Heat Wave in the Northern Hemisphere. *J. Clim.* 31, 6947–6966. doi:10.1175/JCLI-D-17-0569.1.
Deser, C., Hurrell, J. W., and Phillips, A. S. (2017). The role of the North Atlantic Oscillation in European climate projections. *Clim. Dyn.* 49, 3141–3157. doi:10.1007/s00382-016-3502-z.
Deser, C., Knutti, R., Solomon, S., and Phillips, A. S. (2012a). Communication of the role of natural variability in future North American climate. *Nat. Clim. Chang.* 2, 775–779. Available at: http://dx.doi.org/10.1038/nclimate1562.
Deser, C., Lehner, F., Rodgers, K. B., Ault, T., Delworth, T. L., DiNezio, P. N., et al. (9999). Strength in numbers: Insights from initial-condition large ensembles with multiple Earth system models and future prospects. *Nat. Clim. Chang.* (submitted.
Deser, C., and Phillips, A. (2017). An overview of decadal-scale sea surface temperature variability in the observational record. *Jt. Issue CLIVAR Exch. PAGES Mag.* 25, 2–6.
Deser, C., Phillips, A., Bourdette, V., and Teng, H. (2012b). Uncertainty in climate change projections: the role of internal variability. *Clim. Dyn.* 38, 527–546. doi:10.1007/s00382-010-0977-x.
Deser, C., Phillips, A. S., Alexander, M. A., and Smoliak, B. V. (2014). Projecting North American climate over the next 50 years: Uncertainty due to internal variability. *J. Clim.* 27, 2271–2296. doi:10.1175/JCLI-D-13-00451.1.
Deser, C., Terray, L., and Phillips, A. S. (2016). Forced and internal components of winter air temperature trends over North America during the past 50 years: Mechanisms and implications. *J. Clim.* 29, 2237–2258. doi:10.1175/JCLI-D-15-0304.1.
Deser, C., Tomas, R. A., and Sun, L. (2015). The Role of Ocean–Atmosphere Coupling in the Zonal-Mean Atmospheric Response to Arctic Sea Ice Loss. *J. Clim.* 28, 2168–2186. doi:10.1175/JCLI-D-14-00325.1.
Dhomse, S. S., Kinnison, D., Chipperfield, M. P., Salawitch, R. J., Cionni, I., Hegglin, M. I., et al. (2018). Estimates of ozone return dates from Chemistry-Climate Model Initiative simulations. *Atmos. Chem. Phys.* 18, 8409–8438. doi:10.5194/acp-18-8409-2018.
Doblas-Reyes, F. J., Andreu-Burillo, I., Chikamoto, Y., García-Serrano, J., Guemas, V., Kimoto, M., et al. (2013). Initialized near-term regional climate change prediction. *Nat. Commun.* 4, 1715. doi:10.1038/ncomms2704.
Dong, B., Gregory, J. M., and Sutton, R. T. (2009). Understanding land-sea warming contrast in response to increasing greenhouse gases. Part I: Transient adjustment. *J. Clim.* 22, 3079–3097.
Donohoe, A., and Battisti, D. S. (2013). The Seasonal Cycle of Atmospheric Heating and Temperature. *J. Clim.* 26, 4962–4980. doi:10.1175/JCLI-D-12-00713.1.
Dosio, A., and Fischer, E. M. (2018). Will Half a Degree Make a Difference? Robust Projections of Indices of Mean and Extreme Climate in Europe Under 1.5°C, 2°C, and 3°C Global Warming. *Geophys. Res. Lett.* 45, 935–944. doi:10.1002/2017GL076222.
Dosio, A., Mentaschi, L., Fischer, E. M., and Wyser, K. (2018). Extreme heat waves under 1.5 °C and 2 °C global warming. *Environ. Res. Lett.* 13, 054006. doi:10.1088/1748-9326/aab827.
Douville, H., Voldoire, A., and Geoffroy, O. (2015). The recent global warming hiatus: What is the role of Pacific variability? *Geophys. Res. Lett.* 42, 880–888. doi:10.1002/2014GL062775.
Drijfhout, S., Bathiany, S., Beaulieu, C., Brovkin, V., Claussen, M., Huntingford, C., et al. (2015). Catalogue of abrupt shifts in Intergovernmental Panel on Climate Change climate models. *Proc. Natl. Acad. Sci. U. S. A.* 112, E5777–E5786. doi:10.1073/pnas.1511451112.
Drost, F., Karoly, D., and Braganza, K. (2012). Communicating global climate change using simple indices: An update. *Clim. Dyn.* 39, 989–999.
Du, Y., Xie, S.-P., Yang, Y.-L., Zheng, X.-T., Liu, L., and Huang, G. (2013). Indian Ocean Variability in the CMIP5 Multimodel Ensemble: The Basin Mode. *J. Clim.* 26, 7240–7266. doi:10.1175/JCLI-D-12-00678.1.
Duan, L. (2019). Climate Response to Pulse Versus Sustained Stratospheric Aerosol Forcing Geophysical Research Letters. 1–9. doi:10.1029/2019GL083701.
Duan, L., Cao, L., Bala, G., and Caldeira, K. (2018). Comparison of the Fast and Slow Climate Response to Three Radiation Management Geoengineering Schemes. *J. Geophys. Res. Atmos.* 123, 11,980-12,001. doi:10.1029/2018JD029034.
Dunn-Sigouin, E., Son, S.-W., and Lin, H. (2013). Evaluation of Northern Hemisphere Blocking Climatology in the Global Environment Multiscale Model. *Mon. Weather Rev.* 141, 707–727. doi:10.1175/MWR-D-12-00134.1.

Dunne, J. P., Stouffer, R. J., and John, J. G. (2013). Reductions in labour capacity from heat stress under climate warming. *Nat. Clim. Chang.* 3, 563–566. doi:10.1038/nclimate1827.
Dunstone, N. J., Smith, D. M., and Eade, R. (2011). Multi-year predictability of the tropical Atlantic atmosphere driven by the high latitude North Atlantic Ocean. *Geophys. Res. Lett.* 38, L14701. doi:10.1029/2011GL047949.
Dwyer, J. G., Biasutti, M., and Sobel, A. H. (2012). Projected Changes in the Seasonal Cycle of Surface Temperature. *J. Clim.* 25, 6359–6374. doi:10.1175/JCLI-D-11-00741.1.
Eade, R., Smith, D., Scaife, A., Wallace, E., Dunstone, N., Hermanson, L., et al. (2014). Do seasonal-to-decadal climate predictions underestimate the predictability of the real world? *Geophys. Res. Lett.* 41, 5620–5628. doi:10.1002/2014GL061146.
Eby, M., Weaver, A. J., Alexander, K., Zickfeld, K., Abe-Ouchi, A., Cimatoribus, A. A., et al. (2013). Historical and Idealized Climate Model Experiments: An EMIC Intercomparison. *Clim. Past* 9, 1111–1140.
Ehlert, D., and Zickfeld, K. (2018). Irreversible ocean thermal expansion under carbon dioxide removal. *Earth Syst. Dynam* 9, 197–210. doi:10.5194/esd-9-197-2018.
Emori, S., and Brown, S. J. (2005). Dynamic and thermodynamic changes in mean and extreme precipitation under changed climate. *Geophys. Res. Lett.* doi:10.1029/2005GL023272.
Endo, H., and Kitoh, A. (2014). Thermodynamic and dynamic effects on regional monsoon rainfall changes in a warmer climate. *Geophys. Res. Lett.* 41, 1704–1710. doi:10.1002/2013GL059158.
Engelbrecht, F., Adegoke, J., Bopape, M.-J., Naidoo, M., Garland, R., Thatcher, M., et al. (2015). Projections of rapidly rising surface temperatures over Africa under low mitigation. *Environ. Res. Lett.* 10, 085004. doi:10.1088/1748-9326/10/8/085004.
England, M. H., McGregor, S., Spence, P., Meehl, G. A., Timmermann, A., Cai, W., et al. (2014). Recent intensification of wind-driven circulation in the Pacific and the ongoing warming hiatus. *Nat. Clim. Chang.* 4, 222. Available at: https://doi.org/10.1038/nclimate2106.
Etminan, M., Myhre, G., Highwood, E. J., and Shine, K. P. (2016). Radiative forcing of carbon dioxide, methane, and nitrous oxide: A significant revision of the methane radiative forcing. *Geophys. Res. Lett.* 43, 12,614-12,623. doi:10.1002/2016GL071930.
Exarchou, E., Kuhlbrodt, T., Gregory, J. M., and Smith, R. S. (2015). Ocean heat uptake processes: A model intercomparison. *J. Clim.* 28, 887–908. doi:10.1175/JCLI-D-14-00235.1.
Eyring, V., Arblaster, J. M., Cionni, I., Sedláček, J., Perlwitz, J., Young, P. J., et al. (2013). Long-term ozone changes and associated climate impacts in CMIP5 simulations. *J. Geophys. Res. Atmos.* 118, 5029–5060. doi:10.1002/jgrd.50316.
Eyring, V., Bony, S., Meehl, G. A., Senior, C. A., Stevens, B., Stouffer, R. J., et al. (2016a). Overview of the {C}oupled {M}odel {I}ntercomparison {P}roject {P}hase 6 ({C}{M}{I}{P}6) experimental design and organization. *Geosci. Model Dev.* 9, 1937–1958.
Eyring, V., Bony, S., Meehl, G. A., Senior, C. A., Stevens, B., Stouffer, R. J., et al. (2016b). Overview of the Coupled Model Intercomparison Project Phase 6 (CMIP6) experimental design and organization. *Geosci. Model Dev.* 9, 1937–1958. doi:10.5194/gmd-9-1937-2016.
Eyring, V., Righi, M., Lauer, A., Evaldsson, M., Wenzel, S., Jones, C., et al. (2016c). ESMValTool (v1.0) – a community diagnostic and performance metrics tool for routine evaluation of Earth system models in CMIP. *Geosci. Model Dev.* 9, 1747–1802. doi:10.5194/gmd-9-1747-2016.
Fasullo, J. T., Sanderson, B. M., and Trenberth, K. E. (2015). Recent Progress in Constraining Climate Sensitivity With Model Ensembles. *Curr. Clim. Chang. Reports* 1, 268–275. doi:10.1007/s40641-015-0021-7.
Fasullo, J. T., Tilmes, S., Richter, J. H., Kravitz, B., MacMartin, D. G., Mills, M. J., et al. (2018). Persistent polar ocean warming in a strategically geoengineered climate. *Nat. Geosci.* 11, 910–914. doi:10.1038/s41561-018-0249-7.
Fedorov, A., Hu, S., Wittenberg, A., Levine, A., and Deser, C. (2019). "Chapter 6 . ENSO low-frequency modulations and mean state interactions," in, ed. S. A. and C. W. McPhaden Mike (AGU Books). Available at: http://www.cgd.ucar.edu/staff/cdeser/docs/submitted.fedorov.enso_lowfrq_modulations.jan19.pdf.
Feely, R. a, Sabine, C. L., Lee, K., Berelson, W., Kleypas, J., Fabry, V. J., et al. (2004). Impact of anthropogenic CO2 on the CaCO3 system in the oceans. *Science* 305, 362–6. doi:10.1126/science.1097329.
Feng, H., and Zhang, M. (2015). Global land moisture trends: drier in dry and wetter in wet over land. *Sci. Rep.* 5, 18018. doi:10.1038/srep18018.
Ferraro, A. J., Charlton-Perez, A. J., and Highwood, E. J. (2015). Stratospheric dynamics and midlatitude jets under geoengineering with space mirrors and sulfate and titania aerosols. *J. Geophys. Res. Atmos.* 120, 414–429. doi:10.1002/2014JD022734.
Ferraro, A. J., and Griffiths, H. G. (2016). Quantifying the temperature-independent effect of stratospheric aerosol geoengineering on global-mean precipitation in a multi-model ensemble. *Environ. Res. Lett.* 11, 034012. doi:10.1088/1748-9326/11/3/034012.
Ferreira, D., Marshall, J., Bitz, C. M., Solomon, S., and Plumb, A. (2015). Antarctic ocean and sea ice response to ozone depletion: A two-time-scale problem. *J. Clim.* 28, 1206–1226. doi:10.1175/JCLI-D-14-00313.1.
Ferro, C. A. T. (2017). Measuring forecast performance in the presence of observation error. *Q. J. R. Meteorol. Soc.* 143, 2665–2676. doi:10.1002/qj.3115.

Field, L., Ivanova, D., Bhattacharyya, S., Mlaker, V., Sholtz, A., Decca, R., et al. (2018). Increasing Arctic Sea Ice Albedo Using Localized Reversible Geoengineering. *Earth's Futur.* 6, 882–901. doi:10.1029/2018EF000820.

Finney, D. L., Doherty, R. M., Wild, O., Stevenson, D. S., MacKenzie, I. A., and Blyth, A. M. (2018a). A projected decrease in lightning under climate change. *Nat. Clim. Chang.* 8, 210–213. doi:10.1038/s41558-018-0072-6.

Finney, D. L., Doherty, R. M., Wild, O., Stevenson, D. S., MacKenzie, I. A., and Blyth, A. M. (2018b). A projected decrease in lightning under climate change. *Nat. Clim. Chang.* 8, 210–213. doi:10.1038/s41558-018-0072-6.

Fischer, E. M., Beyerle, U., and Knutti, R. (2013). Robust spatially aggregated projections of climate extremes. *Nat. Clim. Chang.* 3, 1033–1038. doi:10.1038/nclimate2051.

Fischer, E. M., and Knutti, R. (2013). Robust projections of combined humidity and temperature extremes. *Nat. Clim. Chang.* 3, 126–130. doi:10.1038/nclimate1682.

Fischer, E. M., and Knutti, R. (2014). Heated debate on cold weather. *Nat. Clim. Chang.* 4, 537–538. Available at: http://dx.doi.org/10.1038/nclimate2286.

Fischer, E. M., Lawrence, D. M., and Sanderson, B. M. (2011). Quantifying uncertainties in projections of extremes-a perturbed land surface parameter experiment. *Clim. Dyn.* 37, 1381–1398. doi:10.1007/s00382-010-0915-y.

Fischer, E. M., Oleson, K. W., and Lawrence, D. M. (2012a). Contrasting urban and rural heat stress responses to climate change. *Geophys. Res. Lett.* 39, L03705. doi:10.1029/2011GL050576.

Fischer, E. M., Rajczak, J., and Schär, C. (2012b). Changes in European summer temperature variability revisited. *Geophys. Res. Lett.* 39, L19702. doi:10.1029/2012GL052730.

Fischer, E. M., and Schär, C. (2010). Consistent geographical patterns of changes in high-impact European heatwaves. *Nat. Geosci.* 3, 398–403. doi:10.1038/ngeo866.

Fischer, E. M., Sedláček, J., Hawkins, E., and Knutti, R. (2014). Models agree on forced response pattern of precipitation and temperature extremes. *Geophys. Res. Lett.* 41, 8554–8562. doi:10.1002/2014GL062018.

Fischer, H., Meissner, K. J., Mix, A. C., Abram, N. J., Austermann, J., Brovkin, V., et al. (2018). Palaeoclimate constraints on the impact of 2 °C anthropogenic warming and beyond. *Nat. Geosci.* 11, 474–485. doi:10.1038/s41561-018-0146-0.

Fix, M. J., Cooley, D., Sain, S. R., and Tebaldi, C. (2018). A comparison of U . S . precipitation extremes under RCP8 . 5 and RCP4 . 5 with an application of pattern scaling. *Clim. Change*, 335–347. doi:10.1007/s10584-016-1656-7.

Fläschner, D., Mauritsen, T., and Stevens, B. (2016). Understanding the intermodel spread in global-mean hydrological sensitivity. *J. Clim.* 29, 801–817. doi:10.1175/JCLI-D-15-0351.1.

Flato, G. M. (2011). Earth system models: an overview. *Wiley Interdiscip. Rev. Clim. Chang.* 2, 783–800. doi:10.1002/wcc.148.

Flato, G., Marotzke, J., Abiodun, B., Braconnot, P., Chou, S. C., Collins, W., et al. (2013). "Evaluation of Climate Models," in *Climate Change 2013: The Physical Science Basis. Contribution of Working Group I to the Fifth Assessment Report of the Intergovernmental Panel on Climate Change*, eds. T. F. Stocker, D. Qin, G.-K. Plattner, M. Tignor, S. K. Allen, J. Boschung, et al. (Cambridge: Cambridge University Press), 741–866. doi:10.1017/CBO9781107415324.

Folland, C. K. (2002). Relative influences of the Interdecadal Pacific Oscillation and ENSO on the South Pacific Convergence Zone. *Geophys. Res. Lett.* 29, 1643. doi:10.1029/2001GL014201.

Foltz, G. R., Seo, K.-H., Dong, C., Chadwick, R., Jiang, J. H., Ma, J., et al. (2018). Responses of the Tropical Atmospheric Circulation to Climate Change and Connection to the Hydrological Cycle. *Annu. Rev. Earth Planet. Sci.* 46, 549–580. doi:10.1146/annurev-earth-082517-010102.

Forster, P. M., Maycock, A. C., McKenna, C. M., and Smith, C. J. (2019). Latest climate models confirm need for urgent mitigation. *Nat. Clim. Chang.* doi:10.1038/s41558-019-0660-0.

Frame, D. J., Macey, A. H., and Allen, M. R. (2014). Cumulative emissions and climate policy. *Nat. Geosci.* 7, 692–693. doi:10.1038/ngeo2254.

Francis, J. A., and Vavrus, S. J. (2015). Evidence for a wavier jet stream in response to rapid Arctic warming. *Environ. Res. Lett.* 10, 014005. doi:10.1088/1748-9326/10/1/014005.

Friedlingstein, P., Meinshausen, M., Arora, V. K., Jones, C. D., Anav, A., Liddicoat, S. K., et al. (2014). Uncertainties in CMIP5 climate projections due to carbon cycle feedbacks. *J. Clim.* 27, 511–526. doi:10.1175/JCLI-D-12-00579.1.

Frieler, K., Meinshausen, M., Mengel, M., Braun, N., and Hare, W. (2012). A scaling approach to probabilistic assessment of regional climate change. *J. Clim.* 25, 3117–3144. doi:10.1175/JCLI-D-11-00199.1.

Frierson, D. M. W., Lu, J., and Chen, G. (2007). Width of the Hadley cell in simple and comprehensive general circulation models. *Geophys. Res. Lett.* 34. doi:10.1029/2007GL031115.

Frisch, M. (2015). Predictivism and old evidence: a critical look at climate model tuning. *Eur. J. Philos. Sci.* 5, 171–190. doi:10.1007/s13194-015-0110-4.

Froelicher, T. L., Sarmiento, J. L., Paynter, D. J., Dunne, J. P., Krasting, J. P., and Winton, M. (2015). Dominance of the Southern Ocean in anthropogenic carbon and heat uptake in CMIP5 models. *J. Clim.* 28, 862–886. doi:10.1175/JCLI-D-14-00117.1.

Frölicher, T. L., and Paynter, D. J. (2015). Extending the relationship between global warming and cumulative carbon emissions to multi-millennial timescales. *Environ. Res. Lett.* 10, 075002. doi:10.1088/1748-9326/10/7/075002.

Frölicher, T. L., Winton, M., and Sarmiento, J. L. (2014a). Continued global warming after CO2 emissions stoppage. *Nat. Clim. Chang.* 4, 40–44. doi:10.1038/nclimate2060.
Frölicher, T. L., Winton, M., and Sarmiento, J. L. (2014b). Continued global warming after CO2 emissions stoppage. *Nat. Clim. Chang.* 4, 40–44. Available at: http://dx.doi.org/10.1038/nclimate2060.
Fu, Q., and Feng, S. (2014). Responses of terrestrial aridity to global warming. *J. Geophys. Res. Atmos.* 119, 7863–7875.
Fučkar, N. S., Volpi, D., Guemas, V., and Doblas-Reyes, F. J. (2014). A posteriori adjustment of near-term climate predictions: Accounting for the drift dependence on the initial conditions. *Geophys. Res. Lett.* 41, 5200–5207. doi:10.1002/2014GL060815.
Fujita, M., Mizuta, R., Ishii, M., Endo, H., Sato, T., Okada, Y., et al. (2019). Precipitation Changes in a Climate With 2-K Surface Warming From Large Ensemble Simulations Using 60-km Global and 20-km Regional Atmospheric Models. *Geophys. Res. Lett.* 46, 435–442. doi:10.1029/2018GL079885.
Fyfe, J. C., Boer, G. J., and Flato, G. M. (1999). The Arctic and Antarctic oscillations and their projected changes under global warming. *Geophys. Res. Lett.* 26, 1601–1604. doi:10.1029/1999GL900317.
G. Chiodo, L. M. P. (2016). Reduction of Climate Sensitivity to Solar Forcing due to Stratospheric Ozone Feedback. 4651–4663. doi:10.1175/JCLI-D-15-0721.1.
Gabriel, C. J., Robock, A., Xia, L., Zambri, B., and Kravitz, B. (2017). The G4Foam Experiment: global climate impacts of regional ocean albedo modification. *Atmos. Chem. Phys.* 17, 595–613. doi:10.5194/acp-17-595-2017.
Gagné, M.-È. È., Fyfe, J. C., Gillett, N. P., Polyakov, I. V., and Flato, G. M. (2017). Aerosol-driven increase in Arctic sea ice over the middle of the twentieth century. *Geophys. Res. Lett.* 44, 7338–7346. doi:10.1002/2016GL071941.
Gagné, M.-È., Gillett, N. P., and Fyfe, J. C. (2015). Impact of aerosol emission controls on future Arctic sea ice cover. *Geophys. Res. Lett.* 42, 8481–8488. doi:10.1002/2015GL065504.
Ganopolski, A., and Rahmstorf, S. (2001). Rapid changes of glacial climate simulated in a coupled climate model. *Nature* 409, 153.
García-Serrano, J., Guemas, V., and Doblas-Reyes, F. J. (2015). Added-value from initialization in predictions of Atlantic multi-decadal variability. *Clim. Dyn.* 44, 2539–2555. doi:10.1007/s00382-014-2370-7.
Garfinkel, C. I., Waugh, D. W., and Polvani, L. M. (2015). Recent Hadley cell expansion: The role of internal atmospheric variability in reconciling modeled and observed trends. *Geophys. Res. Lett.* 42, 10,824-10,831. doi:10.1002/2015GL066942.
Gasparini, B., and Lohmann, U. (2016). Why cirrus cloud seeding cannot substantially cool the planet. *J. Geophys. Res. Atmos.* 121, 4877–4893. doi:10.1002/2015JD024666.
Gasparini, B., Münch, S., Poncet, L., Feldmann, M., and Lohmann, U. (2017). Is increasing ice crystal sedimentation velocity in geoengineering simulations a good proxy for cirrus cloud seeding? *Atmos. Chem. Phys.* 17, 4871–4885. doi:10.5194/acp-17-4871-2017.
Geden, O., and Loeschel, A. (2017). Define limits for temperature overshoot targets. *Nat. Geosci.* 10, 881–882. doi:10.1038/s41561-017-0026-z.
Geng, T., Yang, Y., and Wu, L. (2019). On the Mechanisms of Pacific Decadal Oscillation Modulation in a Warming Climate. *J. Clim.* 32, 1443–1459. doi:10.1175/JCLI-D-18-0337.1.
Gidden, M. J., Riahi, K., Smith, S. J., Fujimori, S., Luderer, G., Kriegler, E., et al. (2018). Global emissions pathways under different socioeconomic scenarios for use in CMIP6: a dataset of harmonized emissions trajectories through the end of the century. *Geosci. Model Dev. Discuss.*, 1–42. doi:10.5194/gmd-2018-266.
Gillett, N. P., Arora, V. K., Matthews, D., and Allen, M. R. (2013). Constraining the Ratio of Global Warming to Cumulative CO2 Emissions Using CMIP5 Simulations. *J. Clim.* 26, 6844–6858. doi:10.1175/JCLI-D-12-00476.1.
Gillett, N. P., and Fyfe, J. C. (2013). Annular mode changes in the CMIP5 simulations. *Geophys. Res. Lett.* 40, 1189–1193. doi:10.1002/grl.50249.
Gillett, N. P., and Von Salzen, K. (2013). The role of reduced aerosol precursor emissions in driving near-term warming. *Environ. Res. Lett.* 8. doi:10.1088/1748-9326/8/3/034008.
Giorgi, F., Torma, C., Coppola, E., Ban, N., Schär, C., and Somot, S. (2016). Enhanced summer convective rainfall at Alpine high elevations in response to climate warming. *Nat. Geosci.* doi:10.1038/ngeo2761.
Goddard, L., Kumar, A., Solomon, A., Smith, D., Boer, G., Gonzalez, P., et al. (2013). A verification framework for interannual-to-decadal predictions experiments. *Clim. Dyn.* 40, 245–272. doi:10.1007/s00382-012-1481-2.
Gong, D., and Wang, S. (1999). Definition of Antarctic Oscillation index. *Geophys. Res. Lett.* 26, 459–462. doi:10.1029/1999GL900003.
González, M. F., Ilyina, T., Sonntag, S., and Schmidt, H. (2018). Enhanced Rates of Regional Warming and Ocean Acidification After Termination of Large‐Scale Ocean Alkalinization. *Geophys. Res. Lett.* 45, 7120–7129. doi:10.1029/2018GL077847.
Good, P., Bamber, J., Halladay, K., Harper, A. B., Jackson, L. C., Kay, G., et al. (2018). Recent progress in understanding climate thresholds: Ice sheets, the Atlantic meridional overturning circulation, tropical forests and responses to ocean acidification. *Prog. Phys. Geogr. Earth Environ.* 42, 24–60.
Good, P., Booth, B. B. B., Chadwick, R., Hawkins, E., Jonko, A., and Lowe, J. A. (2016). Large differences in regional

precipitation change between a first and second 2 K of global warming. *Nat. Commun.* 7, 13667. doi:10.1038/ncomms13667.
Good, P., Lowe, J. A., Andrews, T., Wiltshire, A., Chadwick, R., Ridley, J. K., et al. (2015). Nonlinear regional warming with increasing CO2concentrations. *Nat. Clim. Chang.* 5, 138–142. doi:10.1038/nclimate2498.
Goodman, J., and Marshall, J. (1999). A Model of Decadal Middle-Latitude Atmosphere–Ocean Coupled Modes. *J. Clim.* 12, 621–641. doi:10.1175/1520-0442(1999)012<0621:AMODML>2.0.CO;2.
Goosse, H., Kay, J. E., Armour, K. C., Bodas-Salcedo, A., Chepfer, H., Docquier, D., et al. (2018). Quantifying climate feedbacks in polar regions. *Nat. Commun.* 9, 1919. doi:10.1038/s41467-018-04173-0.
Graff, L. S., and LaCasce, J. H. (2014). Changes in Cyclone Characteristics in Response to Modified SSTs. *J. Clim.* 27, 4273–4295. doi:10.1175/JCLI-D-13-00353.1.
Gregory, J. M., and Mitchell, J. F. B. (1995). Simulation of daily variability of surface temperature and precipitation over europe in the current and 2 × Co2 climates using the UKMO climate model. *Q. J. R. Meteorol. Soc.* 121, 1451–1476. doi:10.1002/qj.49712152611.
Greve, P., Orlowsky, B., Mueller, B., Sheffield, J., Reichstein, M., and Seneviratne, S. I. (2014). Global assessment of trends in wetting and drying over land. *Nat. Geosci.* 7, 716–721.
Grieger, J., Leckebusch, G. C., Donat, M. G., Schuster, M., and Ulbrich, U. (2014). Southern Hemisphere winter cyclone activity under recent and future climate conditions in multi-model AOGCM simulations. *Int. J. Climatol.* 34, 3400–3416. doi:10.1002/joc.3917.
Grise, K. M., and Polvani, L. M. (2014a). Is climate sensitivity related to dynamical sensitivity? A Southern Hemisphere perspective. *Geophys. Res. Lett.* 41, 534–540. doi:10.1002/2013GL058466.
Grise, K. M., and Polvani, L. M. (2014b). The response of midlatitude jets to increased CO2: Distinguishing the roles of sea surface temperature and direct radiative forcing. *Geophys. Res. Lett.* 41, 6863–6871. doi:10.1002/2014GL061638.
Grise, K. M., and Polvani, L. M. (2016). Is climate sensitivity related to dynamical sensitivity? *J. Geophys. Res. Atmos.* 121, 5159–5176. doi:10.1002/2015JD024687.
Grise, K. M., and Polvani, L. M. (2017). Understanding the Time Scales of the Tropospheric Circulation Response to Abrupt CO 2 Forcing in the Southern Hemisphere: Seasonality and the Role of the Stratosphere. *J. Clim.* 30, 8497–8515. doi:10.1175/JCLI-D-16-0849.1.
Grose, M. R., Gregory, J., Colman, R., and Andrews, T. (2018). What Climate Sensitivity Index Is Most Useful for Projections? *Geophys. Res. Lett.* 45, 1559–1566.
Gruber, S., Blahak, U., Haenel, F., Kottmeier, C., Leisner, T., Muskatel, H., et al. (2019). A Process Study on Thinning of Arctic Winter Cirrus Clouds With High-Resolution ICON-ART Simulations. *J. Geophys. Res. Atmos.* doi:10.1029/2018JD029815.
Guemas, V., Blanchard-Wrigglesworth, E., Chevallier, M., Day, J. J., Déqué, M., Doblas-Reyes, F. J., et al. (2016). A review on Arctic sea-ice predictability and prediction on seasonal to decadal time-scales. *Q. J. R. Meteorol. Soc.* 142, 546–561. doi:10.1002/qj.2401.
Guemas, V., Corti, S., García-Serrano, J., Doblas-Reyes, F. J., Balmaseda, M., and Magnusson, L. (2013a). The Indian Ocean: The Region of Highest Skill Worldwide in Decadal Climate Prediction. *J. Clim.* 26, 726–739. doi:10.1175/JCLI-D-12-00049.1.
Guemas, V., Doblas-Reyes, F. J., Andreu-Burillo, I., and Asif, M. (2013b). Retrospective prediction of the global warming slowdown in the past decade. *Nat. Clim. Chang.* 3, 649–653. doi:10.1038/nclimate1863.
Hall, A. (2004). The Role of Surface Albedo Feedback in Climate. *J. Clim.* 17, 1550–1568. doi:10.1175/1520-0442(2004)017<1550:TROSAF>2.0.CO;2.
Hall, A., and Qu, X. (2006). Using the current seasonal cycle to constrain snow albedo feedback in future climate change. *Geophys. Res. Lett.* 33, L03502. doi:10.1029/2005GL025127.
Hanna, E., Fettweis, X., and Hall, R. J. (2018). Brief communication: Recent changes in summer Greenland blocking captured by none of the CMIP5 models. *Cryosph.* 12, 3287–3292. doi:10.5194/tc-12-3287-2018.
Hansen, J., Lacis, A., Rind, D., Russell, G., Stone, P., Fung, I., et al. (1984). *Climate sensitivity: Analysis of feedback mechanisms*. doi:10.1029/GM029p0130.
Harrington, L. J., Frame, D. J., Fischer, E. M., Hawkins, E., Joshi, M., and Jones, C. D. (2016). Poorest countries experience earlier anthropogenic emergence of daily temperature extremes. *Environ. Res. Lett.* 11. doi:10.1088/1748-9326/11/5/055007.
Hartmann, D. L., Klein Tank, A. M. G., Rusticucci, M., Alexander, L. V., Brönnimann, S., Charabi, Y. A. R., et al. (2013). "Observations: Atmosphere and Surface," in *Climate Change 2013: The Physical Science Basis. Contribution of Working Group I to the Fifth Assessment Report of the Intergovernmental Panel on Climate Change*, eds. T. F. Stocker, D. Qin, G.-K. Plattner, M. Tignor, S. K. Allen, J. Boschung, et al. (Cambridge: Cambridge University Press), 159–254. Available at: https://www.cambridge.org/core/product/identifier/CBO9781107415324A016/type/book_part.
Harvey, B. J., Shaffrey, L. C., and Woollings, T. J. (2014). Equator-to-pole temperature differences and the extra-tropical storm track responses of the CMIP5 climate models. *Clim. Dyn.* 43, 1171–1182. doi:10.1007/s00382-013-1883-9.

Harvey, B. J., Shaffrey, L. C., and Woollings, T. J. (2015). Deconstructing the climate change response of the Northern Hemisphere wintertime storm tracks. *Clim. Dyn.* 45, 2847–2860. doi:10.1007/s00382-015-2510-8.

Hawcroft, M., Walsh, E., Hodges, K., and Zappa, G. (2018). Significantly increased extreme precipitation expected in Europe and North America from extratropical cyclones. *Environ. Res. Lett.* 13, 124006. doi:10.1088/1748-9326/aaed59.

Hawkins, E., Anderson, B., Diffenbaugh, N., Mahlstein, I., Betts, R., Hegerl, G., et al. (2014). Uncertainties in the timing of unprecedented climates. *Nature* 511, E3–E5. doi:10.1038/nature13523.

Hawkins, E., Smith, R. S., Gregory, J. M., and Stainforth, D. A. (2016). Irreducible uncertainty in near-term climate projections. *Clim. Dyn.* 46, 3807–3819. doi:10.1007/s00382-015-2806-8.

Hawkins, E., and Sutton, R. (2009). The Potential to Narrow Uncertainty in Regional Climate Predictions. *Bull. Am. Meteorol. Soc.* 90, 1095–1108. doi:10.1175/2009BAMS2607.1.

Hawkins, E., and Sutton, R. (2011). The potential to narrow uncertainty in projections of regional precipitation change. *Clim. Dyn.* 37, 407–418. doi:10.1007/s00382-010-0810-6.

Hawkins, E., and Sutton, R. (2012). Time of emergence of climate signals. *Geophys. Res. Lett.* 39, 1–6. doi:10.1029/2011GL050087.

Hawkins, E., and Sutton, R. (2016). Connecting Climate Model Projections of Global Temperature Change with the Real World. *Bull. Am. Meteorol. Soc.* 97, 963–980. doi:10.1175/BAMS-D-14-00154.1.

Hazeleger, W., Guemas, V., Wouters, B., Corti, S., Andreu-Burillo, I., Doblas-Reyes, F. J., et al. (2013). Multiyear climate predictions using two initialization strategies. *Geophys. Res. Lett.* 40, 1794–1798. doi:10.1002/grl.50355.

Hazeleger, W., Van Den Hurk, B. J. J. M., Min, E., Van Oldenborgh, G. J., Petersen, A. C., Stainforth, D. A., et al. (2015). Tales of future weather. *Nat. Clim. Chang.* 5, 107–113. doi:10.1038/nclimate2450.

Hedemann, C., Mauritsen, T., Jungclaus, J., and Marotzke, J. (2017). The subtle origins of surface-warming hiatuses. *Nat. Clim. Chang.* 7, 336–339. doi:10.1038/nclimate3274.

Held, I. M., and Soden, B. J. (2006). Robust responses of the hydrological cycle to global warming. *J. Clim.* 19, 5686–5699. doi:10.1175/JCLI3990.1.

Held, I. M., Winton, M., Takahashi, K., Delworth, T., Zeng, F. R., and Vallis, G. K. (2010). Probing the Fast and Slow Components of Global Warming by Returning Abruptly to Preindustrial Forcing. *J. Clim.* 23, 2418–2427.

Henley, B. J. (2017). Pacific decadal climate variability: Indices, patterns and tropical-extratropical interactions. *Glob. Planet. Change* 155, 42–55. doi:https://doi.org/10.1016/j.gloplacha.2017.06.004.

Herger, N., Abramowitz, G., Knutti, R., Angélil, O., Lehmann, K., and Sanderson, B. M. (2018). Selecting a climate model subset to optimise key ensemble properties. *Earth Syst. Dyn.* 9, 135–151.

Herger, N., Sanderson, B. M., and Knutti, R. (2015). Improved pattern scaling approaches for the use in climate impact studies. *Geophys. Res. Lett.* 42, 3486–3494. doi:10.1002/2015GL063569.

Hermanson, L., Eade, R., Robinson, N. H., Dunstone, N. J., Andrews, M. B., Knight, J. R., et al. (2014). Forecast cooling of the Atlantic subpolar gyre and associated impacts. *Geophys. Res. Lett.* 41, 5167–5174. doi:10.1002/2014gl060420.

Hewitt, A. J., Booth, B. B. B., Jones, C. D., Robertson, E. S., Wiltshire, A. J., Sansom, P. G., et al. (2016). Sources of Uncertainty in Future Projections of the Carbon Cycle. *J. Clim.* 29, 7203–7213. doi:10.1175/JCLI-D-16-0161.1.

Hezel, P. J., Fichefet, T., and Massonnet, F. (2014). Modeled Arctic sea ice evolution through 2300 in CMIP5 extended RCPs. *Cryosph.* 8, 1195–1204.

Hienola, A., Matthews, D., Korhonen, H., Pietikäinen, J.-P., O'Donnell, D., Partanen, A.-I., et al. (2018). The impact of aerosol emissions on the 1.5oC pathways. *Environ. Res. Lett.* doi:10.1088/1748-9326/aab1b2.

Hingray, B., and Saïd, M. (2014). Partitioning Internal Variability and Model Uncertainty Components in a Multimember Multimodel Ensemble of Climate Projections. *J. Clim.* 27, 6779–6798. doi:10.1175/JCLI-D-13-00629.1.

Hoegh-Guldberg, O., Jacob, D., Taylor, M., Bindi, M., Brown, S., Camilloni, I., et al. (2018). "Impacts of 1.5°C Global Warming on Natural and Human Systems," in *Global Warming of 1.5°C. An IPCC Special Report on the impacts of global warming of 1.5°C above pre-industrial levels and related global greenhouse gas emission pathways, in the context of strengthening the global response to the threat of climate change,* eds. V. Masson-Delmotte, P. Zhai, H.-O. Pörtner, D. Roberts, J. Skea, P. R. Shukla, et al. (In Press). Available at: https://www.ipcc.ch/sr15.

Hoerling, M., Hurrell, J., Kumar, A., Terray, L., Eischeid, J., Pegion, P., et al. (2011). On North American Decadal Climate for 2011–20. *J. Clim.* 24, 4519–4528. doi:10.1175/2011JCLI4137.1.

Holland, M. M., and Bitz, C. M. (2003). Polar amplification of climate change in coupled models. *Clim. Dyn.* 21, 221–232. doi:10.1007/s00382-003-0332-6.

Holmes, C. R., Woollings, T., Hawkins, E., and de Vries, H. (2016). Robust Future Changes in Temperature Variability under Greenhouse Gas Forcing and the Relationship with Thermal Advection. *J. Clim.* 29, 2221–2236. doi:10.1175/JCLI-D-14-00735.1.

Hong, Y., Moore, J. C., Jevrejeva, S., Ji, D., Phipps, S. J., Lenton, A., et al. (2017). Impact of the GeoMIP G1 sunshade geoengineering experiment on the Atlantic meridional overturning circulation. *Environ. Res. Lett.* 12. doi:10.1088/1748-9326/aa5fb8.

Horton, R. M., Mankin, J. S., Lesk, C., Coffel, E., and Raymond, C. (2016). A Review of Recent Advances in Research

on Extreme Heat Events. *Curr. Clim. Chang. Reports* 2, 242–259. doi:10.1007/s40641-016-0042-x.
Hoskins, B., and Woollings, T. (2015). Persistent Extratropical Regimes and Climate Extremes. *Curr. Clim. Chang. Reports* 1, 115–124. doi:10.1007/s40641-015-0020-8.
Hsu, P., Li, T., Murakami, H., and Kitoh, A. (2013). Future change of the global monsoon revealed from 19 CMIP5 models. *J. Geophys. Res. Atmos.* 118, 1247–1260. doi:10.1002/jgrd.50145.
Huang, P., and Xie, S. P. (2015). Mechanisms of change in ENSO-induced tropical Pacific rainfall variability in a warming climate. *Nat. Geosci.* doi:10.1038/ngeo2571.
Huang, P., Xie, S. P., Hu, K., Huang, G., and Huang, R. (2013). Patterns of the seasonal response of tropical rainfall to global warming. *Nat. Geosci.* 6, 357–361. doi:10.1038/ngeo1792.
Huntingford, C., Jones, P. D., Livina, V. N., Lenton, T. M., and Cox, P. M. (2013). No increase in global temperature variability despite changing regional patterns. *Nature* 500, 327–330. doi:10.1038/nature12310.
Hurd, C. L., Lenton, A., Tilbrook, B., and Boyd, P. W. (2018). Current understanding and challenges for oceans in a higher-CO2 world. *Nat. Clim. Chang.* 8, 686–694. doi:10.1038/s41558-018-0211-0.
Hwang, Y.-T. Y.-T., Frierson, D. M. W., and Kang, S. M. (2013). Anthropogenic sulfate aerosol and the southward shift of tropical precipitation in the late 20th century. *Geophys. Res. Lett.* 40, 2845–2850. doi:10.1002/grl.50502.
Iglesias-Suarez, F., Rap, A., Kinnison, D. E., Wild, O., Maycock, A. C., and Young, P. J. (2018). Key drivers of ozone change and its radiative forcing over the 21st century. *Atmos. Chem. Phys.* 18, 6121–6139. doi:10.5194/acp-18-6121-2018.
Iles, C. E., and Hegerl, G. C. (2014). The global precipitation response to volcanic eruptions in the CMIP5 models. *Environ. Res. Lett.* 9, 104012. doi:10.1088/1748-9326/9/10/104012.
Iles, C. E., and Hegerl, G. C. (2015). Systematic change in global patterns of streamflow following volcanic eruptions. *Nat. Geosci.* 8, 838–842. doi:10.1038/ngeo2545.
Iles, C. E., Hegerl, G. C., Schurer, A. P., and Zhang, X. (2013). The effect of volcanic eruptions on global precipitation. *J. Geophys. Res. Atmos.* 118, 8770–8786. doi:10.1002/jgrd.50678.
IPCC (2014). *Climate Change 2014: Mitigation of Climate Change*. doi:10.1017/CBO9781107415416.
Irvine, P., Emanuel, K., He, J., Horowitz, L. W., Vecchi, G., and Keith, D. (2019). Halving warming with idealized solar geoengineering moderates key climate hazards. *Nat. Clim. Chang.* 9, 295–299. doi:10.1038/s41558-019-0398-8.
Irvine, P. J., Kravitz, B., Lawrence, M. G., and Muri, H. (2016). An overview of the Earth system science of solar geoengineering. *Wiley Interdiscip. Rev. Clim. Chang.* 7, 815–833. doi:10.1002/wcc.423.
Ishizaki, Y., Shiogama, H., Emori, S., Yokohata, T., Nozawa, T., Takahashi, K., et al. (2013). Dependence of Precipitation Scaling Patterns on Emission Scenarios for Representative Concentration Pathways. *J. Clim.* 26, 8868–8879. doi:10.1175/JCLI-D-12-00540.1.
Izumi, K., Bartlein, P. J., and Harrison, S. P. (2013). Consistent large-scale temperature responses in warm and cold climates. *Geophys. Res. Lett.* 40, 1817–1823.
Jackson, L. C., Peterson, K. A., Roberts, C. D., and Wood, R. A. (2016a). Recent slowing of Atlantic overturning circulation as a recovery from earlier strengthening. *Nat. Geosci.* 9, 518–522. doi:10.1038/ngeo2715.
Jackson, L. C., Schaller, N., Smith, R. S., Palmer, M. D., and Vellinga, M. (2014). Response of the Atlantic meridional overturning circulation to a reversal of greenhouse gas increases. *Clim. Dyn.* 42, 3323–3336.
Jackson, L. C., and Wood, R. A. (2018). Hysteresis and Resilience of the AMOC in an Eddy-Permitting GCM. *Geophys. Res. Lett.* 45, 8547–8556.
Jackson, L. S., Crook, J. A., and Forster, P. M. (2016b). An intensified hydrological cycle in the simulation of geoengineering by cirrus cloud thinning using ice crystal fall speed changes. *J. Geophys. Res. Atmos.* 121, 6822–6840. doi:10.1002/2015JD024304.
Jacob, D., Kotova, L., Teichmann, C., Sobolowski, S. P., Vautard, R., Donnelly, C., et al. (2018). Climate Impacts in Europe Under +1.5°C Global Warming. *Earth's Futur.* 6, 264–285. doi:10.1002/2017EF000710.
Jahn, A. (2018). Reduced probability of ice-free summers for 1.5 °C compared to 2 °C warming. *Nat. Clim. Chang.* 8, 409–413. doi:10.1038/s41558-018-0127-8.
James, R., Washington, R., Schleussner, C.-F., Rogelj, J., and Conway, D. (2017). Characterizing half-a-degree difference: a review of methods for identifying regional climate responses to global warming targets. *Wiley Interdiscip. Rev. Clim. Chang.* 8, e457. doi:10.1002/wcc.457.
Jiang, J., Cao, L., Macmartin, D. G., Simpson, I. R., Kravitz, B., and Cheng, W. (2019). Stratospheric Sulfate Aerosol Geoengineering Could Alter the High‐Latitude Seasonal Cycle Geophysical Research Letters. 1–11. doi:10.1029/2019GL085758.
Jiménez-de-la-Cuesta, D., and Mauritsen, T. (2019a). Emergent constraints on Earth's transient and equilibrium response to doubled CO2 from post-1970s global warming. *Nat. Geosci.* 12, 902–905. doi:10.1038/s41561-019-0463-y.
Jiménez-de-la-Cuesta, D., and Mauritsen, T. (2019b). Emergent constraints on Earth's transient and equilibrium response to doubled CO2 from post-1970s global warming. *Nat. Geosci.* 12, 902–905. doi:10.1038/s41561-019-0463-y.

John, J. G., Stock, C. A., and Dunne, J. P. (2015). A more productive, but different, ocean after mitigation. *Geophys. Res. Lett.* 42, 9836–9845.
Johnson, J. S., Regayre, L. A., Yoshioka, M., Pringle, K. J., Lee, L. A., Sexton, D. M. H., et al. (2018). The importance of comprehensive parameter sampling and multiple observations for robust constraint of aerosol radiative forcing. *Atmos. Chem. Phys.* 18, 13031–13053. doi:10.5194/acp-18-13031-2018.
Jones, A. C., Hawcroft, M. K., Haywood, J. M., Moore, J. C., Jones, A., and Guo, X. (2018). Regional Climate Impacts of Stabilizing GlobalWarming at 1.5 K Using Solar Geoengineering. *Earth's Futur.* 6, 1–22. doi:10.1002/2017EF000720.
Jones, A., Haywood, J. M., Alterskjær, K., Boucher, O., Cole, J. N. S., Curry, C. L., et al. (2013). The impact of abrupt suspension of solar radiation management (termination effect) in experiment G2 of the Geoengineering Model Intercomparison Project (GeoMIP). *J. Geophys. Res. Atmos.* 118, 9743–9752. doi:10.1002/jgrd.50762.
Jones, C. D., Frölicher, T. L., Koven, C., MacDougall, A. H., Matthews, H. D., Zickfeld, K., et al. (2019a). The Zero Emission Commitment Model Intercomparison Project (ZECMIP) contribution to CMIP6: Quantifying committed climate changes following zero carbon emissions. *Geosci. Model Dev. Discuss.* doi:10.5194/gmd-2019-153.
Jones, C. D., Frölicher, T. L., Koven, C., MacDougall, A. H., Matthews, H. D., Zickfeld, K., et al. (2019b). The Zero Emissions Commitment Model Intercomparison Project (ZECMIP) contribution to C4MIP: quantifying committed climate changes following zero carbon emissions. *Geosci. Model Dev.* 12, 4375–4385. doi:10.5194/gmd-12-4375-2019.
Jones, C., Lowe, J., Liddicoat, S., and Betts, R. (2009). Committed terrestrial ecosystem changes due to climate change. *Nat. Geosci.* doi:10.1038/ngeo555.
Joos, F., Roth, R., Fuglestvedt, J. S., Peters, G. P., Enting, I. G., von Bloh, W., et al. (2013). Carbon dioxide and climate impulse response functions for the computation of greenhouse gas metrics: a multi-model analysis. *Atmos. Chem. Phys.* 13, 2793–2825. doi:10.5194/acp-13-2793-2013.
Joshi, M., and Gregory, J. (2008). Dependence of the land-sea contrast in surface climate response on the nature of the forcing. *Geophys. Res. Lett.* 35, L24802. doi:10.1029/2008GL036234.
Joshi, M. M., Gregory, J. M., Webb, M. J., Sexton, D. M. H., and Johns, T. C. (2008). Mechanisms for the land/sea warming contrast exhibited by simulations of climate change. *Clim. Dyn.* 30, 455–465.
Joshi, M. M., Lambert, F. H., and Webb, M. J. (2013). An explanation for the difference between twentieth and twenty-first century land–sea warming ratio in climate models. *Clim. Dyn.* 41, 1853–1869. doi:10.1007/s00382-013-1664-5.
Jungclaus, J. H., Lorenz, S. J., Timmreck, C., Reick, C. H., Brovkin, V., Six, K., et al. (2010). Climate and carbon-cycle variability over the last millennium. *Clim. Past* 6, 723–737. doi:doi:10.5194/cp-6-723-2010.
Juricke, S., MacLeod, D., Weisheimer, A., Zanna, L., and Palmer, T. N. (2018). Seasonal to annual ocean forecasting skill and the role of model and observational uncertainty. *Q. J. R. Meteorol. Soc.* 144, 1947–1964. doi:10.1002/qj.3394.
Kadow, C., Illing, S., Kröner, I., Ulbrich, U., and Cubasch, U. (2017). Decadal climate predictions improved by ocean ensemble dispersion filtering. *J. Adv. Model. Earth Syst.* 9, 1138–1149. doi:10.1002/2016MS000787.
Kalidindi, S., Bala, G., Modak, A., and Caldeira, K. (2015). Modeling of solar radiation management: a comparison of simulations using reduced solar constant and stratospheric sulphate aerosols. *Clim. Dyn.* 44, 2909–2925. doi:10.1007/s00382-014-2240-3.
Kamae, Y., and Watanabe, M. (2012). On the robustness of tropospheric adjustment in CMIP5 models. *Geophys. Res. Lett.* 39, L23808. doi:10.1029/2012GL054275.
Kamae, Y., and Watanabe, M. (2013). Tropospheric adjustment to increasing CO2: Its timescale and the role of land-sea contrast. *Clim. Dyn.* 41, 3007–3024. doi:10.1007/s00382-012-1555-1.
Kang, S., and Eltahir, E. A. B. (2018). North China Plain threatened by deadly heatwaves due to climate change and irrigation. *Nat. Commun.* 9, 2894. doi:10.1038/s41467-018-05252-y.
Kar-Man Chang, E. (2018). CMIP5 Projected Change in Northern Hemisphere Winter Cyclones with Associated Extreme Winds. *J. Clim.* 31, 6527–6542. doi:10.1175/JCLI-D-17-0899.1.
Karspeck, A. R., Stammer, D., Köhl, A., Danabasoglu, G., Balmaseda, M., Smith, D. M., et al. (2017). Comparison of the Atlantic meridional overturning circulation between 1960 and 2007 in six ocean reanalysis products. *Clim. Dyn.* 49, 957–982. doi:10.1007/s00382-015-2787-7.
Karspeck, A., Yeager, S., Danabasoglu, G., and Teng, H. (2015). An evaluation of experimental decadal predictions using CCSM4. *Clim. Dyn.* 44, 907–923. doi:10.1007/s00382-014-2212-7.
Kashimura, H., Abe, M., Watanabe, S., Sekiya, T., Ji, D., Moore, J. C., et al. (2017). Shortwave radiative forcing, rapid adjustment, and feedback to the surface by sulfate geoengineering: Analysis of the Geoengineering Model Intercomparison Project G4 scenario. *Atmos. Chem. Phys.* 17, 3339–3356. doi:10.5194/acp-17-3339-2017.
Kasoar, M., Shawki, D., and Voulgarakis, A. (2018). Similar spatial patterns of global climate response to aerosols from different regions. *npj Clim. Atmos. Sci.* doi:10.1038/s41612-018-0022-z.
Kay, J. E., Deser, C., Phillips, A., Mai, A., Hannay, C., Strand, G., et al. (2015). The Community Earth System Model (CESM) Large Ensemble project : A community resource for studying climate change in the presence of internal

climate variability. *Bull. Am. Meteorol. Soc.* 96, 1333–1349. doi:10.1175/BAMS-D-13-00255.1.
Keith, D. W., and MacMartin, D. G. (2015). A temporary, moderate and responsive scenario for solar geoengineering. *Nat. Clim. Chang.* 5, 201–206. doi:10.1038/nclimate2493.
Keith Moore, J., Fu, W., Primeau, F., Britten, G. L., Lindsay, K., Long, M., et al. (2018). Sustained climate warming drives declining marine biological productivity. *Science (80-. ).* doi:10.1126/science.aao6379.
Keller, D. P., Feng, E. Y., and Oschlies, A. (2014). Potential climate engineering effectiveness and side effects during a high carbon dioxide-emission scenario. *Nat. Commun.* 5, 3304. doi:10.1038/ncomms4304.
Keller, D. P., Lenton, A., Scott, V., Vaughan, N. E., Bauer, N., Ji, D., et al. (2018). The Carbon Dioxide Removal Model Intercomparison Project (CDRMIP): rationale and experimental protocol for CMIP6. *Geosci. Model Dev.* 11, 1133–1160. doi:10.5194/gmd-11-1133-2018.
Kendon, E. J., Roberts, N. M., Fowler, H. J., Roberts, M. J., Chan, S. C., and Senior, C. A. (2014). Heavier summer downpours with climate change revealed by weather forecast resolution model. *Nat. Clim. Chang.* doi:10.1038/nclimate2258.
Kennedy, D., Parker, T., Woollings, T., Harvey, B., and Shaffrey, L. (2016). The response of high-impact blocking weather systems to climate change. *Geophys. Res. Lett.* 43, 7250–7258. doi:10.1002/2016GL069725.
Kent, C., Chadwick, R., and Rowell, D. P. (2015). Understanding Uncertainties in Future Projections of Seasonal Tropical Precipitation. *J. Clim.* 28, 4390–4413. doi:10.1175/JCLI-D-14-00613.1.
Kharin, V. V., Boer, G. J., Merryfield, W. J., Scinocca, J. F., and Lee, W. S. (2012). Statistical adjustment of decadal predictions in a changing climate. *Geophys. Res. Lett.* 39, n/a-n/a. doi:10.1029/2012GL052647.
Kharin, V. V., Flato, G. M., Zhang, X., Gillett, N. P., Zwiers, F., and Anderson, K. J. (2018). Risks from Climate Extremes Change Differently from 1.5°C to 2.0°C Depending on Rarity. *Earth's Futur.* 6, 704–715. doi:10.1002/2018EF000813.
Khodri, M., Izumo, T., Vialard, J., Janicot, S., Cassou, C., Lengaigne, M., et al. (2017a). Tropical explosive volcanic eruptions can trigger El Ninõ by cooling tropical Africa. *Nat. Commun.* 8, 1–12. doi:10.1038/s41467-017-00755-6.
Khodri, M., Izumo, T., Vialard, J., Janicot, S., Cassou, C., Lengaigne, M., et al. (2017b). Tropical explosive volcanic eruptions can trigger El Ninõ by cooling tropical Africa. *Nat. Commun.* 8, 1–12. doi:10.1038/s41467-017-00755-6.
Kidston, J., and Gerber, E. P. (2010). Intermodel variability of the poleward shift of the austral jet stream in the CMIP3 integrations linked to biases in 20th century climatology. *Geophys. Res. Lett.* 37, 1–5. doi:10.1029/2010GL042873.
Kilbourne, K. H., Alexander, M. A., and Nye, J. A. (2014). A low latitude paleoclimate perspective on Atlantic multidecadal variability. *J. Mar. Syst.* 133, 4–13. doi:https://doi.org/10.1016/j.jmarsys.2013.09.004.
Kim, S. T., Cai, W., Jin, F.-F., Santoso, A., Wu, L., Guilyardi, E., et al. (2014). Response of El Niño sea surface temperature variability to greenhouse warming. *Nat. Clim. Chang.* 4, 786–790. doi:10.1038/nclimate2326.
Kimmritz, M., Counillon, F., Bitz, C. M., Massonnet, F., Bethke, I., and Gao, Y. (2018). Optimising assimilation of sea ice concentration in an Earth system model with a multicategory sea ice model. *Tellus A Dyn. Meteorol. Oceanogr.* 70, 1–23. doi:10.1080/16000870.2018.1435945.
Kirchmeier-Young, M. C., Wan, H., Zhang, X., and Seneviratne, S. I. (2019). Importance of Framing for Extreme Event Attribution: The Role of Spatial and Temporal Scales. *Earth's Futur.* doi:10.1029/2019EF001253.
Kirchmeier-Young, M. C., Zwiers, F. W., and Gillett, N. P. (2017). Attribution of Extreme Events in Arctic Sea Ice Extent. *J. Clim.* 30, 553–571. doi:10.1175/JCLI-D-16-0412.1.
Kirtman, B., Power, S. B., Adedoyin, J. A., Boer, G. J., Bojariu, R., Camilloni, I., et al. (2013). "Near-term climate change: projections and predictability," in *Climate Change 2013: The Physical Science Basis. Contribution of Working Group I to the Fifth Assessment Report of the Intergovernmental Panel on Climate Change*, eds. T. F. Stocker, D. Qin, G.-K. Plattner, M. Tignor, S. K. Allen, J. Boschung, et al. (Cambridge, United Kingdom and New York, NY, USA: Cambridge University Press ), 953–1028.
Kitano, Y., and Yamada, T. J. (2016). Relationship between atmospheric blocking and cold day extremes in current and RCP8.5 future climate conditions over Japan and the surrounding area. *Atmos. Sci. Lett.* 17, 616–622. doi:10.1002/asl.711.
Kitoh, A., and Endo, H. (2016). Changes in precipitation extremes projected by a 20-km mesh global atmospheric model. *Weather Clim. Extrem.* 11, 41–52. doi:https://doi.org/10.1016/j.wace.2015.09.001.
Kitoh, A., Endo, H., Krishna Kumar, K., Cavalcanti, I. F. A., Goswami, P., and Zhou, T. (2013). Monsoons in a changing world: A regional perspective in a global context. *J. Geophys. Res. Atmos.* 118, 3053–3065. doi:10.1002/jgrd.50258.
Kjellström, E., Nikulin, G., Strandberg, G., Christensen, O. B., Jacob, D., Keuler, K., et al. (2018). European climate change at global mean temperature increases of 1.5 and 2 °C above pre-industrial conditions as simulated by the EURO-CORDEX regional climate models. *Earth Syst. Dyn.* 9, 459–478. doi:10.5194/esd-9-459-2018.
Kleinschmitt, C., Boucher, O., and Platt, U. (2018). Sensitivity of the radiative forcing by stratospheric sulfur geoengineering to the amount and strategy of the \chem{SO_2} injection studied with the LMDZ-S3A model. *Atmos. Chem. Phys.* 18, 2769–2786. doi:10.5194/acp-18-2769-2018.

Klus, A., Prange, M., Varma, V., Tremblay, L. B., and Schulz, M. (2018). Abrupt cold events in the North Atlantic Ocean in a transient Holocene simulation. *Clim. Past* 14, 1165–1178. doi:10.5194/cp-14-1165-2018.

Knight, J. R., Andrews, M. B., Smith, D. M., Arribas, A., Colman, A. W., Dunstone, N. J., et al. (2014). Predictions of Climate Several Years Ahead Using an Improved Decadal Prediction System. *J. Clim.* 27, 7550–7567. doi:10.1175/JCLI-D-14-00069.1.

Knudsen, M., Seidenkrantz, M.-S., Jacobsen, B. H., and Kuijpers, A. (2011). Tracking the Atlantic Multidecadal Oscialltion through the last 8000years. *Nat. Commun.* 2, 1–8.

Knutson, T. R., and Ploshay, J. J. (2016). Detection of anthropogenic influence on a summertime heat stress index. *Clim. Change* 138, 25–39. doi:10.1007/s10584-016-1708-z.

Knutti, R., Furrer, R., Tebaldi, C., Cermak, J., and Meehl, G. a. (2010). Challenges in Combining Projections from Multiple Climate Models. *J. Clim.* 23, 2739–2758. doi:10.1175/2009JCLI3361.1.

Knutti, R., Masson, D., and Gettelman, A. (2013a). Climate model genealogy: Generation CMIP5 and how we got there. *Geophys. Res. Lett.* 40, 1194–1199. doi:10.1002/grl.50256.

Knutti, R., and Rugenstein, M. A. A. (2015). Feedbacks, climate sensitivity and the limits of linear models. *Philos. Trans. R. Soc. A Math. Phys. Eng. Sci.* 373, 20150146. doi:10.1098/rsta.2015.0146.

Knutti, R., Sedláček, J., Sanderson, B. M., Lorenz, R., Fischer, E. M., and Eyring, V. (2017). A climate model projection weighting scheme accounting for performance and interdependence. *Geophys. Res. Lett.* 44, 1909–1918. doi:10.1002/2016GL072012.

Knutti, R., Sedláček, J., and Sedlacek, J. (2013b). Robustness and uncertainties in the new CMIP5 climate model projections. *Nat. Clim. Chang.* 3, 369–373. doi:10.1038/nclimate1716.

Koenigk, T., Devasthale, A., and Karlsson, K. G. (2014). Summer arctic sea ice albedo in CMIP5 models. *Atmos. Chem. Phys.* 14, 1987–1998. doi:10.5194/acp-14-1987-2014.

Kohyama, T., and Hartmann, D. L. (2017). Nonlinear ENSO Warming Suppression (NEWS). *J. Clim.* 30, 4227–4251. doi:10.1175/JCLI-D-16-0541.1.

Kopp, R. E., Shwom, R. L., Wagner, G., and Yuan, J. (2016). Tipping elements and climate--economic shocks: Pathways toward integrated assessment. *Earth's Futur.* 4, 346–372.

Kosaka, Y., and Xie, S.-P. (2013). Recent global-warming hiatus tied to equatorial Pacific surface cooling. *Nature* 501, 403–407. doi:10.1038/nature12534.

Kosaka, Y., and Xie, S.-P. (2016). The tropical Pacific as a key pacemaker of the variable rates of global warming. *Nat. Geosci.* 9, 669–673. doi:10.1038/ngeo2770.

Kostov, Y., Marshall, J., Hausmann, U., Armour, K. C., Ferreira, D., and Holland, M. M. (2017). Fast and slow responses of Southern Ocean sea surface temperature to SAM in coupled climate models. *Clim. Dyn.* 48, 1595–1609. doi:10.1007/s00382-016-3162-z.

Kravitz, B., Caldeira, K., Boucher, O., Robock, A., Rasch, P. J., Alterskjær, K., et al. (2013a). Climate model response from the Geoengineering Model Intercomparison Project (GeoMIP). *J. Geophys. Res. Atmos.* 118, 8320–8332. doi:10.1002/jgrd.50646.

Kravitz, B., Forster, P. M., Jones, A., Robock, A., Alterskjaer, K., Boucher, O., et al. (2013b). Sea spray geoengineering experiments in the geoengineering model intercomparison project (GeoMIP): Experimental design and preliminary results. *J. Geophys. Res. Atmos.* 118, 11,175-11,186. doi:10.1002/jgrd.50856.

Kravitz, B., MacMartin, D. G., Mills, M. J., Richter, J. H., Tilmes, S., Lamarque, J.-F., et al. (2017a). First simulations of designing stratospheric sulfate aerosol geoengineering to meet multiple simultaneous climate objectives. *J. Geophys. Res. Atmos.* doi:10.1002/2017JD026874.

Kravitz, B., MacMartin, D. G., Mills, M. J., Richter, J. H., Tilmes, S., Lamarque, J.-F., et al. (2017b). First Simulations of Designing Stratospheric Sulfate Aerosol Geoengineering to Meet Multiple Simultaneous Climate Objectives. *J. Geophys. Res. Atmos.* 122, 12,616-12,634. doi:10.1002/2017JD026874.

Kravitz, B., Macmartin, D. G., Robock, A., Rasch, P. J., Ricke, K. L., Cole, J. N. S., et al. (2014). A multi-model assessment of regional climate disparities caused by solar geoengineering. *Environ. Res. Lett.* 9. doi:10.1088/1748-9326/9/7/074013.

Kravitz, B., Macmartin, D. G., Wang, H., and Rasch, P. J. (2016). Geoengineering as a design problem. *Earth Syst. Dyn.*, 469–497. doi:10.5194/esd-7-469-2016.

Kravitz, B., Rasch, P. J., Wang, H., Robock, A., Gabriel, C., Boucher, O., et al. (2018). The climate effects of increasing ocean albedo: an idealized representation of solar geoengineering. *Atmos. Chem. Phys.* 18, 13097–13113. doi:10.5194/acp-18-13097-2018.

Kravitz, B., Robock, A., Boucher, O., Schmidt, H., Taylor, K. E., Stenchikov, G., et al. (2011). The Geoengineering Model Intercomparison Project ( GeoMIP ). *Atmos. Sci. Lett.* doi:10.1002/asl.316.

Kravitz, B., Robock, A., Tilmes, S., Boucher, O., English, J. M., Irvine, P. J., et al. (2015). The Geoengineering Model Intercomparison Project Phase 6 (GeoMIP6): simulation design and preliminary results. *Geosci. Model Dev.* 8, 3379–3392. doi:10.5194/gmd-8-3379-2015.

Kriegler, E., Luderer, G., Bauer, N., Baumstark, L., Fujimori, S., Popp, A., et al. (2018). Pathways limiting warming to 1.5°C: A tale of turning around in no time? *Philos. Trans. R. Soc. A Math. Phys. Eng. Sci.* doi:10.1098/rsta.2016.0457.

Krishna-Pillai Sukumara-Pillai, K., Bala, G., Cao, L., Duan, L., and Caldeira, K. (2019). Climate System Response to Stratospheric Sulfate Aerosols: Sensitivity to Altitude of Aerosol Layer. *Earth Syst. Dyn. Discuss.*, 1–30. doi:10.5194/esd-2019-21.

Krishnan, R., Sabin, T. P., Vellore, R., Mujumdar, M., Sanjay, J., Goswami, B. N., et al. (2016). Deciphering the desiccation trend of the South Asian monsoon hydroclimate in a warming world. *Clim. Dyn.* 47, 1007–1027. doi:10.1007/s00382-015-2886-5.

Kristjánsson, J. E., Muri, H., and Schmidt, H. (2015). The hydrological cycle response to cirrus cloud thinning. *Geophys. Res. Lett.* 42, 10807–10815. doi:10.1002/2015GL066795.

Kröger, J., Pohlmann, H., Sienz, F., Marotzke, J., Baehr, J., Köhl, A., et al. (2018). Full-field initialized decadal predictions with the MPI Earth system model: an initial shock in the North Atlantic. *Clim. Dyn.* 51, 2593–2608. doi:10.1007/s00382-017-4030-1.

Kröner, N., Kotlarski, S., Fischer, E., Lüthi, D., Zubler, E., and Schär, C. (2017). Separating climate change signals into thermodynamic, lapse-rate and circulation effects: theory and application to the European summer climate. *Clim. Dyn.* 48, 3425–3440. doi:10.1007/s00382-016-3276-3.

Kruschke, T., Rust, H. W., Kadow, C., Müller, W. A., Pohlmann, H., Leckebusch, G. C., et al. (2016). Probabilistic evaluation of decadal prediction skill regarding Northern Hemisphere winter storms. *Meteorol. Zeitschrift* 25, 721–738. doi:10.1127/metz/2015/0641.

Kushnir, Y., Scaife, A. A., Arritt, R., Balsamo, G., Boer, G., Doblas-Reyes, F., et al. (2019). Towards operational predictions of the near-term climate. *Nat. Clim. Chang.* 9, 94–101. doi:10.1038/s41558-018-0359-7.

Lambert, F. H., and Allen, M. R. (2009). Are changes in global precipitation constrained by the tropospheric energy budget? *J. Clim.* 22, 499–517. doi:10.1175/2008JCLI2135.1.

Lambert, F. H., and Chiang, J. C. H. (2007). Control of land-ocean temperature contrast by ocean heat uptake. *Geophys. Res. Lett.* 34, n/a-n/a. doi:10.1029/2007GL029755.

Lambert, F. H., Ferraro, A. J., and Chadwick, R. (2017). Land–Ocean Shifts in Tropical Precipitation Linked to Surface Temperature and Humidity Change. *J. Clim.* 30, 4527–4545. doi:10.1175/JCLI-D-16-0649.1.

Lambert, F. H., Webb, M. J., and Joshi, M. M. (2011). The relationship between land-ocean surface temperature contrast and radiative forcing. *J. Clim.* 24, 3239–3256.

Langenbrunner, B., Neelin, J. D., Lintner, B. R., and Anderson, B. T. (2015). Patterns of Precipitation Change and Climatological Uncertainty among CMIP5 Models, with a Focus on the Midlatitude Pacific Storm Track. *J. Clim.* 28, 7857–7872. doi:10.1175/JCLI-D-14-00800.1.

Lapp, S. L., St. Jacques, J.-M., Barrow, E. M., and Sauchyn, D. J. (2012). GCM projections for the Pacific Decadal Oscillation under greenhouse forcing for the early 21st century. *Int. J. Climatol.* 32, 1423–1442. doi:10.1002/joc.2364.

Latham, J., Bower, K., Choularton, T., Coe, H., Connolly, P., Cooper, G., et al. (2012). Marine cloud brightening. *Philos. Trans. R. Soc. A Math. Phys. Eng. Sci.* 370, 4217–4262. doi:10.1098/rsta.2012.0086.

Leduc, M., Matthews, H. D., and de Elía, R. (2016). Regional estimates of the transient climate response to cumulative CO2 emissions. *Nat. Clim. Chang.* 6, 474–478. doi:10.1038/nclimate2913.

Leduc, M., Matthews, H. D., and De Elía, R. (2015). Quantifying the limits of a linear temperature response to cumulative CO2 emissions. *J. Clim.* 28, 9955–9968. doi:10.1175/JCLI-D-14-00500.1.

Lee, C.-J., Liao, Y.-C., Lan, C.-W., Chiang, J. C. H. C. H., Chung, C.-H., and Chou, C. (2013). Increase in the range between wet and dry season precipitation. *Nat. Geosci.* 6, 263–267. doi:10.1038/ngeo1744.

Lee, D. Y., and Ahn, J.-B. (2017). Future change in the frequency and intensity of wintertime North Pacific blocking in CMIP5 models. *Int. J. Climatol.* 37, 2765–2781. doi:10.1002/joc.4878.

Lee, H. J., Kwon, M. O., Yeh, S.-W., Kwon, Y.-O., Park, W., Park, J.-H., et al. (2017). Impact of Poleward Moisture Transport from the North Pacific on the Acceleration of Sea Ice Loss in the Arctic since 2002. *J. Clim.* 30, 6757–6769. doi:10.1175/JCLI-D-16-0461.1.

Lee, J. Y., and Wang, B. (2014). Future change of global monsoon in the CMIP5. *Clim. Dyn.* 42, 101–119. doi:10.1007/s00382-012-1564-0.

Lee, S., Gong, T., Johnson, N., Feldstein, S. B., and Pollard, D. (2011). On the Possible Link between Tropical Convection and the Northern Hemisphere Arctic Surface Air Temperature Change between 1958 and 2001. *J. Clim.* 24, 4350–4367. doi:10.1175/2011JCLI4003.1.

Lehmann, J., Coumou, D., Frieler, K., Eliseev, A. V, and Levermann, A. (2014). Future changes in extratropical storm tracks and baroclinicity under climate change. *Environ. Res. Lett.* 9, 084002. doi:10.1088/1748-9326/9/8/084002.

Lehner, F., Deser, C., Maher, N., Marotzke, J., Fischer, E., Brunner, L., et al. (9999). Partitioning climate projection uncertainty with multiple Large Ensembles and CMIP5 / 6. *Earth Syst. Dyn.* (submitted.

Lehner, F., Deser, C., and Sanderson, B. M. (2018). Future risk of record-breaking summer temperatures and its mitigation. *Clim. Change*, 363–375. doi:10.1007/s10584-016-1616-2.

Lehner, F., Deser, C., and Terray, L. (2017). Toward a new estimate of "Time of Emergence" of anthropogenic warming: Insights from dynamical adjustment and a large initial-condition model ensemble. *J. Clim.* 30, 7739–7756. doi:10.1175/JCLI-D-16-0792.1.

Lelieveld, J., Klingmüller, K., Pozzer, A., Burnett, R. T., Haines, A., and Ramanathan, V. (2019). Effects of fossil fuel

and total anthropogenic emission removal on public health and climate. *Proc. Natl. Acad. Sci.* 0, 201819989. doi:10.1073/pnas.1819989116.

Lenderink, G., van den Hurk, B. J. J. M., Klein Tank, A. M. G., van Oldenborgh, G. J., van Meijgaard, E., de Vries, H., et al. (2014). Preparing local climate change scenarios for the Netherlands using resampling of climate model output. *Environ. Res. Lett.* 9, 115008. doi:10.1088/1748-9326/9/11/115008.

Levy, H., Horowitz, L. W., Schwarzkopf, M. D., Ming, Y., Golaz, J.-C., Naik, V., et al. (2013). The roles of aerosol direct and indirect effects in past and future climate change. *J. Geophys. Res. Atmos.* 118, 4521–4532. doi:10.1002/jgrd.50192.

Li, C., Michel, C., Seland Graff, L., Bethke, I., Zappa, G., Bracegirdle, T. J., et al. (2018a). Midlatitude atmospheric circulation responses under 1.5 and 2.0 °C warming and implications for regional impacts. *Earth Syst. Dyn.* 9, 359–382. doi:10.5194/esd-9-359-2018.

Li, C., von Storch, J.-S., and Marotzke, J. (2013). Deep-ocean heat uptake and equilibrium climate response. *Clim. Dyn.* 40, 1071–1086. doi:10.1007/s00382-012-1350-z.

Li, C., Zhang, X., Zwiers, F., Fang, Y., and Michalak, A. M. (2017). Recent Very Hot Summers in Northern Hemispheric Land Areas Measured by Wet Bulb Globe Temperature Will Be the Norm Within 20 Years. *Earth's Futur.* 5, 1203–1216. doi:10.1002/2017EF000639.

Li, G., Xie, S.-P., and Du, Y. (2016a). A Robust but Spurious Pattern of Climate Change in Model Projections over the Tropical Indian Ocean. *J. Clim.* 29, 5589–5608. doi:10.1175/JCLI-D-15-0565.1.

Li, H., Ilyina, T., Müller, W. A., and Landschützer, P. (2019). Predicting the variable ocean carbon sink. *Sci. Adv.* 5, eaav6471. doi:10.1126/sciadv.aav6471.

Li, H., Ilyina, T., Müller, W. A., and Sienz, F. (2016b). Decadal predictions of the North Atlantic CO2 uptake. *Nat. Commun.* 7, 10.1038/ncomms11076. doi:10.1038/ncomms11076.

Li, J., Chen, Y. D., Gan, T. Y., and Lau, N.-C. (2018b). Elevated increases in human-perceived temperature under climate warming. *Nat. Clim. Chang.* 8, 43–47. doi:10.1038/s41558-017-0036-2.

Li, J., and Wang, J. X. L. (2003). A modified zonal index and its physical sense. *Geophys. Res. Lett.* 30. doi:10.1029/2003GL017441.

Li, M., Woollings, T., Hodges, K., and Masato, G. (2014). Extratropical cyclones in a warmer, moister climate: A recent Atlantic analogue. *Geophys. Res. Lett.* 41, 8594–8601. doi:10.1002/2014GL062186.

Liang, Y., Gillett, N. P., and Monahan, A. H. (9999). Climate model projections of 21st century global warming constrained using the observed warming trend. *Geophys. Res. Lett.* (submitted.

Lin, R., Zhou, T., and Qian, Y. (2014). Evaluation of Global Monsoon Precipitation Changes based on Five Reanalysis Datasets. *J. Clim.* 27, 1271–1289. doi:10.1175/JCLI-D-13-00215.1.

Lipat, B. R., Voigt, A., Tselioudis, G., and Polvani, L. M. (2018). Model uncertainty in cloud-circulation coupling, and cloud-radiative response to increasing CO2, linked to biases in climatological circulation. *J. Clim.* 31, 10013–10020. doi:10.1175/JCLI-D-17-0665.1.

Liu, C., Becker, A., Kendon, E. J., Arkin, P. A., Zhang, X., Ingram, W. J., et al. (2014). Challenges in Quantifying Changes in the Global Water Cycle. *Bull. Am. Meteorol. Soc.* 96, 1097–1115. doi:10.1175/bams-d-13-00212.1.

Liu, L., Shawki, D., Voulgarakis, A., Kasoar, M., Samset, B. H., Myhre, G., et al. (2018a). A PDRMIP Multimodel Study on the Impacts of Regional Aerosol Forcings on Global and Regional Precipitation. *J. Clim.* 31, 4429–4447. doi:10.1175/JCLI-D-17-0439.1.

Liu, W., Lu, J., Xie, S.-P., and Fedorov, A. (2018b). Southern Ocean Heat Uptake, Redistribution, and Storage in a Warming Climate: The Role of Meridional Overturning Circulation. *J. Clim.* 31, 4727–4743. doi:10.1175/JCLI-D-17-0761.1.

Liu, W., Xie, S.-P., Liu, Z., and Zhu, J. (2017). Overlooked possibility of a collapsed Atlantic Meridional Overturning Circulation in warming climate. *Sci. Adv.* 3, e1601666. doi:10.1126/sciadv.1601666.

Liu, Y., Hallberg, R., Sergienko, O., Samuels, B. L., Harrison, M., and Oppenheimer, M. (2018c). Climate response to the meltwater runoff from Greenland ice sheet: evolving sensitivity to discharging locations. *Clim. Dyn.* 51, 1733–1751. doi:10.1007/s00382-017-3980-7.

Liu, Z. (2012). Dynamics of Interdecadal Climate Variability: A Historical Perspective*. *J. Clim.* 25, 1963–1995. doi:10.1175/2011JCLI3980.1.

Liu, Z., and Di Lorenzo, E. (2018). Mechanisms and Predictability of Pacific Decadal Variability. *Curr. Clim. Chang. Reports* 4, 128–144. doi:10.1007/s40641-018-0090-5.

Lo, Y. T. E., Charlton-Perez, A. J., Lott, F. C., and Highwood, E. J. (2016). Detecting sulphate aerosol geoengineering with different methods. *Sci. Rep.* 6, 1–10. doi:10.1038/srep39169.

Lohmann, U., and Gasparini, B. (2017). A cirrus cloud climate dial? *Science (80-. ).* 357, 248–249. doi:10.1126/science.aan3325.

Lopez, A., Suckling, E. B., and Smith, L. A. (2014). Robustness of pattern scaled climate change scenarios for adaptation decision support. *Clim. Change* 122, 555–566. doi:10.1007/s10584-013-1022-y.

Losada, T., and Rodríguez-Fonseca, B. (2016). Tropical atmospheric response to decadal changes in the Atlantic Equatorial Mode. *Clim. Dyn.* 47, 1211–1224. doi:10.1007/s00382-015-2897-2.

Lovenduski, N. S., McKinley, G. A., Fay, A. R., Lindsay, K., and Long, M. C. (2016). Partitioning uncertainty in ocean

carbon uptake projections: Internal variability, emission scenario, and model structure. *Global Biogeochem. Cycles* 30, 1276–1287. doi:10.1002/2016GB005426.

Lovenduski, N. S., Yeager, S. G., Lindsay, K., and Long, M. C. (2019). Predicting near-term variability in ocean carbon uptake. *Earth Syst. Dyn.* 10, 45–57. doi:10.5194/esd-10-45-2019.

Lu, J., Vecchi, G. A., and Reichler, T. (2007). Expansion of the Hadley cell under global warming. *Geophys. Res. Lett.* 34. doi:10.1029/2006GL028443.

Lübbecke, J. F., Rodríguez-Fonseca, B., Richter, I., Martín-Rey, M., Losada, T., Polo, I., et al. (2018). Equatorial Atlantic variability-Modes, mechanisms, and global teleconnections. *Wiley Interdiscip. Rev. Clim. Chang.* 9, e527. doi:10.1002/wcc.527.

Luo, Y., Lu, J., Liu, F., and Garuba, O. (2017). The role of ocean dynamical thermostat in delaying the El Niño--like response over the equatorial Pacific to climate warming. *J. Clim.* 30, 2811–2827.

MacCracken, M. C. (2016). The rationale for accelerating regionally focused climate intervention research. *Earth's Futur.* 4, 649–657. doi:10.1002/2016EF000450.

MacCracken, M. C., Shin, H. J., Caldeira, K., and Ban-Weiss, G. A. (2013). Climate response to imposed solar radiation reductions in high latitudes. *Earth Syst. Dyn.* 4, 301–315. doi:10.5194/esd-4-301-2013.

MacDougall, A. H. (2013). Reversing climate warming by artificial atmospheric carbon-dioxide removal: Can a Holocene-like climate be restored? *Geophys. Res. Lett.* 40, 5480–5485.

MacDougall, A. H., Frolicher, T. L., Jones, C. D., Rogelj, J., Matthews, H. D., Zickfeld, K., et al. (9999). Is there warming in the pipeline? A multi-model analysis of the zero emission commitment from CO2. *Biogeosciences Discuss.* (submitted.

MacLachlan, C., Arribas, A., Peterson, K. A., Maidens, A., Fereday, D., Scaife, A. A., et al. (2015). Global Seasonal forecast system version 5 (GloSea5): a high-resolution seasonal forecast system. *Q. J. R. Meteorol. Soc.* 141, 1072–1084. doi:10.1002/qj.2396.

MacMartin, D. G., and Kravitz, B. (2019). The Engineering of Climate Engineering. *Annu. Rev. Control. Robot. Auton. Syst.* 2, 445–467. doi:10.1146/annurev-control-053018-023725.

MacMartin, D. G., Kravitz, B., Tilmes, S., Richter, J. H., Mills, M. J., Lamarque, J.-F., et al. (2017). The Climate Response to Stratospheric Aerosol Geoengineering Can Be Tailored Using Multiple Injection Locations. *J. Geophys. Res. Atmos.* 122, 12,574-12,590. doi:10.1002/2017JD026868.

MacMartin, D. G., Ricke, K. L., and Keith, D. W. (2018). Solar geoengineering as part of an overall strategy for meeting the 1.5°C Paris target. *Philos. Trans. R. Soc. A Math. Phys. Eng. Sci.* 376, 20160454. doi:10.1098/rsta.2016.0454.

MacMartin, D. G., Wang, W., Kravitz, B., Tilmes, S., Richter, J. H., and Mills, M. J. (2019). Timescale for Detecting the Climate Response to Stratospheric Aerosol Geoengineering. *J. Geophys. Res. Atmos.* 124, 1233–1247. doi:10.1029/2018JD028906.

Madsen, M. S., Langen, P. L., Boberg, F., and Christensen, J. H. (2017). Inflated Uncertainty in Multimodel-Based Regional Climate Projections. *Geophys. Res. Lett.* doi:10.1002/2017GL075627.

Magnusson, L., Alonso-Balmaseda, M., Corti, S., Molteni, F., and Stockdale, T. (2013). Evaluation of forecast strategies for seasonal and decadal forecasts in presence of systematic model errors. *Clim. Dyn.* 41, 2393–2409. doi:10.1007/s00382-012-1599-2.

Maher, N., Lehner, F., and Marotzke, J. (9999a). Quantifying the role of internal variability in the climate we will observe in the coming decades. *Environ. Res. Lett.* (submitted.

Maher, N., Matei, D., Milinski, S., and Marotzke, J. (2018). ENSO Change in Climate Projections: Forced Response or Internal Variability? *Geophys. Res. Lett.* 45, 11,390-11,398. doi:10.1029/2018GL079764.

Maher, N., McGregor, S., England, M. H., and Gupta, A. Sen (2015). Effects of volcanism on tropical variability. *Geophys. Res. Lett.* 42, 6024–6033. doi:10.1002/2015GL064751.

Maher, N., Milinski, S., Suarez-Gutierrez, L., Botzet, M., Kornblueh, L., Takano, Y., et al. (2019). The Max Planck Institute Grand Ensemble – enabling the exploration of climate system variability. *J. Adv. Model. Earth Syst.*, submitted.

Maher, N., Power, S. B., and Marotzke, J. (9999b). Robust assessment of model-to-model agreement in projections of future climate. *Nat. Clim. Chang.* (submitted.

Mahlstein, I., and Knutti, R. (2011). Ocean Heat Transport as a Cause for Model Uncertainty in Projected Arctic Warming. *J. Clim.* 24, 1451–1460. doi:10.1175/2010JCLI3713.1.

Mahowald, N. M. ., Randerson, J. T. ., Lindsay, K., Muñoz, E., Doney, S. C. ., Lawrence, P., et al. (2017). Interactions between land use change and carbon cycle feedbacks Analysis of direct , quasi-direct , and indirect impacts of land use and land. *Global Biogeochem. Cycles*. doi:10.1002/2016GB005374.Related.

Man, W., Zhou, T., and Jungclaus, J. H. (2014). Effects of Large Volcanic Eruptions on Global Summer Climate and East Asian Monsoon Changes during the Last Millennium: Analysis of MPI-ESM Simulations. *J. Clim.* 27, 7394–7409. doi:10.1175/JCLI-D-13-00739.1.

Manabe, S., and Stouffer, R. J. (1980). Sensitivity of a global climate model to an increase of CO 2 concentration in the atmosphere. *J. Geophys. Res.* 85, 5529–5554. doi:10.1029/JC085iC10p05529.

Manabe, S., Stouffer, R. J., Spelman, M. J., and Bryan, K. (1991). Transient responses of a coupled ocean-atmosphere

model to gradual changes of atmospheric CO2. Part I: Annual Mean Response. *J. Clim.* 4, 785–818.
Manabe, S., and Wetherald, R. T. (1975). The Effects of Doubling the CO 2 Concentration on the climate of a General Circulation Model. *J. Atmos. Sci.* 32, 3–15. doi:10.1175/1520-0469(1975)032<0003:TEODTC>2.0.CO;2.
Manabe, S., and Wetherald, R. T. (1980). On the Distribution of Climate Change Resulting from an Increase in CO 2 Content of the Atmosphere. *J. Atmos. Sci.* 37, 99–118. doi:10.1175/1520-0469(1980)037<0099:OTDOCC>2.0.CO;2.
Mantua, N. J., Hare, S. R., Zhang, Y., Wallace, J. M., and Francis, R. C. (1997). A Pacific Interdecadal Climate Oscillation with Impacts on Salmon Production. *Bull. Am. Meteorol. Soc.* 78, 1069–1079. doi:10.1175/1520-0477(1997)078<1069:APICOW>2.0.CO;2.
Manzini, E., Karpechko, A. Y., Anstey, J., Baldwin, M. P., Black, R. X., Cagnazzo, C., et al. (2014). Northern winter climate change: Assessment of uncertainty in CMIP5 projections related to stratosphere-troposphere coupling. *J. Geophys. Res. Atmos.* 119, 7979–7998. doi:10.1002/2013JD021403.
Marini, C., Polkova, I., Köhl, A., and Stammer, D. (2016). A Comparison of Two Ensemble Generation Methods Using Oceanic Singular Vectors and Atmospheric Lagged Initialization for Decadal Climate Prediction. *Mon. Weather Rev.* 144, 2719–2738. doi:10.1175/MWR-D-15-0350.1.
Marotzke, J. (2019). Quantifying the irreducible uncertainty in near-term climate projections. *Wiley Interdiscip. Rev. Clim. Chang.* 10, e563. doi:doi:10.1002/wcc.563.
Marotzke, J., and Forster, P. M. (2015). Forcing, feedback and internal variability in global temperature trends. *Nature* 517, 565–570. doi:10.1038/nature14117.
Marotzke, J., Müller, W. A., Vamborg, F. S. E., Becker, P., Cubasch, U., Feldmann, H., et al. (2016). MiKlip: A national research project on decadal climate prediction. *Bull. Am. Meteorol. Soc.* 97, 2379–2394. doi:10.1175/BAMS-D-15-00184.1.
Marshall, G. J. (2003). Trends in the Southern Annular Mode from Observations and Reanalyses. *J. Clim.* 16, 4134–4143. doi:10.1175/1520-0442(2003)016<4134:TITSAM>2.0.CO;2.
Marshall, J., Armour, K. C., Scott, J. R., Kostov, Y., Hausmann, U., Ferreira, D., et al. (2014). The ocean's role in polar climate change: asymmetric Arctic and Antarctic responses to greenhouse gas and ozone forcing. *Philos. Trans. R. Soc. A Math. Phys. Eng. Sci.* 372, 20130040–20130040. doi:10.1098/rsta.2013.0040.
Marshall, J., Scott, J. R., Armour, K. C., Campin, J.-M., Kelley, M., and Romanou, A. (2015a). The ocean's role in the transient response of climate to abrupt greenhouse gas forcing. *Clim. Dyn.* 44, 2287–2299. doi:10.1007/s00382-014-2308-0.
Marshall, J., Scott, J. R., Armour, K. C., Campin, J.-M., Kelley, M., and Romanou, A. (2015b). The ocean's role in the transient response of climate to abrupt greenhouse gas forcing. *Clim. Dyn.* 44, 2287–2299. doi:10.1007/s00382-014-2308-0.
Martín-Rey, M., Polo, I., Rodríguez-Fonseca, B., Losada, T., and Lazar, A. (2017). Is There Evidence of Changes in Tropical Atlantic Variability Modes under AMO Phases in the Observational Record? *J. Clim.* 41, 3071–3089. doi:10.1007/s00382-015-2471-y.
Martín-Rey, M., Rodríguez-Fonseca, B., Polo, I., and Kucharski, F. (2014). On the Atlantic–Pacific Niños connection: a multidecadal modulated mode. *Clim. Dyn.* 43, 3163–3178. doi:10.1007/s00382-014-2305-3.
Martin, E. R., and Thorncroft, C. (2014a). Sahel rainfall in multimodel CMIP5 decadal hindcasts. *Geophys. Res. Lett.* 41, 2169–2175. doi:10.1002/2014GL059338.
Martin, E. R., and Thorncroft, C. D. (2014b). The impact of the AMO on the West African monsoon annual cycle. *Q. J. R. Meteorol. Soc.* 140, 31–46. doi:10.1002/qj.2107.
Marvel, K., Schmidt, G. A., Miller, R. L., and Nazarenko, L. S. (2016). Implications for climate sensitivity from the response to individual forcings. *Nat. Clim. Chang.* 6, 386–389. doi:10.1038/nclimate2888.
Masato, G., Hoskins, B. J., and Woollings, T. (2013). Winter and Summer Northern Hemisphere Blocking in CMIP5 Models. *J. Clim.* 26, 7044–7059. doi:10.1175/JCLI-D-12-00466.1.
Masson-Delmotte, V., Zhai, P., Pörtner, H.-O., Roberts, D., Skea, J., Shukla, P. R., et al. (2018a). Global warming of 1.5°C An IPCC Special Report. *Rep. Intergov. Panel Clim. Chang.* 265, 37–46. Available at: https://report.ipcc.ch/sr15/pdf/sr15_spm_final.pdf.
Masson-Delmotte, V., Zhai, P., Pörtner, H.-O., Roberts, D., Skea, J., Shukla, P. R., et al. (2018b). Global warming of 1.5°C An IPCC Special Report. *Rep. Intergov. Panel Clim. Chang.* 265, 37–46.
Massonnet, F. (2019). Climate Models as Guidance for the Design of Observing Systems: the Case of Polar Climate and Sea Ice Prediction. *Curr. Clim. Chang. Reports* 5, 334–344. doi:10.1007/s40641-019-00151-w.
Massonnet, F., Bellprat, O., Guemas, V., and Doblas-Reyes, F. J. (2016). Using climate models to estimate the quality of global observational data sets. *Science (80-. ).* 354, 452–455. doi:10.1126/science.aaf6369.
Mathesius, S., Hofmann, M., Caldeira, K., and Schellnhuber, H. J. (2015). Long-term response of oceans to CO 2 removal from the atmosphere. *Nat. Clim. Chang.* 5, 1107.
Matsueda, M., and Endo, H. (2017). The robustness of future changes in Northern Hemisphere blocking: A large ensemble projection with multiple sea surface temperature patterns. *Geophys. Res. Lett.* 44, 5158–5166. doi:10.1002/2017GL073336.
Matthes, K., Funke, B., Andersson, M. E., Barnard, L., Beer, J., Charbonneau, P., et al. (2017). Solar forcing for CMIP6

(v3.2). *Geosci. Model Dev.* 10, 2247–2302. doi:10.5194/gmd-10-2247-2017.
Matthews, H. D. (2010). Can carbon cycle geoengineering be a useful complement to ambitious climate mitigation ? *Management* 1, 135–144.
Matthews, H. D., and Caldeira, K. (2007). Transient climate carbon simulations of planetary geoengineering. *Proc. Natl. Acad. Sci.* 104, 9949–9954. doi:10.1073/pnas.0700419104.
Matthews, H. D., and Caldeira, K. (2008). Stabilizing climate requires near-zero emissions. *Geophys. Res. Lett.* 35, L04705. doi:10.1029/2007GL032388.
Matthews, H. D., and Solomon, S. (2013). Irreversible does not mean unavoidable. *Science (80-. ).* doi:10.1126/science.1236372.
Matthews, H. D., and Weaver, A. J. (2010). Committed climate warming. *Nat. Geosci.* doi:10.1038/ngeo813.
Matthews, H. D., and Zickfeld, K. (2012). Climate response to zeroed emissions of greenhouse gases and aerosols. *Nat. Clim. Chang.* 2, 338–341. doi:10.1038/nclimate1424.
Matthews, H. D., Zickfeld, K., Knutti, R., and Allen, M. R. (2018). Focus on cumulative emissions, global carbon budgets and the implications for climate mitigation targets. *Environ. Res. Lett.* 13, 010201. doi:10.1088/1748-9326/aa98c9.
McCusker, K. E., Armour, K. C., Bitz, C. M., and Battisti, D. S. (2014). Rapid and extensive warming following cessation of solar radiation management. *Environ. Res. Lett.* 9, 024005. doi:10.1088/1748-9326/9/2/024005.
McCusker, K. E., Fyfe, J. C., and Sigmond, M. (2016). Twenty-five winters of unexpected Eurasian cooling unlikely due to Arctic sea-ice loss. *Nat. Geosci.* 9, 838–842. doi:10.1038/ngeo2820.
McCusker, K. E., Kushner, P. J., Fyfe, J. C., Sigmond, M., Kharin, V. V, and Bitz, C. M. (2017). Remarkable separability of circulation response to Arctic sea ice loss and greenhouse gas forcing. *Geophys. Res. Lett.* 44, 7955–7964. doi:10.1002/2017GL074327.
McGregor, S., Timmermann, A., and Timm, O. (2010). A unified proxy for ENSO and PDO variability since 1650. *Clim. Past* 6, 1–17. doi:10.5194/cp-6-1-2010.
McKenna, C. M., Bracegirdle, T. J., Shuckburgh, E. F., Haynes, P. H., and Joshi, M. M. (2018). Arctic Sea Ice Loss in Different Regions Leads to Contrasting Northern Hemisphere Impacts. *Geophys. Res. Lett.* 45, 945–954. doi:10.1002/2017GL076433.
McKinnon, K. A., Poppick, A., Dunn-Sigouin, E., and Deser, C. (2017). An “Observational Large Ensemble” to Compare Observed and Modeled Temperature Trend Uncertainty due to Internal Variability. *J. Clim.* 30, 7585–7598. doi:10.1175/JCLI-D-16-0905.1.
McSweeney, C. F., and Jones, R. G. (2013). No consensus on consensus: the challenge of finding a universal approach to measuring and mapping ensemble consistency in GCM projections. *Clim. Change* 119, 617–629. doi:10.1007/s10584-013-0781-9.
Mearns, L. O., Rosenzweig, C., and Goldberg, R. (1997). Mean and variance change in climate scenarios: Methods, agricultural applications, and measures of uncertainty. *Clim. Change* 35, 367–396. doi:10.1023/A:100535813.
Meccia, V. L., Fabiano, F., Davini, P., and Corti, S. (2019). Stochastic parameterizations and the climate response to external forcing : An experiment with EC-Earth . *Geophys. Res. Lett.*
Meehl, G. A., Arblaster, J. M., Fasullo, J. T., Hu, A., and Trenberth, K. E. (2011). Model-based evidence of deep-ocean heat uptake during surface-temperature hiatus periods. *Nat. Clim. Chang.* 1, 360–364. doi:10.1038/nclimate1229.
Meehl, G. A., and Coauthors (2007). “Global climate projections,” in *Climate {C}hange 2007: {T}he {P}hysical {S}cience {B}asis*, eds. S. Solomon, D. Qin, M. Manning, Z. Chen, M. Marquis, K. B. Averyt, et al. (Cambridge University Press), 747–846.
Meehl, G. A., Goddard, L., Boer, G., Burgman, R., Branstator, G., Cassou, C., et al. (2014a). Decadal climate prediction an update from the trenches. *Bull. Am. Meteorol. Soc.* 95, 243–267. doi:10.1175/BAMS-D-12-00241.1.
Meehl, G. A., Hu, A., and Teng, H. (2016). Initialized decadal prediction for transition to positive phase of the Interdecadal Pacific Oscillation. *Nat. Commun.* 7, 11718. doi:10.1038/ncomms11718.
Meehl, G. A., Senior, C. A., Eyring, V., Flato, G., Lamarque, J.-F., Stouffer, R. J., et al. (9999). Context for interpreting equilibrium climate sensitivity and transient climate response from the CMIP6 earth system models. *Sci. Adv.* (submitted.
Meehl, G. A., and Teng, H. (2012). Case studies for initialized decadal hindcasts and predictions for the Pacific region. *Geophys. Res. Lett.* 39, n/a-n/a. doi:10.1029/2012GL053423.
Meehl, G. A., Teng, H., and Arblaster, J. M. (2014b). Climate model simulations of the observed early-2000s hiatus of global warming. *Nat. Clim. Chang.* 4, 898. Available at: https://doi.org/10.1038/nclimate2357.
Meehl, G. A., Teng, H., Maher, N., and England, M. H. (2015). Effects of the Mount Pinatubo eruption on decadal climate prediction skill of Pacific sea surface temperatures. *Geophys. Res. Lett.* 42, 10,840-10,846. doi:10.1002/2015GL066608.
Meinshausen, M., Meinshausen, N., Hare, W., Raper, S. C. B., Frieler, K., Knutti, R., et al. (2009). Greenhouse-gas emission targets for limiting global warming to 2°C. *Nature* 458, 1158–1162. doi:10.1038/nature08017.
Meinshausen, M., Nicholls, Z., Lewis, J., Gidden, M. J., Vogel, E., Freund, M., et al. (2019a). The SSP greenhouse gas concentrations and their extensions to 2500. *Geosci. Model Dev. Discuss.* 2019, 1–77. doi:10.5194/gmd-2019-222.

Meinshausen, M., Nicholls, Z., Lewis, J., Gidden, M. J., Vogel, E., Freund, M., et al. (2019b). The SSP greenhouse gas concentrations and their extensions to 2500. *Geosci. Model Dev. Discuss.* 2019, 1–77. doi:10.5194/gmd-2019-222.

Meinshausen, M., Nicholls, Z., Lewis, J., Mutch, S. J., Tescari, E., and Nattala, U. (9999). Diagnosing time-varying effective climate sensitivities in CMIP6 Earth System Models. *Geophys. Res. Lett.* (submitted.

Meinshausen, M., Smith, S. J., Calvin, K., Daniel, J. S., Kainuma, M. L. T., Lamarque, J.-F., et al. (2011). The RCP greenhouse gas concentrations and their extensions from 1765 to 2300. *Clim. Change* 109, 213–241. doi:10.1007/s10584-011-0156-z.

Menary, M. B., and Hermanson, L. (2018). Limits on determining the skill of North Atlantic Ocean decadal predictions. *Nat. Commun.* 9, 1694. doi:10.1038/s41467-018-04043-9.

Menary, M. B., Hodson, D. L. R., Robson, J. I., Sutton, R. T., Wood, R. A., and Hunt, J. A. (2015). Exploring the impact of CMIP5 model biases on the simulation of North Atlantic decadal variability. *Geophys. Res. Lett.* 42, 5926–5934. doi:10.1002/2015GL064360.

Mengis, N., Keller, D. P., Rickels, W., Quaas, M., and Oschlies, A. (2019). Climate engineering–induced changes in correlations between Earth system variables—implications for appropriate indicator selection. *Clim. Change* 153, 305–322. doi:10.1007/s10584-019-02389-7.

Mengis, N., Martin, T., Keller, D. P., and Oschlies, A. (2016). Assessing climate impacts and risks of ocean albedo modification in the Arctic. *J. Geophys. Res. Ocean.* 121, 3044–3057. doi:10.1002/2015JC011433.

Michaelis, A. C., Willison, J., Lackmann, G. M., and Robinson, W. A. (2017). Changes in Winter North Atlantic Extratropical Cyclones in High-Resolution Regional Pseudo–Global Warming Simulations. *J. Clim.* 30, 6905–6925. doi:10.1175/JCLI-D-16-0697.1.

Mignot, J., García-Serrano, J., Swingedouw, D., Germe, A., Nguyen, S., Ortega, P., et al. (2016). Decadal prediction skill in the ocean with surface nudging in the IPSL-CM5A-LR climate model. *Clim. Dyn.* 47, 1225–1246. doi:10.1007/s00382-015-2898-1.

Milinski, S., Maher, N., and Olonscheck, D. (2019). How large does a large ensemble need to be? *Earth Syst. Dynam. Discuss.* 2019, 1–19. doi:10.5194/esd-2019-70.

Millar, R. J., Fuglestvedt, J. S., Friedlingstein, P., Rogelj, J., Grubb, M. J., Matthews, H. D., et al. (2017). Emission budgets and pathways consistent with limiting warming to 1.5 degrees C. *Nat. Geosci.* 10, 741–748. doi:10.1038/ngeo3031.

Millar, R. J., Fuglestvedt, J. S., Friedlingstein, P., Rogelj, J., Grubb, M. J., Matthews, H. D., et al. (2018a). Author Correction: Emission budgets and pathways consistent with limiting warming to 1.5°C (Nature Geoscience (2017) DOI: 10.1038/ngeo3031). *Nat. Geosci.* 11, 454–455. doi:10.1038/s41561-018-0153-1.

Millar, R. J., Fuglestvedt, J. S., Friedlingstein, P., Rogelj, J., Grubb, M. J., Matthews, H. D., et al. (2018b). Reply to "Interpretations of the Paris climate target." *Nat. Geosci.* 11, 222. doi:10.1038/s41561-018-0087-7.

Mindlin, J., Shepherd, T. G., Vera, C. S., Osman, M., Zappa, G., Lee, R. W., et al. (9999). Storyline description of Southern Hemisphere midlatitude circulation and precipitation response to greenhouse gas forcing. *Clim. Dyn.* (submitted.

Mitchell, D., AchutaRao, K., Allen, M., Bethke, I., Beyerle, U., Ciavarella, A., et al. (2017). Half a degree additional warming, prognosis and projected impacts (HAPPI): background and experimental design. *Geosci. Model Dev.* 10, 571–583. doi:10.5194/gmd-10-571-2017.

Mitchell, D. L., and Finnegan, W. (2009). Modification of cirrus clouds to reduce global warming. *Environ. Res. Lett.* 4, 045102. doi:10.1088/1748-9326/4/4/045102.

Mitchell, T. D. (2003). Pattern Scaling: An Examination of the Accuracy of the Technique for Describing Future Climates. *Clim. Change* 60, 217–242. doi:10.1023/A:1026035305597.

Mizuta, R., Arakawa, O., Ose, T., Kusunoki, S., Endo, H., and Kitoh, A. (2014). Classification of CMIP5 Future Climate Responses by the Tropical Sea Surface Temperature Changes. *SOLA* 10, 167–171. doi:10.2151/sola.2014-035.

Mochizuki, T., Chikamoto, Y., Kimoto, M., Ishii, M., Tatebe, H., Komuro, Y., et al. (2012). Decadal Prediction Using a Recent Series of MIROC Global Climate Models. *J. Meteorol. Soc. Japan* 90A, 373–383. doi:10.2151/jmsj.2012-A22.

Mochizuki, T., Ishii, M., Kimoto, M., Chikamoto, Y., Watanabe, M., Nozawa, T., et al. (2010). Pacific decadal oscillation hindcasts relevant to near-term climate prediction. *Proc. Natl. Acad. Sci.* 107, 1833–1837. doi:10.1073/pnas.0906531107.

Modak, A., and Bala, G. (2019). Efficacy of black carbon aerosols : the role of shortwave cloud feedback Ef fi cacy of black carbon aerosols : the role of shortwave cloud feedback.

Modak, A., Bala, G., Caldeira, K., and Cao, L. (2018a). Does shortwave absorption by methane influence its effectiveness? *Clim. Dyn.* 0, 1–20. doi:10.1007/s00382-018-4102-x.

Modak, A., Bala, G., Caldeira, K., and Cao, L. (2018b). Does shortwave absorption by methane influence its effectiveness? *Clim. Dyn.* 51, 3653–3672. doi:10.1007/s00382-018-4102-x.

Modak, A., Bala, G., Cao, L., and Caldeira, K. (2016). Why must a solar forcing be larger than a CO2 forcing to cause the same global mean surface temperature change? *Environ. Res. Lett.* 11, 044013. doi:10.1088/1748-

9326/11/4/044013.
Mohino, E., Keenlyside, N., and Pohlmann, H. (2016). Decadal prediction of Sahel rainfall: where does the skill (or lack thereof) come from? *Clim. Dyn.* 47, 3593–3612. doi:10.1007/s00382-016-3416-9.
Mohino, E., and Losada, T. (2015). Impacts of the Atlantic Equatorial Mode in a warmer climate. *Clim. Dyn.* 45, 2255–2271. doi:10.1007/s00382-015-2471-y.
Mohino, E., Rodríguez-Fonseca, B., Mechoso, C. R., Losada, T., and Polo, I. (2019). Relationships among Intermodel Spread and Biases in Tropical Atlantic Sea Surface Temperatures. *J. Clim.* 32, 3615–3635. doi:10.1175/JCLI-D-18-0846.1.
Mohtadi, M., Prange, M., and Steinke, S. (2016). Palaeoclimatic insights into forcing and response of monsoon rainfall. *Nature*. doi:10.1038/nature17450.
Monerie, P.-A., Coquart, L., Maisonnave, É., Moine, M.-P., Terray, L., and Valcke, S. (2017). Decadal prediction skill using a high-resolution climate model. *Clim. Dyn.* 49, 3527–3550. doi:10.1007/s00382-017-3528-x.
Moore, G. W. K., Halfar, J., Majeed, H., Adey, W., and Kronz, A. (2017). Amplification of the Atlantic Multidecadal Oscillation associated with the onset of the industrial-era warming. *Sci. Rep.* 7, 40861. doi:10.1038/srep40861.
Moore, J. C., Rinke, A., Yu, X., Ji, D., Cui, X., Li, Y., et al. (2014). Arctic sea ice and atmospheric circulation under the GeoMIP G1 scenario. *J. Geophys. Res. Atmos.* 119, 567–583. doi:10.1002/2013JD021060.
Mori, M., Watanabe, M., Shiogama, H., Inoue, J., and Kimoto, M. (2014). Robust Arctic sea-ice influence on the frequent Eurasian cold winters in past decades. *Nat. Geosci.* 7, 869–873. doi:10.1038/ngeo2277.
Morice, C. P., Kennedy, J. J., Rayner, N. A., Winn, J. P., Hogan, E., Killick, R. E., et al. (9999a). An updated assessment of near-surface temperature change from 1850 : the HadCRUT5 dataset. *J. Geophys. Res. Atmos.* (submitted.
Morice, C. P., Kennedy, J. J., Rayner, N. A., Winn, J. P., Hogan, E., Killick, R. E., et al. (9999b). An updated assessment of near-surface temperature change from 1850: the HadCRUT5 dataset. *J. Geophys. Res. Atmos.* (submitted.
Msadek, R., Vecchi, G. A., Winton, M., and Gudgel, R. G. (2014). Importance of initial conditions in seasonal predictions of Arctic sea ice extent. *Geophys. Res. Lett.* 41, 5208–5215. doi:10.1002/2014GL060799.
Muri, H., Kristjansson, J. E., Storelvmo, T., and Pfeffer, M. A. (2014). The climatic effects of modifying cirrus clouds in a climate engineering framework. *J. Geophys. Res. Atmos.* 119, 4174–4191. doi:10.1002/2013JD021063.
Muri, H., Tjiputra, J., Otterå, O. H., Adakudlu, M., Lauvset, S. K., Grini, A., et al. (2018a). Climate response to aerosol geoengineering: A multimethod comparison. *J. Clim.* 31, 6319–6340. doi:10.1175/JCLI-D-17-0620.1.
Muri, H., Tjiputra, J., Otterå, O. H., Adakudlu, M., Lauvset, S. K., Grini, A., et al. (2018b). Climate Response to Aerosol Geoengineering: A Multimethod Comparison. *J. Clim.* 31, 6319–6340. doi:10.1175/JCLI-D-17-0620.1.
Murphy, J. M., Sexton, D. M. H., Barnett, D. N., Jones, G. S., Webb, M. J., Collins, M., et al. (2004). Quantification of modelling uncertainties in a large ensemble of climate change simulations. *Nature* 430, 768–772. Available at: http://dx.doi.org/10.1038/nature02771.
Muthyala, R., Bala, G., and Nalam, A. (2018a). Regional Scale Analysis of Climate Extremes in an SRM Geoengineering Simulation, Part 1:Precipitation Extremes. *Curr. Sci.* 114, 1024–1035. doi:10.18520/cs/v114/i05/1024-1035.
Muthyala, R., Bala, G., and Nalam, A. (2018b). Regional Scale Analysis of Climate Extremes in an SRM Geoengineering Simulation, Part 2:Temperature Extremes. *Curr. Sci.* 114, 1036–1045. doi:10.18520/cs/v114/i05/1036-1045.
Myhre, G., Forster, P. M., Samset, B. H., Hodnebrog, Ø., Sillmann, J., Aalbergsjø, S. G., et al. (2017). PDRMIP: A Precipitation Driver and Response Model Intercomparison Project—Protocol and Preliminary Results. *Bull. Am. Meteorol. Soc.* 98, 1185–1198. doi:10.1175/BAMS-D-16-0019.1.
Myhre, G., Kramer, R. J., Smith, C. J., Hodnebrog, Ø., Forster, P., Soden, B. J., et al. (2018a). Quantifying the Importance of Rapid Adjustments for Global Precipitation Changes. *Geophys. Res. Lett.* 45, 11,311-399,405. doi:10.1029/2018GL079474.
Myhre, G., Samset, B. H., Hodnebrog, O., Andrews, T., Boucher, O., Faluvegi, G., et al. (2018b). Sensible heat has significantly affected the global hydrological cycle over the historical period. *Nat. Commun.* 9. doi:10.1038/s41467-018-04307-4.
Nadiga, B. T., Verma, T., Weijer, W., and Urban, N. M. (2019). Enhancing Skill of Initialized Decadal Predictions Using a Dynamic Model of Drift. *Geophys. Res. Lett.* 46, 9991–9999. doi:10.1029/2019GL084223.
Najafi, M. R., Zwiers, F. W., and Gillett, N. P. (2015). Attribution of Arctic temperature change to greenhouse-gas and aerosol influences. *Nat. Clim. Chang.* 5, 246–249. doi:10.1038/nclimate2524.
Nakashiki, N., Kim, D.-H., Bryan, F. O., Yoshida, Y., Tsumune, D., Maruyama, K., et al. (2006). Recovery of thermohaline circulation under CO2 stabilization and overshoot scenarios. *Ocean Model.* 15, 200–217.
Nalam, A., Bala, G., and Modak, A. (2018). Effects of Arctic geoengineering on precipitation in the tropical monsoon regions. *Clim. Dyn.* 50, 3375–3395. doi:10.1007/s00382-017-3810-y.
National Research Council (2015a). *Climate Intervention: Carbon Dioxide Removal and Reliable Sequestration*. Washington, DC: The National Academies Press doi:10.17226/18805.
National Research Council (2015b). *Climate Intervention: Reflecting Sunlight to Cool Earth*. Washington, DC: The

National Academies Press doi:10.17226/18988.
Neely, R. R., Marsh, D. R., Smith, K. L., Davis, S. M., and Polvani, L. M. (2014). Biases in southern hemisphere climate trends induced by coarsely specifying the temporal resolution of stratospheric ozone. *Geophys. Res. Lett.* 41, 8602–8610. doi:10.1002/2014GL061627.
Negrete-García, G., Lovenduski, N. S., Hauri, C., Krumhardt, K. M., and Lauvset, S. K. (2019). Sudden emergence of a shallow aragonite saturation horizon in the Southern Ocean. *Nat. Clim. Chang.* 9, 313–317. doi:10.1038/s41558-019-0418-8.
Newman, M., Alexander, M. A., Ault, T. R., Cobb, K. M., Deser, C., Di Lorenzo, E., et al. (2016a). The Pacific decadal oscillation, revisited. *J. Clim.* 29, 4399–4427. doi:10.1175/JCLI-D-15-0508.1.
Newman, M., Alexander, M. A., Ault, T. R., Cobb, K. M., Deser, C., Di Lorenzo, E., et al. (2016b). The Pacific Decadal Oscillation, Revisited. *J. Clim.* 29, 4399–4427. doi:10.1175/JCLI-D-15-0508.1.
Niederdrenk, A. L., and Notz, D. (2018). Arctic Sea Ice in a 1.5°C Warmer World. *Geophys. Res. Lett.* 45, 1963–1971. doi:10.1002/2017GL076159.
Niemeier, U., and Schmidt, H. (2017). Changing transport processes in the stratosphere by radiative heating of sulfate aerosols. *Atmos. Chem. Phys.* 17, 14871–14886. doi:10.5194/acp-17-14871-2017.
Niemeier, U., and Timmreck, C. (2015). What is the limit of climate engineering by stratospheric injection of SO2? *Atmos. Chem. Phys.* 15, 9129–9141. doi:10.5194/acp-15-9129-2015.
Nisbet, E. G., Manning, M. R., Dlugokencky, E. J., Fisher, R. E., Lowry, D., Michel, S. E., et al. (2019). Very Strong Atmospheric Methane Growth in the 4 Years 2014–2017: Implications for the Paris Agreement. *Global Biogeochem. Cycles*, 2018GB006009. doi:10.1029/2018GB006009.
Nohara, D., Tsutsui, J., Watanabe, S., Tachiiri, K., Hajima, T., Okajima, H., et al. (2015). Examination of a climate stabilization pathway via zero-emissions using Earth system models. *Environ. Res. Lett.* 10, 095005. doi:10.1088/1748-9326/10/9/095005.
Notz, D. (2015). How well must climate models agree with observations? *Philos. Trans. R. Soc. A Math. Phys. Eng. Sci.* 373, 20140164. doi:10.1098/rsta.2014.0164.
Notz, D., Jahn, A., Holland, M., Hunke, E., Massonnet, F., Stroeve, J., et al. (2016). The CMIP6 Sea-Ice Model Intercomparison Project (SIMIP): understanding sea ice through climate-model simulations. *Geosci. Model Dev.* 9, 3427–3446. doi:10.5194/gmd-9-3427-2016.
Notz, D., and Marotzke, J. (2012). Observations reveal external driver for Arctic sea-ice retreat. *Geophys. Res. Lett.* 39, n/a-n/a. doi:10.1029/2012GL051094.
Notz, D., and Stroeve, J. (2016). Observed Arctic sea-ice loss directly follows anthropogenic CO2 emission. *Science (80-. ).* 354, 747–750. doi:10.1126/science.aag2345.
Notz, D., and Stroeve, J. (2018). The Trajectory Towards a Seasonally Ice-Free Arctic Ocean. *Curr. Clim. Chang. Reports* 4, 407–416. doi:10.1007/s40641-018-0113-2.
Nummelin, A., Li, C., and Hezel, P. J. (2017). Connecting ocean heat transport changes from the midlatitudes to the Arctic Ocean. *Geophys. Res. Lett.* 44, 1899–1908. doi:10.1002/2016GL071333.
O'Gorman, P. A., Allan, R. P., Byrne, M. P., and Previdi, M. (2012). Energetic Constraints on Precipitation Under Climate Change. *Surv. Geophys.* 33, 585–608. doi:10.1007/s10712-011-9159-6.
O'Neill, B. C., Oppenheimer, M., Warren, R., Hallegatte, S., Kopp, R. E., Pörtner, H. O., et al. (2017). IPCC reasons for concern regarding climate change risks. *Nat. Clim. Chang.* 7, 28–37. doi:10.1038/nclimate3179.
O'Neill, B. C., Tebaldi, C., van Vuuren, D. P., Eyring, V., Friedlingstein, P., Hurtt, G., et al. (2016). The Scenario Model Intercomparison Project (ScenarioMIP) for CMIP6. *Geosci. Model Dev.* 9, 3461–3482. doi:10.5194/gmd-9-3461-2016.
O'Reilly, C. H., Huber, M., Woollings, T., and Zanna, L. (2016). The signature of low-frequency oceanic forcing in the Atlantic Multidecadal Oscillation. *Geophys. Res. Lett.* 43, 2810–2818. doi:10.1002/2016GL067925.
Ohba, M., Shiogama, H., Yokohata, T., and Watanabe, M. (2013). Impact of strong tropical volcanic eruptions on enso simulated in a coupled gcm. *J. Clim.* 26, 5169–5182. doi:10.1175/JCLI-D-12-00471.1.
Ohba, M., Tsutsui, J., and Nohara, D. (2014). Statistical parameterization expressing ENSO variability and reversibility in response to CO2 concentration changes. *J. Clim.* 27, 398–410.
Oldenburg, D., Armour, K. C., Thompson, L. A., and Bitz, C. M. (2018). Distinct Mechanisms of Ocean Heat Transport Into the Arctic Under Internal Variability and Climate Change. *Geophys. Res. Lett.* 45, 7692–7700. doi:10.1029/2018GL078719.
Oleson, K. W., Anderson, G. B., Jones, B., Mcginnis, S. A., and Sanderson, B. (2018). Avoided climate impacts of urban and rural heat and cold waves over the U . S . using large climate model ensembles. 377–392. doi:10.1007/s10584-015-1504-1.
Olonscheck, D., and Notz, D. (2017). Consistently Estimating Internal Climate Variability from Climate Model Simulations. *J. Clim.* 30, 9555–9573. doi:10.1175/JCLI-D-16-0428.1.
Olson, R., An, S.-I., Fan, Y., Chang, W., Evans, J. P., and Lee, J.-Y. (2019a). A novel method to test non-exclusive hypotheses applied to Arctic ice projections from dependent models. *Nat. Commun.* 10, 3016. doi:10.1038/s41467-019-10561-x.
Olson, R., An, S.-I., Fan, Y., Chang, W., Evans, J. P., and Lee, J.-Y. (2019b). A novel method to test non-exclusive

hypotheses applied to Arctic ice projections from dependent models. *Nat. Commun.* 10, 3016. doi:10.1038/s41467-019-10561-x.
Olson, R., An, S.-I., Fan, Y., Evans, J. P., and Caesar, L. (2018). North Atlantic observations sharpen meridional overturning projections. *Clim. Dyn.* 50, 4171–4188. doi:10.1007/s00382-017-3867-7.
Organisation, W. M. (2014). *Scientific Assessment of Ozone Depletion: 2014*.
Organisation, W. M. (2019a). *Scientific Assessment of Ozone Depletion: 2018, World Meteorological Organisation Global Ozone Research and Monitoring Project-Report No. 58*. Available at: http://ozone.unep.org/science/assessment/sap.
Organisation, W. M. (2019b). *Scientific Assessment of Ozone Depletion: 2018, World Meteorological Organisation Global Ozone Research and Monitoring Project-Report No. 58*.
Osborn, T. J., Wallace, C. J., Lowe, J. A., and Bernie, D. (2018). Performance of Pattern-Scaled Climate Projections under High-End Warming. Part I: Surface Air Temperature over Land. *J. Clim.* 31, 5667–5680. doi:10.1175/JCLI-D-17-0780.1.
Oudar, T., Sanchez-Gomez, E., Chauvin, F., Cattiaux, J., Terray, L., and Cassou, C. (2017). Respective roles of direct GHG radiative forcing and induced Arctic sea ice loss on the Northern Hemisphere atmospheric circulation. *Clim. Dyn.* 49, 3693–3713. doi:10.1007/s00382-017-3541-0.
Pal, J. S., and Eltahir, E. A. B. (2016). Future temperature in southwest Asia projected to exceed a threshold for human adaptability. *Nat. Clim. Chang.* 6, 197–200. doi:10.1038/nclimate2833.
Palmer, M. D., Harris, G. R., and Gregory, J. M. (2018). Extending CMIP5 projections of global mean temperature change and sea level rise due to thermal expansion using a physically-based emulator. *Environ. Res. Lett.* 13, 84003.
Palter, J. B., Frölicher, T. L., Paynter, D., and John, J. G. (2018a). Climate, ocean circulation, and sea level changes under stabilization and overshoot pathways to 1.5 K warming. *Earth Syst. Dyn.* 9, 817–828. doi:10.5194/esd-9-817-2018.
Palter, J. B., Frölicher, T. L., Paynter, D., and John, J. G. (2018b). Climate, ocean circulation, and sea level changes under stabilization and overshoot pathways to 1.5 K warming. *Earth Syst. Dyn.* 9, 817–828. doi:10.5194/esd-9-817-2018.
Park, J.-Y., Stock, C. A., Dunne, J. P., Yang, X., and Rosati, A. (2019). Seasonal to multiannual marine ecosystem prediction with a global Earth system model. *Science (80-. ).* 365, 284–288.
Parker, A., and Irvine, P. J. (2018). The Risk of Termination Shock From Solar Geoengineering. *Earth's Futur.* 6, 456–467. doi:10.1002/2017EF000735.
Parker, W. S. (2009). Confirmation and adequacy-for-purpose in climate modelling. *Aristot. Soc. Suppl. Vol.* 83, 233–249. doi:10.1111/j.1467-8349.2009.00180.x.
Parsons, S., Renwick, J. A., and McDonald, A. J. (2016). An Assessment of Future Southern Hemisphere Blocking Using CMIP5 Projections from Four GCMs. *J. Clim.* 29, 7599–7611. doi:10.1175/JCLI-D-15-0754.1.
Pausata, F. S. R., Chafik, L., Caballero, R., and Battisti, D. S. (2015). Impacts of high-latitude volcanic eruptions on ENSO and AMOC. *Proc. Natl. Acad. Sci. U. S. A.* 112, 13784–13788. doi:10.1073/pnas.1509153112.
Peings, Y., Cattiaux, J., Vavrus, S., and Magnusdottir, G. (2017). Late twenty-first-century changes in the midlatitude atmospheric circulation in the CESM large ensemble. *J. Clim.* 30, 5943–5960. doi:10.1175/JCLI-D-16-0340.1.
Peings, Y., Simpkins, G., and Magnusdottir, G. (2016). Multidecadal fluctuations of the North Atlantic Ocean and feedback on the winter climate in CMIP5 control simulations. *J. Geophys. Res. Atmos.* 121, 2571–2592. doi:10.1002/2015JD024107.
Pendergrass, A. G., and Hartmann, D. L. (2014). The Atmospheric Energy Constraint on Global-Mean Precipitation Change. *J. Clim.* 27, 757–768. doi:10.1175/JCLI-D-13-00163.1.
Pendergrass, A. G., Knutti, R., Lehner, F., Deser, C., and Sanderson, B. M. (2017). Precipitation variability increases in a warmer climate. *Sci. Rep.* doi:10.1038/s41598-017-17966-y.
Penner, J. E., Zhou, C., and Liu, X. (2015). Can cirrus cloud seeding be used for geoengineering? *Geophys. Res. Lett.* 42, 8775–8782. doi:10.1002/2015GL065992.
Pfahl, S., O'Gorman, P. A., and Singh, M. S. (2015). Extratropical Cyclones in Idealized Simulations of Changed Climates. *J. Clim.* 28, 9373–9392. doi:10.1175/JCLI-D-14-00816.1.
Pitari, G., Aquila, V., Kravitz, B., Robock, A., Watanabe, S., Cionni, I., et al. (2014). Stratospheric ozone response to sulfate geoengineering: Results from the geoengineering model intercomparison project (GeoMip). *J. Geophys. Res.* 119, 2629–2653. doi:10.1002/2013JD020566.
Pithan, F., and Mauritsen, T. (2014). Arctic amplification dominated by temperature feedbacks in contemporary climate models. *Nat. Geosci.* 7, 181–184. doi:10.1038/ngeo2071.
Plazzotta, M., Séférian, R., Douville, H., Kravitz, B., and Tjiputra, J. (2018). Land Surface Cooling Induced by Sulfate Geoengineering Constrained by Major Volcanic Eruptions. *Geophys. Res. Lett.* 45, 5663–5671. doi:10.1029/2018GL077583.
Pohlmann, H., Jungclaus, J. H., Köhl, A., Stammer, D., and Marotzke, J. (2009). Initializing decadal climate predictions with the GECCO oceanic synthesis: Effects on the North Atlantic. *J. Clim.* 22, 3926–3938.
Pohlmann, H., Kröger, J., Greatbatch, R. J., and Müller, W. A. (2017). Initialization shock in decadal hindcasts due to

errors in wind stress over the tropical Pacific. *Clim. Dyn.* 49, 2685–2693. doi:10.1007/s00382-016-3486-8.
Pohlmann, H., Müller, W. A., Kulkarni, K., Kameswarrao, M., Matei, D., Vamborg, F. S. E., et al. (2013). Improved forecast skill in the tropics in the new MiKlip decadal climate predictions. *Geophys. Res. Lett.* 40, 5798–5802. doi:10.1002/2013GL058051.
Polkova, I., Brune, S., Kadow, C., Romanova, V., Gollan, G., Baehr, J., et al. (2019). Initialization and Ensemble Generation for Decadal Climate Predictions: A Comparison of Different Methods. *J. Adv. Model. Earth Syst.* 11, 149–172. doi:10.1029/2018MS001439.
Polkova, I., Köhl, A., and Stammer, D. (2014). Impact of initialization procedures on the predictive skill of a coupled ocean–atmosphere model. *Clim. Dyn.* 42, 3151–3169. doi:10.1007/s00382-013-1969-4.
Polson, D., Bollasina, M., Hegerl, G. C., and Wilcox, L. J. (2014). Decreased monsoon precipitation in the Northern Hemisphere due to anthropogenic aerosols. *Geophys. Res. Lett.* 41, 6023–6029. doi:10.1002/2014GL060811.
Power, S. B., Delage, F., Colman, R., and Moise, A. (2012). Consensus on Twenty-First-Century Rainfall Projections in Climate Models More Widespread than Previously Thought. *J. Clim.* 25, 3792–3809. doi:10.1175/JCLI-D-11-00354.1.
Power, S., Delage, F., Chung, C., Kociuba, G., and Keay, K. (2013). Robust twenty-first-century projections of El Niño and related precipitation variability. *Nature* 502, 541–545. doi:10.1038/nature12580.
Predybaylo, E., Stenchikov, G. L., Wittenberg, A. T., and Zeng, F. (2017). Impacts of a pinatubo-size volcanic eruption on ENSO. *J. Geophys. Res.* 122, 925–947. doi:10.1002/2016JD025796.
Proctor, J., Hsiang, S., Burney, J., Burke, M., and Schlenker, W. (2018). Estimating global agricultural effects of geoengineering using volcanic eruptions. *Nature* 560, 480–483. doi:10.1038/s41586-018-0417-3.
Pugh, T. A. M., Jones, C. D., Huntingford, C., Burton, C., Arneth, A., Brovkin, V., et al. (2018). A Large Committed Long-Term Sink of Carbon due to Vegetation Dynamics. *Earth's Futur.* 6, 1413–1432. doi:10.1029/2018EF000935.
Putnam, A. E., and Broecker, W. S. (2017). Human-induced changes in the distribution of rainfall. *Sci. Adv.* 3. doi:10.1126/sciadv.1600871.
Rahmstorf, S., and Ganopolski, A. (1999). Long-term global warming scenarios computed with an efficient coupled climate model. *Clim. Change* 43, 353–367.
Ramanathan, V., Chung, C., Kim, D., Bettge, T., Buja, L., Kiehl, J. T., et al. (2005). Atmospheric brown clouds: Impacts on South Asian climate and hydrological cycle. *Proc. Natl. Acad. Sci.* 102, 5326–5333. doi:10.1073/pnas.0500656102.
Ramanathan, V., and Feng, Y. (2008). On avoiding dangerous anthropogenic interference with the climate system: Formidable challenges ahead. *Proc. Natl. Acad. Sci. U. S. A.* doi:10.1073/pnas.0803838105.
Ramesh, K. V, and Goswami, P. (2014). Assessing reliability of regional climate projections: the case of Indian monsoon. *Sci. Rep.* 4, 4071. doi:10.1038/srep04071.
Randerson, J. T., Lindsay, K., Munoz, E., Fu, W., Moore, J. K., Hoffman, F. M., et al. (2015). Multicentury changes in ocean and land contributions to the climate-carbon feedback. *Global Biogeochem. Cycles*. doi:10.1002/2014GB005079.
Rao, S., Klimont, Z., Smith, S. J., Van Dingenen, R., Dentener, F., Bouwman, L., et al. (2017). Future air pollution in the Shared Socio-economic Pathways. *Glob. Environ. Chang.* 42, 346–358.
Regayre, L. A., Johnson, J. S., Yoshioka, M., Pringle, K. J., Sexton, D. M. H., Booth, B. B. B., et al. (2018). Aerosol and physical atmosphere model parameters are both important sources of uncertainty in aerosol ERF. *Atmos. Chem. Phys.* 18, 9975–10006. doi:10.5194/acp-18-9975-2018.
Riahi, K., van Vuuren, D. P., Kriegler, E., Edmonds, J., O'Neill, B. C., Fujimori, S., et al. (2017). The Shared Socioeconomic Pathways and their energy, land use, and greenhouse gas emissions implications: An overview. *Glob. Environ. Chang.* 42, 153–168. doi:10.1016/j.gloenvcha.2016.05.009.
Ribes, A., Qasmi, S., and Gillett, N. (9999). Kriging climate change to narrow uncertainty on past and future human-induced warming. *Geophys. Res. Lett.* (submitted.
Richardson, T. B., Forster, P. M., Andrews, T., Boucher, O., Faluvegi, G., Fläschner, D., et al. (2018a). Carbon Dioxide Physiological Forcing Dominates Projected Eastern Amazonian Drying. *Geophys. Res. Lett.* 45, 2815–2825. doi:10.1002/2017GL076520.
Richardson, T. B., Forster, P. M., Andrews, T., Boucher, O., Faluvegi, G., Fläschner, D., et al. (2018b). Drivers of Precipitation Change: An Energetic Understanding. *J. Clim.* 31, 9641–9657. doi:10.1175/JCLI-D-17-0240.1.
Richardson, T. B., Forster, P. M., Andrews, T., and Parker, D. J. (2016). Understanding the Rapid Precipitation Response to CO 2 and Aerosol Forcing on a Regional Scale. *J. Clim.* 29, 583–594. doi:10.1175/JCLI-D-15-0174.1.
Richardson, T., Forster, P. M., Smith, C. J., Maycock, A. C., Wood, T., Andrews, T., et al. (2019). Efficacy of climate forcings in PDRMIP models. *J. Geophys. Res.* submitted.
Richter Jadwiga, H., Simone, T., Anne, G., Ben, K., G., M. D., J., M. M., et al. (2018). Stratospheric Response in the First Geoengineering Simulation Meeting Multiple Surface Climate Objectives. *J. Geophys. Res. Atmos.* 123, 5762–5782. doi:10.1029/2018JD028285.
Ricke, K. L., and Caldeira, K. (2014). Maximum warming occurs about one decade after a carbon dioxide emission.

*Environ. Res. Lett.* 9, 124002. doi:10.1088/1748-9326/9/12/124002.
Rickels, W., Reith, F., Keller, D., Oschlies, A., and Quaas, M. F. (2018). Integrated Assessment of Carbon Dioxide Removal. *Earth's Futur.* 6, 565–582. doi:10.1002/2017EF000724.
Ridley, H. E., Asmerom, Y., Baldini, J. U. L., Breitenbach, S. F. M., Aquino, V. V, Prufer, K. M., et al. (2015). Aerosol forcing of the position of the intertropical convergence zone since ad 1550. *Nat. Geosci.* 8, 195–200. doi:10.1038/ngeo2353.
Ridley, J., Gregory, J. M., Huybrechts, P., and Lowe, J. (2010). Thresholds for irreversible decline of the Greenland ice sheet. *Clim. Dyn.* 35, 1049–1057. doi:10.1007/s00382-009-0646-0.
Robock, A. (1983). Ice and snow feedbacks and the latitudinal and seasonal distribution of climate sensitivity. *J. Atmos. Sci.* 40, 986–997.
Robock, A., Bunzl, M., Kravitz, B., and Stenchikov, G. L. (2010). A Test for Geoengineering ? *Science (80-. ).* 38, 9–10.
Robock, A., MacMartin, D. G., Duren, R., and Christensen, M. W. (2013). Studying geoengineering with natural and anthropogenic analogs. *Clim. Change* 121, 445–458. doi:10.1007/s10584-013-0777-5.
Robock, A., Oman, L., and Stenchikov, G. (2008). Regional climate responses to geoengineering with tropical and Artic SO2 injections. *J. Geophys. Res.* 113, 1–15. doi:10.1029/2008JD010050.
Robson, J., Hodson, D., Hawkins, E., and Sutton, R. (2014a). Atlantic overturning in decline? *Nat. Geosci.* 7, 2–3. doi:10.1038/ngeo2050.
Robson, J. I., Sutton, R. T., and Smith, D. M. (2012). Initialized decadal predictions of the rapid warming of the North Atlantic Ocean in the mid 1990s. *Geophys. Res. Lett.* 39, n/a-n/a. doi:10.1029/2012GL053370.
Robson, J., Sutton, R., and Smith, D. (2014b). Decadal predictions of the cooling and freshening of the North Atlantic in the 1960s and the role of ocean circulation. *Clim. Dyn.* 42, 2353–2365. doi:10.1007/s00382-014-2115-7.
Rodgers, K. B., Lin, J., and Frölicher, T. L. (2015). Emergence of multiple ocean ecosystem drivers in a large ensemble suite with an Earth system model. *Biogeosciences* 12, 3301–3320. doi:10.5194/bg-12-3301-2015.
Rogelj, J., Popp, A., Calvin, K. V., Luderer, G., Emmerling, J., Gernaat, D., et al. (2018a). Scenarios towards limiting global mean temperature increase below 1.5 °c. *Nat. Clim. Chang.* 8, 325–332. doi:10.1038/s41558-018-0091-3.
Rogelj, J., Schaeffer, M., Meinshausen, M., Shindell, D. T., Hare, W., Klimont, Z., et al. (2014). Disentangling the effects of CO2 and short-lived climate forcer mitigation. *Proc. Natl. Acad. Sci.* 111, 16325–16330. doi:10.1073/pnas.1415631111.
Rogelj, J., Shindell, D., Jiang, K., Fifita, S., Forster, P., Ginzburg, V., et al. (2018b). "Mitigation Pathways Compatible with 1.5°C in the Context of Sustainable Development Supplementary Material," in *Global Warming of 1.5°C. An IPCC Special Report on the impacts of global warming of 1.5°C above pre-industrial levels and related global greenhouse gas emission pathways, in the context of strengthening the global response to the threat of climate change,* eds. V. Masson-Delmotte, P. Zhai, H.-O. Pörtner, D. Roberts, J. Skea, P. R. Shukla, et al. (In Press). Available at: https://www.ipcc.ch/sr15.
Rotstayn, L. D. (2013). Projected effects of declining anthropogenic aerosols on the southern annular mode. *Environ. Res. Lett.* 8, 044028. doi:10.1088/1748-9326/8/4/044028.
Rowell, D. P. (2012). Sources of uncertainty in future changes in local precipitation. *Clim. Dyn.* doi:10.1007/s00382-011-1210-2.
Royal Society (2009). *Geoengineering the climate*. London.
Rugenstein, M. A. A., Caldeira, K., and Knutti, R. (2016). Dependence of global radiative feedbacks on evolving patterns of surface heat fluxes. *Geophys. Res. Lett.* 43, 9877–9885.
Rugenstein, M., Bloch-Johnson, J., Abe-Ouchi, A., Andrews, T., Beyerle, U., Cao, L., et al. (2019a). LongRunMIP – motivation and design for a large collection of millennial-length AO-GCM simulations. *Bull. Am. Meteorol. Soc.* doi:10.1175/bams-d-19-0068.1.
Rugenstein, M., Bloch‐Johnson, J., Gregory, J., Andrews, T., Mauritsen, T., Li, C., et al. (2019b). Equilibrium climate sensitivity estimated by equilibrating climate models. *Geophys. Res. Lett.* doi:10.1029/2019GL083898.
Ruiz-Barradas, A., Nigam, S., and Kavvada, A. (2013). The Atlantic Multidecadal Oscillation in twentieth century climate simulations: uneven progress from CMIP3 to CMIP5. *Clim. Dyn.* 41, 3301–3315. doi:10.1007/s00382-013-1810-0.
Ruprich-Robert, Y., and Cassou, C. (2015). Combined influences of seasonal East Atlantic Pattern and North Atlantic Oscillation to excite Atlantic multidecadal variability in a climate model. *Clim. Dyn.* 44, 229–253. doi:10.1007/s00382-014-2176-7.
Russo, S., Sillmann, J., and Sterl, A. (2017). Humid heat waves at different warming levels. *Sci. Rep.* 7, 7477. doi:10.1038/s41598-017-07536-7.
Russotto, R. D., and Ackerman, T. P. (2018). Changes in clouds and thermodynamics under solar geoengineering and implications for required solar reduction. *Atmos. Chem. Phys.* 18, 11905–11925. doi:10.5194/acp-18-11905-2018.
Saffioti, C., Fischer, E. M., and Knutti, R. (2017). Improved Consistency of Climate Projections over Europe after Accounting for Atmospheric Circulation Variability. *J. Clim.* 30, 7271–7291. doi:10.1175/JCLI-D-16-0695.1.
Samset, B. H., Fuglestvedt, J. S., and Lund, M. T. (9999). Curbing our expectations: Global temperature impacts from

strong mitigation of individual climate forcers. *Nat. Commun.* (submitted.
Samset, B. H., Myhre, G., Forster, P. M., Hodnebrog, Ø., Andrews, T., Boucher, O., et al. (2018a). Weak hydrological sensitivity to temperature change over land, independent of climate forcing. *npj Clim. Atmos. Sci.* 1, 20173. doi:10.1038/s41612-017-0005-5.
Samset, B. H., Myhre, G., Forster, P. M., Hodnebrog, Ø., Andrews, T., Faluvegi, G., et al. (2016). Fast and slow precipitation responses to individual climate forcers: A PDRMIP multimodel study. *Geophys. Res. Lett.* 43, 2782–2791. doi:10.1002/2016GL068064.
Samset, B. H., Sand, M., Smith, C. J., Bauer, S. E., Forster, P. M., Fuglestvedt, J. S., et al. (2018b). Climate Impacts From a Removal of Anthropogenic Aerosol Emissions. *Geophys. Res. Lett.* 45, 1020–1029. doi:10.1002/2017GL076079.
Sanchez, C., Williams, K. D., and Collins, M. (2016). Improved stochastic physics schemes for global weather and climate models. *Q. J. R. Meteorol. Soc.* 142, 147–159. doi:10.1002/qj.2640.
Sanchez, D. J., and Simon, M. C. (2018). Transcriptional control of kidney cancer. *Science (80-. ).* 361, 226–227. doi:10.1126/science.aau4385.
Sand, M., Berntsen, T. K., von Salzen, K., Flanner, M. G., Langner, J., and Victor, D. G. (2016). Response of Arctic temperature to changes in emissions of short-lived climate forcers. *Nat. Clim. Chang.* 6, 286–289. doi:10.1038/nclimate2880.
Sanderson, B. M., Knutti, R., and Caldwell, P. (2015). Addressing Interdependency in a Multimodel Ensemble by Interpolation of Model Properties. *J. Clim.* 28, 5150–5170. doi:10.1175/JCLI-D-14-00361.1.
Sanderson, B. M., O'Neill, B. C., Kiehl, J. T., Meehl, G. A., Knutti, R., and Washington, W. M. (2011). The response of the climate system to very high greenhouse gas emission scenarios. *Environ. Res. Lett.* doi:10.1088/1748-9326/6/3/034005.
Sanderson, B. M., Oleson, K. W., Strand, W. G., Lehner, F., and O'Neill, B. C. (2018). A new ensemble of GCM simulations to assess avoided impacts in a climate mitigation scenario. *Clim. Change* 146, 303–318. doi:10.1007/s10584-015-1567-z.
Sanderson, B. M., Wehner, M., and Knutti, R. (2017a). Skill and independence weighting for multi-model assessments. *Geosci. Model Dev.* 10, 2379–2395. doi:10.5194/gmd-10-2379-2017.
Sanderson, B. M., Xu, Y., Tebaldi, C., Wehner, M., Neill, B. O., Jahn, A., et al. (2017b). Community climate simulations to assess avoided impacts in 1 . 5 and 2 ◦ C futures. 827–847.
Santer, B. D., Bonfils, C., Painter, J. F., Zelinka, M. D., Mears, C., Solomon, S., et al. (2014). Volcanic contribution to decadal changes in tropospheric temperature. *Nat. Geosci.* 7, 185–189. doi:10.1038/ngeo2098.
Santer, B. D. D., Po-Chedley, S., Zelinka, M. D. D., Cvijanovic, I., Bonfils, C., Durack, P. J. J., et al. (2018). Human influence on the seasonal cycle of tropospheric temperature. *Science (80-. ).* 361, eaas8806. doi:10.1126/science.aas8806.
Scaife, A. A., and Smith, D. (2018). A signal-to-noise paradox in climate science. *npj Clim. Atmos. Sci.* 1, 28. doi:10.1038/s41612-018-0038-4.
Schleussner, C.-F., Pfleiderer, P., and Fischer, E. M. (2017a). In the observational record half a degree matters. *Nat. Clim. Chang.* 7, 460–462. doi:10.1038/nclimate3320.
Schleussner, C.-F., Pfleiderer, P., and Fischer, E. M. (2017b). In the observational record half a degree matters. *Nat. Clim. Chang.* 7, 460–462. doi:10.1038/nclimate3320.
Schloesser, F., Friedrich, T., Timmermann, A., DeConto, R. M., and Pollard, D. (2019). Antarctic iceberg impacts on future Southern Hemisphere climate. *Nat. Clim. Chang.* doi:10.1038/s41558-019-0546-1.
Schmidt, H., Alterskjær, K., Alterskjær, K., Bou Karam, D., Boucher, O., Jones, A., et al. (2012). Solar irradiance reduction to counteract radiative forcing from a quadrupling of CO2: Climate responses simulated by four earth system models. *Earth Syst. Dyn.* 3, 63–78. doi:10.5194/esd-3-63-2012.
Schneider, S. H. (2001). What is "dangerous" climate change? *Nature* 411, 17–19.
Schneider, T., O'Gorman, P. A., and Levine, X. J. (2010). Water vapor and the dynamics of climate changes. *Rev. Geophys.* 48, RG3001.
Schurer, A. P., Cowtan, K., Hawkins, E., Mann, M. E., Scott, V., and Tett, S. F. B. (2018). Interpretations of the Paris climate target. *Nat. Geosci.* 11, 220–221. doi:10.1038/s41561-018-0086-8.
Schwierz, C., Croci-Maspoli, M., and Davies, H. C. (2004). Perspicacious indicators of atmospheric blocking. *Geophys. Res. Lett.* 31, n/a-n/a. doi:10.1029/2003GL019341.
Schwingshackl, C., Sillmann, J., Sandstad, M., and Aunan, K. (9999). Heat stress indicators in CMIP6: Estimating future trends and exceedances of critical physiological thresholds. *Environ. Res. Lett.* (submitted.
Screen, J. A. (2014). Arctic amplification decreases temperature variance in northern mid- to high-latitudes. *Nat. Clim. Chang.* 4, 577–582. doi:10.1038/nclimate2268.
Screen, J. A. (2018). Arctic sea ice at 1.5 and 2 °C. *Nat. Clim. Chang.* 8, 362–363. doi:10.1038/s41558-018-0137-6.
Screen, J. A., Bracegirdle, T. J., and Simmonds, I. (2018a). Polar Climate Change as Manifest in Atmospheric Circulation. *Curr. Clim. Chang. Reports* 4, 383–395. doi:10.1007/s40641-018-0111-4.
Screen, J. A., Deser, C., Smith, D. M., Zhang, X., Blackport, R., Kushner, P. J., et al. (2018b). Consistency and discrepancy in the atmospheric response to Arctic sea-ice loss across climate models. *Nat. Geosci.* 11, 155–163.

doi:10.1038/s41561-018-0059-y.
Screen, J. A., and Williamson, D. (2017). Ice-free Arctic at 1.5 °C? *Nat. Clim. Chang.* 7, 230–231.
Seager, R., Liu, H., Henderson, N., Simpson, I., Kelley, C., Shaw, T., et al. (2014a). Causes of increasing aridification of the {M}editerranean region in response to rising greenhouse gases. *J. Clim.* 27, 4655–4676.
Seager, R., Neelin, D., Simpson, I., Liu, H., Henderson, N., Shaw, T., et al. (2014b). Dynamical and thermodynamical causes of large-scale changes in the hydrological cycle over {N}orth {A}merica in response to global warming. *J. Clim.* 27, 7921–7948.
Seiffert, R., and von Storch, J.-S. (2008). Impact of atmospheric small-scale fluctuations on climate sensitivity. *Geophys. Res. Lett.* 35, L10704. doi:10.1029/2008GL033483.
Seiler, C., and Zwiers, F. W. (2016). How will climate change affect explosive cyclones in the extratropics of the Northern Hemisphere? *Clim. Dyn.* 46, 3633–3644. doi:10.1007/s00382-015-2791-y.
Sellar, A. A., Jones, C. G., Mulcahy, J., Tang, Y., Yool, A., Wiltshire, A., et al. (2019). UKESM1: Description and evaluation of the UK Earth System Model. *J. Adv. Model. Earth Syst.* doi:10.1029/2019ms001739.
Selten, F. M., Branstator, G. W., Dijkstra, H. A., and Kliphuis, M. (2004). Tropical origins for recent and future Northern Hemisphere climate change. *Geophys. Res. Lett.* 31, L21205. doi:10.1029/2004GL020739.
Seneviratne, S. I., Donat, M. G., Pitman, A. J., Knutti, R., and Wilby, R. L. (2016a). Allowable CO2 emissions based on regional and impact-related climate targets. *Nature* 529, 477–483. doi:10.1038/nature16542.
Seneviratne, S. I., Donat, M. G., Pitman, A. J., Knutti, R., and Wilby, R. L. (2016b). Allowable CO2 emissions based on regional and impact-related climate targets. *Nature* 529, 477–483. doi:10.1038/nature16542.
Seneviratne, S. I., Lüthi, D., Litschi, M., and Schär, C. (2006). Land–atmosphere coupling and climate change in Europe. *Nature* 443, 205–209. doi:10.1038/nature05095.
Seneviratne, S. I., Phipps, S. J., Pitman, A. J., Hirsch, A. L., Davin, E. L., Donat, M. G., et al. (2018a). Land radiative management as contributor to regional-scale climate adaptation and mitigation. *Nat. Geosci.* 11, 88–96. doi:10.1038/s41561-017-0057-5.
Seneviratne, S. I., Wartenburger, R., Guillod, B. P., Hirsch, A. L., Vogel, M. M., Brovkin, V., et al. (2018b). Climate extremes, land–climate feedbacks and land-use forcing at 1.5°C. *Philos. Trans. R. Soc. A Math. Phys. Eng. Sci.* 376, 20160450. doi:10.1098/rsta.2016.0450.
Serreze, M. C., and Barry, R. G. (2011). Processes and impacts of Arctic amplification: A research synthesis. *Glob. Planet. Change* 77, 85–96. doi:10.1016/j.gloplacha.2011.03.004.
Servain, J., Caniaux, G., Kouadio, Y. K., McPhaden, M. J., and Araujo, M. (2014). Recent climatic trends in the tropical Atlantic. *Clim. Dyn.* 43, 3071–3089. doi:10.1007/s00382-014-2168-7.
Sgubin, G., Swingedouw, D., Drijfhout, S., Hagemann, S., and Robertson, E. (2014). Multimodel analysis on the response of the AMOC under an increase of radiative forcing and its symmetrical reversal. *Clim. Dyn.* 45. doi:10.1007/s00382-014-2391-2.
Sgubin, G., Swingedouw, D., Drijfhout, S., Hagemann, S., and Robertson, E. (2015). Multimodel analysis on the response of the AMOC under an increase of radiative forcing and its symmetrical reversal. *Clim. Dyn.* 45, 1429–1450. doi:10.1007/s00382-014-2391-2.
Shaffrey, L. C., Hodson, D., Robson, J., Stevens, D. P., Hawkins, E., Polo, I., et al. (2017). Decadal predictions with the HiGEM high resolution global coupled climate model: description and basic evaluation. *Clim. Dyn.* 48, 297–311. doi:10.1007/s00382-016-3075-x.
Shaw, T. A. (2019). Mechanisms of Future Predicted Changes in the Zonal Mean Mid-Latitude Circulation. *Curr. Clim. Chang. Reports*, 345–357. doi:10.1007/s40641-019-00145-8.
Shaw, T. A., Baldwin, M., Barnes, E. A., Caballero, R., Garfinkel, C. I., Hwang, Y.-T., et al. (2016). Storm track processes and the opposing influences of climate change. *Nat. Geosci.* 9, 656–664. doi:10.1038/ngeo2783.
Shaw, T. A., and Voigt, A. (2015). Tug of war on summertime circulation between radiative forcing and sea surface warming. *Nat. Geosci.* 8, 560–566. doi:10.1038/ngeo2449.
Shawki, D., Voulgarakis, A., Chakraborty, A., Kasoar, M., and Srinivasan, J. (2018). The South Asian Monsoon Response to Remote Aerosols: Global and Regional Mechanisms. *J. Geophys. Res. Atmos.* 123, 11,511-585,601. doi:10.1029/2018JD028623.
Sheen, K. L., Smith, D. M., Dunstone, N. J., Eade, R., Rowell, D. P., and Vellinga, M. (2017). Skilful prediction of Sahel summer rainfall on inter-annual and multi-year timescales. *Nat. Commun.* 8, 14966. Available at: http://dx.doi.org/10.1038/ncomms14966.
Shepherd, T. G. (2014). Atmospheric circulation as a source of uncertainty in climate change projections. *Nat. Geosci.* 7, 703–708. doi:10.1038/ngeo2253.
Shepherd, T. G. (2019). Storyline approach to the construction of regional climate change information. *Proc. R. Soc. A Math. Phys. Eng. Sci.* 475. doi:10.1098/rspa.2019.0013.
Shepherd, T. G., Boyd, E., Calel, R. A., Chapman, S. C., Dessai, S., Dima-West, I. M., et al. (2018). Storylines: an alternative approach to representing uncertainty in physical aspects of climate change. *Clim. Change* 151, 555–571. doi:10.1007/s10584-018-2317-9.
Sherwood, S. C., Bony, S., Boucher, O., Bretherton, C., Forster, P. M., Gregory, J. M., et al. (2015). Adjustments in the Forcing-Feedback Framework for Understanding Climate Change. *Bull. Am. Meteorol. Soc.* 96, 217–228.

doi:10.1175/BAMS-D-13-00167.1.
Shindell, D., Borgford-Parnell, N., Brauer, M., Haines, A., Kuylenstierna, J. C. I., Leonard, S. A., et al. (2017). A climate policy pathway for near- and long-term benefits. *Science (80-. ).* 356, 493–494. doi:10.1126/science.aak9521.
Shindell, D., Kuylenstierna, J. C. I., Vignati, E., Van Dingenen, R., Amann, M., Klimont, Z., et al. (2012). Simultaneously mitigating near-term climate change and improving human health and food security. *Science (80-. ).* 335, 183–189. doi:10.1126/science.1210026.
Shindell, D., and Smith, C. J. (2019a). Climate and air-quality benefits of a realistic phase-out of fossil fuels. *Nature* 573, 408–411. doi:10.1038/s41586-019-1554-z.
Shindell, D., and Smith, C. J. (2019b). Climate and air-quality benefits of a realistic phase-out of fossil fuels. *Nature* 573, 408–411. doi:10.1038/s41586-019-1554-z.
Shindell, D., and Smith, C. J. (2019c). Climate and air-quality benefits of a realistic phase-out of fossil fuels. *Nature*. doi:10.1038/s41586-019-1554-z.
Shiogama, H., Stone, D., Emori, S., Takahashi, K., Mori, S., Maeda, A., et al. (2016). Predicting future uncertainty constraints on global warming projections. *Sci. Rep.* 6, 18903. Available at: https://doi.org/10.1038/srep18903.
Shu, Q., Song, Z., and Qiao, F. (2015). Assessment of sea ice simulations in the CMIP5 models. *Cryosph.* 9, 399–409. doi:10.5194/tc-9-399-2015.
Sienz, F., Müller, W. A., and Pohlmann, H. (2016). Ensemble size impact on the decadal predictive skill assessment. *Meteorol. Zeitschrift* 25, 645–655. doi:10.1127/metz/2016/0670.
Sigmond, M., and Fyfe, J. C. (2016). Tropical Pacific impacts on cooling North American winters. *Nat. Clim. Chang.* 6, 970–974. doi:10.1038/nclimate3069.
Sigmond, M., Fyfe, J. C., Saenko, O. A., and Swart, N. C. (9999). Ongoing AMOC and related sea level and temperature changes after stabilization at 1.5°C, 2.0°C and 3.0°C global warming. *Nat. Clim. Chang.* (submitted.
Sigmond, M., Fyfe, J. C., and Swart, N. C. (2018). Ice-free Arctic projections under the Paris Agreement. *Nat. Clim. Chang.* 8, 404–408. doi:10.1038/s41558-018-0124-y.
Sime, L. C., Hopcroft, P. O., and Rhodes, R. H. (2019). Impact of abrupt sea ice loss on Greenland water isotopes during the last glacial period. *Proc. Natl. Acad. Sci. U. S. A.* 116, 4099–4104. doi:10.1073/pnas.1807261116.
SIMIP Community (9999). Arctic Sea Ice in CMIP6. *Geophys. Res. Lett.* (submitted.
Simpson, I. R., Deser, C., McKinnon, K. A., and Barnes, E. A. (2018a). Modeled and observed multidecadal variability in the North Atlantic jet stream and its connection to sea surface temperatures. *J. Clim.* 31, 8313–8338. doi:10.1175/JCLI-D-18-0168.1.
Simpson, I. R., Deser, C., McKinnon, K. A., and Barnes, E. A. (2018b). Modeled and Observed Multidecadal Variability in the North Atlantic Jet Stream and Its Connection to Sea Surface Temperatures. *J. Clim.* 31, 8313–8338. doi:10.1175/JCLI-D-18-0168.1.
Simpson, I. R., Hitchcock, P., Seager, R., Wu, Y., and Callaghan, P. (2018c). The Downward Influence of Uncertainty in the Northern Hemisphere Stratospheric Polar Vortex Response to Climate Change. *J. Clim.* 31, 6371–6391. doi:10.1175/JCLI-D-18-0041.1.
Simpson, I. R., and Polvani, L. M. (2016). Revisiting the relationship between jet position, forced response, and annular mode variability in the southern midlatitudes. *Geophys. Res. Lett.* 43, 2896–2903. doi:10.1002/2016GL067989.
Simpson, I. R., Shaw, T. A., and Seager, R. (2014). A Diagnosis of the Seasonally and Longitudinally Varying Midlatitude Circulation Response to Global Warming*. *J. Atmos. Sci.* 71, 2489–2515. doi:10.1175/JAS-D-13-0325.1.
Simpson, I. R., Tilmes, S., Richter, J. H., Kravitz, B., MacMartin, D. G., Mills, M. J., et al. (2019a). The regional hydroclimate response to stratospheric sulfate geoengineering and the role of stratospheric heating. *J. Geophys. Res. Atmos.*, 2019JD031093. doi:10.1029/2019JD031093.
Simpson, I. R., Yeager, S. G., McKinnon, K. A., and Deser, C. (2019b). Decadal predictability of late winter precipitation in western Europe through an ocean–jet stream connection. *Nat. Geosci.* 12, 613–619. doi:10.1038/s41561-019-0391-x.
Simpson, I. R., Yeager, S. G., McKinnon, K. A., and Deser, C. (2019c). Decadal predictability of late winter precipitation in western Europe through an ocean–jet stream connection. *Nat. Geosci.* 12, 613–619. doi:10.1038/s41561-019-0391-x.
Singh, H. A., Rasch, P. J., and Rose, B. E. J. (2017). Increased Ocean Heat Convergence Into the High Latitudes With CO 2 Doubling Enhances Polar-Amplified Warming. *Geophys. Res. Lett.* 44, 10,583-10,591. doi:10.1002/2017GL074561.
Sippel, S., Meinshausen, N., Merrifield, A., Lehner, F., Pendergrass, A. G., Fischer, E., et al. (2019). Uncovering the forced climate response from a single ensemble member using statistical learning. *J. Clim.* doi:10.1175/JCLI-D-18-0882.1.
Smith, C. J., Forster, P. M., Allen, M., Fuglestvedt, J., Millar, R. J., Rogelj, J., et al. (2019a). Current fossil fuel infrastructure does not yet commit us to 1.5 °C warming. *Nat. Commun.* doi:10.1038/s41467-018-07999-w.
Smith, D. M., Eade, R., and Pohlmann, H. (2013a). A comparison of full-field and anomaly initialization for seasonal to decadal climate prediction. *Clim. Dyn.* 41, 3325–3338. doi:10.1007/s00382-013-1683-2.

Smith, D. M., Eade, R., Scaife, A. A., Caron, L.-P., Danabasoglu, G., DelSole, T. M., et al. (2019b). Robust skill of decadal climate predictions. *npj Clim. Atmos. Sci.* 2, 13. doi:10.1038/s41612-019-0071-y.

Smith, D. M., Eade, R., Scaife, A. A., Caron, L.-P., Danabasoglu, G., DelSole, T. M., et al. (2019c). Robust skill of decadal climate predictions. *npj Clim. Atmos. Sci.* 2, 13. doi:10.1038/s41612-019-0071-y.

Smith, D. M., Scaife, A. A., Boer, G. J., Caian, M., Doblas-Reyes, F. J., Guemas, V., et al. (2013b). Real-time multi-model decadal climate predictions. *Clim. Dyn.* 41, 2875–2888. doi:10.1007/s00382-012-1600-0.

Smith, D. M., Scaife, A. A., Eade, R., Athanasiadis, P., Bellucci, A., Bethke, I., et al. (2019d). Gross underestimation of atmospheric circulation signals in climate models.

Smith, D. M., Scaife, A. A., Eade, R., Athanasiadis, P., Bellucci, A., Bethke, I., et al. (9999). Gross underestimation of atmospheric circulation signals in climate models. *Nature* (submitted.

Smith, D. M., Scaife, A. A., Hawkins, E., Bilbao, R., Boer, G. J., Caian, M., et al. (2018). Predicted Chance That Global Warming Will Temporarily Exceed 1.5 °C. *Geophys. Res. Lett.* 45, 11,895-11,903. doi:10.1029/2018GL079362.

Smith, P., Davis, S. J., Creutzig, F., Fuss, S., Minx, J., Gabrielle, B., et al. (2016). Biophysical and economic limits to negative CO2emissions. *Nat. Clim. Chang.* doi:10.1038/nclimate2870.

Smith, S. J., and Mizrahi, A. (2013). Near-term climate mitigation by short-lived forcers. *Proc. Natl. Acad. Sci.* 110, 14202–14206. doi:10.1073/pnas.1308470110.

Sobel, A. H., and Camargo, S. J. (2011). Projected Future Seasonal Changes in Tropical Summer Climate. *J. Clim.* 24, 473–487. doi:10.1175/2010JCLI3748.1.

Soden, B. J., Wetherald, R. T., Stenchikov, G. L., and Robock, A. (2002). Global Cooling After the Eruption of Mount Pinatubo : A Test of Climate Feedback by Water Vapor. 296, 727–731.

Solomon, A., and Polvani, L. M. (2016). Highly Significant Responses to Anthropogenic Forcings of the Midlatitude Jet in the Southern Hemisphere. *J. Clim.* 29, 3463–3470. doi:10.1175/JCLI-D-16-0034.1.

Solomon, S., Ivy, D. J., Kinnison, D., Mills, M. J., Iii, R. R. N., and Schmidt, A. (2016). Antarctic ozone layer. *Science (80-. ).* 353, 269–274.

Solomon, S., Plattner, G.-K., Knutti, R., and Friedlingstein, P. (2009). Irreversible climate change due to carbon dioxide emissions. *Proc. Natl. Acad. Sci.* 106, 1704–1709. doi:10.1073/pnas.0812721106.

Sonntag, S. (2018). Quantifying effects and side-effects of climate engineering on the Earth system. *Earth's Futur.* 6. doi:10.1002/eft2.285.

Sospedra-Alfonso, R., and Boer, G. J. (2019). Assessing the impact of initialization on decadal prediction skill. *Geophisical Res. Lett.* Submitted, 1–13.

Sospedra-Alfonso, R., and Boer, G. J. (9999). Assessing the impact of initialization on decadal prediction skill. *Geophys. Res. Lett.* (submitted.

Spring, A., Ilyina, T., and Marotzke, J. (9999). Inherent uncertainty disguises attribution of reduced atmospheric CO2 growth to mitigation for up to a decade. *Environ. Res. Lett.* (submitted.

Steffen, W., Rockström, J., Richardson, K., Lenton, T. M., Folke, C., Liverman, D., et al. (2018). Trajectories of the Earth System in the Anthropocene. *Proc. Natl. Acad. Sci.* 115, 8252–8259. doi:10.1073/pnas.1810141115.

Steinman, B. A., Mann, M. E., and Miller, S. K. (2015). Atlantic and Pacific multidecadal oscillations and Northern Hemisphere temperatures. *Science (80-. ).* 347, 988–991. doi:10.1126/science.1257856.

Steptoe, H., Wilcox, L. J., and Highwood, E. J. (2016). Is there a robust effect of anthropogenic aerosols on the Southern Annular Mode? *J. Geophys. Res. Atmos.* 121, 10,029-10,042. doi:10.1002/2015JD024218.

Stevenson, S., Otto-Bliesner, B., Fasullo, J., and Brady, E. (2016). "El Niño Like" hydroclimate responses to last millennium volcanic eruptions. *J. Clim.* 29, 2907–2921. doi:10.1175/JCLI-D-15-0239.1.

Stevenson, S., Wittenberg, A. T., Fasullo, J., Coats, S., and Otto-Bliesner, B. (2019). Understanding diverse model projections of future extreme El Nino. *Submitt. to J. Clim.*

Stjern, C. W., Muri, H., Ahlm, L., Boucher, O., Cole, J. N. S., Ji, D., et al. (2018a). Response to marine cloud brightening in a multi-model ensemble. *Atmos. Chem. Phys.* 18, 621–634. doi:10.5194/acp-18-621-2018.

Stjern, C. W., Muri, H., Ahlm, L., Boucher, O., Cole, J. N. S., Ji, D., et al. (2018b). Response to marine cloud brightening in a multi-model ensemble. *Atmos. Chem. Phys.* 18, 621–634. doi:10.5194/acp-18-621-2018.

Stjern, C. W., Samset, B. H., Myhre, G., Forster, P. M., Hodnebrog, Ø., Andrews, T., et al. (2017). Rapid Adjustments Cause Weak Surface Temperature Response to Increased Black Carbon Concentrations. *J. Geophys. Res. Atmos.* 122, 11,462-11,481. doi:10.1002/2017JD027326.

Stocker, T. F., Qin, D., Plattner, G. K., Tignor, M., Allen, S. K., Boschung, J., et al. (2013). "Climate Change 2013: The Physical Science Basis. Contribution of Working Group I to the Fifth Assessment Report of the Intergovernmental Panel on Climate Change," in (Cambridge University Press).

Stohl, A., Aamaas, B., Amann, M., Baker, L. H., Bellouin, N., Berntsen, T. K., et al. (2015). Evaluating the climate and air quality impacts of short-lived pollutants. *Atmos. Chem. Phys.* 15, 10529–10566. doi:10.5194/acp-15-10529-2015.

Stolpe, M. B., Medhaug, I., Sedláček, J., and Knutti, R. (2018). Multidecadal Variability in Global Surface Temperatures Related to the Atlantic Meridional Overturning Circulation. *J. Clim.* 31, 2889–2906. doi:10.1175/jcli-d-17-0444.1.

Storelvmo, T., Boos, W. R., and Herger, N. (2014). Cirrus cloud seeding: a climate engineering mechanism with reduced side effects? *Philos. Trans. R. Soc. A Math. Phys. Eng. Sci.* 372, 20140116. doi:10.1098/rsta.2014.0116.

Storelvmo, T., Kristjansson, J. E., Muri, H., Pfeffer, M., Barahona, D., and Nenes, A. (2013). Cirrus cloud seeding has potential to cool climate. *Geophys. Res. Lett.* 40, 178–182. doi:10.1029/2012GL054201.

Stott, P., Good, P., Jones, G., Gillett, N., and Hawkins, E. (2013). The upper end of climate model temperature projections is inconsistent with past warming. *Environ. Res. Lett.* 8, 014024. doi:10.1088/1748-9326/8/1/014024.

Stouffer, R. J., and Manabe, S. (1999). Response of a Coupled Ocean–Atmosphere Model to Increasing Atmospheric Carbon Dioxide: Sensitivity to the Rate of Increase. *J. Clim.* 12, 2224–2237. doi:10.1175/1520-0442(1999)012<2224:ROACOA>2.0.CO;2.

Stroeve, J., Barrett, A., Serreze, M., and Schweiger, A. (2014). Using records from submarine, aircraft and satellites to evaluate climate model simulations of Arctic sea ice thickness. *Cryosph.* 8, 1839–1854. doi:10.5194/tc-8-1839-2014.

Stroeve, J., and Notz, D. (2015). Insights on past and future sea-ice evolution from combining observations and models. *Glob. Planet. Change* 135, 119–132. doi:10.1016/J.GLOPLACHA.2015.10.011.

Strømmen, K., Christensen, H. M., Berner, J., and Palmer, T. N. (2018). The impact of stochastic parametrisations on the representation of the Asian summer monsoon. *Clim. Dyn.* 50, 2269–2282. doi:10.1007/s00382-017-3749-z.

Strommen, K., Watson, P. A. G., and Palmer, T. N. (2019). The Impact of a Stochastic Parameterization Scheme on Climate Sensitivity in EC-Earth. *J. Geophys. Res. Atmos.* n/a. doi:10.1029/2019JD030732.

Stuecker, M. F., Bitz, C. M., Armour, K. C., Proistosescu, C., Kang, S. M., Xie, S.-P., et al. (2018). Polar amplification dominated by local forcing and feedbacks. *Nat. Clim. Chang.* 8, 1076–1081. doi:10.1038/s41558-018-0339-y.

Stuecker, M. F., Timmermann, A., Jin, F.-F., Chikamoto, Y., Zhang, W., Wittenberg, A. T., et al. (2017). Revisiting ENSO/Indian Ocean Dipole phase relationships. *Geophys. Res. Lett.* 44, 2481–2492. doi:10.1002/2016GL072308.

Suarez-Gutierrez, L., Li, C., Müller, W. A., and Marotzke, J. (2018). Internal variability in European summer temperatures at 1.5 °C and 2 °C of global warming. *Environ. Res. Lett.* 13, 064026. doi:10.1088/1748-9326/aaba58.

Suárez-Gutiérrez, L., Li, C., Thorne, P. W., and Marotzke, J. (2017). Internal variability in simulated and observed tropical tropospheric temperature trends. *Geophys. Res. Lett.* 44, 5709–5719. doi:10.1002/2017GL073798.

Sugiyama, M., Arino, Y., Kosugi, T., Kurosawa, A., and Watanabe, S. (2018). Next steps in geoengineering scenario research: limited deployment scenarios and beyond. *Clim. Policy* 18, 681–689. doi:10.1080/14693062.2017.1323721.

Sutton, R. T. (2018). ESD Ideas: a simple proposal to improve the contribution of IPCC WGI to the assessment and communication of climate change risks. *Earth Syst. Dyn.* 9, 1155–1158. doi:10.5194/esd-9-1155-2018.

Sutton, R. T., Dong, B., and Gregory, J. M. (2007). Land/sea warming ratio in response to climate change: IPCC AR4 model results and comparison with observations. *Geophys. Res. Lett.* 34, L02701. doi:10.1029/2006GL028164.

Svendsen, L., Hetzinger, S., Keenlyside, N., and Gao, Y. (2014). Marine-based multiproxy reconstruction of Atlantic multidecadal variability. *Geophys. Res. Lett.* 41, 1295–1300. doi:10.1002/2013GL059076.

Swart, N. C., Cole, J. N. S., Kharin, V. V., Lazare, M., Scinocca, J. F., Gillett, N. P., et al. (2019). The Canadian Earth System Model version 5 (CanESM5.0.3). *Geosci. Model Dev. Discuss.* doi:10.5194/gmd-2019-177.

Swart, N. C., Gille, S. T., Fyfe, J. C., and Gillett, N. P. (2018). Recent Southern Ocean warming and freshening driven by greenhouse gas emissions and ozone depletion. *Nat. Geosci.* 11, 836–841. doi:10.1038/s41561-018-0226-1.

Takahashi, H. G., Watanabe, S., Nakata, M., and Takemura, T. (2018). Response of the atmospheric hydrological cycle over the tropical Asian monsoon regions to anthropogenic aerosols and its seasonality. *Prog. Earth Planet. Sci.* 5. doi:10.1186/s40645-018-0197-2.

Tamarin-Brodsky, T., and Kaspi, Y. (2017). Enhanced poleward propagation of storms under climate change. *Nat. Geosci.* 10, 908–913. doi:10.1038/s41561-017-0001-8.

Tao, W., Huang, G., Hu, K., Qu, X., Wen, G., and Gong, H. (2015). Interdecadal modulation of ENSO teleconnections to the Indian Ocean Basin Mode and their relationship under global warming in CMIP5 models. *Int. J. Climatol.* 35, 391–407. doi:10.1002/joc.3987.

Taylor, K. E., Stouffer, R. J., and Meehl, G. A. (2012). An Overview of CMIP5 and the Experiment Design. *Bull. Am. Meteorol. Soc.* 93, 485–498. doi:10.1175/BAMS-D-11-00094.1.

Tebaldi, C., and Arblaster, J. M. (2014). Pattern scaling: Its strengths and limitations, and an update on the latest model simulations. *Clim. Change* 122, 459–471. doi:10.1007/s10584-013-1032-9.

Tebaldi, C., Arblaster, J. M., and Knutti, R. (2011). Mapping model agreement on future climate projections. *Geophys. Res. Lett.* 38, n/a-n/a. doi:10.1029/2011GL049863.

Tebaldi, C., and Friedlingstein, P. (2013). Delayed detection of climate mitigation benefits due to climate inertia and variability. *Proc. Natl. Acad. Sci.* 110, 17229–17234. doi:10.1073/pnas.1300005110.

Tebaldi, C., and Knutti, R. (2007). The use of the multi-model ensemble in probabilistic climate projections. *Philos. Trans. R. Soc. A Math. Phys. Eng. Sci.* doi:10.1098/rsta.2007.2076.

Tebaldi, C., and Knutti, R. (2018a). Evaluating the accuracy of climate change pattern emulation for low warming targets. *Environ. Res. Lett.* 13, 055006. doi:10.1088/1748-9326/aabef2.

Tebaldi, C., and Knutti, R. (2018b). Evaluating the accuracy of climate change pattern emulation for low warming targets. *Environ. Res. Lett.* 13, 055006. doi:10.1088/1748-9326/aabef2.
Tebaldi, C., O'Neill, B., and Lamarque, J.-F. (2015). Sensitivity of regional climate to global temperature and forcing. *Environ. Res. Lett.* 10, 74001. doi:10.1088/1748-9326/10/7/074001.
Tebaldi, C., and Wehner, M. F. (2018). Benefits of mitigation for future heat extremes under RCP4.5 compared to RCP8.5. *Clim. Change* 146, 349–361. doi:10.1007/s10584-016-1605-5.
Teng, H., Meehl, G. A., Branstator, G., Yeager, S., and Karspeck, A. (2017). Initialization Shock in CCSM4 Decadal Prediction Experiments. *Past Glob. Chang. Mag.* 25, 41–46. doi:10.22498/pages.25.1.41.
Thoma, M., Gerdes, R., Greatbatch, R. J., and Ding, H. (2015a). Partially coupled spin-up of the MPI-ESM: implementation and first results. *Geosci. Model Dev.* 8, 51–68. doi:10.5194/gmd-8-51-2015.
Thoma, M., Greatbatch, R. J., Kadow, C., and Gerdes, R. (2015b). Decadal hindcasts initialized using observed surface wind stress: Evaluation and prediction out to 2024. *Geophys. Res. Lett.* 42, 6454–6461. doi:10.1002/2015GL064833.
Thompson, D. W. J., Barnes, E. A., Deser, C., Foust, W. E., and Phillips, A. S. (2015). Quantifying the Role of Internal Climate Variability in Future Climate Trends. *J. Clim.* 28, 6443–6456. doi:10.1175/JCLI-D-14-00830.1.
Tilmes, S., Fasullo, J., Lamarque, J. F., Marsh, D. R., Mills, M., Alterskjær, K., et al. (2013). The hydrological impact of geoengineering in the Geoengineering Model Intercomparison Project (GeoMIP). *J. Geophys. Res. Atmos.* 118, 11036–11058. doi:10.1002/jgrd.50868.
Tilmes, S., Jahn, A., Kay, J. E., Holland, M., and Lamarque, J. (2014). Can regional climate engineering save the summer Arctic sea ice ? 880–885. doi:10.1002/2013GL058731.1.
Tilmes, S., Richter, J. H., Kravitz, B., MacMartin, D. G., Mills, M. J., Simpson, I. R., et al. (2018a). CESM1(WACCM) Stratospheric Aerosol Geoengineering Large Ensemble Project. *Bull. Am. Meteorol. Soc.* 99, 2361–2371. doi:10.1175/BAMS-D-17-0267.1.
Tilmes, S., Richter, J. H., Mills, M. J., Kravitz, B., MacMartin, D. G., Garcia, R. R., et al. (2018b). Effects of Different Stratospheric SO2Injection Altitudes on Stratospheric Chemistry and Dynamics. *J. Geophys. Res. Atmos.* 123, 4654–4673. doi:10.1002/2017JD028146.
Tilmes, S., Richter, J. H., Mills, M. J., Kravitz, B., MacMartin, D. G., Vitt, F., et al. (2017). Sensitivity of aerosol distribution and climate response to stratospheric $SO_2$ injection locations. *J. Geophys. Res. Atmos.* doi:10.1002/2017JD026888.
Tilmes, S., Sanderson, B. M., and O'Neill, B. C. (2016). Climate impacts of geoengineering in a delayed mitigation scenario. *Geophys. Res. Lett.* 43, 8222–8229. doi:10.1002/2016GL070122.
Timmermann, A., An, S.-I., Kug, J.-S., Jin, F.-F., Cai, W., Capotondi, A., et al. (2018). El Niño–Southern Oscillation complexity. *Nature* 559, 535–545. doi:10.1038/s41586-018-0252-6.
Timmreck, C., Pohlmann, H., Illing, S., and Kadow, C. (2016). The impact of stratospheric volcanic aerosol on decadal-scale climate predictions. *Geophys. Res. Lett.* 43, 834–842. doi:10.1002/2015GL067431.
Tjiputra, J. F., Grini, A., and Lee, H. (2016). Impact of idealized future stratospheric aerosol injection on the large-scale ocean and land carbon cycles. *J. Geophys. Res. Biogeosciences* 121, 2–27. doi:10.1002/2015JG003045.
Tokarska, K. B., Gillett, N. P., Weaver, A. J., Arora, V. K., and Eby, M. (2016). The climate response to five trillion tonnes of carbon. *Nat. Clim. Chang.* doi:10.1038/nclimate3036.
Tokarska, K. B., Stolple, M. B., Sippel, S., Fischer, E. M., Smith, C. J., Lehner, F., et al. (9999). Past warming trend constrains future warming in CMIP6 models. *Sci. Adv.* (submitted.
Tokarska, K. B., and Zickfeld, K. (2015). The effectiveness of net negative carbon dioxide emissions in reversing anthropogenic climate change. *Environ. Res. Lett.* 10, 094013. doi:10.1088/1748-9326/10/9/094013.
Trisos, C. H., Amatulli, G., Gurevitch, J., Robock, A., Xia, L., and Zambri, B. (2018). Potentially dangerous consequences for biodiversity of solar geoengineering implementation and termination. *Nat. Ecol. Evol.* 2, 475–482. doi:10.1038/s41559-017-0431-0.
Tsutsui, J., Yoshida, Y., Kim, D.-H., Kitabata, H., Nishizawa, K., Nakashiki, N., et al. (2007). Long-term climate response to stabilized and overshoot anthropogenic forcings beyond the twenty-first century. *Clim. Dyn.* 28, 199–214.
Tung, K.-K., Chen, X., Zhou, J., and Li, K.-F. (2019). Interdecadal variability in pan-Pacific and global SST, revisited. *Clim. Dyn.* 52, 2145–2157. doi:10.1007/s00382-018-4240-1.
Turner, A. G., and Annamalai, H. (2012). Climate change and the South Asian summer monsoon. *Nat. Clim. Chang.* 2, 587.
UNEP (2011). *Near-term climate protection and clean air benefits: actions for controlling shortlived climate forcers. A UNEP synthesis report*.
Valdes, P. (2011). Built for stability. *Nat. Geosci.* 4, 414–416. doi:10.1038/ngeo1200.
Vallis, G. K., Zurita-Gotor, P., Cairns, C., and Kidston, J. (2015). Response of the large-scale structure of the atmosphere to global warming. *Q. J. R. Meteorol. Soc.* 141, 1479–1501. doi:10.1002/qj.2456.
van Oldenborgh, G. J., Doblas-Reyes, F. J., Wouters, B., and Hazeleger, W. (2012). Decadal prediction skill in a multi-model ensemble. *Clim. Dyn.* 38, 1263–1280. doi:10.1007/s00382-012-1313-4.
van Vuuren, D. P., Edmonds, J., Kainuma, M., Riahi, K., Thomson, A., Hibbard, K., et al. (2011a). The representative

concentration pathways: an overview. *Clim. Change* 109, 5–31. doi:10.1007/s10584-011-0148-z.
van Vuuren, D. P., Edmonds, J., Kainuma, M., Riahi, K., Thomson, A., Hibbard, K., et al. (2011b). The representative concentration pathways: an overview. *Clim. Change* 109, 5–31. doi:10.1007/s10584-011-0148-z.
van Vuuren, D. P., van Soest, H., Riahi, K., Clarke, L., Krey, V., Kriegler, E., et al. (2016). Carbon budgets and energy transition pathways. *Environ. Res. Lett.* 11, 75002. doi:10.1088/1748-9326/11/7/075002.
Vautard, R., Gobiet, A., Sobolowski, S., Kjellström, E., Stegehuis, A., Watkiss, P., et al. (2014). The European climate under a 2 °C global warming. *Environ. Res. Lett.* 9, 034006. doi:10.1088/1748-9326/9/3/034006.
Vecchi, G. A., Delworth, T., Gudgel, R., Kapnick, S., Rosati, A., Wittenberg, A. T., et al. (2014). On the Seasonal Forecasting of Regional Tropical Cyclone Activity. *J. Clim.* 27, 7994–8016. doi:10.1175/JCLI-D-14-00158.1.
Vecchi, G. A., and Soden, B. J. (2007). Global warming and the weakening of the tropical circulation. *J. Clim.* 20, 4316–4340. doi:10.1175/JCLI4258.1.
Vial, J., Dufresne, J.-L., and Bony, S. (2013). On the interpretation of inter-model spread in CMIP5 climate sensitivity estimates. *Clim. Dyn.* 41, 3339–3362.
Vicente-Serrano, S. M. M., Nieto, R., Gimeno, L., Azorin-Molina, C., Drumond, A., El Kenawy, A., et al. (2018). Recent changes of relative humidity: regional connections with land and ocean processes. *Earth Syst. Dyn.* 9, 915–937. doi:10.5194/esd-9-915-2018.
Villamayor, J., Ambrizzi, T., and Mohino, E. (2018). Influence of decadal sea surface temperature variability on northern Brazil rainfall in CMIP5 simulations. *Clim. Dyn.* 51, 563–579. doi:10.1007/s00382-017-3941-1.
Visioni, D., Pitari, G., and Aquila, V. (2017). Sulfate geoengineering: a review of the factors controlling the needed injection of sulfur dioxide. *Atmos. Chem. Phys.* 17, 3879–3889. doi:10.5194/acp-17-3879-2017.
Vogel, M. M., Orth, R., Cheruy, F., Hagemann, S., Lorenz, R., van den Hurk, B. J. J. M., et al. (2017). Regional amplification of projected changes in extreme temperatures strongly controlled by soil moisture-temperature feedbacks. *Geophys. Res. Lett.* 44, 1511–1519. doi:10.1002/2016GL071235.
Voigt, A., Albern, N., and Papavasileiou, G. (2019). The atmospheric pathway of the cloud-radiative impact on the circulation response to global warming: Important and uncertain. *J. Clim.* 32, 3051–3067. doi:10.1175/JCLI-D-18-0810.1.
Voigt, A., Pincus, R., Stevens, B., Bony, S., Boucher, O., Bellouin, N., et al. (2017). Fast and slow shifts of the zonal-mean intertropical convergence zone in response to an idealized anthropogenic aerosol. *J. Adv. Model. Earth Syst.* 9, 870–892. doi:10.1002/2016MS000902.
Voigt, A., and Shaw, T. A. (2015). Circulation response to warming shaped by radiative changes of clouds and water vapour. *Nat. Geosci.* 8, 102–106.
Voigt, A., and Shaw, T. A. (2016a). Impact of regional atmospheric cloud radiative changes on shifts of the extratropical jet stream in response to global warming. *J. Clim.* 29, 8399–8421. doi:10.1175/JCLI-D-16-0140.1.
Voigt, A., and Shaw, T. A. (2016b). Impact of Regional Atmospheric Cloud Radiative Changes on Shifts of the Extratropical Jet Stream in Response to Global Warming. *J. Clim.* 29, 8399–8421. doi:10.1175/JCLI-D-16-0140.1.
Waisman, H., Coninck, H. De, and Rogelj, J. (2019). Key technological enablers for ambitious climate goals: insights from the {IPCC} special report on global warming of 1.5 {\textdegree}C. *Environ. Res. Lett.* 14, 111001. doi:10.1088/1748-9326/ab4c0b.
Wang, B., Biasutti, M., Byrne, M., Castro, C., Chang, C.-P., Cook, K., et al. (2019). Monsoon climate change assessment. *Bull. Am. Meteorol. Soc.* submitted.
Wang, B., Biasutti, M., Byrne, M., Castro, C., Chang, C.-P., Cook, K., et al. (9999a). Monsoon climate change assessment. *Bull. Am. Meteorol. Soc.* (submitted.
Wang, B., and Ding, Q. (2008). Global monsoon: Dominant mode of annual variation in the tropics. *Dyn. Atmos. Ocean.* 44, 165–183. doi:10.1016/j.dynatmoce.2007.05.002.
Wang, B., Jin, C., and Liu, J. (9999b). Future change of global monsoon projected by CMIP6 models. *J. Clim.* (submitted.
Wang, B., Li, J., Cane, M. A., Liu, J., Webster, P. J., Xiang, B., et al. (2018a). Toward Predicting Changes in the Land Monsoon Rainfall a Decade in Advance. *J. Clim.* 31, 2699–2714. doi:10.1175/JCLI-D-17-0521.1.
Wang, B., Liu, J., Kim, H.-J., Webster, P. J., Yim, S.-Y., and Xiang, B. (2013). Northern Hemisphere summer monsoon intensified by mega-El Niño/southern oscillation and Atlantic multidecadal oscillation. *Proc. Natl. Acad. Sci.* 110, 5347 LP-5352. Available at: http://www.pnas.org/content/110/14/5347.abstract.
Wang, G., Cai, W., and Purich, A. (2014). Trends in Southern Hemisphere wind-driven circulation in CMIP5 models over the 21st century: Ozone recovery versus greenhouse forcing. *J. Geophys. Res. Ocean.* 119, 2974–2986. doi:10.1002/2013JC009589.
Wang, J., Kim, H.-M., and Chang, E. K. M. (2017a). Changes in Northern Hemisphere Winter Storm Tracks under the Background of Arctic Amplification. *J. Clim.* 30, 3705–3724. doi:10.1175/JCLI-D-16-0650.1.
Wang, J., Yang, B., Ljungqvist, F. C., Luterbacher, J., Osborn, T. J., Briffa, K. R., et al. (2017b). Internal and external forcing of multidecadal Atlantic climate variability over the past 1,200 years. *Nat. Geosci.* doi:10.1038/ngeo2962.
Wang, P. X., Wang, B., Cheng, H., Fasullo, J., Guo, Z., Kiefer, T., et al. (2017c). The global monsoon across time scales: Mechanisms and outstanding issues. *Earth-Science Rev.* 174, 84–121.

doi:10.1016/j.earscirev.2017.07.006.
Wang, Y., Jiang, J. H., Su, H., Choi, Y.-S., Huang, L., Guo, J., et al. (2018b). Elucidating the Role of Anthropogenic Aerosols in Arctic Sea Ice Variations. *J. Clim.* 31, 99–114. doi:10.1175/JCLI-D-17-0287.1.
Wang, Y., Zhang, G. J., and Craig, G. C. (2016). Stochastic convective parameterization improving the simulation of tropical precipitation variability in the NCAR CAM5. *Geophys. Res. Lett.* 43, 6612–6619. doi:10.1002/2016GL069818.
Watanabe, M., Kamae, Y., Shiogama, H., DeAngelis, A. M., and Suzuki, K. (2018). Low clouds link equilibrium climate sensitivity to hydrological sensitivity. *Nat. Clim. Chang.* 8, 901–906. doi:10.1038/s41558-018-0272-0.
Watanabe, M., Kug, J.-S., Jin, F.-F., Collins, M., Ohba, M., and Wittenberg, A. T. (2012). Uncertainty in the ENSO amplitude change from the past to the future. *Geophys. Res. Lett.* 39, L20703. doi:10.1029/2012GL053305.
Watanabe, M., Shiogama, H., Tatebe, H., Hayashi, M., Ishii, M., and Kimoto, M. (2014). Contribution of natural decadal variability to global warming acceleration and hiatus. *Nat. Clim. Chang.* 4, 893–897. Available at: https://doi.org/10.1038/nclimate2355.
Watson, P. A. G., Berner, J., Corti, S., Davini, P., von Hardenberg, J., Sanchez, C., et al. (2017). The impact of stochastic physics on tropical rainfall variability in global climate models on daily to weekly time scales. *J. Geophys. Res. Atmos.* 122, 5738–5762. doi:10.1002/2016JD026386.
Weigel, A. P., Knutti, R., Liniger, M. A., and Appenzeller, C. (2010). Risks of Model Weighting in Multimodel Climate Projections. *J. Clim.* 23, 4175–4191. doi:10.1175/2010JCLI3594.1.
Weisheimer, A., Corti, S., Palmer, T., and Vitart, F. (2014). Addressing model error through atmospheric stochastic physical parametrizations: Impact on the coupled ECMWF seasonal forecasting system. *Philos. Trans. R. Soc. A Math. Phys. Eng. Sci.* doi:10.1098/rsta.2013.0290.
Wen, Q., Yao, J., Döös, K., and Yang, H. (2018). Decoding Hosing and Heating Effects on Global Temperature and Meridional Circulations in a Warming Climate. *J. Clim.* 31, 9605–9623. doi:10.1175/JCLI-D-18-0297.1.
Westra, S., Alexander, L. V, and Zwiers, F. W. (2013). Global Increasing Trends in Annual Maximum Daily Precipitation. *J. Clim.* 26, 3904–3918. doi:10.1175/JCLI-D-12-00502.1.
Wigley, T. M. L. (2018). The Paris warming targets: emissions requirements and sea level consequences. *Clim. Change* 147, 31–45.
Williams, R. G., Roussenov, V., Frölicher, T. L., and Goodwin, P. (2017). Drivers of Continued Surface Warming After Cessation of Carbon Emissions. *Geophys. Res. Lett.* 44, 10,610-633,642. doi:10.1002/2017GL075080.
Willison, J., Robinson, W. A., and Lackmann, G. M. (2015). North Atlantic Storm-Track Sensitivity to Warming Increases with Model Resolution. *J. Clim.* 28, 4513–4524. doi:10.1175/JCLI-D-14-00715.1.
Wills, R. C. J., Armour, K. C., Battisti, D. S., and Hartmann, D. L. (2019). Ocean–Atmosphere Dynamical Coupling Fundamental to the Atlantic Multidecadal Oscillation. *J. Clim.* 32, 251–272. doi:10.1175/JCLI-D-18-0269.1.
Winton, M. (2006). Amplified Arctic climate change: What does surface albedo feedback have to do with it? *Geophys. Res. Lett.* 33, L03701. doi:10.1029/2005GL025244.
Wittenberg, A. T. (2009). Are historical records sufficient to constrain ENSO simulations? *Geophys. Res. Lett.* 36, L12702. doi:10.1029/2009GL038710.
Wobus, C., Flanner, M., Sarofim, M. C., Moura, M. C. P., and Smith, S. J. (2016). Future Arctic temperature change resulting from a range of aerosol emissions scenarios. *Earth's Futur.* 4, 270–281. doi:10.1002/2016EF000361.
Woods, C., and Caballero, R. (2016). The Role of Moist Intrusions in Winter Arctic Warming and Sea Ice Decline. *J. Clim.* 29, 4473–4485. doi:10.1175/JCLI-D-15-0773.1.
Woollings, T., Barriopedro, D., Methven, J., Son, S.-W., Martius, O., Harvey, B., et al. (2018). Blocking and its Response to Climate Change. *Curr. Clim. Chang. Reports* 4, 287–300. doi:10.1007/s40641-018-0108-z.
World Meteorological Organisation (2010). Scientific Assessment of Ozone Depletion: 2010. 2010.
World Meteorological Organization (2018). *Scienti c Assessment of Ozone Depletion : 2018 Executive Summary*.
Wouters, B., Hazeleger, W., Drijfhout, S., Oldenborgh, G. J., and Guemas, V. (2013). Multiyear predictability of the North Atlantic subpolar gyre. *Geophys. Res. Lett.* 40, 3080–3084. doi:10.1002/grl.50585.
Wu, P., Jackson, L., Pardaens, A., and Schaller, N. (2011). Extended warming of the northern high latitudes due to an overshoot of the Atlantic meridional overturning circulation. *Geophys. Res. Lett.* 38.
Wu, P., Ridley, J., Pardaens, A., Levine, R., and Lowe, J. (2015). The reversibility of CO 2 induced climate change. *Clim. Dyn.* 45, 745–754.
Wu, P., Wood, R., Ridley, J., and Lowe, J. (2010). Temporary acceleration of the hydrological cycle in response to a CO 2 rampdown. *Geophys. Res. Lett.* doi:10.1029/2010GL043730.
Xie, S.-P., Deser, C., Vecchi, G. A., Collins, M., Delworth, T. L., Hall, A., et al. (2015). Towards predictive understanding of regional climate change. *Nat. Clim. Chang.* 5, 921–930. doi:10.1038/nclimate2689.
Xie, S.-P., Hu, K., Hafner, J., Tokinaga, H., Du, Y., Huang, G., et al. (2009). Indian Ocean Capacitor Effect on Indo–Western Pacific Climate during the Summer following El Niño. *J. Clim.* 22, 730–747. doi:10.1175/2008JCLI2544.1.
Xie, S.-P., Lu, B., and Xiang, B. (2013). Similar spatial patterns of climate responses to aerosol and greenhouse gas changes. *Nat. Geosci.* 6, 828–832.
Xu, Y., and Hu, A. (2017). How Would the Twenty-First-Century Warming Influence Pacific Decadal Variability and

Its Connection to North American Rainfall: Assessment Based on a Revised Procedure for the IPO/PDO. *J. Clim.* 31, 1547–1563. doi:10.1175/JCLI-D-17-0319.1.
Xu, Y., and Ramanathan, V. (2017). Well below 2 °C: Mitigation strategies for avoiding dangerous to catastrophic climate changes. *Proc. Natl. Acad. Sci. U. S. A.* doi:10.1073/pnas.1618481114.
Yang, C., Christensen, H. M., Corti, S., von Hardenberg, J., and Davini, P. (2019). The impact of stochastic physics on the El Niño Southern Oscillation in the EC-Earth coupled model. *Clim. Dyn.* doi:10.1007/s00382-019-04660-0.
Yeager, S. G., Danabasoglu, G., Rosenbloom, N. A., Strand, W., Bates, S. C., Meehl, G. A., et al. (2018a). Predicting Near-Term Changes in the Earth System: A Large Ensemble of Initialized Decadal Prediction Simulations Using the Community Earth System Model. *Bull. Am. Meteorol. Soc.* 99, 1867–1886. doi:10.1175/BAMS-D-17-0098.1.
Yeager, S. G., Danabasoglu, G., Rosenbloom, N. A., Strand, W., Bates, S. C., Meehl, G. A., et al. (2018b). Predicting Near-Term Changes in the Earth System: A Large Ensemble of Initialized Decadal Prediction Simulations Using the Community Earth System Model. *Bull. Am. Meteorol. Soc.* 99, 1867–1886. doi:10.1175/BAMS-D-17-0098.1.
Yeager, S. G., Karspeck, A. R., and Danabasoglu, G. (2015). Predicted slowdown in the rate of Atlantic sea ice loss. *Geophys. Res. Lett.* 42, 10,704-10,713. doi:10.1002/2015GL065364.
Yeager, S. G., and Robson, J. I. (2017). Recent Progress in Understanding and Predicting Atlantic Decadal Climate Variability. *Curr. Clim. Chang. Reports* 3, 112–127. doi:10.1007/s40641-017-0064-z.
Yettella, V., and Kay, J. E. (2017). How will precipitation change in extratropical cyclones as the planet warms? Insights from a large initial condition climate model ensemble. *Clim. Dyn.* 49, 1765–1781. doi:10.1007/s00382-016-3410-2.
Young, P. J., Davis, S. M., Hassler, B., Solomon, S., and Rosenlof, K. H. (2014). Modeling the climate impact of Southern Hemisphere ozone depletion: The importance of the ozone data set. *Geophys. Res. Lett.* 41, 9033–9039. doi:10.1002/2014GL061738.
Zanna, L., Khatiwala, S., Gregory, J. M., Ison, J., and Heimbach, P. (2019). Global reconstruction of historical ocean heat storage and transport. *Proc. Natl. Acad. Sci.* 116, 1126–1131. doi:10.1073/pnas.1808838115.
Zappa, G. (2019). Regional climate impacts of future changes in the mid-latitude atmospheric circulation: a storylines view. *Curr. Clim. Chang. Reports*, 358–371. doi:10.1007/s40641-019-00146-7.
Zappa, G., Hoskins, B. J., and Shepherd, T. G. (2015). Improving Climate Change Detection through Optimal Seasonal Averaging: The Case of the North Atlantic Jet and European Precipitation. *J. Clim.* 28, 6381–6397. doi:10.1175/JCLI-D-14-00823.1.
Zappa, G., Pithan, F., and Shepherd, T. G. (2018a). Multimodel Evidence for an Atmospheric Circulation Response to Arctic Sea Ice Loss in the CMIP5 Future Projections. *Geophys. Res. Lett.* 45, 1011–1019. doi:10.1002/2017GL076096.
Zappa, G., Pithan, F., and Shepherd, T. G. (2018b). Multimodel Evidence for an Atmospheric Circulation Response to Arctic Sea Ice Loss in the CMIP5 Future Projections. *Geophys. Res. Lett.* 45, 1011–1019. doi:10.1002/2017GL076096.
Zappa, G., and Shepherd, T. G. (2017). Storylines of Atmospheric Circulation Change for European Regional Climate Impact Assessment. *J. Clim.* 30, 6561–6577. doi:10.1175/JCLI-D-16-0807.1.
Zelinka, M. D., Myers, T. A., McCoy, D. T., Po-Chedley, S., Caldwell, P. M., Ceppi, P., et al. (2020a). Causes of higher climate sensitivity in CMIP6 models. *Geophys. Res. Lett.* doi:10.1029/2019gl085782.
Zelinka, M. D., Myers, T. A., McCoy, D. T., Po‐Chedley, S., Caldwell, P. M., Ceppi, P., et al. (2020b). Causes of higher climate sensitivity in CMIP6 models. *Geophys. Res. Lett.*, 2019GL085782. doi:10.1029/2019GL085782.
Zhang, H., and Delworth, T. L. (2018). Robustness of anthropogenically forced decadal precipitation changes projected for the 21st century. *Nat. Commun.* 9, 1150. doi:10.1038/s41467-018-03611-3.
Zhang, L., and Delworth, T. L. (2016). Simulated Response of the Pacific Decadal Oscillation to Climate Change. *J. Clim.* 29, 5999–6018. doi:10.1175/JCLI-D-15-0690.1.
Zhang, R., Sutton, R., Danabasoglu, G., Delworth, T. L., Kim, W. M., Robson, J., et al. (2016). Comment on "The Atlantic Multidecadal Oscillation without a role for ocean circulation." *Science (80-. ).* 352, 1527–1527. doi:10.1126/science.aaf1660.
Zhang, W., Zhou, T., Zou, L., Zhang, L., and Chen, X. (2018). Reduced exposure to extreme precipitation from 0.5 °C less warming in global land monsoon regions. *Nat. Commun.* 9, 3153. doi:10.1038/s41467-018-05633-3.
Zhang, Y., Wallace, J. M., and Battisti, D. S. (1997). ENSO-like Interdecadal Variability: 1900–93. *J. Clim.* 10, 1004–1020. doi:10.1175/1520-0442(1997)010<1004:ELIV>2.0.CO;2.
Zhao, Y., Ducharne, A., Sultan, B., Braconnot, P., and Vautard, R. (2015). Estimating heat stress from climate-based indicators: present-day biases and future spreads in the CMIP5 global climate model ensemble. *Environ. Res. Lett.* 10, 084013. doi:10.1088/1748-9326/10/8/084013.
Zheng, F., Li, J., Clark, R. T., and Nnamchi, H. C. (2013a). Simulation and Projection of the Southern Hemisphere Annular Mode in CMIP5 Models. *J. Clim.* 26, 9860–9879. doi:10.1175/JCLI-D-13-00204.1.
Zheng, X.-T., Hui, C., and Yeh, S.-W. (2018). Response of ENSO amplitude to global warming in CESM large ensemble: uncertainty due to internal variability. *Clim. Dyn.* 50, 4019–4035. doi:10.1007/s00382-017-3859-7.
Zheng, X.-T., Xie, S.-P., Du, Y., Liu, L., Huang, G., and Liu, Q. (2013b). Indian Ocean Dipole Response to Global

Warming in the CMIP5 Multimodel Ensemble. *J. Clim.* 26, 6067–6080. doi:10.1175/JCLI-D-12-00638.1.
Zheng, X.-T., Xie, S.-P., Lv, L.-H., and Zhou, Z.-Q. (2016). Intermodel Uncertainty in ENSO Amplitude Change Tied to Pacific Ocean Warming Pattern. *J. Clim.* 29, 7265–7279. doi:10.1175/JCLI-D-16-0039.1.
Zhou, J., Tung, K.-K., and Li, K.-F. (2016). Multi-decadal variability in the Greenland ice core records obtained using intrinsic timescale decomposition. *Clim. Dyn.* 47, 739–752. doi:10.1007/s00382-015-2866-9.
Zickfeld, K., Eby, M., Weaver, A. J., Alexander, K., Crespin, E., Edwards, N. R., et al. (2013). Long-Term Climate Change Commitment and Reversibility: An EMIC Intercomparison. *J. Clim.* 26, 5782–5809. doi:10.1175/JCLI-D-12-00584.1.
Zickfeld, K., and Herrington, T. (2015). The time lag between a carbon dioxide emission and maximum warming increases with the size of the emission. *Environ. Res. Lett.* 10, 31001. doi:10.1088/1748-9326/10/3/031001.
Zickfeld, K., MacDougall, A. H., and Matthews, H. D. (2016). On the proportionality between global temperature change and cumulative CO2 emissions during periods of net negative CO2 emissions. *Environ. Res. Lett.* 11, 055006. doi:10.1088/1748-9326/11/5/055006.
Zickfeld, K., Solomon, S., and Gilford, D. M. (2017). Centuries of thermal sea-level rise due to anthropogenic emissions of short-lived greenhouse gases. *Proc. Natl. Acad. Sci.* 114, 657–662. doi:10.1073/pnas.1612066114.
Zuo, M., Man, W., Zhou, T., and Guo, Z. (2018). Different Impacts of Northern, Tropical, and Southern Volcanic Eruptions on the Tropical Pacific SST in the Last Millennium. *J. Clim.* 31, 6729–6744. doi:10.1175/JCLI-D-17-0571.1.

**Figures**

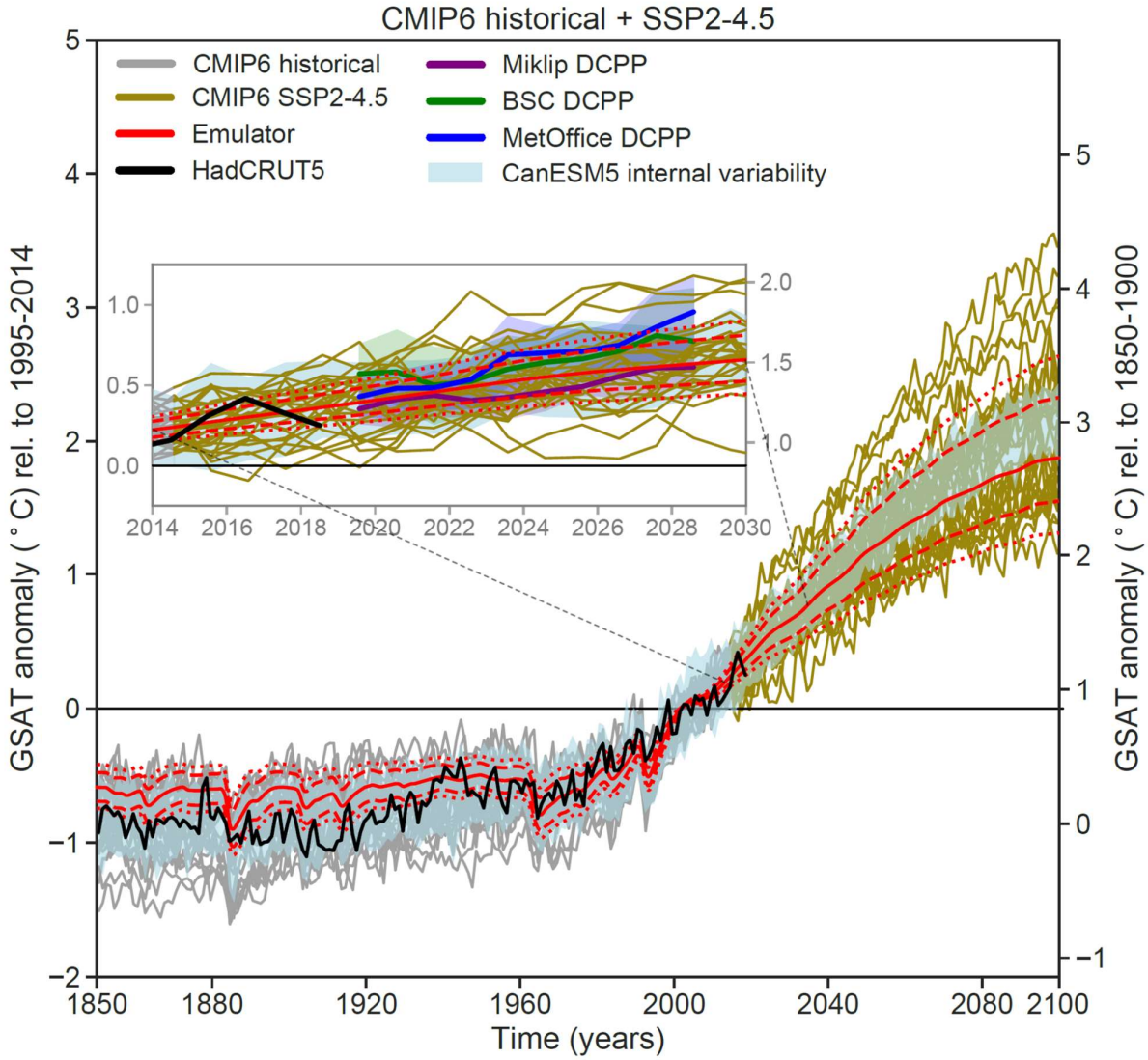


**Box 4.1, Figure 1:** CMIP6 annual-mean GSAT simulations and various contributions to uncertainty in the projections ensemble. The figure shows anomalies relative to the period 1995–2014 (left y-axis), converted to anomalies relative to 1850–1900 (right y-axis); the difference between the y-axes is 0.86°C (Box 1.2). Shown are historical simulations with 29 CMIP6 models (grey) and projections simulations following scenario SSP2-4.5 (dark yellow). The black curve shows the observations (HadCRUT5, (Morice et al., submitted)). Light blue shading shows the 50-member ensemble CanESM5, such that the deviations from the CanESM5 ensemble mean have been added to the CMIP6 multi-model mean. The red curves are from the emulator and show the best estimate (solid), *likely* range (dashed), and *very likely* range (dotted) for GSAT. The inset shows a cut-out from the main plot and additionally for the period 2019–2028 in purple, green, and blue the initialised prediction ensembles from three models contributing to DCPP (Boer et al., 2016); solid curves show the ensemble means and shading the range of each prediction system.

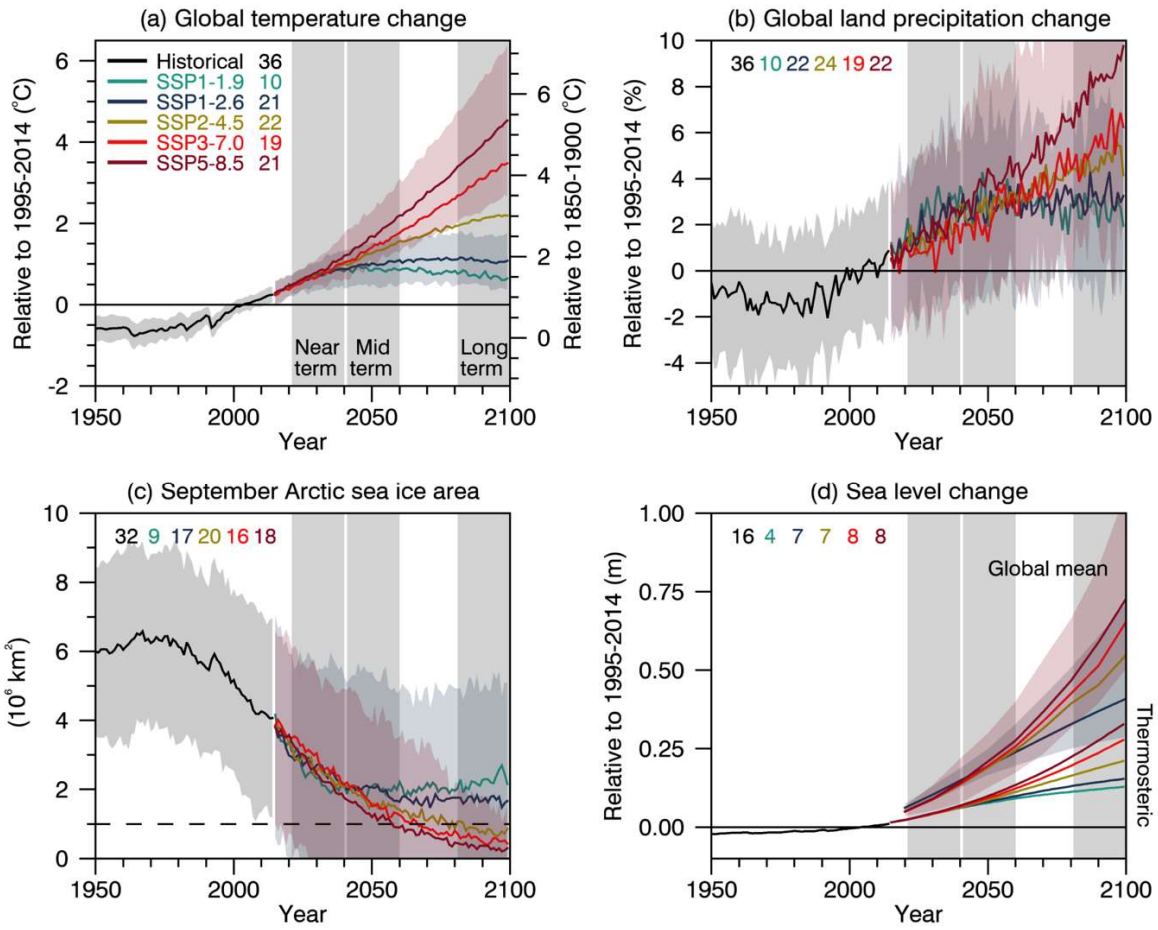


**Figure 4.1:** Selected indicators of global climate change from CMIP6 historical and scenario simulations. (a) Global surface air temperature changes relative to the 1995–2014 average (left axis) and relative to the 1850–1900 average (right axis). (b) Global land precipitation changes relative to the 1995–2014 average. (c) September Arctic sea-ice area. (d) Sea level change relative to the 1995–2014 average. Curves with shading are global mean sea level (GMSL) and curves without shading are the contributions due to thermal expansion. (a), (b) and (d) are annual averages, (c) are September averages. In (a)-(c), the curves show averages over the r1 simulations contributed to the CMIP6 exercise, the shadings around the SSP1-2.6 and SSP5-8.5 curves show 5 to 95% ranges (i.e. mean ± standard deviation × 1.645), and the numbers near the top show the number of model simulations.

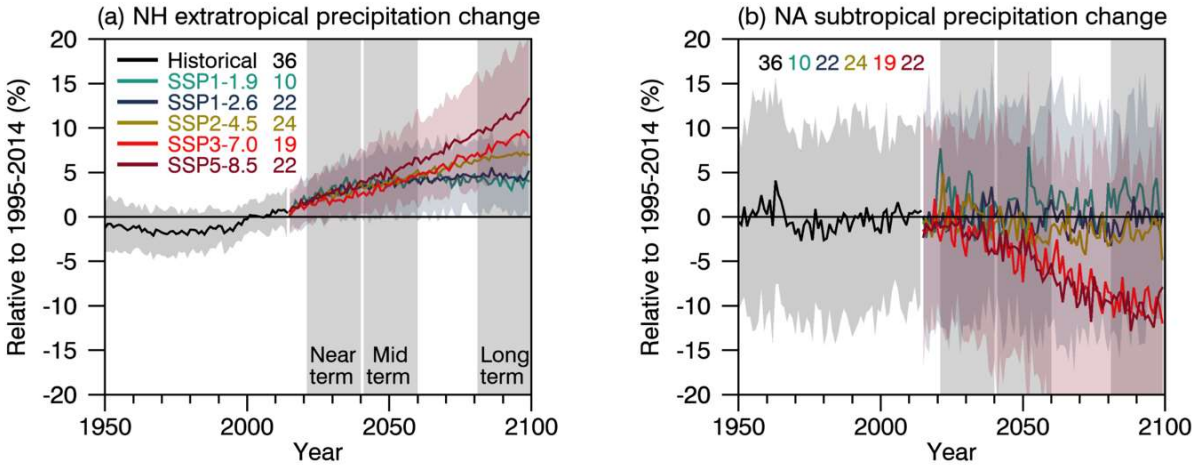


**Figure 4.2:** CMIP6 annual mean precipitation changes (%) from historical and scenario simulations. (a) Northern Hemisphere (NH) extratropics (30°N–90°N). (b) North Atlantic (NA) subtropics (5°N–30°N, 80°W–0°). Changes are relative to 1995–2014 averages. The curves show averages over the r1 simulations contributed to the CMIP6 exercise. The shadings around the SSP1-2.6 and SSP5-8.5 curves are the 5 to 95% ranges across the ensembles (i.e. mean ± standard deviation x 1.645). The numbers inside each panel are the number of model simulations.

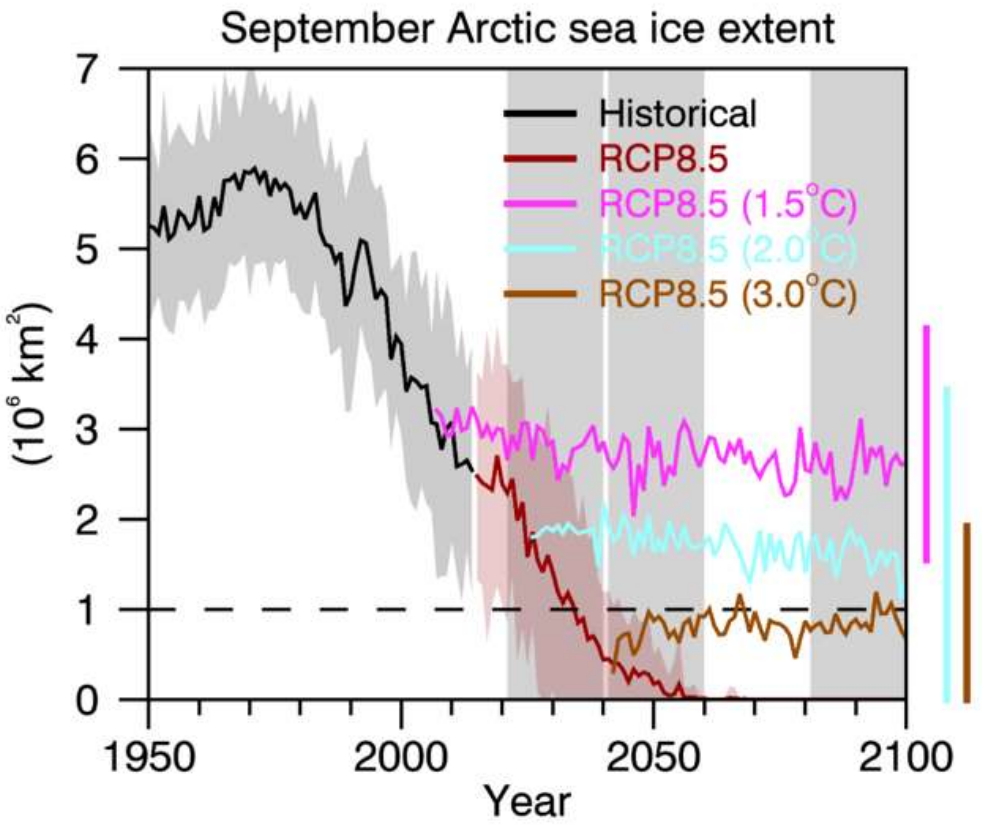


**Figure 4.3:** Arctic sea ice extent in September in a large initial-condition ensemble of observationally-constrained simulations of an Earth System Model (CanESM2). The black curve is the average over twenty simulations following historical forcings to 2015 and RCP8.5 extensions to 2100. The coloured curves are averages over twenty simulations each after GSAT has been stabilized at the indicated degree of global mean warming relative to pre-industrial. The bars to the right are the minimum to maximum ranges over 2081-2100 (Sigmond et al., 2018).

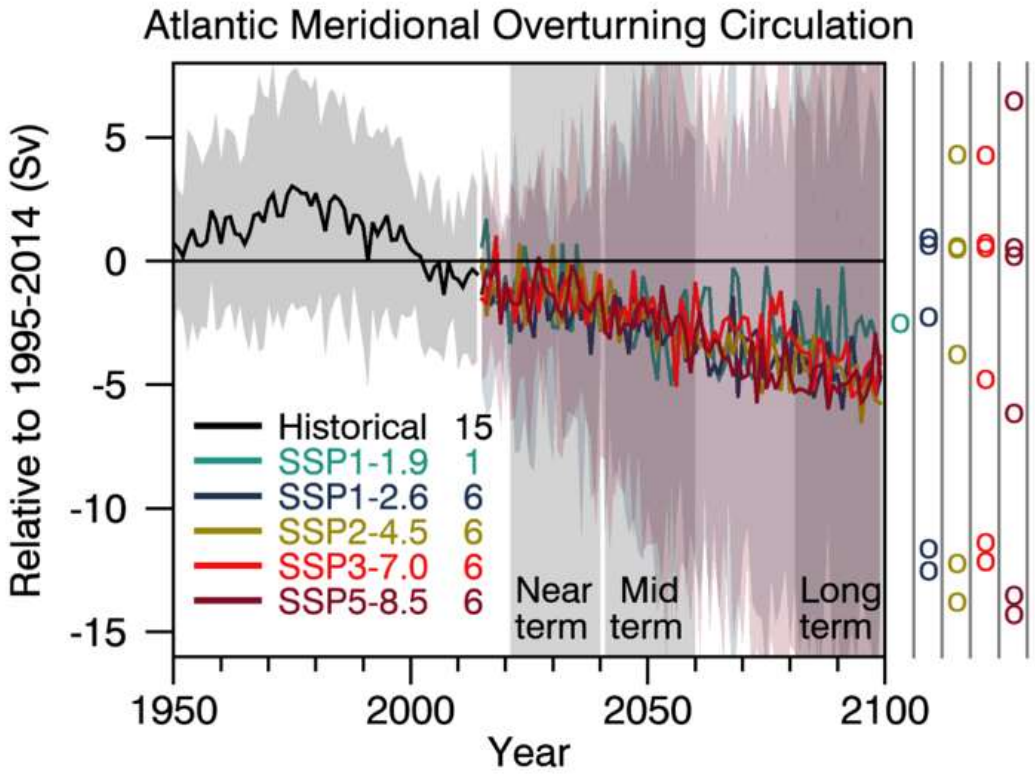


**Figure 4.4:** CMIP6 annual mean AMOC change in historical and scenario simulations. Changes are relative to averages from 1995–2014. The curves show averages over the r1 simulations contributed to the CMIP6 exercise. The shadings around the SSP1-2.6 and SSP5-8.5 curves are the 5–95% ranges across those ensembles (i.e. mean ± standard deviation x 1.645). The circles to the right of the panel show the anomalies averaged from 2081-2100 (long-term) across all of the individual model simulations. The numbers inside the panel are the number of model simulations. Here, the strength of the AMOC is computed as the maximum value of annual-mean ocean meridional overturning mass streamfunction (msftmz) in the Atlantic north of 30°N and below 500 m.

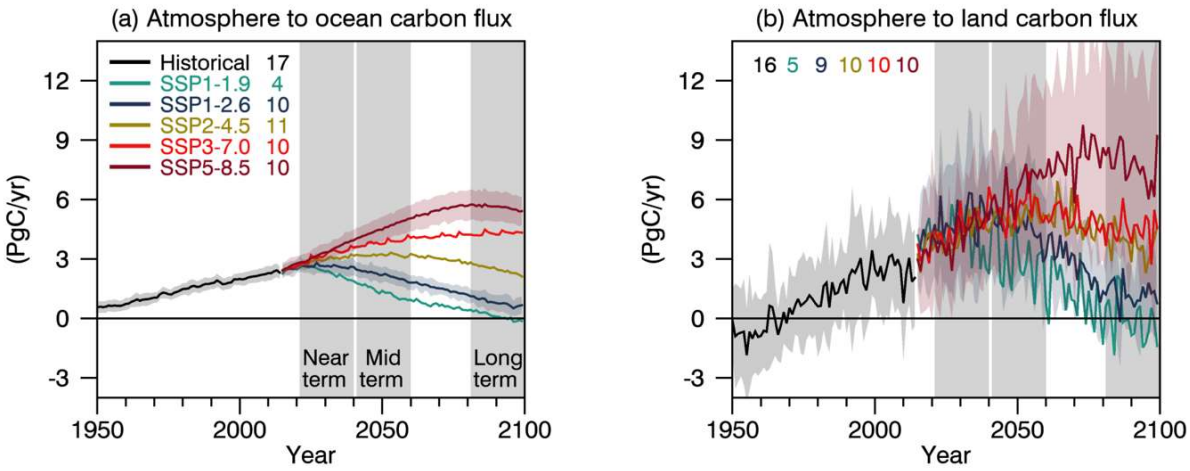


**Figure 4.5:** CMIP6 carbon uptake in historical and scenario simulations. (a) Net ocean uptake rate (PgC $yr^{-1}$). (b) Net land uptake rate (PgC $yr^{-1}$). The curves show averages over the r1 simulations contributed to the CMIP6 exercise. The shadings around the SSP1-2.6 and SSP5-8.5 curves are the 5–95% ranges across those ensembles (i.e. mean ± standard deviation x 1.645). The numbers inside each panel are the number of model simulations. The land uptake is taken as Net Biome Productivity (NBP) and so includes any modelled net land-use change emissions.

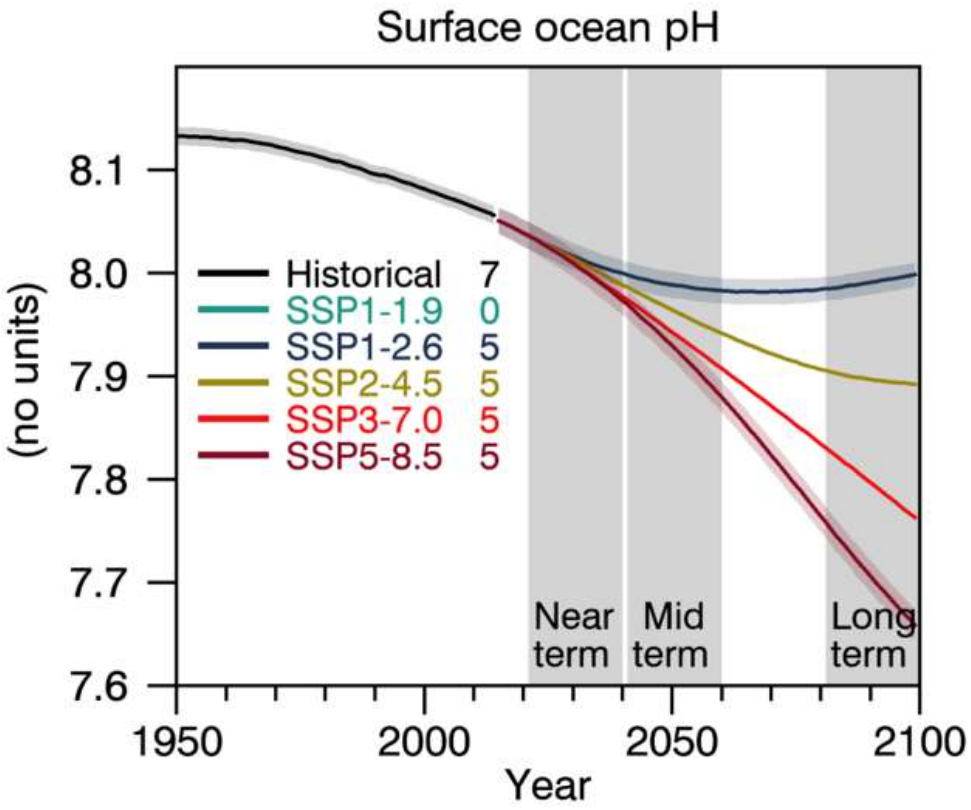


**Figure 4.6:** Surface ocean pH. The shadings around the SSP1-2.6 and SSP5-8.5 curves are the 5–95% ranges across those ensembles (i.e. mean ± standard deviation x 1.645). The numbers inside each panel are the number of model simulations. Note that surface ocean pH under SSP1-1.9 is currently unavailable from any CMIP6 model.

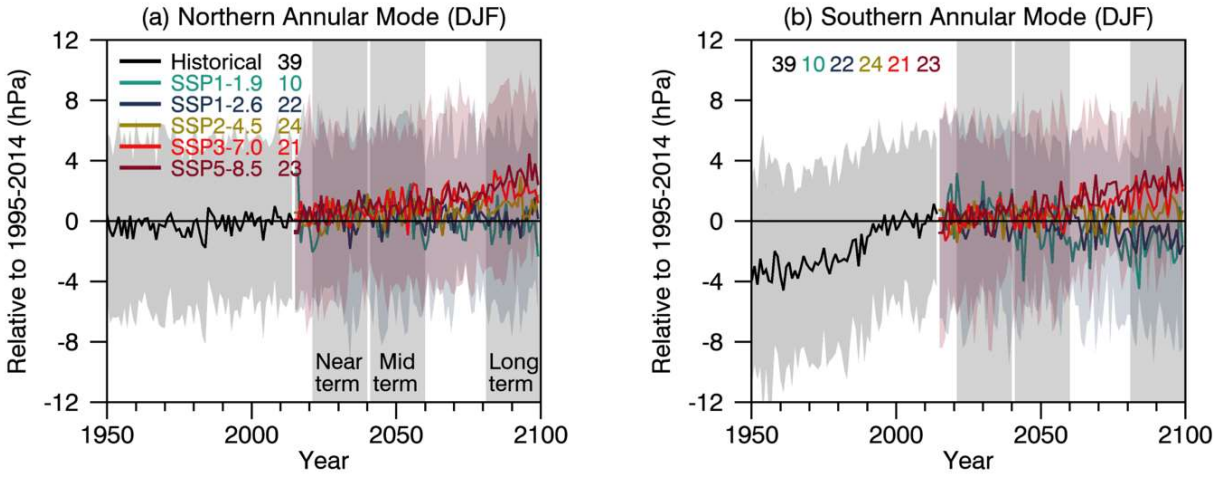


**Figure 4.7:** CMIP6 simulations of boreal wintertime (DJF) Annular Mode indices: (a) NAM and (b) SAM. The NAM is defined as the difference in zonal mean SLP at 35°N and 65°N (Li and Wang, 2003) and the SAM as the difference in zonal mean SLP at 40°S and 65°S (Gong and Wang, 1999). All anomalies are relative to averages from 1995-2014. The curves show multi-model ensemble averages over the r1 simulations contributed to the CMIP6 exercise. The shadings around the SSP1-2.6 and SSP5-8.5 curves denote the 5 to 95% ranges of the ensembles (i.e. mean ± standard deviation x 1.64). The numbers inside each panel are the number of model simulations.

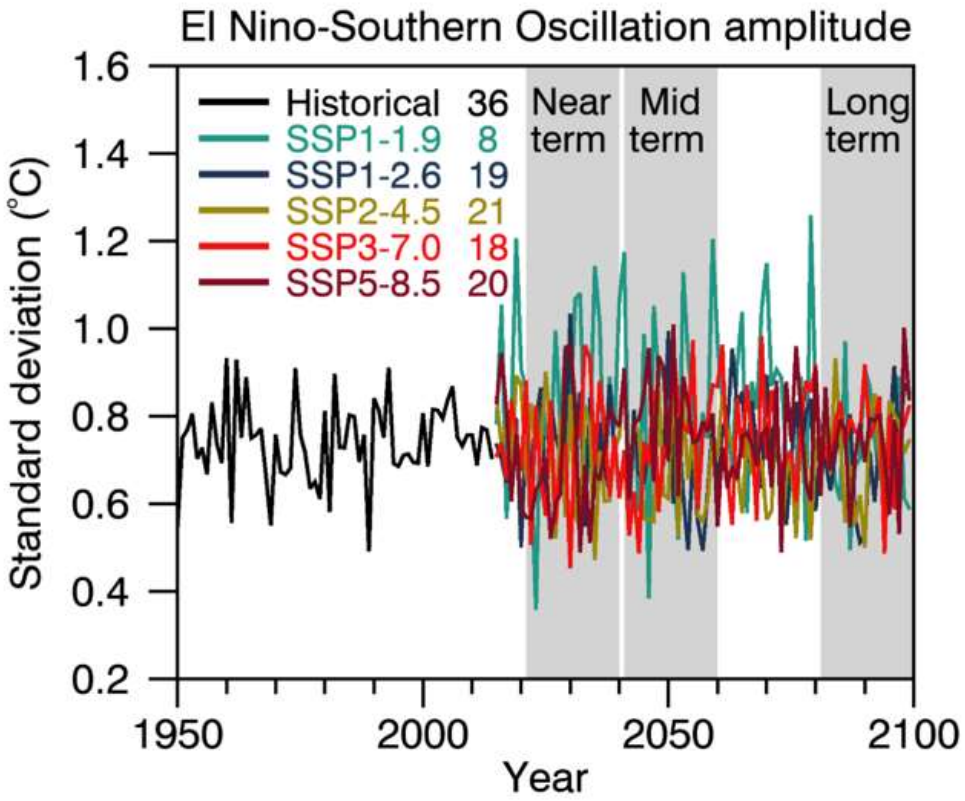


**Figure 4.8:** CMIP6 simulations of the annual amplitude of the ENSO index. Here, the amplitude is defined as the standard deviation across the individual model Niño3.4 index values in a given year and each historical and SSP simulation. To account for potential background changes in the Niño3.4 index, the model average Niño 3.4 index is fitted to a third-order polynomial and then removed from each model by linear regression. The curves show averages over the r1 simulations contributed to the CMIP6 exercise. The numbers inside the panel are the number of model simulations.

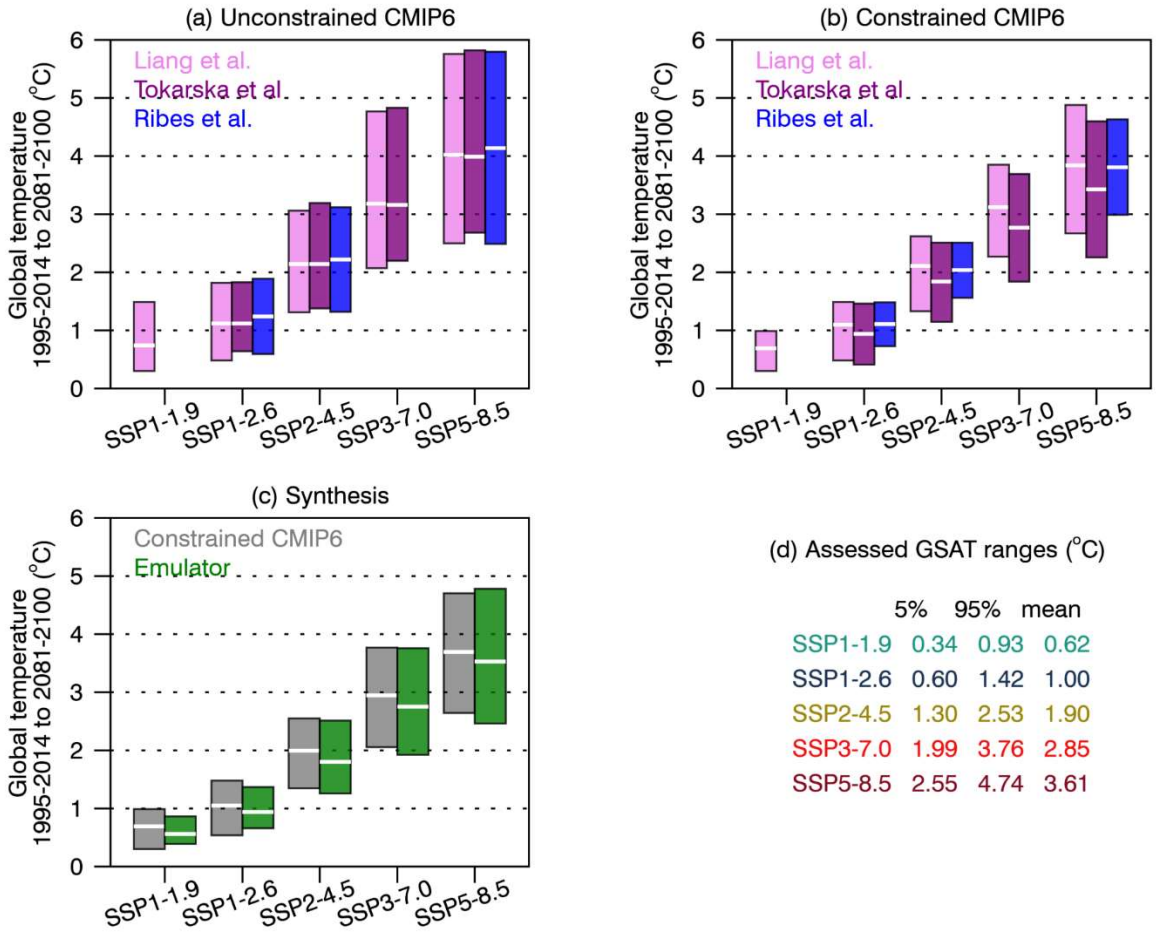


**Figure 4.9:** Multiple lines of evidence for GSAT changes for the long-term period, 2081–2100, relative to the average over 1995–2014. The unconstrained CMIP6 5–95% ranges (coloured bars) in (a) differ slightly because different authors used different subsamples of the CMIP6 archive. The constrained CMIP6 5–95% ranges (coloured bars) in (b) are smaller than the unconstrained ranges in (a) and differ because of different samples from the CMIP6 archive and because different observations and methods are used. In (c), the average of the ranges in (b) is formed (grey bars). Green bars in (c) show the emulator ranges, defined such that the best estimate, lower bound of the *very likely range*, and upper bound of the *very likely* range of climate feedback parameter and ocean heat uptake coefficient take the values that map onto the corresponding values of ECS and TCR of Section 7.5 (see Box 4.1). The table in (d) is constructed by taking the average of the constrained CMIP6 estimates (grey bars in c) and the emulator estimates (green bars in c).

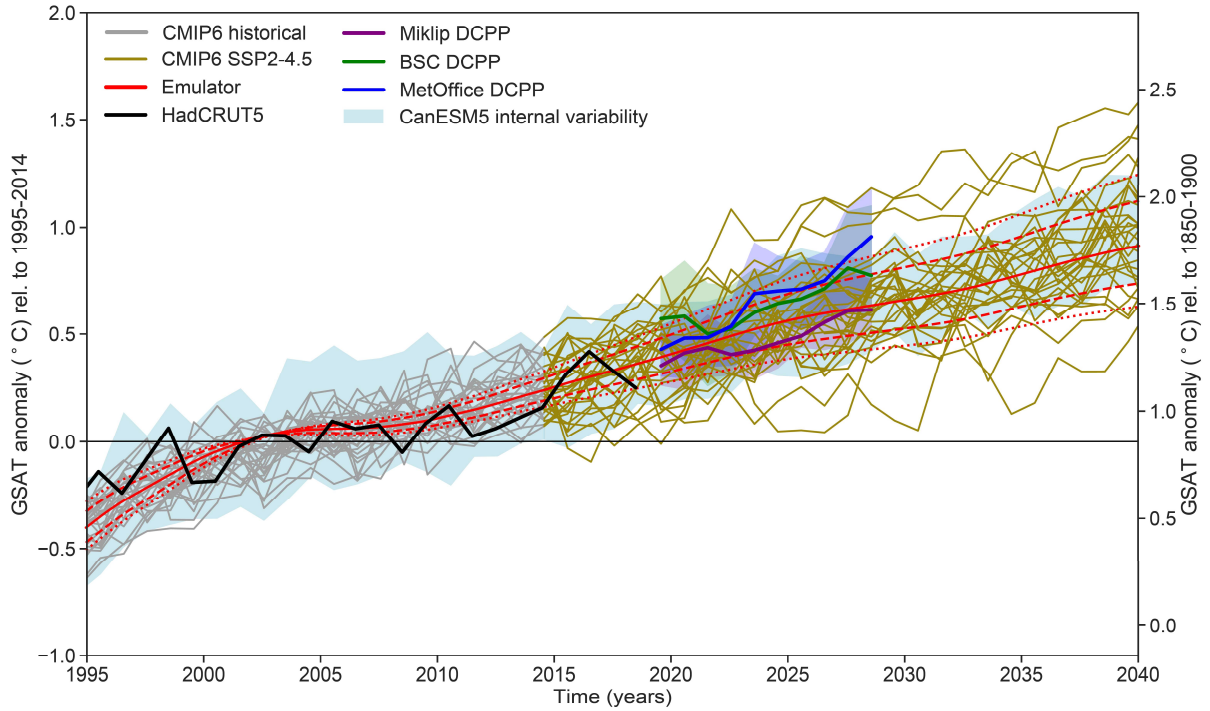


**Figure 4.10:** CMIP6 annual-mean GSAT simulations for the recent past and the near term. The figure shows anomalies relative to the period 1995–2014 (left y-axis), converted to anomalies relative to 1850–1900 (right y-axis); the difference between the y-axes is 0.86°C (Box 1.2). Shown are historical simulations with 29 CMIP6 models (grey) and projections simulations with the same models, following scenario SSP2-4.5 (dark yellow). For the other scenarios, the projections would look similar, apart from the contribution by internal variability (see Section 4.6.3). The black curve shows the observations (HadCRUT5, (Morice et al., submitted)). Light blue shading shows the 50-member ensemble CanESM5, such that the deviations from the CanESM5 ensemble mean have been added to the CMIP6 multi-model mean. The red curves are from the emulator and show the best estimate (solid), *likely* range (dashed), and *very likely* range (dotted) for GSAT (Box 4.1). Forecasts for the period 2019–2028 from three prediction systems contributing to DCPP (Boer et al., 2016) are shown in purple, green, and blue. The DCPP results have been drift-removed and referenced to the time-averaged hindcasts for 1995–2014 lead-year by lead-year, following (Kharin et al., 2012; Kruschke et al., 2016), and have then been ensemble-averaged for each prediction system (solid); the shading shows the ensemble range for each prediction system.

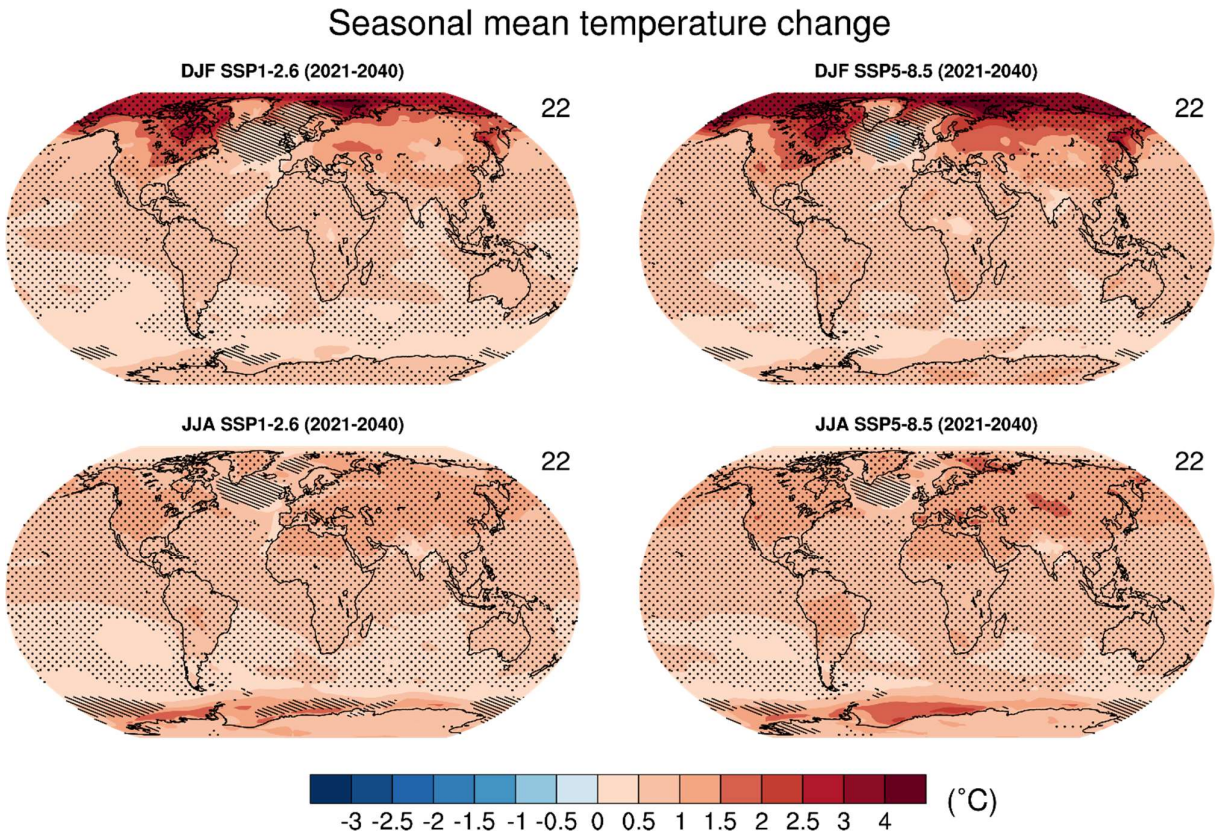


**Figure 4.11:** CMIP6 multi-model mean change (°C) in (top) DJF and (bottom) JJA near-surface air temperature in 2021–2040 from SSP1-2.6 and SSP5-8.5 relative to 1995–2014 based on 22 models.

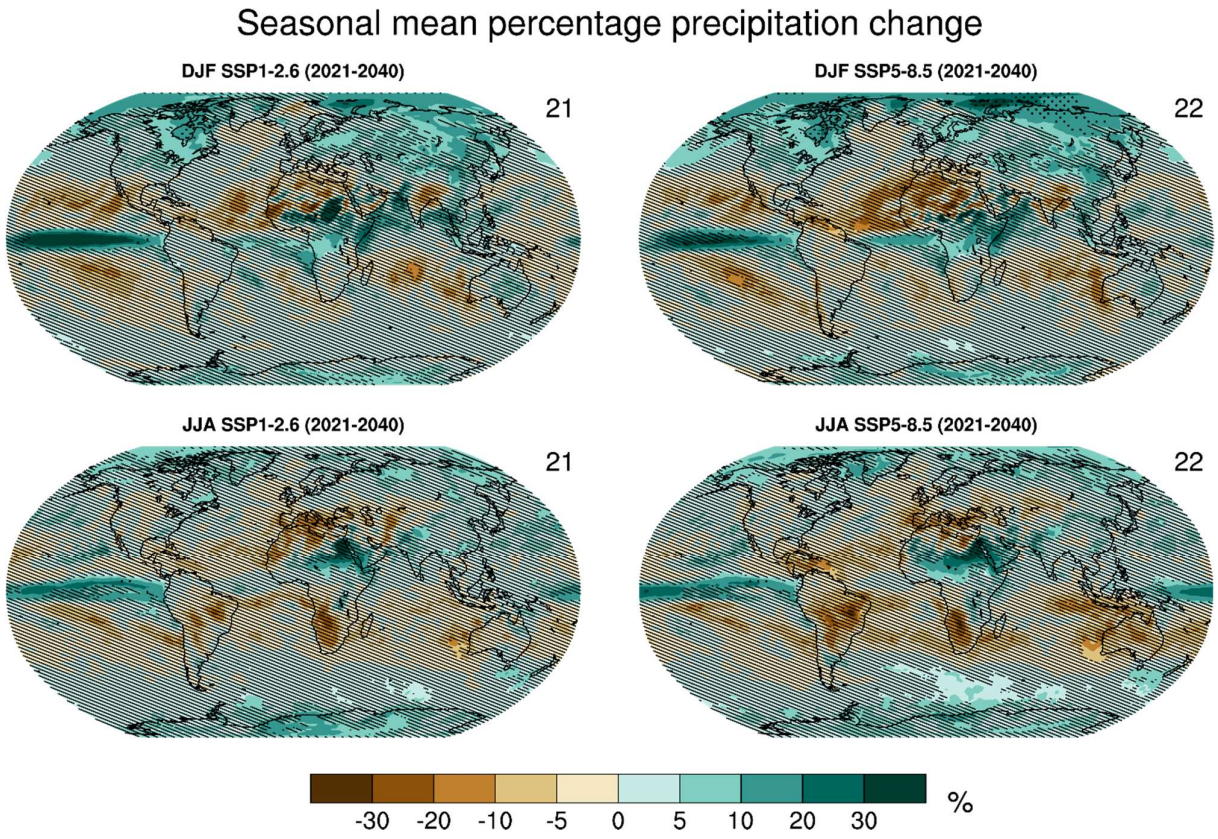


**Figure 4.12:** CMIP6 multi-model mean change (%) in (top) DJF and (bottom) JJA precipitation from SSP1-2.6 (21 models) and SSP5-8.5 (22 models) in 2021–2040 relative to 1995–2014.

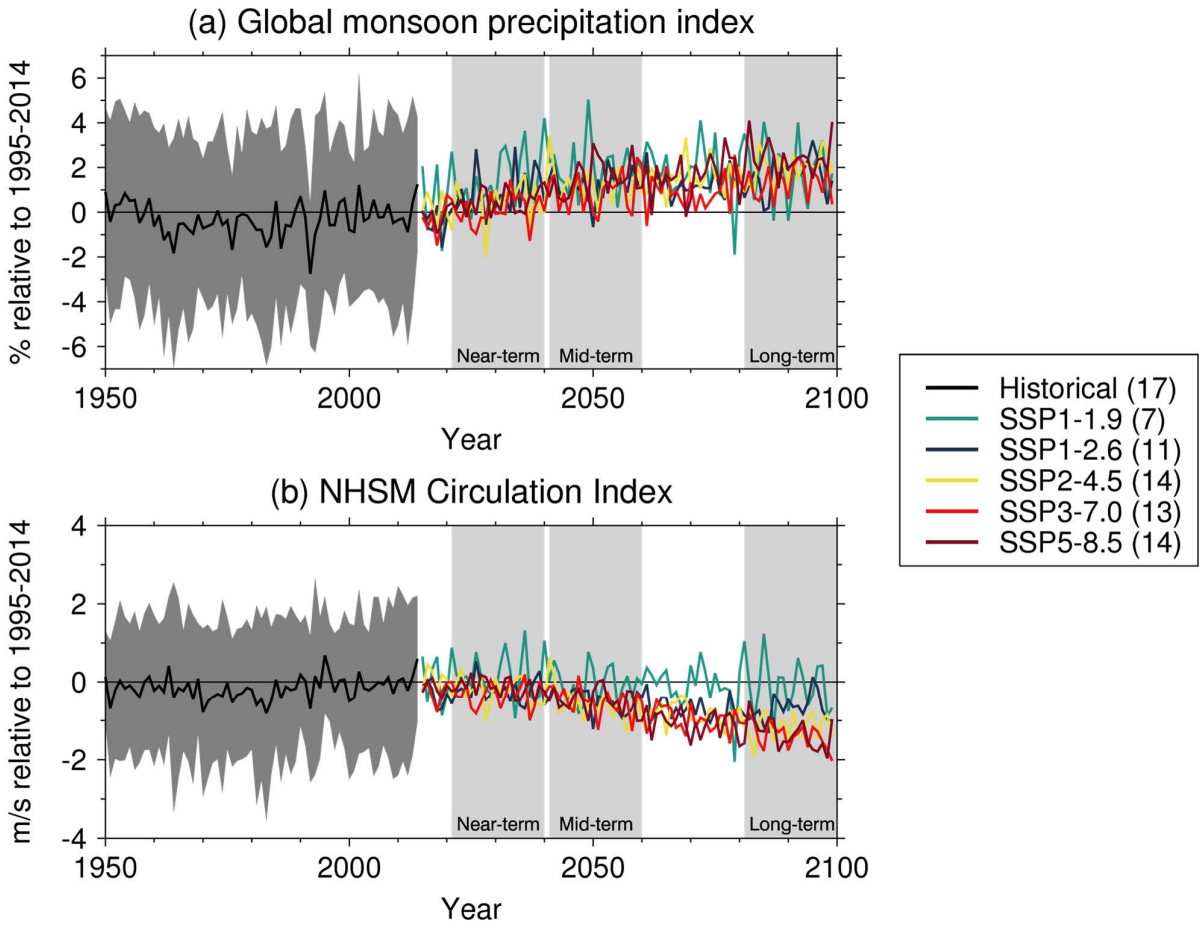


**Figure 4.13:** (a) Global land monsoon precipitation index anomalies (Unit: %) defined as the area-weighted mean precipitation rate in the global land monsoon domain defined by Wang et al. (2013) for the CMIP6 historical simulation and five SSPs. (b) Tropical monsoon circulation index anomalies (Unit: m/s) defined as the vertical shear of zonal winds between 850 and 200 hPa averaged in a zone stretching from Mexico eastward to the Philippines (0°–20°N, 120°W–120°E) (Wang et al., 2013) in the CMIP6 historical simulation and five SSPs. One realization is averaged from each model. Anomalies are shown relative to the present-day (1995–2014) mean. The number of models included in each simulation is given in the legend.

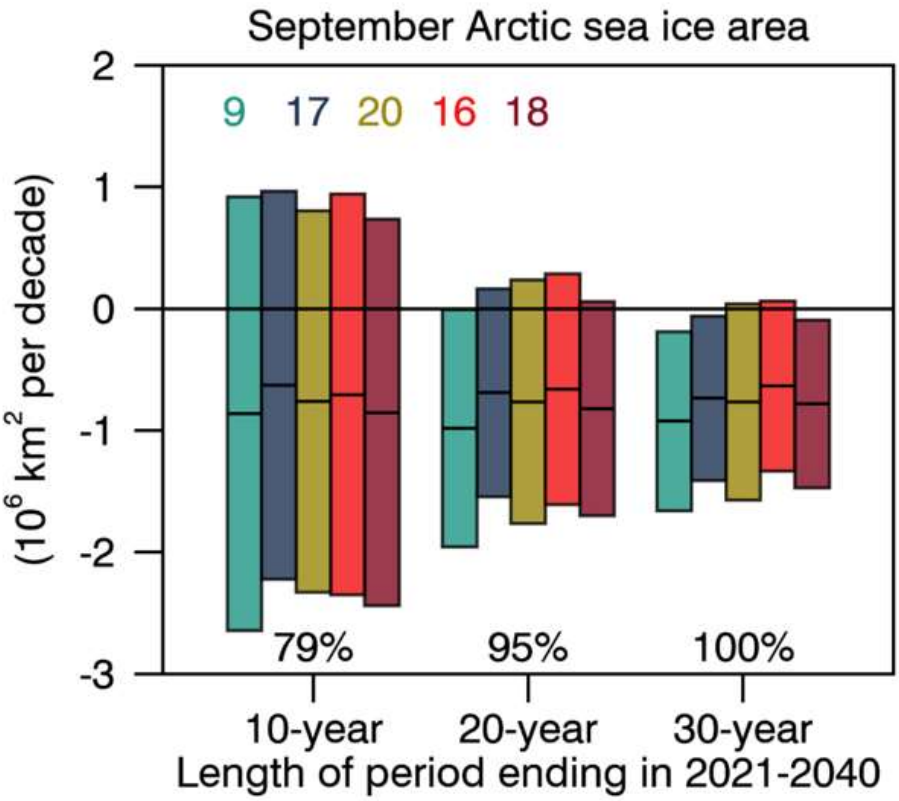


**Figure 4.14:** CMIP6 linear trends in September Arctic sea ice area ($10^6$ $km^2$ per decade) for 10-year, 20-year, and 30-year periods ending in 2021–2040 following five SSPs. Plotted are the 5-95% ranges (i.e. mean ± standard deviation x 1.64) across the r1 simulations contributed to the CMIP6 exercise. The numbers at the top of the plot are the number of model simulations in each SSP ensemble. The numbers near the bottom of the plot indicate the SSP-average percentage of simulated trends that are negative (i.e. indicating decreasing sea ice area).

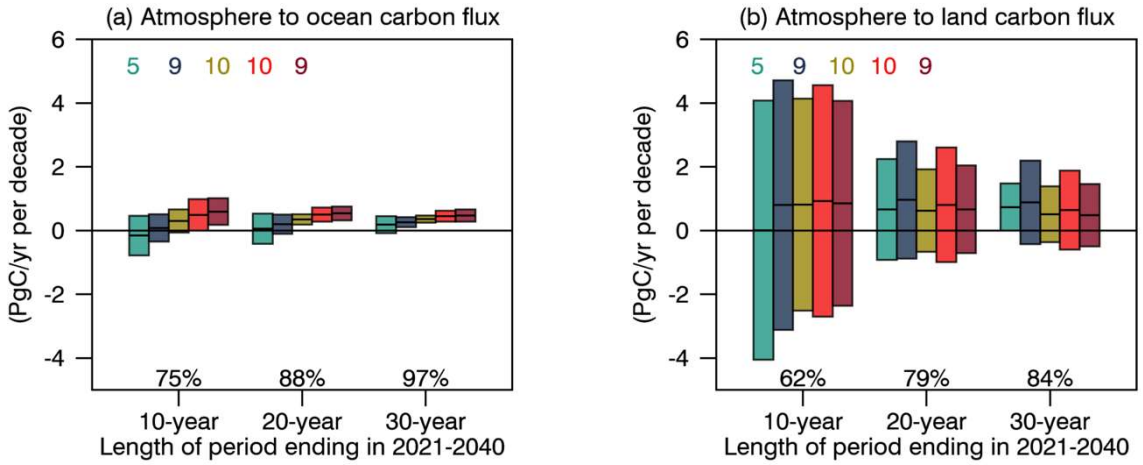


**Figure 4.15:** CMIP6 trends in carbon uptake (PgC/yr per decade) for 10-year, 20-year, and 30-year periods ending in 2021–2040 following five SSPs. (a) Ocean carbon uptake. (b) Land carbon uptake. Plotted are the 5-95% ranges (i.e. mean ± standard deviation x 1.64) across the r1 simulations contributed to the CMIP6 exercise. The numbers at the top of the plot are the number of model simulations in each SSP ensemble. The numbers near the bottom of the plot indicate the SSP-average percentage of simulated trends that are positive (i.e. indicating increasing carbon flux from the atmosphere into the ocean or land).

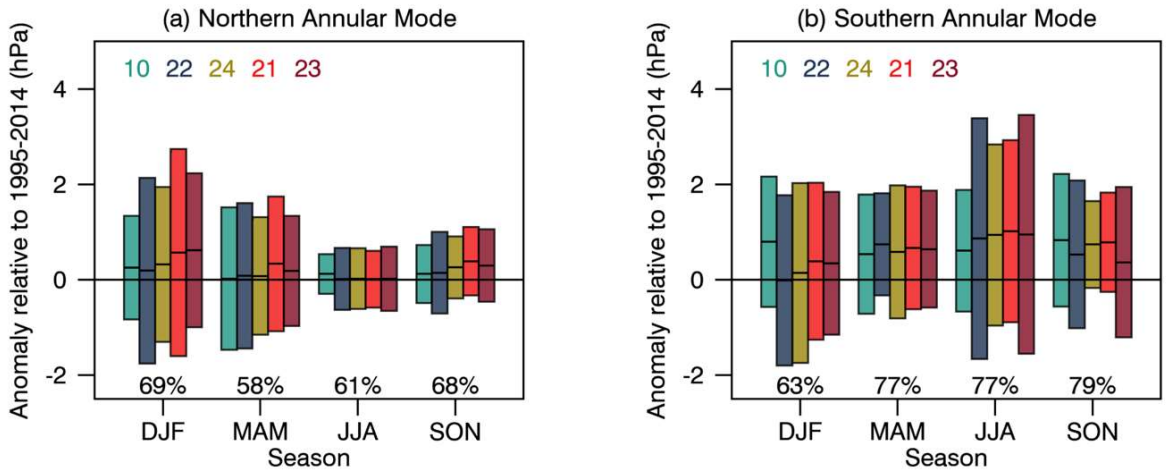


**Figure 4.16:** CMIP6 Annular Mode index change (hPa) from 1995-2014 (present-day; as an average) to 2021-2040 (near-term; as an average). (a) NAM and (b) SAM. The NAM is defined as the difference in zonal mean sea-level pressure (SLP) at 35°N and 65°N (Li and Wang, 2003) and the SAM as the difference in zonal mean SLP at 40°S and 65°S (Gong and Wang, 1999). The shadings are the 5 to 95% ranges (i.e. mean ± standard deviation x 1.64). The numbers near the top of each panel are the numbers of model simulations in each SSP ensemble. The numbers near the bottom of the panels are the SSP-averaged percentage of simulations with positive anomalies.

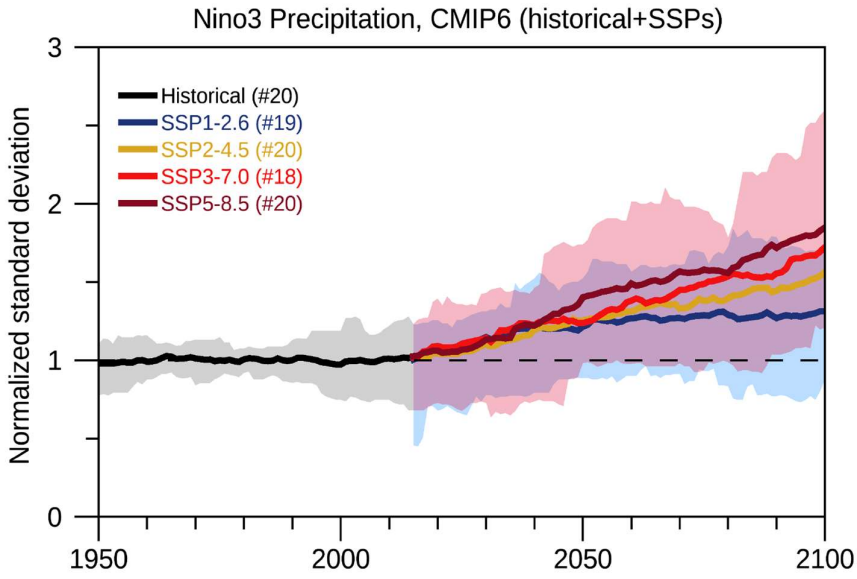


**Figure 4.17:** Multi-model mean (thick line) of changes in amplitude of ENSO precipitation variability from CMIP6 historical simulation from 1950 to 2014 and four SSPs from 2015 to 2100. Shading is 10-90% likely range whining models for historical simulation (grey), SSP1-2.6 (mid blue) and SSP5-8.5 (pink), respectively. The amplitude of ENSO precipitation variability is defined as the standard deviation of the Niño3-area averaged precipitation index over 30-year running windows. The standard deviation in every single model is normalized by each model's present-day standard deviation averaged from 1950 to 1999. The number of available model is listed in parentheses.

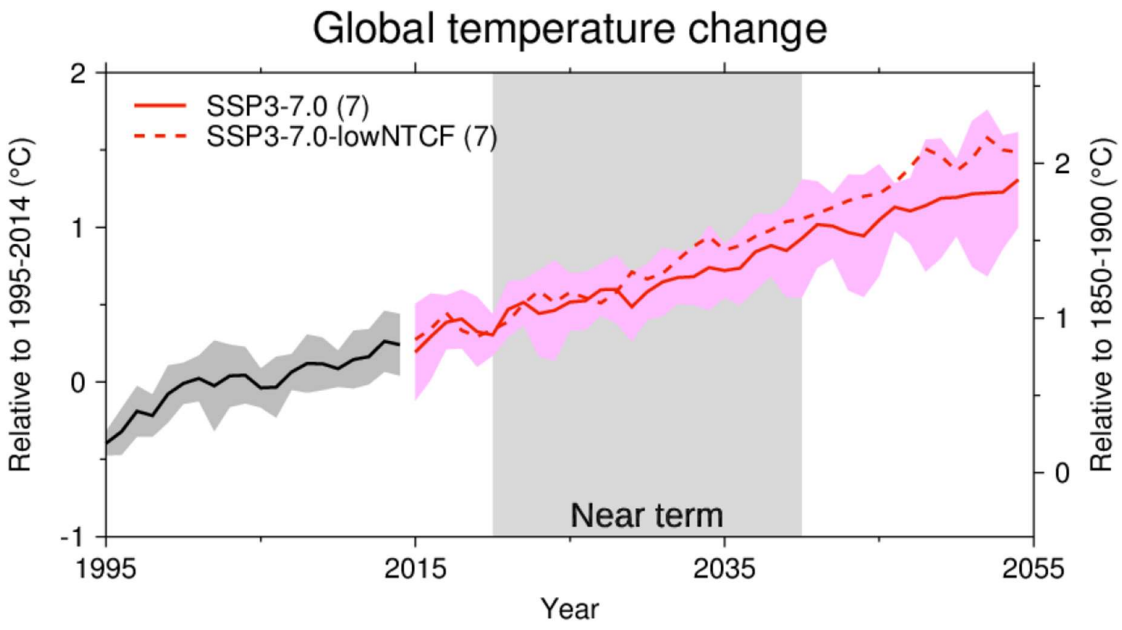


**Figure 4.18:** Global surface air temperature change relative to the 1995–2014 average (left axis) and relative to the 1850–1900 average (right axis). The comparison is for CMIP6 models for the AerChemMIP (Collins et al., 2017b) SSP3-7.0-lowNTCF experiment, where concentrations of short-lived species are reduced compared to reference SSP3-7.0 scenario. The curves show averages over the r1 simulations contributed to the CMIP6 exercise, the shadings around the SSP3-7.0 curve shows 5 to 95% ranges (i.e. mean ± standard deviation x 1.645), and the numbers near the top show the number of model simulations.

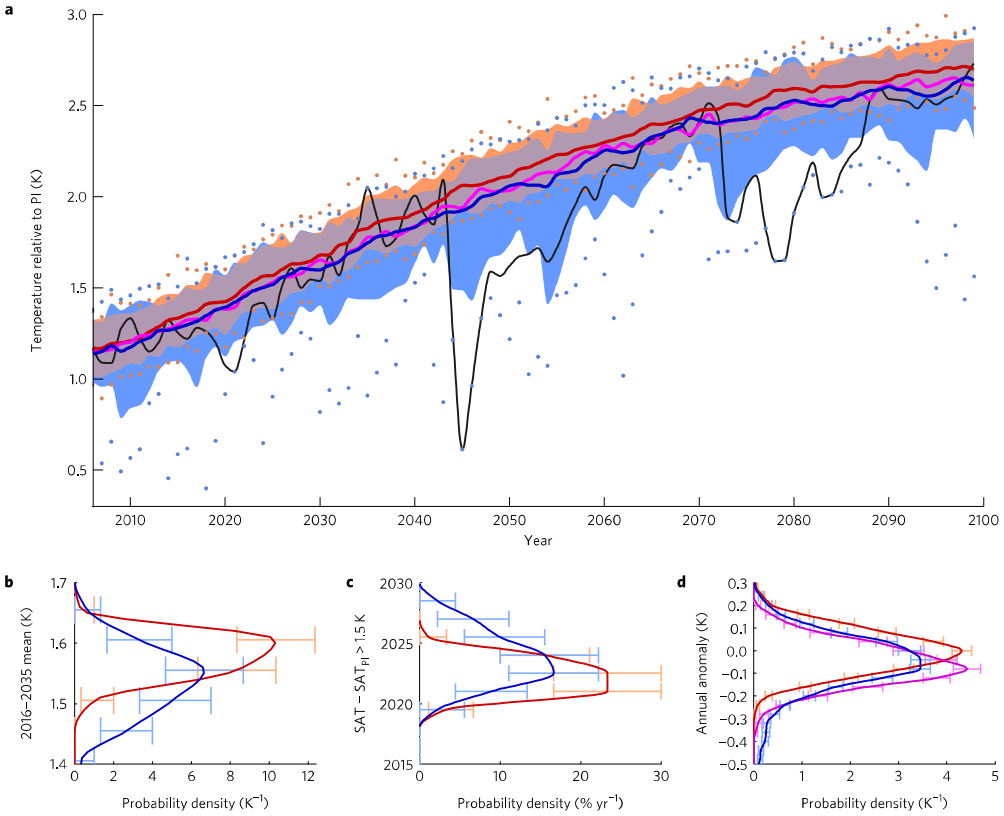


**Figure 4.19:** Annual-mean GSAT. a, Ensemble mean (solid) of VOLC (blue), VOLC-CONST (magenta) and NO-VOLC (red/orange) with 5–95% range (shading) and ensemble minima/maxima (dots) for VOLC and NO-VOLC; evolution of the most extreme member (black). b, Probability density function (PDF) of the 2016–2035 mean relative to pre-industrial (PI), with 5–95% bootstrap confidence bounds. c, PDF of the time when GSAT change relative to PI (20-year running average) exceeds 1.5°C. d, PDF of annual anomalies with anthropogenic trend removed. The spread of VOLC-CONST is linearly shifted relative to NO-VOLC, and therefore not shown in a–c. These calculations are based on three 21st-century simulation ensembles with the Norwegian Earth System Model (NorESM), which use the same mid-range anthropogenic forcing scenario RCP4.5 but differ in their volcanic forcing: a 60-member ensemble using plausible stochastic volcanic forcing (VOLC); a 60-member reference ensemble using zero volcanic forcing (NO-VOLC); and a 20-member ensemble using 1850–2000 averaged volcanic forcing (VOLC-CONST). [This figure is adopted from (Bethke et al., 2017).]

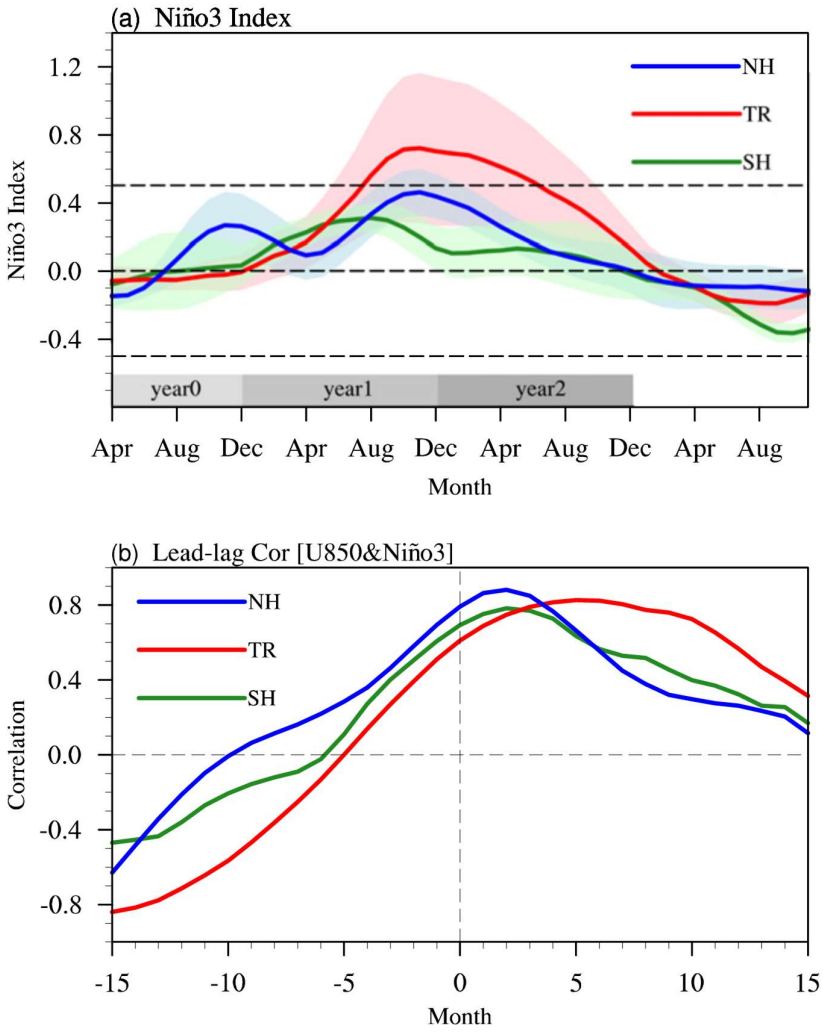


**Figure 4.20:** (a) Evolution of the composite Niño-3 index with zonal mean removed (units: 8°C) after northern eruptions (blue line), tropical eruptions (red line), and southern eruptions (green line). The spreads of the individual volcanic eruptions are denoted by the blue, red, and green shading, respectively. (b) The lead–lag correlation between the Niño-3 index (5°S–5°N, 150°–90°W) and the 850-hPa zonal wind in the western-to-central equatorial Pacific (5°S–5°N, 110°E–150°W) following northern (blue line), tropical (red line), and southern eruptions (green line). The positive value of the horizontal axis indicates that the Niño-3 index lags the 850-hPa zonal wind. [This figure is adapted from Zuo et al. (2018).]

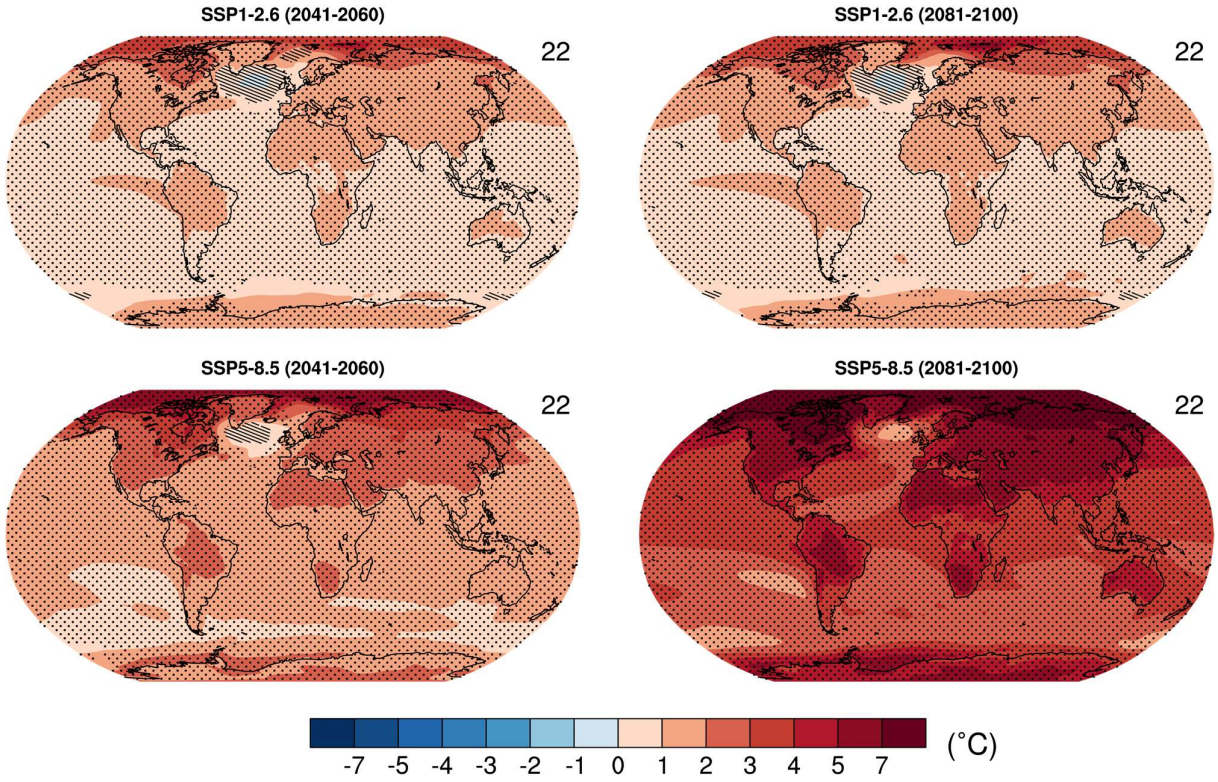


**Figure 4.21:** Multi-model mean change in annual mean near-surface air temperature (°C) in 2041–2060 and 2081–2100 in (top) SSP1-2.6 and (bottom) SSP5-8.5 relative to 1995–2014.

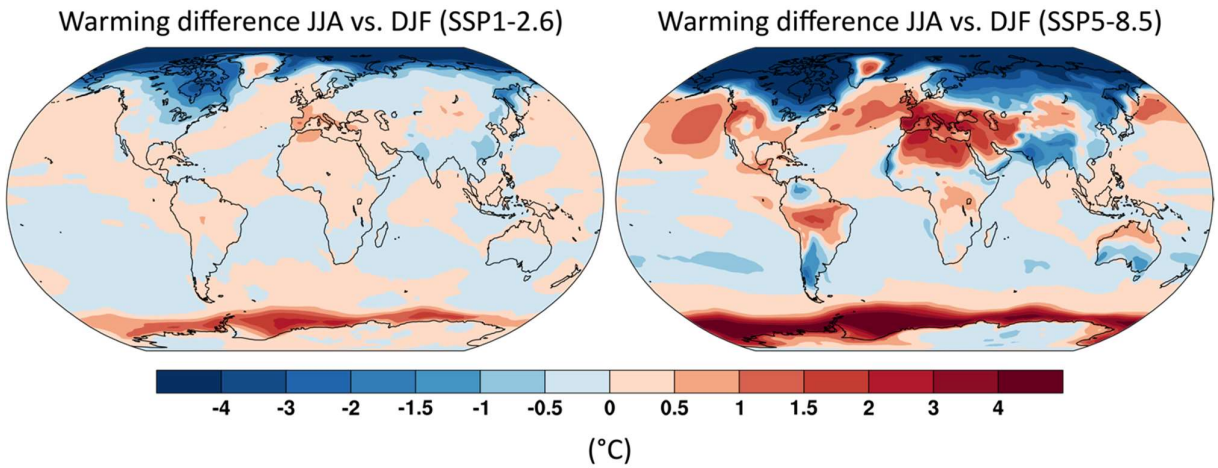


**Figure 4.22:** Multi-model mean difference in projected warming in JJA minus warming in DJF in 2081-2100 relative to 1995–2014 for (left) SSP1-2.6 and (right) SSP5-8.5. Particularly over the extratropics the warming difference is a simple approximation for the change in the amplitude of the seasonal cycle.

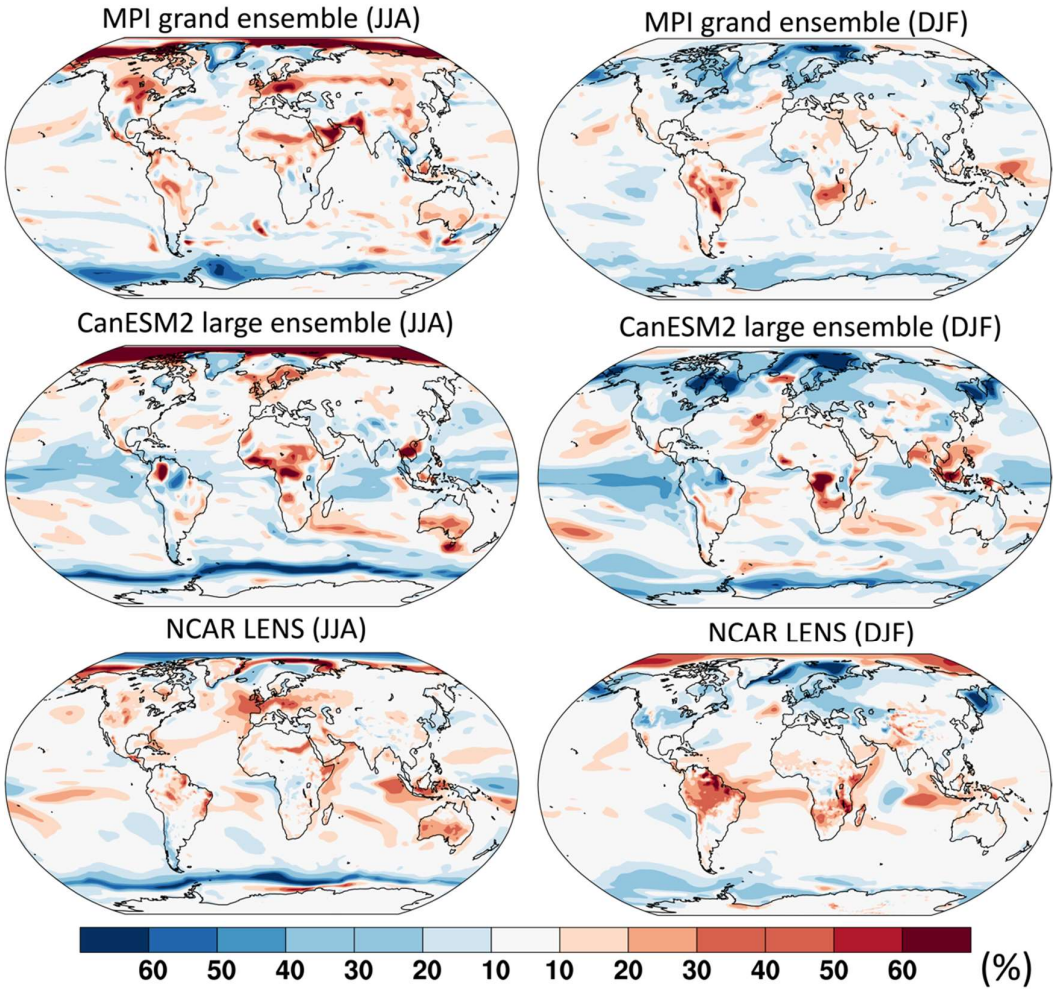


**Figure 4.23:** Relative change in variability of (left) JJA and (right) DJF mean temperature in three large initial condition ensembles. Changes are shown as percentage changes of standard deviation across local seasonal mean temperatures calculated as the average standard deviation across members of the large ensembles for every given year. Changes are shown for MPI 100-member grand ensemble by 2081–2100 (Maher et al., 2019), CanESM2 50-member ensemble (Kirchmeier-Young et al., 2017) and NCAR-CESM 30-member ensemble (Kay et al., 2015) for RCP8.5.

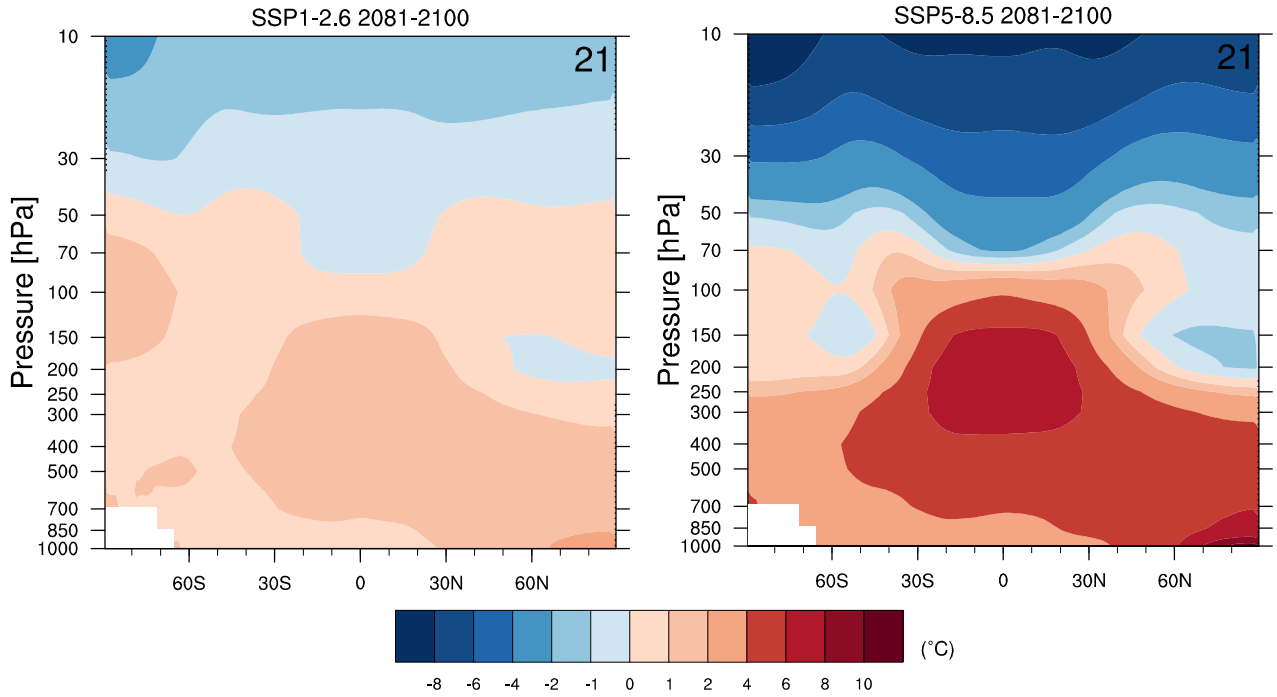


**Figure 4.24:** Change in annual mean atmospheric temperature (°C) in 2081–2100 in (left) SSP1-2.6 and (right) SSP5-8.5 relative to 1995–2014 for CMIP6 models.

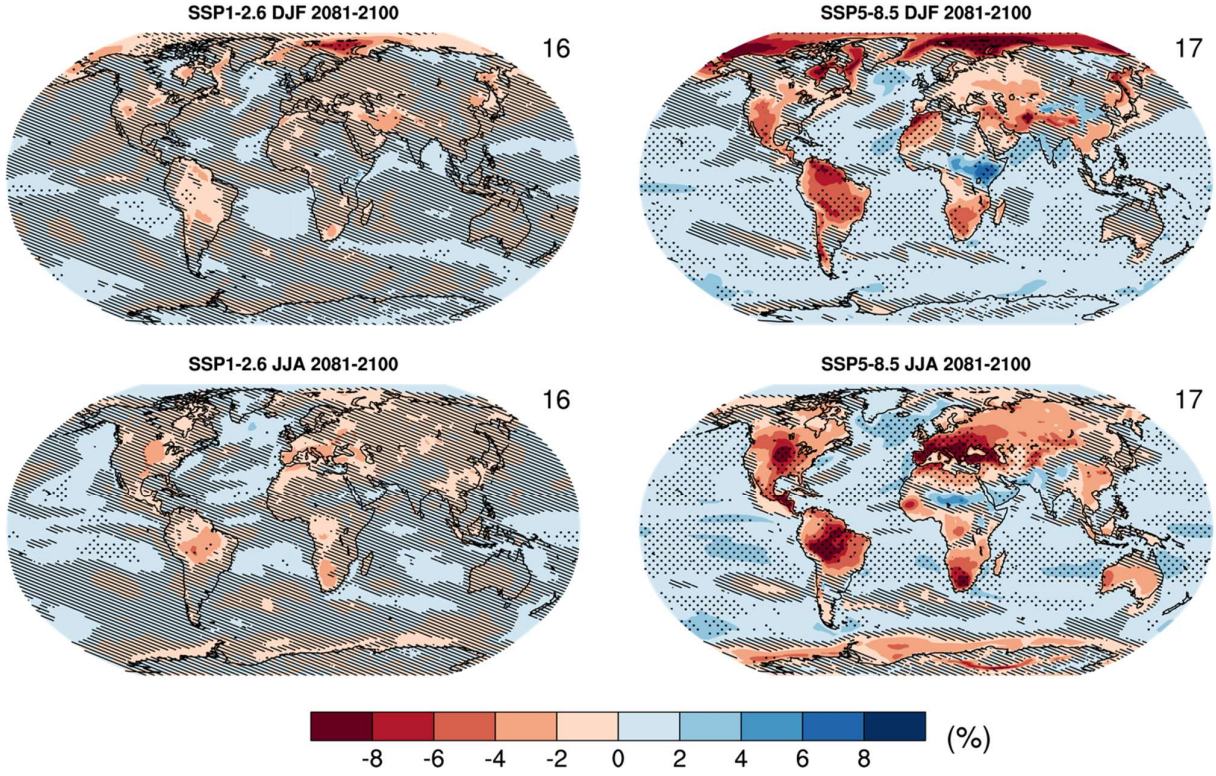


**Figure 4.25:** Multi-model mean change (%) in seasonal (left) DJF and (right) JJA mean near-surface relative humidity in 2041–2060 and 2081–2100 in SSP5-8.5 relative to 1995–2014 CMIP6 models.]

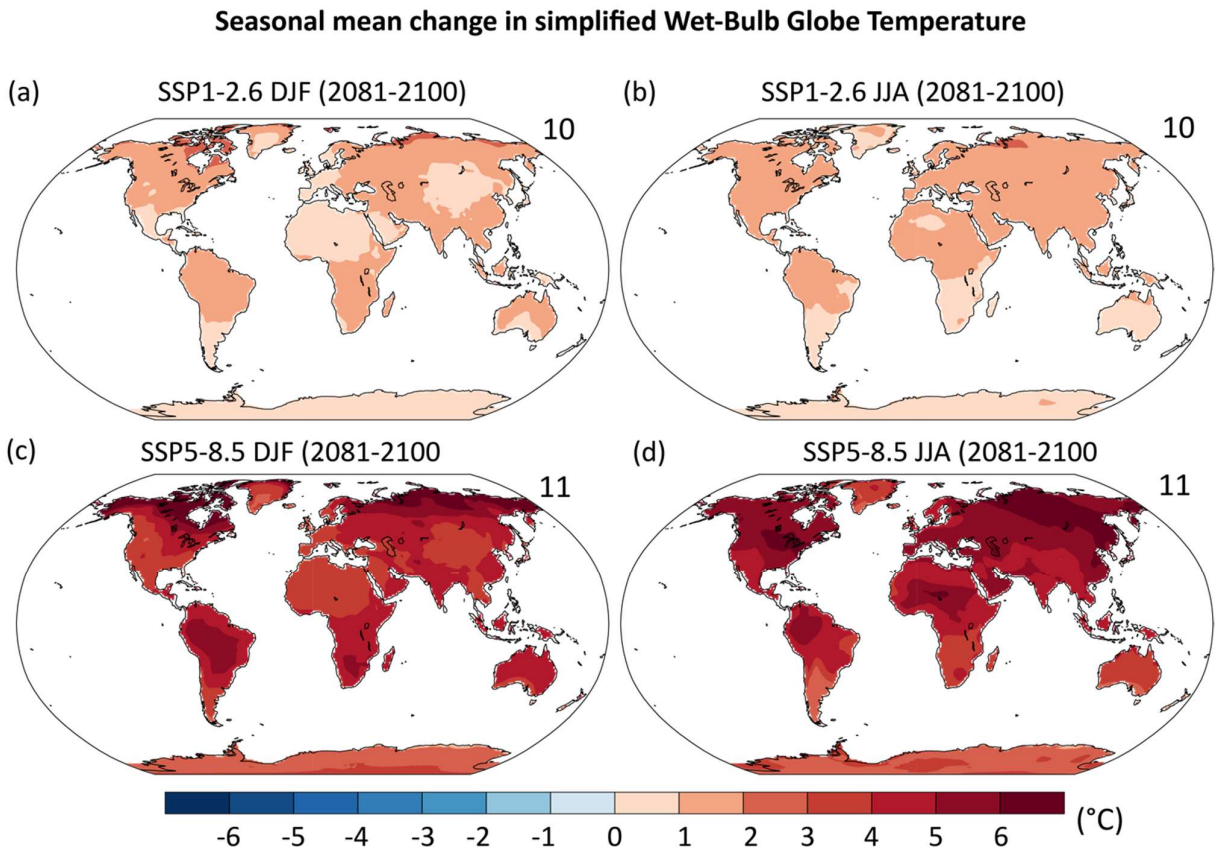


**Figure 4.26:** Multi-model mean change (°C) in seasonal (left) DJF and (right) JJA mean simplified wet-bulb globe temperature in 2081–2100 in SSP1-2.6 and SSP5-8.5 relative to 1995–2014 based on 10 and 11 CMIP6 models, respectively. The data is based on seasonal averages of daily values calculated in Schwingshackl et al. (2020).

1

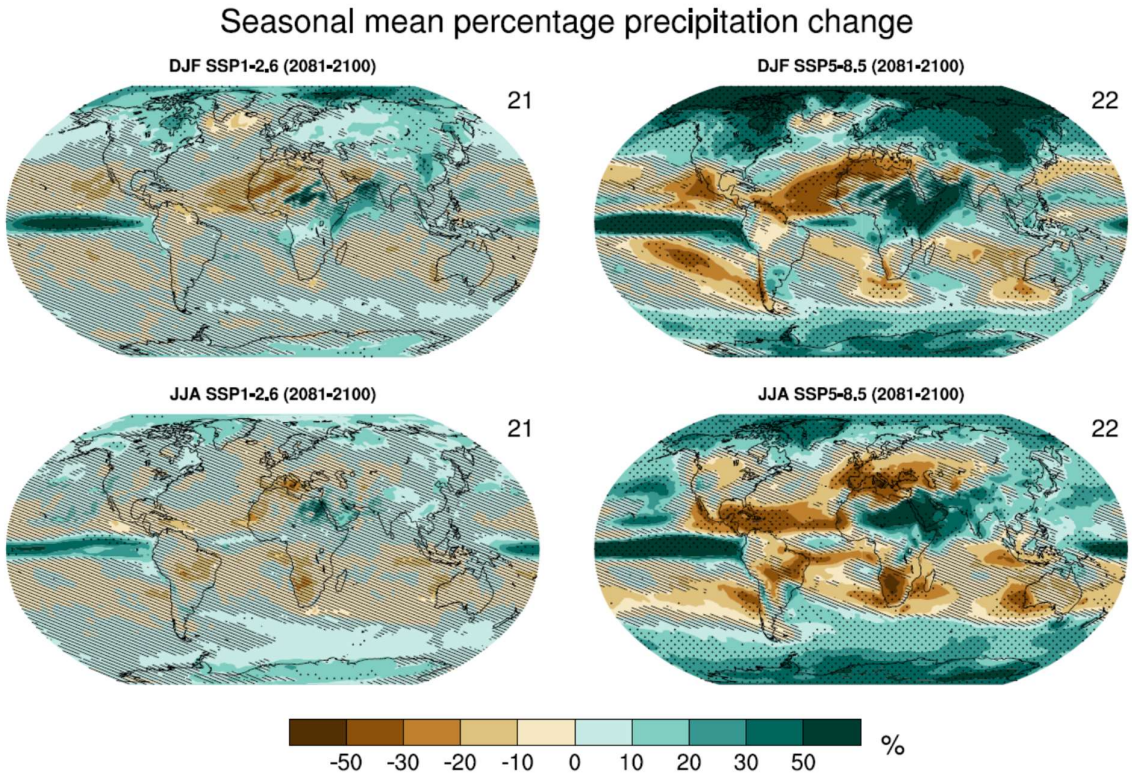


2

3 **Figure 4.27:** Multi-model mean change (%) in annual mean precipitation in 2041–2060 (left) and 2081–2100 (right)
4 relative to 1995–2014 from (top) SSP1-2.6 and (bottom) SSP5-8.5.

5

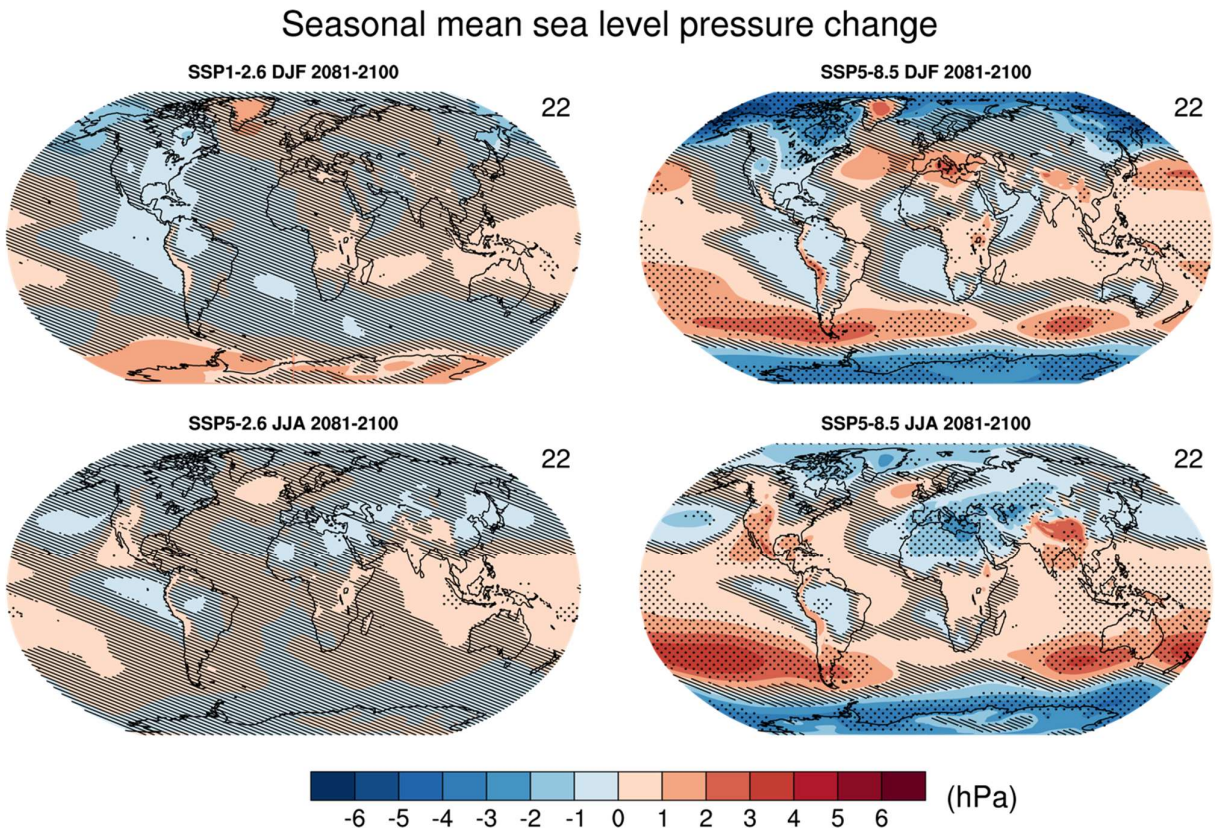


**Figure 4.28:** Multi-model mean change in JJA and DJF mean sea level pressure (hPa) in 2081–2100 in SSP1-2.6 and SSP5-8.5 relative to 1995–2014.

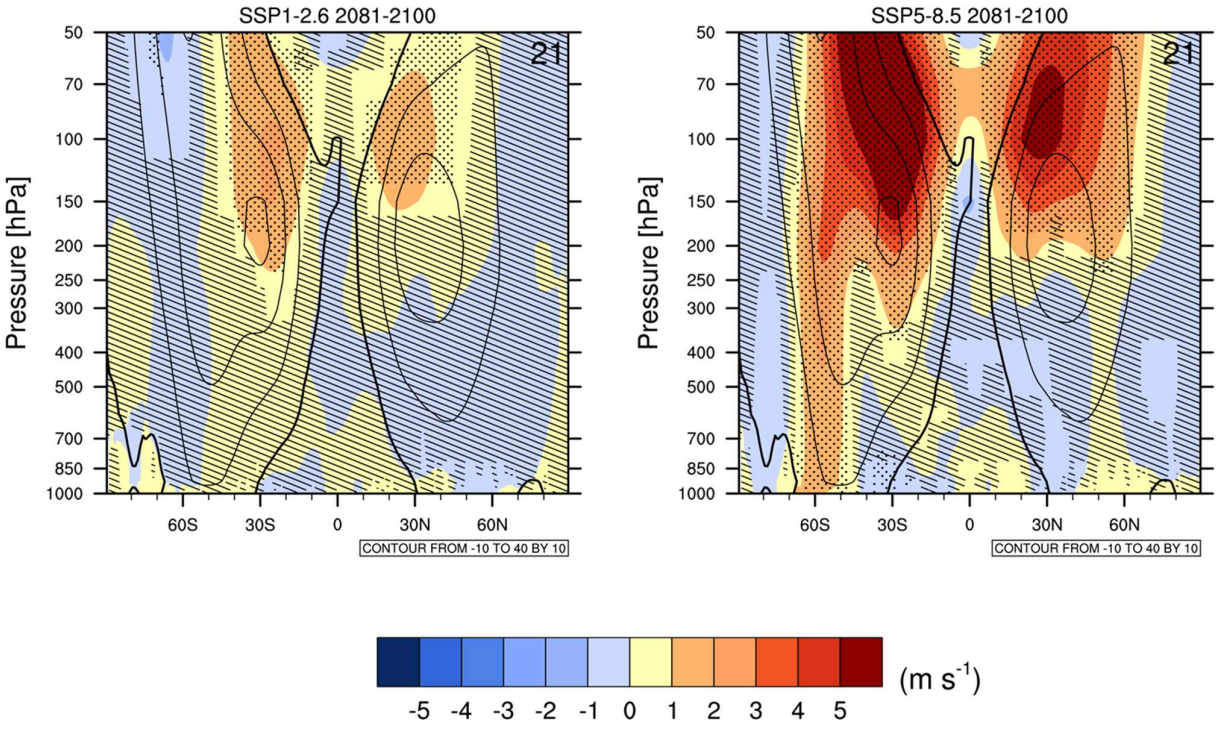


**Figure 4.29:** Multi-model mean annual mean zonal mean zonal wind change (m $s^{-1}$) in 2081–2100 in (left) SSP1-2.6 and (right) SSP5-8.5 relative to 1995–2014. The 1995–2014 climatology is shown in contours with spacing 10 m $s^{-1}$.

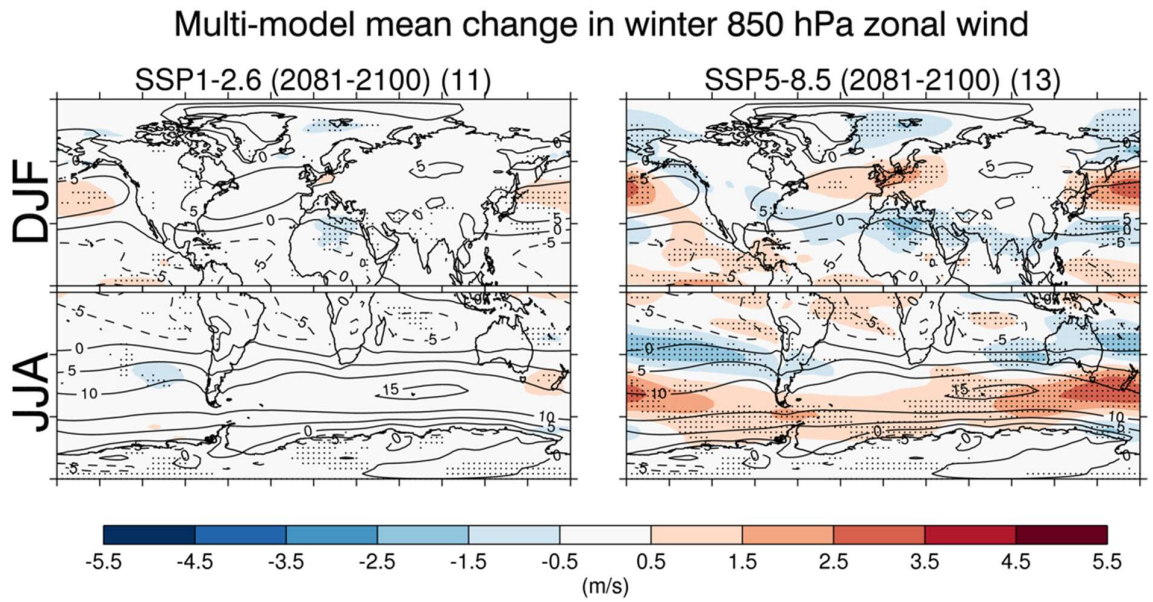


**Figure 4.30:** Multi-model mean change in winter (NH DJF, SH JJA) zonal wind at 850 hPa (*u850*) in 2081–2100 in (left) SSP1-2.6 and (right) SSP5-8.5 relative to 1995–2014. The 1995–2014 climatology is shown in contours with spacing 5 m $s^{-1}$. Stippling denotes where at least 90% of models agree on the sign of change.

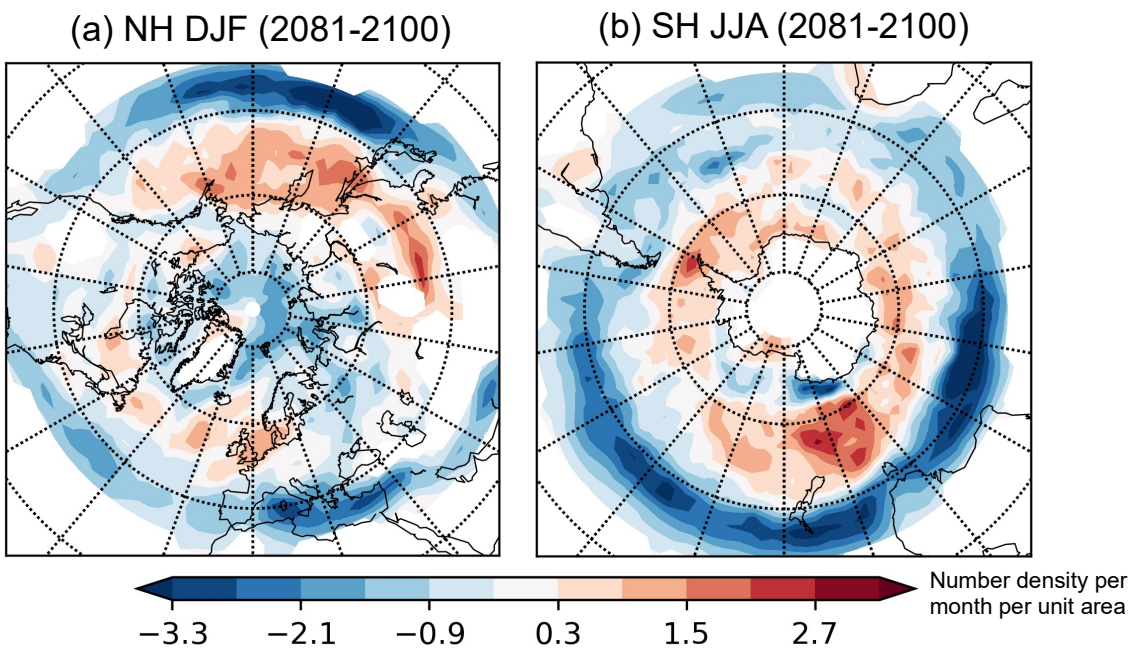


**Figure 4.31:** Multi-model mean change of extratropical storm track density in winter (NH DJF and SH JJA) in 2081-2100 in SSP5-8.5 relative to 1995-2014 based on 5 CMIP6 models. [Figure will be updated with further CMIP6 models and uncertainty assessment as additional models provide high frequency output].

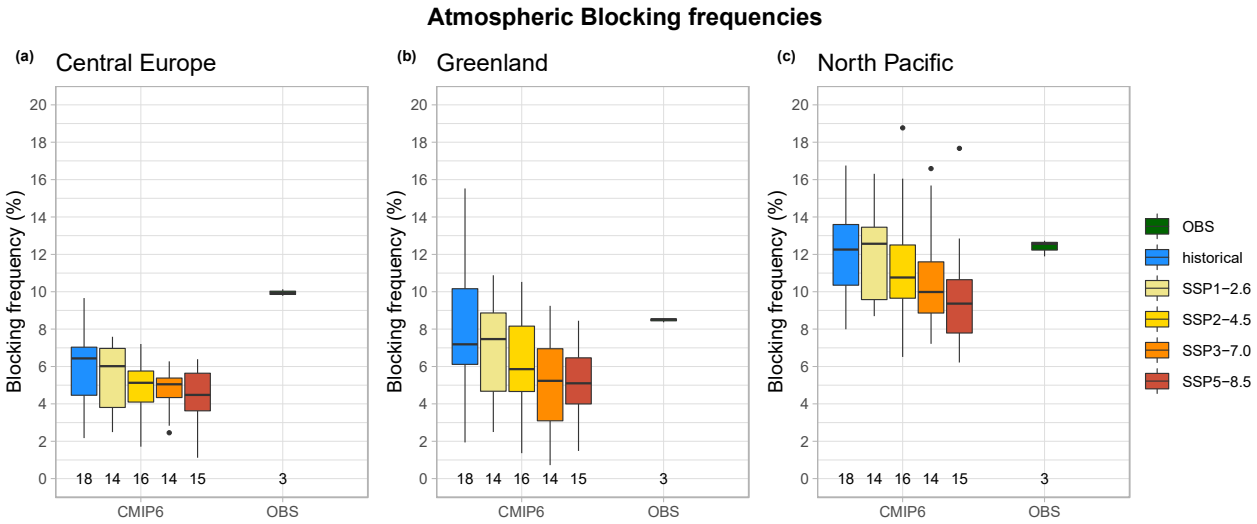


**Figure 4.32:** Box plot showing wintertime (December to March) present-day (historical simulations, 1995-2014) and future climate (SSP simulations, 2081–2100) atmospheric blocking frequencies over (a) the Greenland region (65°W–20°W, 62.5°N–72.5°N), (b) the Central European region (20°W–20°E, 45°N–65°N), (c) the North Pacific region (130°E–150°W, 60°N–75°N). Values show the percentage of blocked days per season following the (Davini et al., 2012) index. Median values are the black horizontal bar. The numbers below each bar report the number of models included. Observationally-based values are obtained as the average of the ERA-Interim Reanalysis, the JRA-55 Reanalysis and the NCEP/NCAR Reanalysis. Adapted from (Davini and D'Andrea, 2019)

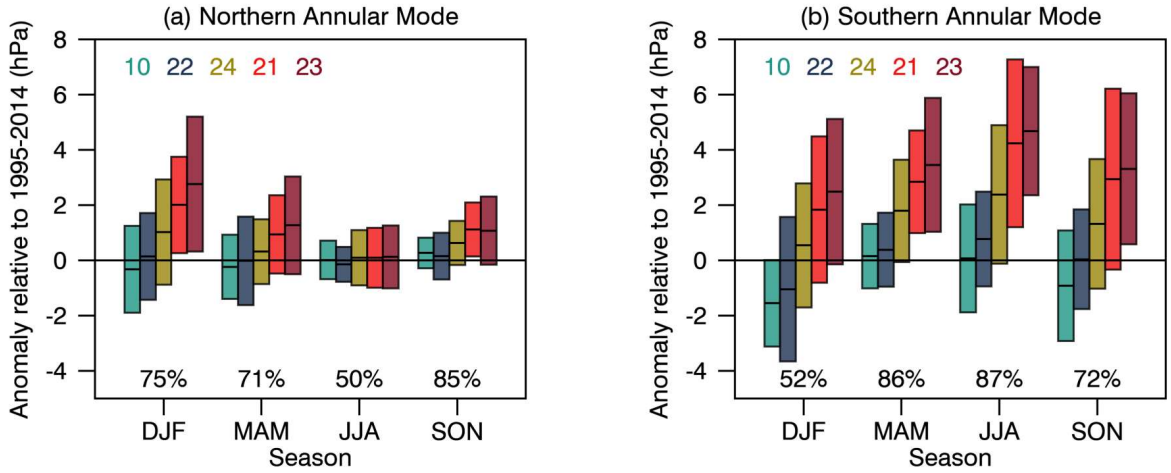


**Figure 4.33:** CMIP6 Annular Mode index change from 1995-2014 (as an average) to 2081-2100 (as an average): (a) NAM and (b) SAM. The NAM is defined as the difference in zonal mean SLP at 35°N and 65°N (Li and Wang, 2003) and the SAM as the difference in zonal mean SLP at 40°S and 65°S (Gong and Wang, 1999). The shadings are the 5 to 95% ranges (i.e. mean ± standard deviation x 1.64). The numbers near the top are the numbers of model simulations in each SSP ensemble. The numbers near the bottom are the SSP-averaged percentage of simulations with positive anomalies.

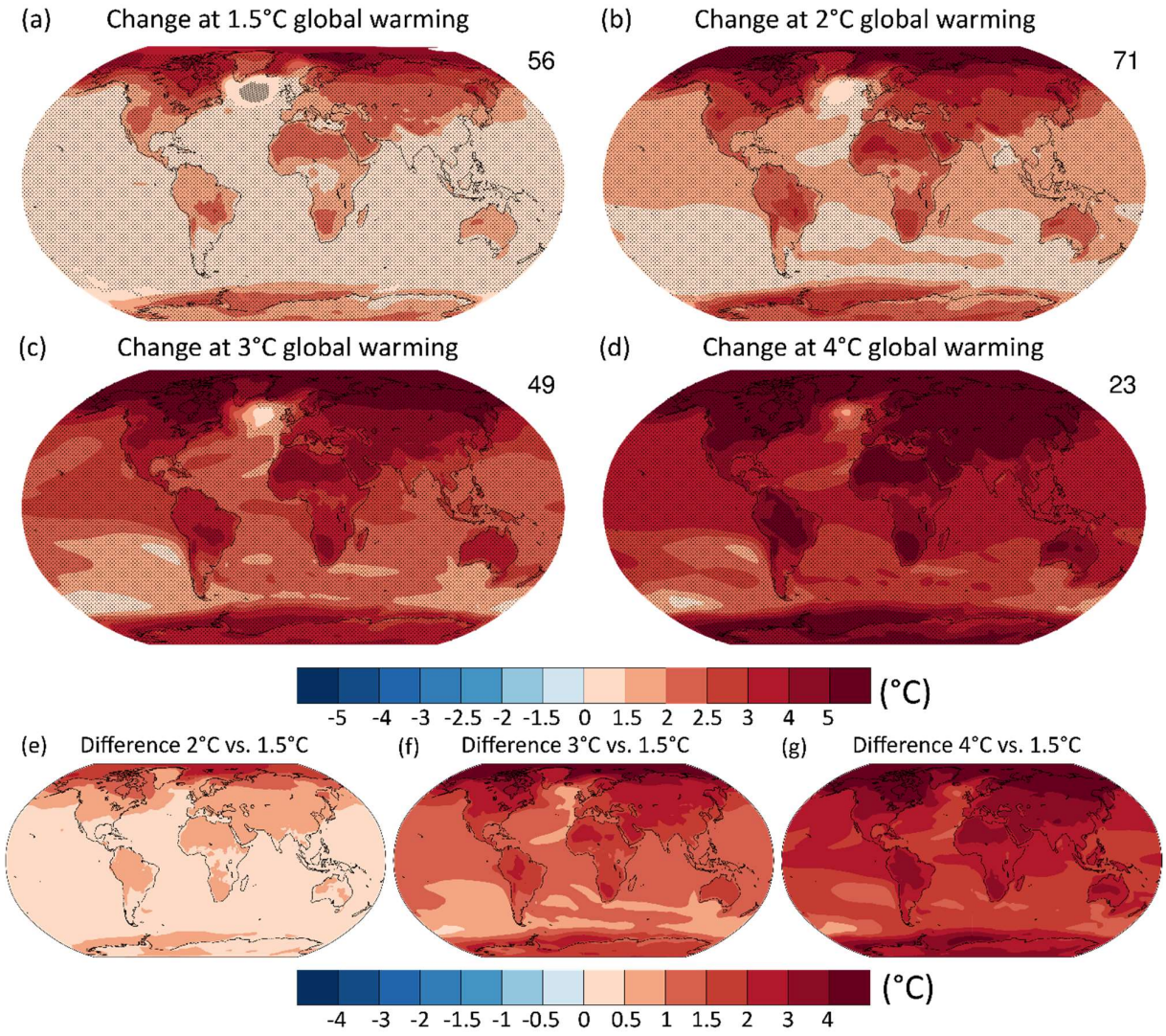


**Figure 4.34:** Projected spatial patterns of changes in annual mean temperature (°C) at 1.5°C, 2°C, 3°C, and 4°C of global warming compared to the pre-industrial period (1850–1900) (top), and the spatial differences of temperature change between 2°C, 3°C, and 4°C of global warming relative to 1.5°C of global warming (bottom). Cross-hatching highlights areas where at least two-thirds of the models agree on the sign of change, as a measure of robustness. Values were assessed from a 20-year period at a given warming level, based on model simulations under the Tier 1 SSPs of CMIP6.

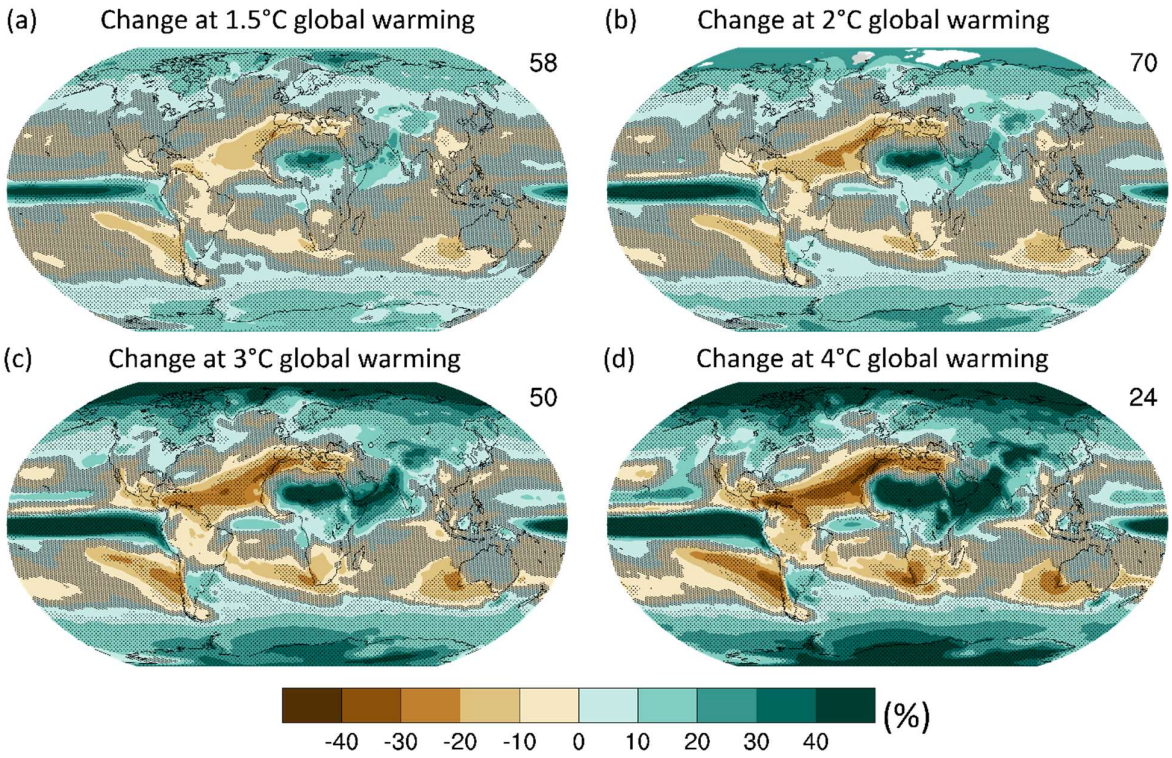


**Figure 4.35:** Projected spatial patterns of changes in annual precipitation (expressed as a % change) at 1.5°C, 2°C, 3°C and 4°C of global warming compared to the pre-industrial period (1850–1900). Values were assessed from a 20-year period at a given warming level, composited from SSP1-2.6, SSP2-4.5, SSP3-7.0 and SSP5-8.5 in CMIP6.

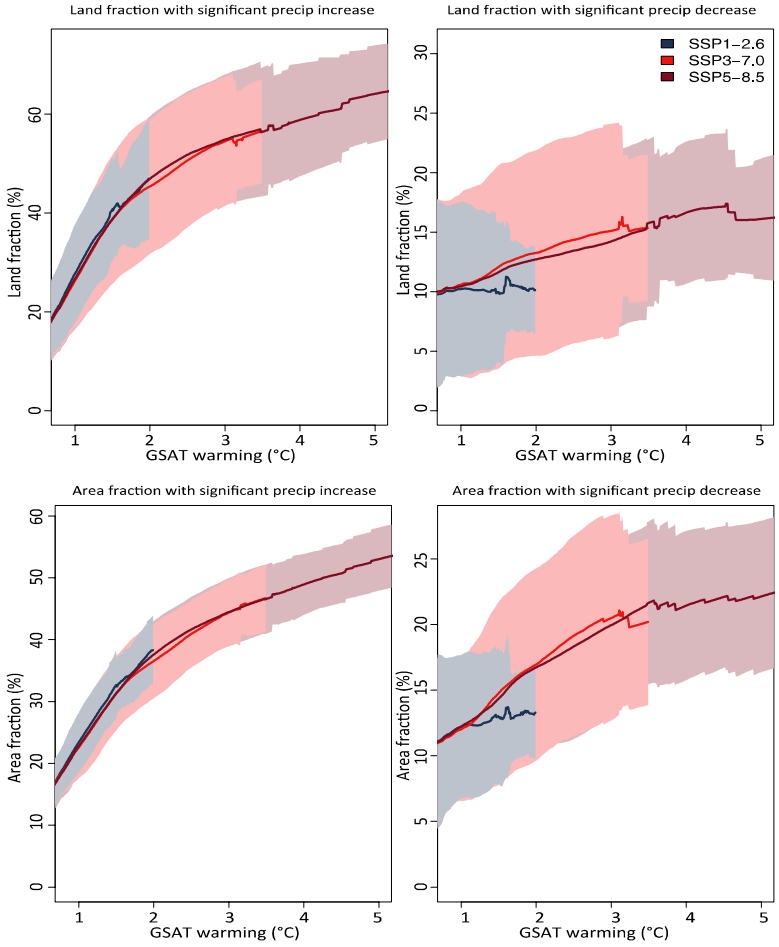


**Figure 4.36:** Area fraction (% change) with significant precipitation increase (left-hand side) and decrease (right-hand side) in the projected annual precipitation change at 1.5°C, 2°C, 3°C and 4°C of global warming compared to the pre-industrial period (1850–1900). Values were assessed from a 20-year period at a given warming level from SSP1-2.6, SSP3-7.0 and SSP5-8.5 in CMIP6.

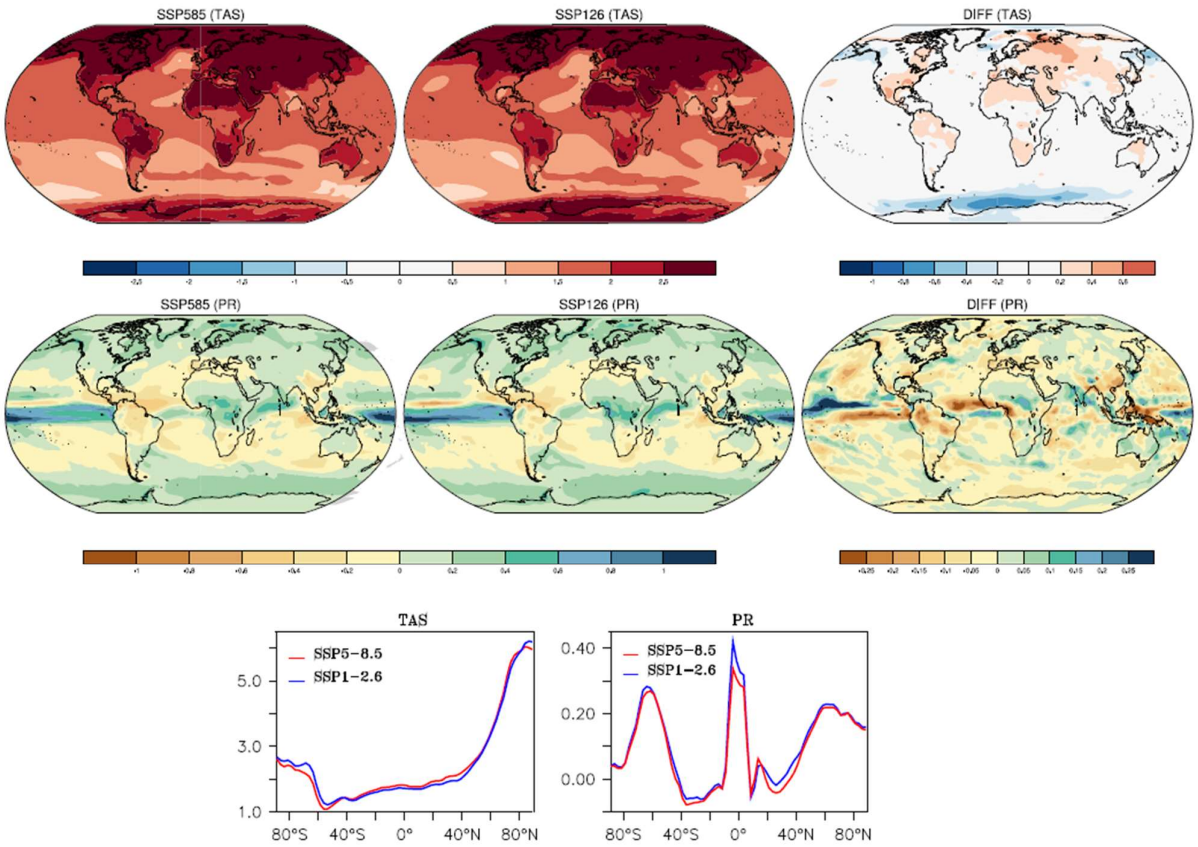


**Figure 4.37:** Projected changes in the global pattern of near-surface temperature (top row) and precipitation (second row) associated with a 2°C increase in global temperature achieved by different pathways from 15 CMIP6 ESMs. Panels show temperature and precipitation changes averaged over 20-year period when GSAT reaches 2 degrees above pre-industrial for two scenarios; SSP5-8.5 and SSP1-2.6. The bottom row and right-hand panels show differences (SSP5-8.5 minus SSP1-2.6) in the temperature and precipitation changes due to path dependence.

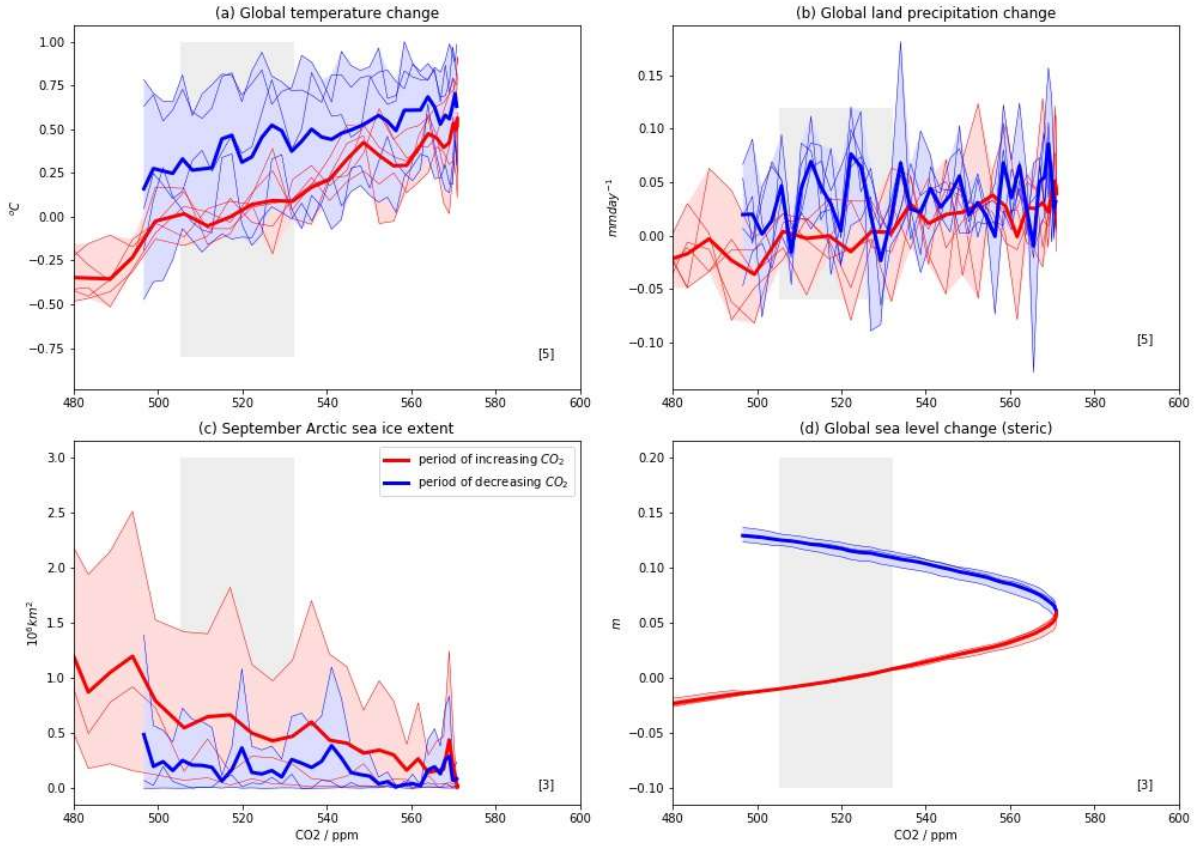


**Figure 4.38:** Simulated changes in climate, plotted against atmospheric $CO_2$ concentration, for SSP5-34-OS from $CO_2$ concentration of 480 up to 571 and back to 500 by 2100. (a) Global temperature change; (b) Global land precipitation change; (c) September Arctic sea ice extent; (d) Global steric sea level. Plotted changes are relative to the 2034-2053 mean which has same $CO_2$ as 2080-2100 mean (shaded grey bar). Red lines denote changes during the period up to 2062 when $CO_2$ is rising, blue lines denote changes after 2062 when $CO_2$ is decreasing again.

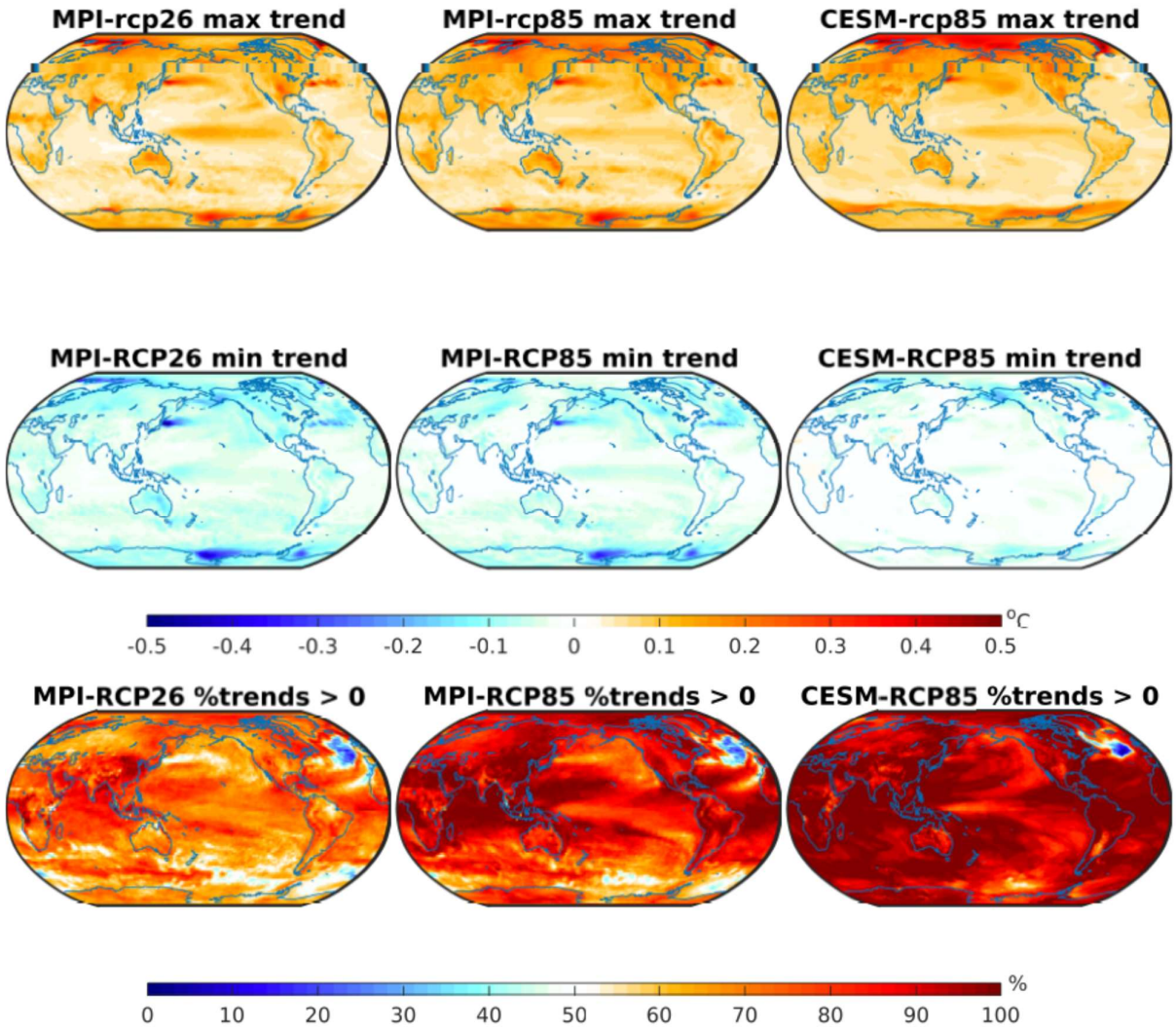


**Figure 4.39:** Near-term (2021-2040) maximum (top row) and minimum (middle row) trends in the initial condition ensemble from MPI (left and centre columns), and CESM (right column) models in the RCP2.6 (left column) and RCP8.5 scenarios (centre and right columns). The percentage of ensemble members which show a warming trend in the near-term is shown in the bottom panels. The panels in the middle row clearly indicate that in the near term in both mitigation (RCP2.6) and non-mitigation (RCP8.5) scenarios, a cooling trend is possible at any individual point on the globe, though not everywhere simultaneously. Modified from (Maher et al., submitted).

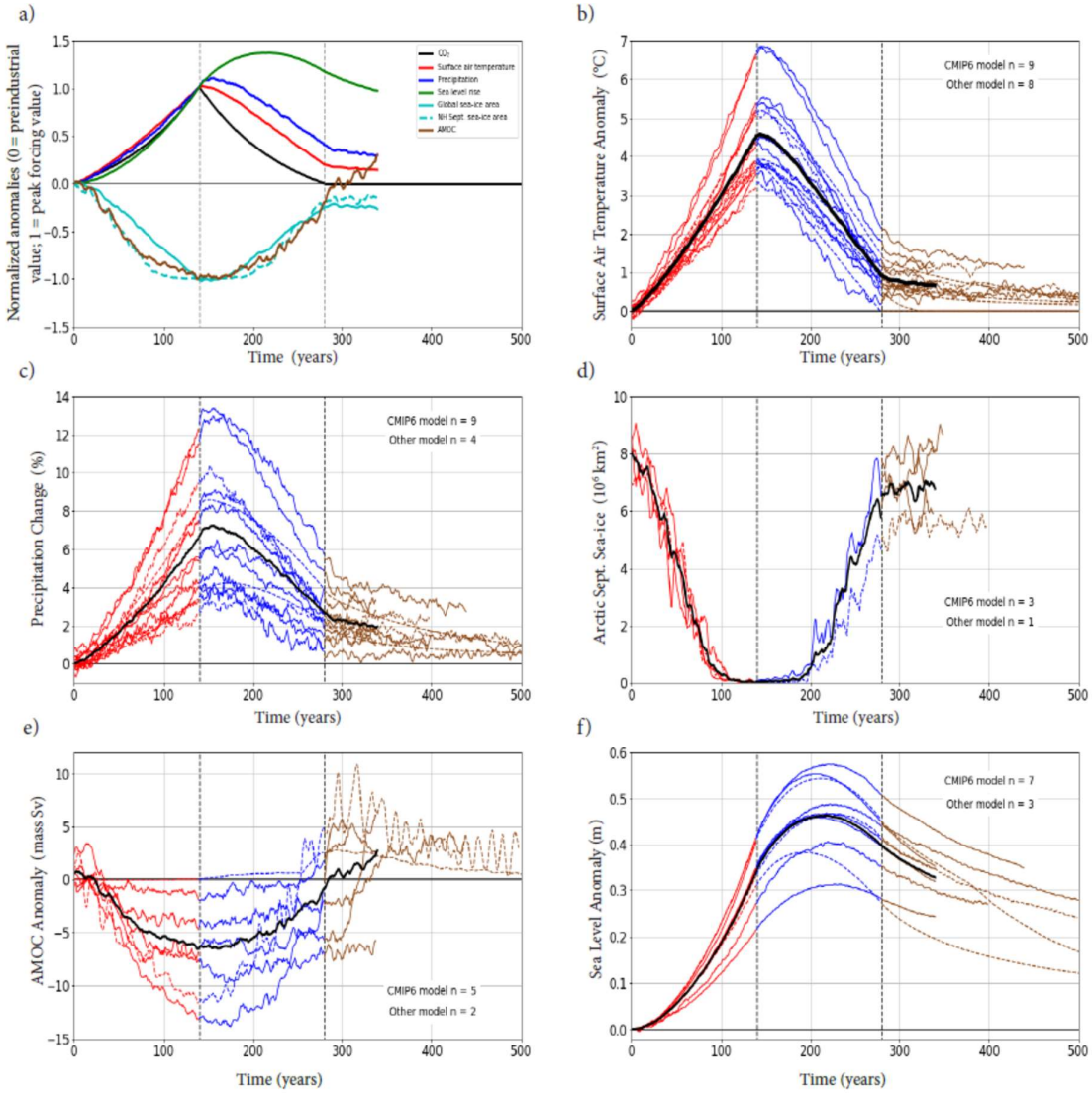


**Figure 4.40:** Multi-model simulated response in global and annual mean climate variables against for a ramp up followed by ramp down of $CO_2$. Atmospheric $CO_2$ increases from pre-industrial level at a rate of 1% $yr^{-1}$ to 4×$CO_2$, then decrease at the same rate to pre-industrial level and then remains constant. a) normalized ensemble mean anomaly of key variables as a function of year, including atmospheric $CO_2$, surface air temperature, precipitation, sea level rise, global sea-ice area, Northern Hemisphere sea ice area in September, and Atlantic meridional overturning circulation (AMOC); b) surface air temperature; c) precipitation; d) Arctic September sea ice area; e) AMOC; f) thermostatic sea level; 5-year running means are shown for all variables except the sea level rise ; In b-f, red lines represent the phase of $CO_2$ ramp up, blue lines represent the phase of $CO_2$ ramp down, brown lines represent the period after $CO_2$ has returned to pre-industrial level, and black lines represent multi-model mean. For all of the segments in b-f, the solid coloured lines are CMIP6 models and the dashed lines are other models (i.e., EMICs, CMIP5 era models). Vertical dashed lines indicate peak $CO_2$ and when $CO_2$ again reaches pre-industrial value. The number of CMIP6 and non-CMIP6 model results used in each panel is indicated in each panel. The time series for the multi-model means (b-f) and the normalized anomalies (a) is terminated when data from all models are not available in order to avoid the discontinuity in the time series.

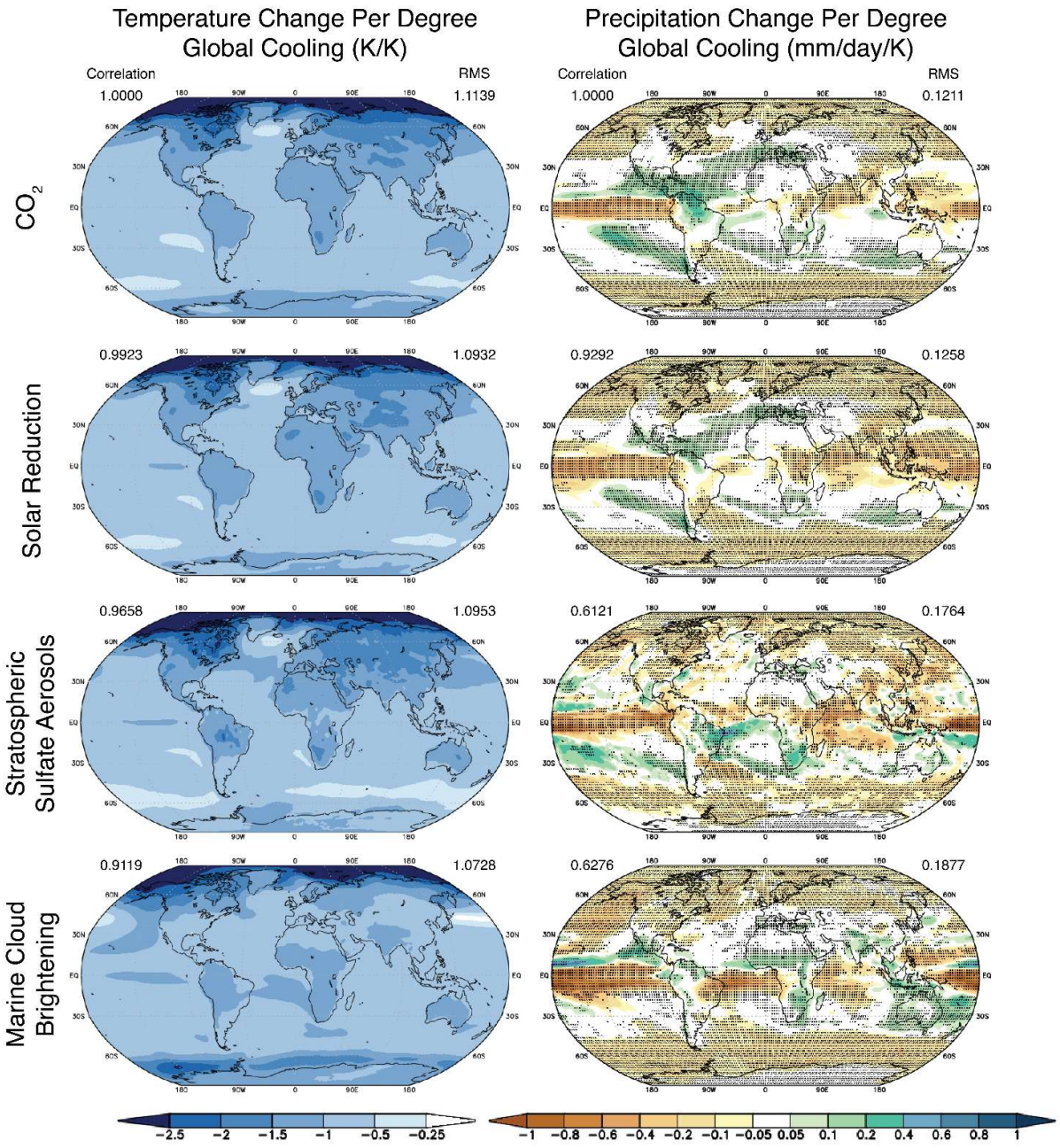


**Figure 4.41:** Multi-model response per degree global mean cooling in temperature (left) and precipitation (right). Top row shows the response to a $CO_2$ decrease, calculated as the difference between piControl and abrupt4xCO2 (11 model average); second row shows the response to a solar reduction, calculated as the difference between GeoMIP experiment G1 and abrupt4xCO2 (11 model average); third row shows the response to stratospheric sulphate aerosol injection, calculated as the difference between GeoMIP experiment G4 and RCP4.5 (6 model average); and bottom row shows the response to marine cloud brightening, calculated as the difference between GeoMIP experiment G4cdnc and RCP4.5 (8 model average). All differences (average of years 11-50 of simulation) are normalized by the global mean cooling in each scenario, averaged over years 11-50. Stippling in the right panels shows regions where 75% of the models agree on the sign of the precipitation response. The values of correlation represent the spatial correlation of each SRM-induced temperature and precipitation change pattern with that of low-$CO_2$ induced change pattern (top row). RMS (root mean square) is calculated based on the fields shown in the maps (normalized by global mean cooling).

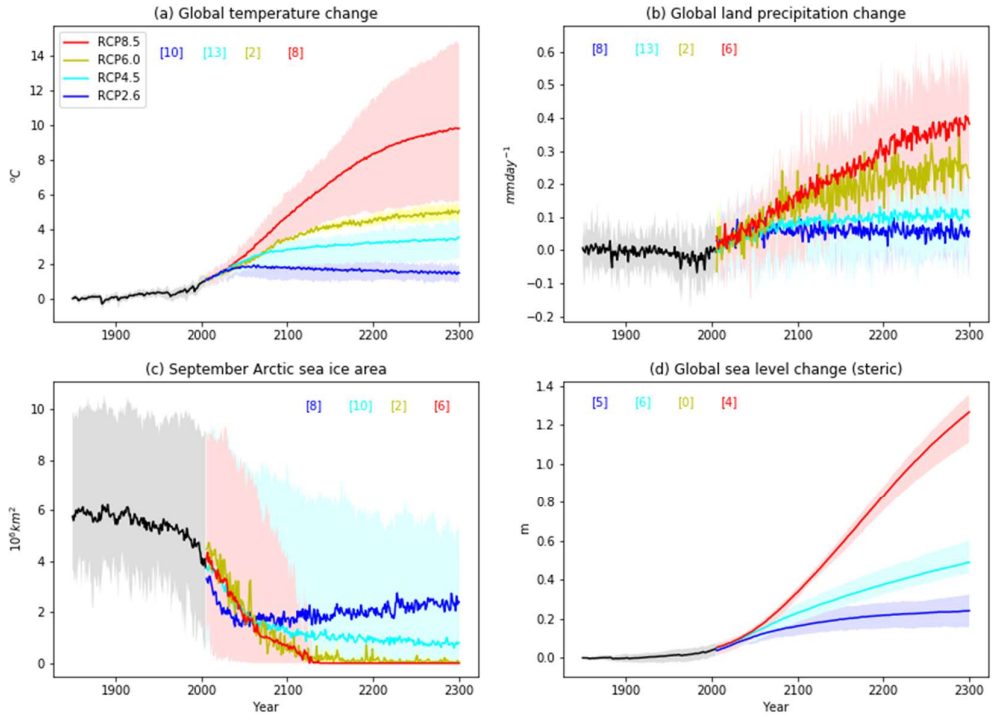


**Figure 4.42:** Simulated climate changes up to 2300 from the CMIP5 multi-model ensemble under the four RCP scenarios. (a) projected GSAT change (b) global land precipitation change (c) September Arctic sea-ice extent (millions square km) (d) thermal steric sea level rise. Coloured numbers denote the number of models included in each panel for each scenario. Models used: CanESM2, bcc-csm1-1, GISS-E2-R, GISS-E2-H, IPSL-CM5A-LR, IPSL-CM5A-MR, CNRM-CM5 MPI-ESM-LR, CESM1-CAM5, CCSM4, CSIRO-Mk3-6-0, HadGEM2-ES, MIROC5, MIROC-ESM.

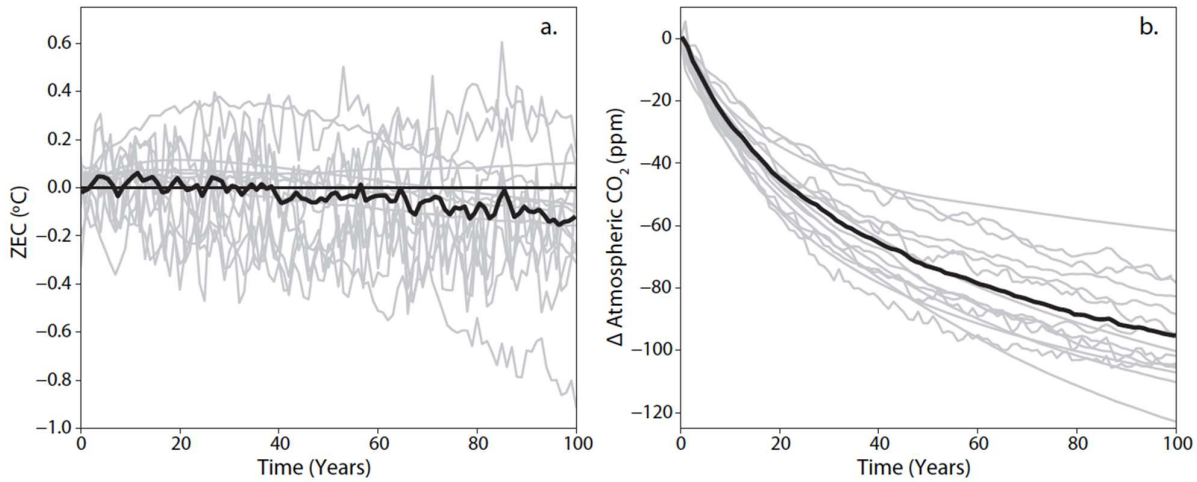


**Figure 4.43:** Zero Emissions Commitment (evolution of GSAT) (panel a) and change in atmospheric $CO_2$ concentration (panel b) following cessation of emissions under the experiment where 1000 PgC was emitted following the 1% experiment (A1; Jones et al., 2019). ZEC is the temperature anomaly relative to the estimated temperature at the year of cessation. $ZEC_{50}$ is the 20-year mean GSAT change centred on 50 years after the time of cessation (see Table 4.8). Multi-model mean shown as thick black line, individual model simulations in grey.

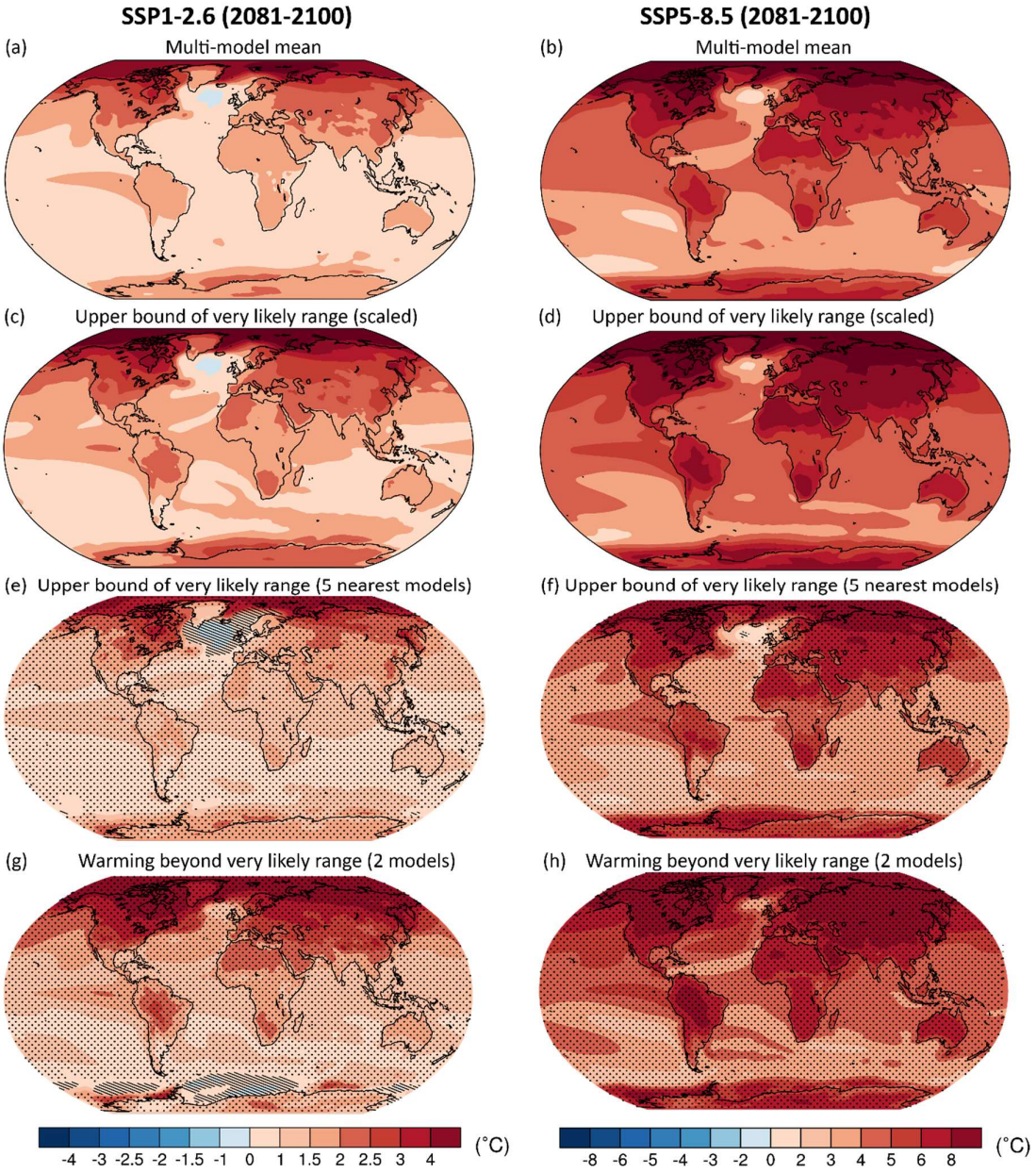


**Figure 4.44:** Changes in annual mean temperature in 2081–2100 relative to 1995–2014 in (left) SSP1-2.6 and (right) SSP5-8.5. (a,b) Multi-model mean changes consistent as in section 4.5.1. (c-h) Estimates for annual mean warming pattern consistent with a storyline representing a physically plausible high-global-warming storyline for 2081-2100. (c,d) Pattern-scaled multi-model mean warming to the GSAT of the upper bound of the assessed *very likely* range (scaled from CMIP6 multi-model mean of 3.9°C for SSP5-8.5 and 1.1°C for SSP1-2.6, see section 4.3.1, to 95% of assessed range 4.61°C for SSP5-8.5 and 1.4°C for SSP1-2.6, see section 4.3.4). (e,f) Average of five models with GSAT warming nearest to the upper estimate of the *very likely* range (CESM2, CNRM-CM6-1, EC-Earth3, EC-Earth3-Veg, IPSL-CM6A-LR for SSP1-2.6 and CESM2, CESM2-WACCM, CNRM-CM6-1, EC-Earth3, EC-Earth3-Veg for SSP5-8.5), (g,h) Average of two models (CanESM5 and UKESM) projecting warming exceeding the *very likely* range.

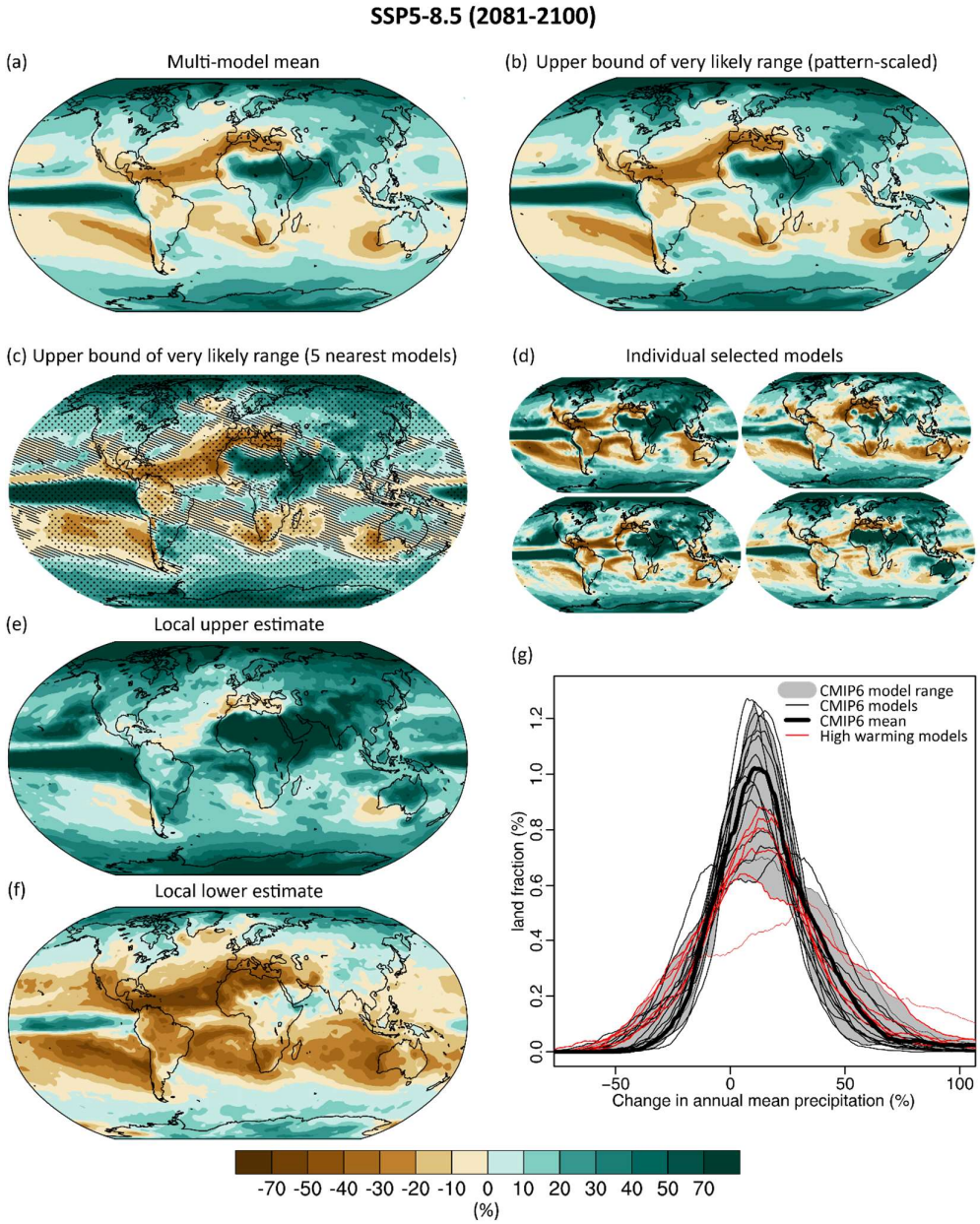


**Figure 4.45:** Changes in annual mean precipitation in 2081–2100 relative to 1995–2014 in SSP5-8.5. (a) Multi-model mean changes consistent as in section 4.5.1. (b,c) Estimates for annual mean precipitation changes consistent with a storyline representing a physically plausible high-global-warming storyline for 2081-2100. (b) Pattern-scaled multi-model mean precipitation to the GSAT of the upper bound of the *very likely* range (scaled from CMIP6 multi-model mean of 3.9°C, see section 4.3.1, to 95% of assessed range see section 4.3.4). (c) Average of five models with GSAT warming nearest to the upper bound of the *very likely* range (CESM2, CESM2-WACCM, CNRM-CM6-1, EC-Earth3, EC-Earth3-Veg) (d) Annual mean precipitation changes in four individual model simulations with high GSAT warming showing. (e,f) Local upper estimate (95% quantile across models) and lower estimate (5% quantile across models) at each gridpoint. Information at individual gridpoints comes from different model simulations and illustrates local uncertainty range but should not be interpreted as a pattern. (g) Area fraction of changes in annual mean precipitation 2081-2100 relative to 1995-2014 for individual model simulations (thin black lines) and models with high GSAT warming (thin red lines). The grey range illustrates the 5-95% range across CMIP6 models for each and the solid black line the area fraction of the multi-model mean pattern shown in (a).

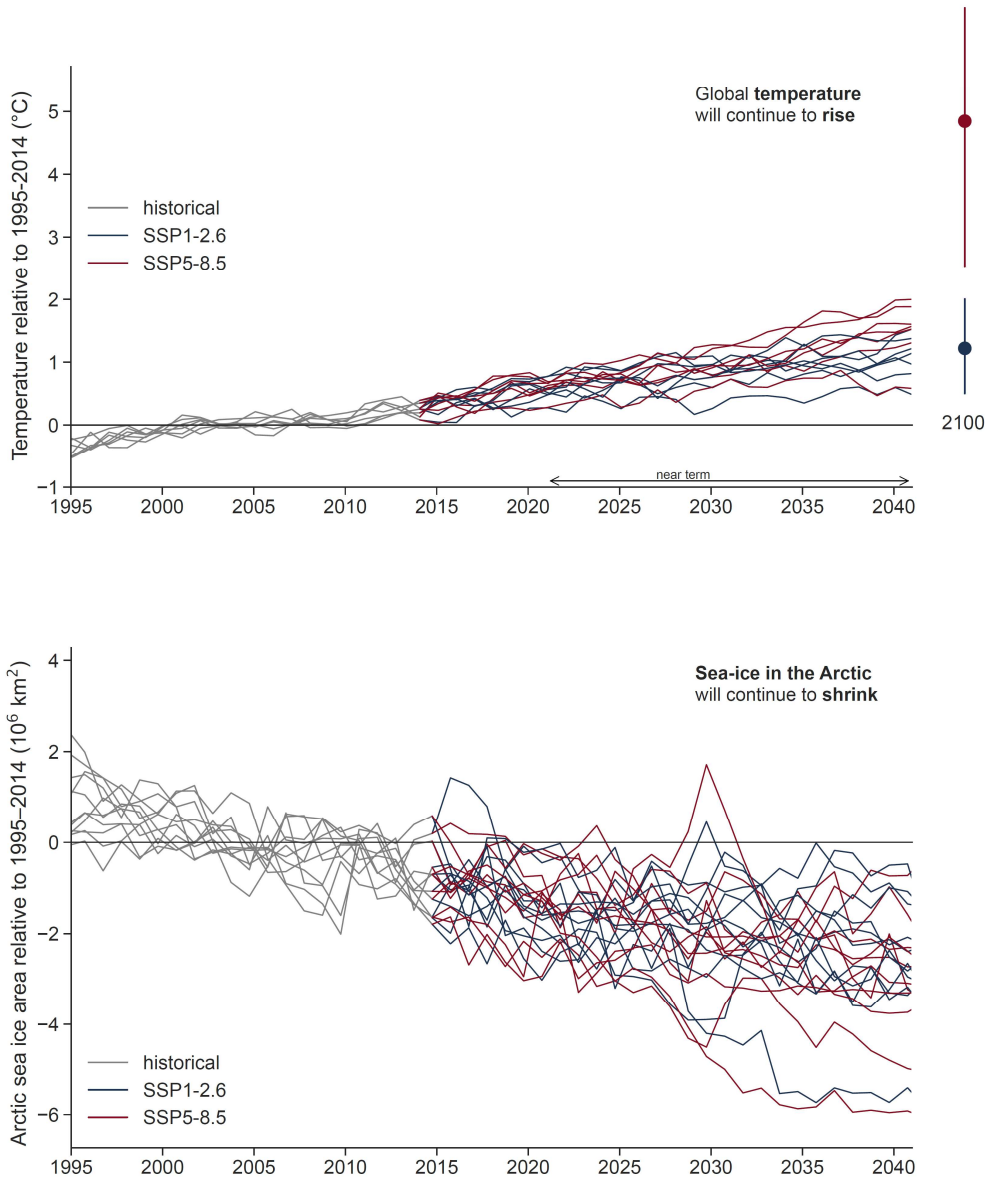


**FAQ 4.1, Figure 1:** Simulations over the period 1995–2040, encompassing the recent past and the near-term future, of two important indicators of global climate change, (a) globally averaged surface air temperature, and (b), the area of Arctic sea ice in September. Both quantities are shown as deviations from the average over the period 1995–2014. The grey curves are for the historical period ending in 2014; the colours refer to one low- and one high-emission SSP scenario as shown in the inlet. In (a), the bars to the right show the range of simulated values for year 2100. In (b), some models simulate an ice-free Arctic in September already in the near term, which is why they show no further decrease. [Placeholder figure, based on eleven currently available CMIP6 models. To be updated with other CMIP6 models and, possibly, shading for indicating uncertainty.]

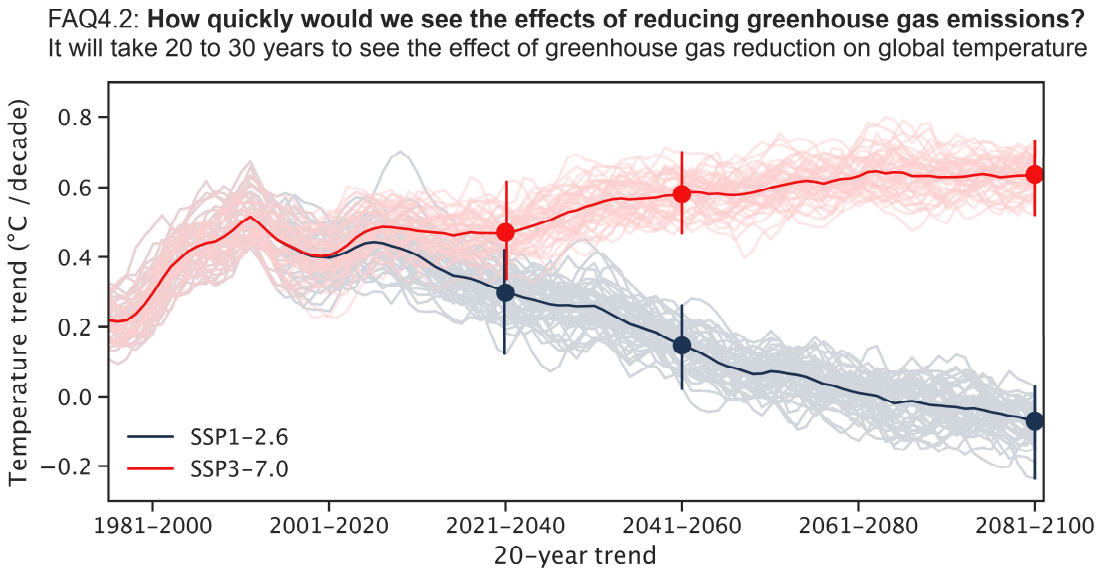


**FAQ 4.2, Figure 1:** Illustrating when the benefits of emissions reduction might become detectable in globally averaged surface air temperature. The figure shows twenty-year linear trends, and the time axis is defined such that in each year, the trend over the preceding twenty years is displayed. Shown are the results from a single CMIP6 model, CanESM5, run under one scenario that can be considered to represent no mitigation (SSP3-7.0) and one scenario that represents mitigation (SSP1-2.6). For each scenario, the model is run fifty times with very slightly different conditions for the year 1850 (each scenario simulation starts from the end of a historical simulation ending in 2014). Differences between individual runs are caused by simulated natural internal variability and can be considered an uncertainty that cannot be reduced. The figure shows the average of all fifty simulations as full-drawn lines and the individual simulations as shaded lines. Three time periods are highlighted, by showing the distribution of simulated twenty-year trends for each scenario, calculated retrospectively in years 2040 (trend over the near-term period), 2060 (trend over the mid-term period), and 2100 (trend over the long-term period). The filled circle shows the average over all fifty simulations, and the bars show the ranges of simulations in each scenario.

## FAQ 4.3: What are the spatial patterns of climate change?

Climate change is not uniform, warming will be stronger in the Arctic, the Northern Hemisphere and on land

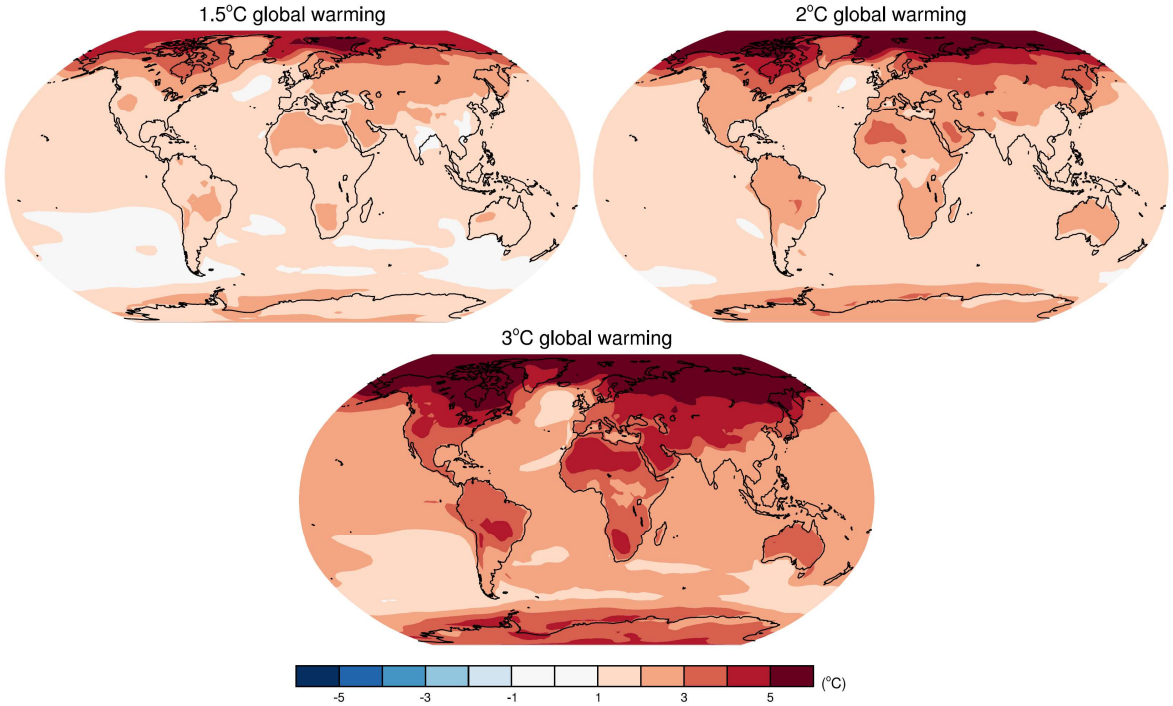


**FAQ 4.3, Figure 1:** Example for a robust warming pattern, which is presented here as the average of fourteen CMIP6 models using the scenario SSP3-7.0. Surface warming relative to 1850–1900 is shown for time periods over which the globally averaged surface warming is 1.5°C, 2°C, and 3°C, respectively. We recognise the strong warming over the Arctic, generally stronger warming over land than over the ocean, generally stronger warming in the Northern Hemisphere than in the Southern Hemisphere, and less warming over the central subpolar North Atlantic.